

https://dspace.org/

Understanding the Karoo dolerite systems using geological and geophysical methods around Beaufort West, South Africa

Dube, Mpumelelo

2021
https://hdl.handle.net/10539/33049

Downloaded from a DSpace repository. https://dspace.org/

Understanding the Karoo dolerite systems using geological and geophysical methods around Beaufort West, South Africa



UNIVERSITY OF THE
WITWATERSRAND,
JOHANNESBURG

Mpumelelo Dube

Student No: 1558006

School of Geosciences, University of the Witwatersrand, Johannesburg, Private Bag 3, 2050 Wits, South Africa

Declaration

I declare that this dissertation is my own, unaided work. It is being submitted for the Master of Science at the University of the Witwatersrand, Johannesburg. It has not been submitted before for any degree or examination at any other University.

_____

(Signature of candidate)

_____08_____day of ___November_____2021_____at___Midrand___

Abstract

Mapping the location of Karoo dolerites is crucial for safe and efficient extraction of shale gas and groundwater exploration around the main Karoo Basin. To aid this mapping, a high-resolution airborne magnetic survey was conducted near Beaufort West in the Western Cape Province. This survey is a component of a five-year geoscientific research project by the Council for Geoscience. Dolerite sills and dykes, and other features, were mapped by filtering the magnetic data. Five lineament orientations associated with dolerite dykes, kimberlites, fractures and faults were mapped: E-W to ESE-WNW, NNW-SSE, NW-SE, NE-SW and NNE-SSW. The magnetic data mapped the extent of the hidden central parts of the sills in the dissected terrain. Sill boundaries are preferentially aligned NW-SE.

Depth estimations were obtained for the magnetic sources using the Radial Averaged Power Spectrum technique and compared with SOEKOR seismic data along line BV21. Power spectrum transformation estimated depths to shallow magnetic sources of approximately 0.3 km or less. Intermediate sources are estimated to lie at depths between 3 km and 0.7 km. A 2D forward magnetic model was also generated over the seismic line. The model confirmed the inclined sheets connected to an inner sill, as mapped on the seismic data. The inner sill was mapped at ~ 1 km depth on the seismic data. This sill is part of the intermediate magnetic sources determined from the depth estimation technique.

The mapped linear features were used to conduct a stress and strain analysis of the study area. Structural trends suggest that the principal compressive stress (σ_1) direction related to the formation of the Cape Fold Belt and development of the Karoo sedimentary basin between ca. 300 and 215 Ma was N-S, but that it switched to NW-SE related to dextral strike-slip tectonics during Gondwana break-up between ca. 190 and 180 Ma. Post-rifting kimberlite dykes display predominant NNE to NE trends, suggesting that the principal extensional stress (σ_1) occupied a NNE-SSW orientation. Kimberlite emplacement occurred during the Early Jurassic (170 Ma) to Mid-Cretaceous (80 Ma). This study shows that aeromagnetic surveys provide valuable complementary data for mapping the shape, size, depth and geometry of magnetic Karoo dolerites, thereby contributing evidence of the tectonic history in the Karoo basin.

In memory of my grandmother

Emelina Dlamini

1936 – 2020

Acknowledgments

I would like to express my gratitude to my principal supervisor Dr. Stephanie Enslin and co-supervisor Prof. Roger Gibson for providing undivided support and guidance during my MSc studies at the Witwatersrand University.

I am grateful to Council for Geoscience for financial support throughout my MSc studies and granting permission to use recently collected geophysical data. My sincere gratitude to Dr. Taufeeq Dhansay and Dr. Thomas Muedi for always being willing to assist with geological discussions whenever I approached them. My sincere gratitude to Dr. Leonie Maré for supervising the physical property measurements in the Petro-physical Laboratory. I would also like to thank my colleagues in the Geophysics and Remote Sensing Competency, especially Dr. Emmanuel Sakala, Mr. Emmanuel Chirenje, Ms. Minenhle Buthelezi and Ms. Mihlali Hobo, for their encouragement, support and the great advice they shared with me.

Special thanks to my family, my husband (Sphiwe Dube) and children (Ungazile and Unawe Dube) for their support and for always cheering for me throughout my studies, and to my mother, Sphiwe Shiba, for her encouraging words shared through our phone calls.

Last but not least, to the Almighty God for His protection and wisdom throughout my studies.

Table of Contents

Declaration i
Abstract ii
Acknowledgments iv
1 CHAPTER ONE - INTRODUCTION 1
1.1 General Introduction 1
1.2 Aim and Objectives 4
1.3 Dissertation structure 4
2 CHAPTER TWO - REGIONAL GEOLOGY 7
2.1 Introduction 7
2.1.1 Dwyka Group 9
2.1.2 Ecca Group 10
2.1.3 Beaufort Group 12
2.1.4 Stormberg Group 13
2.2 Karoo Dolerite Suite and Drakensberg Group 15
2.2.1 Karoo Dolerite Suite 15
2.2.2 Drakensberg Group 23
2.3 Tectonic setting 24
2.3.1 Karoo foreland basin phase 26
2.3.2 Terminal-phase rifting and magmatism 29
2.4 Fossil fuel resources of the Karoo Basin 33
2.5 Summary 36
3 CHAPTER THREE - LOCAL GEOLOGY 37
3.1 Lithostratigraphy 40
3.1.1 Abrahamskraal Formation 40
3.1.2 Middleton Formation 40
3.1.3 Balfour Formation 40
3.1.4 Jurassic Age Dolerites 41
3.1.5 Kimberlites 44
3.1.6 Quaternary sediments 45
3.2 Structural geology 45
3.2.1 Folds 46
3.2.2 Faults 46
3.2.3 Fractures 47
3.2.4 Foliation 49

3.3 Monitoring boreholes 52
3.4 Summary 55
4 CHAPTER FOUR – MAGNETIC METHOD 57
4.1 Introduction 57
4.1.1 Induced magnetism 57
4.1.2 Natural Remanent Magnetism (NRM) 58
4.1.3 Magnetic susceptibility 58
4.1.4 Magnetic survey instrumentation 59
4.2 Magnetic standard processing 60
4.2.1 Diurnal variations 60
4.2.2 Levelling 60
4.2.3 International Geomagnetic Reference Field (IGRF) 60
4.3 Magnetic data filtering techniques 61
4.3.1 Sunshading 61
4.3.2 Vertical derivative 63
4.3.3 Analytic signal 64
4.3.4 Wavenumber domain 65
4.3.5 Reduce to the pole 66
4.3.6 Power spectrum transformation 67
4.4 Summary 70
5 CHAPTER FIVE – DTM, MAGNETIC AND SEISMIC DATA 71
5.1 Introduction 71
5.2 Digital Terrain Model (DTM) data 73
5.3 Magnetic Data 74
5.3.1 Survey specifications 74
5.3.2 Processing 77
5.3.3 Results 79
5.4 Seismic Data 85
5.5 Summary 87
6 CHAPTER SIX - PHYSICAL PROPERTIES DATA 88
6.1 Introduction 88
6.1.1 Sample preparation 88
6.1.2 Magnetic susceptibility measurement 90
6.1.3 Natural Remanent Magnetisation (NRM) 93
6.1.4 Density measurement 95

6.2 Summary 102
7 **CHAPTER SEVEN – INTERPRETATION** 103
7.1 Mapping using Filtered Magnetic Data 103
7.1.1 Separating Deep Sources 103
7.1.2 Shallow magnetic lineaments 105
7.1.3 Shallow Magnetic Bodies 110
7.2 Mapping using Seismic Data 112
7.3 Estimating Depths using the Radial Averaged Power Spectrum Method 114
7.4 Summary 123
8 CHAPTER EIGHT - FORWARD MODELLING 125
8.1 Magnetic Modelling 125
8.2 Forward modelling interpretation 128
8.3 Summary 141
9 CHAPTER NINE – DISCUSSION AND CONCLUSION 142
9.1 Summary of geology results 142
9.2 Summary of geophysical results 143
9.2.1 Deep sources 143
9.2.2 Shallow magnetic component 143
9.3 Tectonics history and stress field based on magnetic data 150
9.3.1 Regional tectonics 150
9.3.2 Stress field analysis 151
9.4 Application of results 156
9.4.1 Shale gas resource 156
9.4.2 Groundwater 157
9.5 Conclusion 157
10 REFERENCES 160
11 APPENDICES 169
11.1 APPENDIX A: Radially Averaged Power spectrum (RAPS) graphs 169

List of Figures

Figure 1-1 Simplified map of the study area showing principal infrastructure and river systems. The study area's location is shown within the map of South Africa (inset). . 3
Figure 2-1 The extent of the Southern African Karoo Basins and flood basalts. The position of the section in Figure 2-2 across the main Karoo Basin is shown. The study area is located in the main Karoo Basin where Beaufort West town is located (Woodford and Chevallier, 2002a). 8
Figure 2-2 Cross-section of the Main Karoo Basin from Woodford and Chevallier (2002), see Figure 2-1 for the location of the section line. The Main Karoo Basin is deepest along its southern margin bounded, by the Cape Fold Belt and becomes shallow to the north. 8
Figure 2-3 Stratigraphy of the Karoo Basin either side of longitude 24° E (from Bamford, 2016, with modifications from Cole *et al.,* 2016a; Smith, 1993; Viglietti *et al.,* 2017; SACS, 2019). 14
Figure 2-4 Schematic cross-section of the Karoo Basin showing the vertical and lateral distribution of the Karoo intrusive network in the Karoo stratigraphy (Galerne, 2009). 16
Figure 2-5 The 5 major sill and ring complex systems (mega-basins) found in the western to eastern Karoo (modified from Woodford and Chevallier (2002b) overlain over simplified geological map. The study area is located southwest of Victoria West major sill and ring complex system..... 17
Figure 2-6 The conceptual saucer-shaped model of a dolerite dyke-sill-ring complex. The model is characterised by an inner sill that forms the saucer bottom; an inclined sheet that connects the lower inner sill and the upper outer sill; the outer sill situated approximately 100 m above the inner sill; minor secondary sills/ring structures found within larger sill-ring complexes, and sub-vertical dykes usually found where ring structures are well developed (Chevallier and Woodford, 1999). 18
Figure 2-7 Victoria West sill and ring complex (Chevallier and Woodford, 1999). ... 20
Figure 2-8 (a) Map showing the locations of SOEKOR boreholes, dolerite thickness greater than 150 m (red triangles), dolerite thickness less than 150 m (green triangles) and zero dolerite south of dolerite line (blue triangles). SOEKOR seismic lines are marked (black lines), including one that passed through the study area (BV21). The surveys (including wells) are divided into regions: northwest region around Fraserburg (FB), southwestern region around Graaff-Reinet (GR) and two regions in the southeast around Somerset-East (SE) and Queenstown (QT). Additional wells are in Aliwal North (AN) and East London (EL). (b) Broadly west-east profile through the main Karoo Basin showing the dolerite distribution (horizontal lines) in SOEKOR deep wells; location of the profile shown by dotted line in (a). Stratigraphic boundaries are marked with dotted lines: BF – Beaufort Group, EC – upper Ecca Group, ES – Ecca shales, DW – Dwyka Group, BV – Bokkeveld (red square), TM – Table Mountain Group (orange triangle), GG – Granite-gneiss basement (blue square). Solid black lines indicate the total well depth. Above 400 m of dolerite occurs in each well in the east/southeast and northwest while <150 m of dolerite is found in the southwest wells (modified after Rowsell and De Swardt, 1976; Scheiber-Enslin *et al.,* 2014b). 22
Figure 2-9 Stratigraphy of the Barkley East Formation and its relation with the Clarens Sandstone at Tafelkop (Eastern Cape Province) (Marsh, 1991). 24

Figure 2-10 Model for the deposition of the main Karoo Basin as a retro-arc foreland basin. Accommodation space was created during phases of loading and unloading of the crust by the Cape Fold Belt, which caused the crust to flex. Renewed thrusting caused orogenic loading that gave rise to foredeep subsidence and uplift in the forebulge. The reverse occurred during orogenic quiescence where the foredeep undergoes uplift as a result of isostatic rebound, compensated by subsidence of the forebulge. The study area is located within the foredeep (Catuneanu, 2004). 28
Figure 2-11 Plate tectonic reconstruction for breakup of East and West Gondwana (Storey and Kyle, 1997; Woodford and Chevallier, 2002a). Mantle plume (red circle) positioned off the east coast of South Africa gave rise to the Karoo flood basalts and dolerites..... 29
Figure 2-12 Structural map of the main Karoo Basin showing the three principal structural domains (Western Karoo Domain, Eastern Karoo Domain and Transkei-Lesotho-Northern Karoo Domain) defined by Woodford and Chevallier (2002b). The study area is located south of Loxton town where the northern part of the study area forms the southern edge of the Western Karoo Domain. 30
Figure 2-13 (A) Block diagram of a transform fault between two rift systems compared with (B) Simplified map of Karoo dyke orientations in the main Karoo Basin interpreting them as an E-W right-lateral shear zone transform fault between two rift systems off the east and west coasts of South Africa (Woodford and Chevallier, 2002b). 31
Figure 2-14 Tectonic and stress field history of the main Karoo Basin from Permian to Jurassic times: A. east-west fold axes of the Cape Fold Belt developed under north-south compressive stress regime; B. Early phase of Godwanaland break-up associated with the formation of NNW jointing and faulting along existing zones of crustal weakness; and C Rifting phase of Gondwanaland break-up where dolerites intruded along NNW fractures and on E-W shear/dislocation zones (Woodford and Chevallier, 2002b). 33
Figure 2-15 A simplified geological map displaying the study area (red outline). The shale gas resource is shown as a dotted black line and was outlined by de Kock *et al.* (2017). 35
Figure 3-1 1: 50 000 geological map of the study area. The dolerite sills and dykes were digitised from SPOT 5 satellite images at a scale of 1: 10 000 by Cole *et al*. (2016b). Faults and fracture measurement locations are shown. The SOEKOR seismic line BV21 is shown in pink and the monitoring boreholes are shown as blue markers. 38
Figure 3-2 Lithostratigraphy of the Beaufort Group showing updated terminology for stratigraphic subdivisions. The Teekloof Formation has been replaced by the Middleton Formation (Poortjie and Hoedemaker Members) and the Balfour Formation (Oukloof and Steenkamps Vlakte Members) west of longitude 24° E, and the Koonap Formation) east of longitude 24° E has been replaced by the Abrahamskraal Formation (SACS, 2019; Viglietti *et al.,* 2017; Cole *et al.,* 2016b). 39
Figure 3-3 Morphology of the Tweeling-Brandwag Dyke, Beaufort West (Campbell, 1975; Woodfordand Chevallier, 2002a). The dyke offset is observed in Tweeling Farm. 42
Figure 3-4 Inclined dolerite sheet cutting through the sub-horizontal Beaufort Group sediments in De Jager's Pass (off-road NE of Beaufort West). 43

Figure 3-5 Contact between Poortjie Member and Karoo dolerite sill where baking of the country-rock is evident. 44
Figure 3-6 Slickenside development on fault plane sub-parallel to bedding. (a) Slickensides are associated with calcite mineralization (location: 22,563° E; -32,493° S) and (b) Groove surfaces associated with quartz mineralization (location: 21,911° E; -32,696° S). 47
Figure 3-7 Foliation development around Beaufort West in response to discrete shearing (co-ordinates: 32.0745 S; 22.7474 E, Cole *et al.,* 2016b). 50
Figure 3-8 Stereo-diagrams of fracture orientations mapped from remote sensing throughout the study area (black rose diagrams) from Dhansay *et al.* (2017). Current stress axes from earthquake focal mechanisms are shown around the study area (red beach balls), the location of the large paleo-seismic event (yellow triangle). Orientations of fracture sets that could be reactivated at hydraulic pressures above hydrostatic pore fluid pressures, e.g. 32 MPa up to approximately 10 MPa, shown by top right insert. 51
Figure 3-9 Graphical borehole logs of R01-BW and R02-BW (Nxokwana *et al.,* 2018). 54
Figure 4-1 Field variation of susceptibility for ferromagnetic, paramagnetic and diamagnetic substances (Hrouda *et al.,* 2009). 59
Figure 4-2 Sun shading linear features (a) presented data; (b) sun shaded data azimuth 0, inclination 30°, order 0; (c) sun shaded data azimuth 0, inclination 30°, order 1 and (d) sun shaded data azimuth 0, inclination 30°, order 5 (Cooper, 2003). 63
Figure 4-3 Stages for filter data from space to wavenumber domains (Reeves, 2005). 1. The input grid is transformed from space to 2D spectrum in the wavenumber domain; 2. 2D spectrum is multiplied with a filter. 3. Filtered 2D spectrum is converted back to space domain through reverse transformation..... 66
Figure 4-4 Skewness of a magnetic anomaly due to a uniform arbitrarily magnetized source below Earth's surface in an obliquely oriented Earth's magnetic field (left) and its reduced-to-pole expression in the vertical magnetization and vertical field conditions (right) (Ravat, 2007). 67
Figure 4-5 Depth estimation technique using the energy spectrum in the wavenumber domain (Reeves, 2005). (a) The radial averaged power spectrum curve after spectrum calculation. (b) Band pass filter was applied to separate the deep magnetic component associated by allowing the low frequencies to pass through and rejecting the higher frequencies. (c) A Butterworth filter was applied by allowing the high frequencies to pass associated with the near-surface magnetic component and rejecting the low frequencies. (d) represents the noise component of the data and it is usually rejected. 69
Figure 5-1 Study area in the Western Cape (hatched block) within the high resolution aeromagnetic and radiometric survey block (larger shaded red block). The small and big square boxes represent 1: 50 000 and 1: 250 000 map sheets respectively. 71
Figure 5-2 Study area (red outline block) within the high-resolution aeromagnetic and radiometric survey block superimposed with N-S survey line direction and E-W tie line direction. This is a zoomed image to show the line path. 72

Figure 5-3 Digital Terrain Model (DTM) of the study area with superimposed towns and rivers. 74
Figure 5-4 Image showing positioning of instrumentation on aircraft (AeroPhysX, 2017). 77
Figure 5-5 Original TMI data with IGRF. (a) Sun-shaded to 45° (NE) and (b) Sun-shaded to 315° (NW) to highlight NE striking anomalies. 80
Figure 5-6 (a) IGRF corrected high-resolution Total Magnetic Intensity (TMI) data image for the study area acquired at 200 m line spacing (b) IGRF corrected regional Total Magnetic Intensity (TMI) data image for the study area acquired at 1 km line spacing. High frequency/short wavelength anomalies are clearly visible on the high-resolution magnetic data in (a) compared to (b). 81
Figure 5-7 Total magnetic intensity data reduced to the pole (RTP) resulting in magnetic anomalies that are aligned with their causative bodies. 83
Figure 5-8 Filtering of the TMI data to better highlight shallow magnetic sources: (a) First vertical derivative and (b) Analytic signal. 84
Figure 5-9: Seismic section BV21 showing the inclined sheet (dark green) and Karoo (WH – Whitehill Formation, light green), Cape Supergroup sediments (BV – Bokkeveld Group, yellow; TBM – Table Mountain Group, blue) and basement (pink). 86
Figure 6-1 Struers Labotom-5 cutting machine: (a) Labelled exterior of the equipment and (b) interior of the equipment (Struers, 2014). 90
Figure 6-2 MFK1-FA multi-function kappabridge instrument setup was used to measure bulk magnetic susceptibility (AGICO). 91
Figure 6-3 (a) JR-6A spinner magnetometer. (b) Measuring positions for semi-automatic mode: P1 represents x direction, P2 represents z-axis of the specimen coordinate system and P3 horizontal in y direction (AGICO, 2018a)..... 94
Figure 6-4 Demagnetizer instrument used to dry the specimen for a period of 24 hours at 110 °C. 96
Figure 6-5 Mettler Toledo instrument used for density measurements. (a) Measuring mass/weight of the sample in the air and (b) measuring the mass/weight of the sample in the beaker with water. 97
Figure 6-6 Sartorius equipment used for density measurements. The bucket contains water to immerse the suspended sample with a copper wire. 97
Figure 7-1 Low-pass filtered image of the regional TMI data for South Africa used to highlight deep magnetic anomalies. The edge of the Namaqua and Natal Belts (black line), and the Beattie and Williston Magnetic Anomalies (dashed black and blue lines) are marked. 104
Figure 7-2 (a) First vertical derivative of the TMI data and (b) Inferred magnetic lineament interpretation derived from the first vertical derivative. The major E-W dyke known as Tweeling-Brandwag dyke is shown by a black arrow on (b) (Campbell, 1975; Woodford and Chevallier, 2002a)..... 108
Figure 7-3 A comparison of rose diagram plots generated from (a) high-resolution airborne magnetic data and (b) the surface geology by Dhansay *et al.* (2017). There is a correlation between surface geology north of Beaufort West and shallow sub-surface geology (<200 m)..... 109
Figure 7-4 (a) Analytic signal of the TMI data and (b) Inferred magnetic bodies (sills and inclined sheet) derived from the analytic signal image in (a). 111

Figure 7-5 (a) 1:50 000 geology of the study area. SOEKOR seismic line (BV21) is indicated (pink line) and extends off the map to the south; (b) Seismic section BV21 showing the inclined sheet (dark green) and Karoo (WH – Whitehill Formation, light green), Cape Supergroup sediments (BV – Bokkeveld Group, yellow; TBM – Table Mountain Group, blue) and basement (pink). 113
Figure 7-6 Reduced to the pole (RTP) data divided into 20 blocks so that the Radially Average Power Spectrum Method could be applied to each block. 114
Figure 7-7 (a) Radial averaged power spectrum of the RTP TMI data over seismic line BV21. The depth to the magnetic sources are estimated from the slope of the curve. The deep magnetic sources (blue line) are at approximately 3 km, intermediate sources at approximately 1 km and shallow magnetic sources (red line) are at approximately 0.3 km. (b) the inner sill depth (~1 km) estimated from radial averaged power spectrum is shown by a red arrow on the seismic data (profile line BV21).. 116
Figure 7-8 Radially averaged power spectrum performed from RTP TMI dataset for block 14. Depth to magnetic sources are estimated from the slope of the curve. The deep magnetic sources (blue line) are at approximately 1.6 km and shallow magnetic sources (red line) are at approximately 0.24 km. Due to the fact that the region was divided into smaller blocks, this means that the “deep” source is not a true reflection of the much deeper basement sources expected in the region. 118
Figure 7-9 Understanding the shallow and deep magnetic sources in the southern portion of the study area (block 14, Figure 7-6): (a) 1:50 000 geological map showing the recently drilled boreholes R01-BW and R02-BW; (b) Reduce to the pole of the TMI data; (c) High-pass filtered magnetic component of the RTP (shallow sources); (d) Low-pass filtered magnetic component of the RTP data (deep sources). 119
Figure 7-10. Radially averaged power spectrum performed on regional RTP TMI data for entire study area. Depth to magnetic sources are estimated from the slope of the curve. The deep magnetic sources (blue line) are at approximately 11 km..... 121
Figure 7-11. Low-pass filtered magnetic component of the RTP data used to highlight deep magnetic sources such as edge of the Namaqua and Natal Belts, and the Beattie and Williston Magnetic Anomalies..... 122
Figure 8-1 TMI and filtered magnetic data: (a) TMI before IGRF is removed (green) and residual TMI after IGRF was removed (red) showing a change in amplitude and slight shift; (b) Residual TMI (red) compared with high pass filtered data with a cutoff of 2000 m (green) and 400 m (blue). The cutoff of 2 000 m still shows regional features compared to a cutoff of 400 m, which highlights shallow features. The long-wavelength magnetic response in the south of the profile on the residual TMI data compared to the high-pass data with a cutoff of 400 m, is related to deep bodies such as those causing the Beattie and Williston Anomalies; (c) Residual TMI (red) compared with high pass filtered data with a cutoff of 400 m (blue) and 150 m (green). The cutoff of 150 m enhances noise in the data, and therefore a cutoff of 400 m was selected. The cultural noise due to two power lines represented by sharp peaks north of magnetic data profile. 126
Figure 8-2 Comparison of (a) Space Shuttle Radar Topography Mission (SRTM) data (orange), high-pass filtered magnetic data with a cutoff of 400 m (blue), and (b) seismic section BV21 showing location of the inclined sheet. The outcropping inclined sheet (black arrow) shows up as a topographic high and magnetic anomaly on (a). 127

Figure 8-3 Investigation of magnetic anomalies along seismic profile BV21: (a) 1:50 000 scale geology map with seismic profile (black line) (modified after Cole *et al.,* 2016b). (b) Google Earth image. (c) Profile with TMI, high pass filtered data (cutoff of 400 m) and elevation data. The location of magnetic anomalies of interest (coloured arrows, labelled 1-6) are marked in a, b and c. 129
Figure 8-4 Outcropping inclined sheet (Anomaly 2, dark blue arrow) on Google Earth with seismic profile BV21 (black line), dolerite sill (black arrow) and minor sill (Anomaly 3, red arrow). 131
Figure 8-5 A 3-D model showing five common morphological and structural features associated with Karoo sills (Chevallier and Woodford, 1999). 131
Figure 8-6 Victoria West sill and ring. Inclined sheet linking the lower inner sill to the upper outer sill and two inclined sheets are connected to an inner sill (Chevallier and Woodford, 1999). The location of the cross-section line is found in Chapter 2, Figure 2-8. 132
Figure 8-7 Model along seismic profile BV21. In (a) Anomaly 3 is modeled as a separate inclined sheet coming off from the 1 km deep sill. The inclined sheet does not outcrop. In (b) Anomaly 3 is modeled as an offshoot from the main inclined sheet. 132
Figure 8-8 Anomaly 4 location (purple arrow) on Google Earth image with seismic profile BV21 marked (black line) and MT stations (green markers). The anomaly could be due to a buried inclined sheet linking the outcropping sheet to the west and east (shown by yellow arrows). 133
Figure 8-9 Magnetotelluric (MT) data (bottom image) collected where seismic line BV21 crosses, location of both surveys are shown on Google Earth in Figure 8-8. The conductive Whitehill Formation is mapped around 2 km depth with a shallower resistive sill above it around 1 km depth from around 6 km distance along the profile. What appears to be a dyke or inclined sheet cross-cutting the Whitehill Formation is mapped at 4 km distance (Integrated Geoscience Solutions, 2018). The dyke appears wider than expected due to the resolution and spacing of the MT data. 134
Figure 8-10 Anomaly 5 location on first vertical derivative image (green arrow in the north of the image). The anomaly could be due to two buried dykes that are very close to each other and have a smooth magnetic signal which could indicate that they are not very close to surface. 135
Figure 8-11 Anomaly 5 and 6 locations (green and brown arrow) on 1:50 000 geology image with seismic section BV21 marked (black line). Anomaly 7 and 8 are due to power lines (pink arrows). 136
Figure 8-12 Final 2D magnetic model over SOEKOR seismic line BV21 showing dolerite sills, sheets and dykes. Magnetic models are non-unique and therefore, anomaly 4 shown by puple arrow is modelled as dyke (a) dyke and (b) an inclined sheet due to a lack of outcropping data to constrain the model. 138
Figure 8-13 Mag2dc model showing a thicker inner sill. The thicker inner sill did not fit the observed magnetic curve suggesting that the sill is thinner. 139
Figure 8-14 A 2D magnetic model, (a) showing a thick sill of 30 m at 2 000 m (b) shows multiple sills of 10 m thickness at different depths (1 000 m, 1 500 m and 2 000 m). Both models shows small magnetic field response and cannot be relied on to map a thick sill at greater depths or multiple sills. 140

Figure 9-1 Lineament interpretation derived from first vertical derivative magnetic data overlain with SPOT 5 interpreted lineaments. Black and pink arrows show some of the lineaments that correlated well from both datasets. The remaining lineaments (shorter lines) were mapped from the magnetic data. 145
Figure 9-2 Diagram showing three major structural features in the Western Karoo Domain Woodford and Chevallier (2002b) Similar features are delineated in the study area from the airborne high-resolution magnetic data. Dolerite dykes are, in general, thick, single and irregular lineaments. Kimberlites are swarms of regular, thin, sub-parallel lineaments. Master joints are dense swarms of evenly spaced, parallel and straight fractures. 146
Figure 9-3 Magnetic bodies interpreted from analytic signal magnetic data overlain with SPOT 5 interpreted dolerite sills. The magnetic data allow for differentiation of individual sills, and confirm their circular to elliptical shape. The shallow subsurface extent of the sills can be mapped using magnetic data, while SPOT 5 data is limited to outcrop. The magnetic data therefore highlights the connected and extensive nature of the dolerite sills..... 147
Figure 9-4 Simplified geological map showing the study area (red outline) partly located on the shale gas resource outlined by de Kock *et al.* (2017) (dotted black outline). 148
Figure 9-5 Rose diagram plots generated from magnetic lineaments mapped. (a) and (b) are from the northwest and northeast of the field area (on the escarpment). These two plots are similar to E-W to ESE-WNW and NE-SW trends. (c) shows E-W to ESE-WNW and NE-SW trends that are located at the edge of the escarpment, and (d) shows a dominant NE-SW trend. All trends are related to Karoo dolerite dykes, kimberlite dykes and fractures and faults. 151
Figure 9-6 A N-S compressional stress regime resulted in structural features in the study area such as fold axis/hinges and thrusts (Cape Fold Belt). This stress regime dominated during the Late Palaeozoic time. 152
Figure 9-7 The stress regime that dominated in Southern Africa during the Jurassic, when the dolerite emplacement took place. A NW compressional stress regime resulted in majority of structural features e.g. dolerite dykes and texture within dolerite sills in the study area being oriented NW. 154

List of Tables

Table 2-1 Tectono-sedimentary history summary of both Cape Fold Belt and Karoo Supergroup (Hälbich *et al.,* 1983). 28
Table 3-1 Fault-slip field measurements in the study area measured by Dhansay *et al.* (2017). 48
Table 3-2 Boreholes drilled within the study area that intersected the Karoo dolerite showing logs and total thicknesses (Nxokwana *et al.,* 2018). 53
Table 5-1 Aircraft type and on-board geophysical equipment (AeroPhysX, 2017). . 75
Table 5-2 Survey Specifications for high-resolution airborne magnetic and radiometric data (AeroPhysX, 2017). 76
Table 5-3 Survey specifications for regional magnetic data. 76
Table 5-4 Acquisition and processing parameters for Karoo Basin SOEKOR seismic surveys (Fatti and Du Toit, 1970). 85
Table 6-1 The magnetic susceptibility measurements of the samples using a MFK1-FA multi-function kappabridge, with three repeats. 91
Table 6-2 Comparison of average measured magnetic susceptibility values and those from Telford *et al.* (1976). 92
Table 6-3 Natural Remanent Magnetism measurements for the specimens. 95
Table 6-4 Dry bulk density measurement measured with Mettler Toledo equipment. 99
Table 6-5 Dry bulk density measurements measured with Sartorius equipment. .. 100
Table 6-6 Comparison of average measured density values and those from Telford *et al.* (1976). 101
Table 7-1 Deep boreholes located close to the study area (Roswell and de Swart, 1976). 112
Table 7-2. Depth Estimations for remaining blocks using Radially Averaged Power spectrum (RAPS). Deep magnetic sources were not resolved due to a small window size used (a limitation of the method), however the shallow sources were delineated. 120
Table 9-1. Kimberlite ages for Victoria West cluster north of the study area. 155

List of symbols and nomenclature

h	Depth of the magnetic source
M	Inducing magnetisation of the material
R	Lambertian reflector
ρ	Density
σ_1	Sigma 1
BMA	Beattie Magnetic Anomaly
CGS	Council for Geoscience
CFB	Cape Fold Belt
NRM	Natural Remanent Magnetism
DMRE	Department of Mineral Resources and Energy
TMI	Total Magnetic intensity
RTP	Reduce to the pole
FFT	Fast Fourier Transformation
RAPS	Radial Averaged Power Spectrum
DTM	Digital Terrain Model
IGRF	International Geomagnetic Reference Field

1 CHAPTER ONE - INTRODUCTION

1.1 General Introduction

Shale gas could be exploited as an energy source in South Africa in the Karoo Basin (Holness *et al.,* 2016). The Basin formed on the Gondwana supercontinent between the Late Carboniferous and Middle Jurassic as a response to subduction of the palaeo-Pacific plate underneath Gondwana (Lock, 1980; Johnson *et al.,* 2006) that gave rise to the formation of the Cape Fold Belt along the southern basin margin. The termination of basin formation was followed by the massive outpouring of lavas related to the onset of regional rifting that culminated in splitting of the Gondwana continent (Chevallier and Woodford, 1999; Duncan and Marsh, 2006). These continental flood basalts were fed by an intricate network of dolerite dykes and sills that intruded the basin (Duncan and Marsh, 2006).

Thermal metamorphism and fracturing related to dolerite intrusion can affect the physical properties of the country rock. In the study area, the country rock includes shale formations at depth that might host gas. Fracturing of the country rock can occur during dolerite magma emplacement and cooling (Woodford and Chevallier, 2002a). These fractures could have trapped gas migrating from heated Karoo shales, or acted as pathways for gas to migrate from the shale formations (Scheiber-Enslin *et al.,* 2014b).

The Department of Mineral Resources and Energy (DMRE) tasked the Council for Geoscience (CGS) to conduct a five-year geo-environmental baseline study in the Karoo region using geological and geophysical methods (Cole *et al.,* 2016b). The geo-environmental baseline study is divided into three phases: Phase 1 is characterised by a regional and local study including 1:50 000 geological mapping, high-resolution magnetic and radiometric acquisition, ground geophysics over selected areas, groundwater investigation and seismological monitoring; Phase 2 involves deep borehole drilling, monitoring boreholes and observation boreholes coupled with downhole geophysics, rock core and groundwater sampling; and Phase 3 includes

borehole results analysis coupled with gas and mineral analysis and continuous monitoring of geo-environmental changes and impacts (Cole *et al.,* 2016b and Nxokwana *et al.,* 2018). The observation boreholes were drilled to characterise shallow groundwater aquifers. The monitoring boreholes were drilled to examine the quality of groundwater at greater depths and its occurrence, and also to examine the lithology and geological structures (Nxokwana *et al.,* 2018).

High-resolution airborne magnetic and radiometric datasets were acquired in the southern part of the main Karoo Basin over a total line of approximately 72 300 km, covering twelve 1:50 000 topography map sheets around the Beaufort West region (AeroPhysX, 2017). This study focuses on a limited region between latitude 31.918° and 32.581° S and longitude 22.417° and 22.916° E. **Figure 1-1** shows the study area overlain with rivers and major infrastructure such as roads, railway line and power lines. The edge of the high plateau that covers a large part of northern South Africa runs through the study area. This edge is called the Great Escarpment. In general, high topography in the area correlates with outcropping resistant dolerite sills. Beaufort West is the only town in the study area.

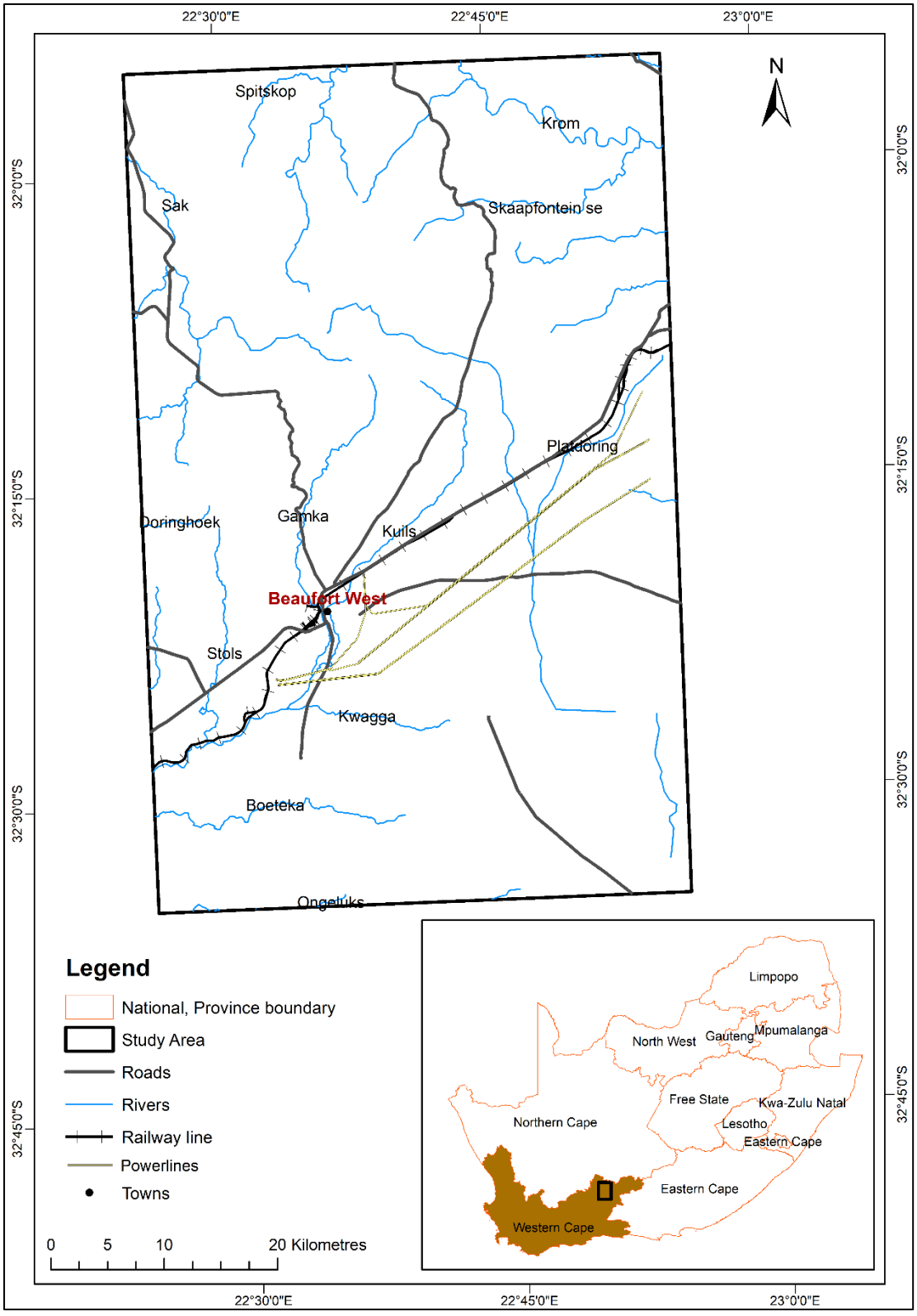

Figure 1-1 Simplified map of the study area showing principal infrastructure and river systems. The study area's location is shown within the map of South Africa (inset).

The main focus of this study is the qualitative and quantitative processing and interpretation of high-resolution airborne magnetic data. This data was used to better understand the geometry of the dolerite dykes and sills that have intruded the Karoo sediments in the study area. The dolerite dykes and sills carry high magnetic values while the Karoo sediments carry no or low magnetic values, therefore, the magnetic data is a very useful tool with which to delineate the dolerites.

1.2 Aim and Objectives

This study aimed at understanding Karoo dolerite dykes and sills using mainly the applications of airborne magnetic data.

The following were the objectives of the proposed research:

- To interpret high-resolution magnetic data to delineate geological structures such as dykes, sills and faults.
- To perform depth estimation for locating both deep and shallow magnetic sources.
- To generate 2D or 3D magnetic models over interesting features (dyke, sill, fault/fracture system) to understand the geometry, depth and thickness of these features.
- To correlate mapped geological structures in the study area with interpreted high-resolution magnetic data structures.
- To determine the large-scale implications of the results obtained from the study area both laterally and vertically.

1.3 Dissertation structure

The dissertation is divided into ten (10) chapters, summarised below:

- Chapter 1 introduces the study background, which includes the formation of the Karoo Basin and the intrusion of the Karoo dolerites into the Karoo sediments. The chapter also explains the main purpose of the geo-environmental baseline

study which the Council for Geoscience is conducting and the aims and objectives of this study.

- Chapter 2 outlines the Karoo stratigraphy, including intrusive and extrusive rocks; as well as the distribution of SOEKOR deep wells together with the overall dolerite thicknesses intersected. The chapter also focuses on the tectonic setting of the Karoo Basin, which includes various Cape Fold Belt and Karoo Basin models and intracontinental rifting linked to the Karoo igneous episode. Finally, it describes the main Karoo Basin structural domains and shale gas potential in the basin.
- Chapter 3 focuses on work done for the geo-environmental baseline study in the area. This includes 1:50 000 geological mapping, coupled with revised stratigraphy and structural mapping, and drilling of observation boreholes.
- Chapter 4 outlines the theory of the magnetic method used to map the Karoo dolerites and related structures, namely; how magnetic data is processed, what filters can be applied to the data and how they work, and interpretation of magnetic data.
- Chapter 5 outlines the data acquisition for the Digital Terrain Model (DTM), regional and high resolution airborne magnetic data and Soekor seismic data. Results are also presented in this chapter.
- Chapter 6 covers measurement of physical properties made in the Council for Geoscience Petro-Physical Laboratory. Measurements include magnetic susceptibility, Natural Remanent Magnetism (NRM) and density on rock samples from the study area. Results are compared with those recorded in the literature.
- Chapter 7 focuses on the interpretation of results and correlation with the published literature. Interpretation involves separation of deep and shallow magnetic sources, mapping shallow linear features, correlating shallow magnetic bodies with seismic and geological data, and depth estimations using Radial Averaged Power Spectrum.
- Chapter 8 shows a 2D magnetic model over SOEKOR seismic line BV21 to confirm that the shape and extent of the bodies mapped from the seismic data correlate with the magnetic anomalies.

- Chapter 9 focuses on the discussion of all results and the large-scale implications of these results. This includes a stress analysis deduced from the interpreted magnetic data.
- Chapter 10 covers the conclusion of all study findings and the recommendations for future work.

2 CHAPTER TWO - REGIONAL GEOLOGY

2.1 Introduction

The Karoo Supergroup comprises sedimentary rocks and minor volcanics between ca. 300 and 183 Ma age that are important for their fossil record and fossil fuel resources (Catuneanu *et al.,* 2005). Karoo Supergroup rocks are preserved in several basins in southern and central Africa and Madagascar, and similar rocks exist in South America, India and Australia (**Figure 2-1**). Their wide distribution across multiple continental fragments provided some of the earliest evidence in support of plate tectonics and the Gondwana supercontinent (Johnston, 2000). In total, these rocks may originally have covered an area of some 4 500 000 km^2 of Gondwana (Johnson *et al.,* 2006), with deposition occurring in contrasting tectonic settings, namely, extensional basins in the north and a foreland basin in the south (Catuneanu *et al.,* 2005). This study is focussed within the main Karoo Basin, located in South Africa, which contains the thickest and most complete Karoo Supergroup stratigraphy (Angielczyk *et al.,* 2014, **Figure 2-1**). The deepest part of the main Karoo Basin lies along the southern margin of the basin, which is bounded by the Cape Fold Belt (CFB), and stratigraphy thins to the north (**Figure 2-2**). To the southeast, the basin is truncated by the Indian Ocean coastline. Towards the north, the Karoo strata overlie a variety of Archaean and Palaeo- to Mesoproterozoic rocks of the Kaapvaal craton and the Namaqua-Natal Belt; however, its southern portions rest on Ordovician to Carboniferous (~500-330 Ma) Cape Supergroup rocks, which unconformably overlie Neoproterozoic basement rocks (Catuneanu *et al.,* 2005; Tankard *et al.,* 2009).

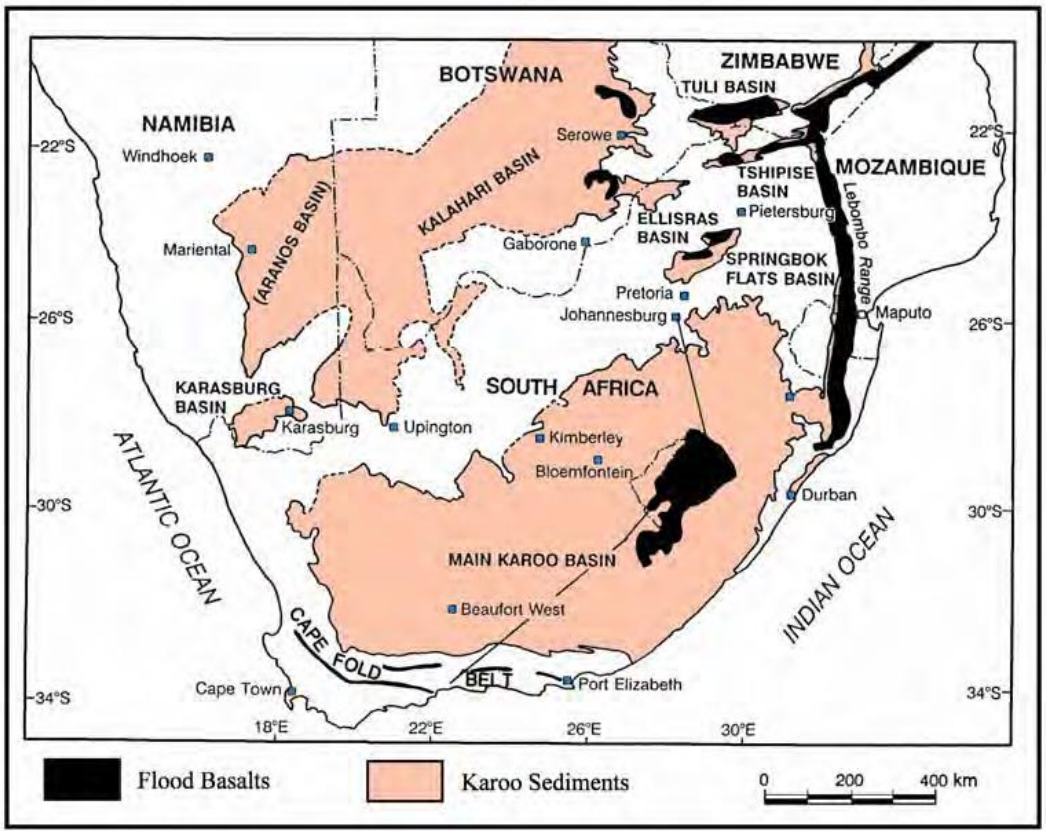

Figure 2-1 The extent of the Southern African Karoo Basins and flood basalts. The position of the section in Figure 2-2 across the main Karoo Basin is shown. The study area is located in the main Karoo Basin where Beaufort West town is located (Woodford and Chevallier, 2002a).

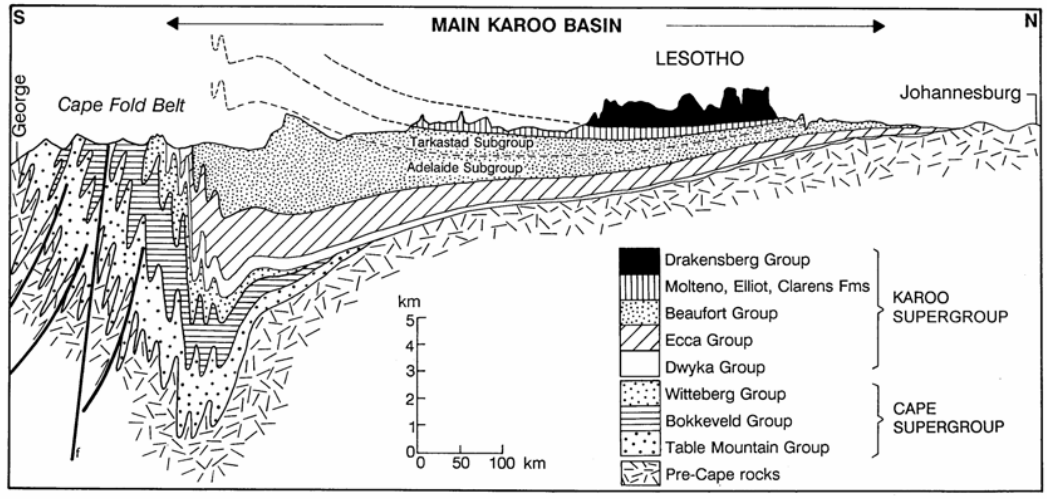

Figure 2-2 Cross-section of the Main Karoo Basin from Woodford and Chevallier (2002a), see Figure 2-1 for the location of the section line. The main Karoo Basin is deepest along its southern margin bounded, by the Cape Fold Belt and becomes shallow to the north.

2.2 Main Karoo Basin stratigraphy

Karoo Supergroup sedimentation began from approximately 300 Ma during Pangea supercontinent formation (formed by amalgamation of Gondwana and Laurussia) to the Middle Jurassic (~183 Ma) breakup of Gondwana. The main Karoo Basin is interpreted by some as a retroarc foreland basin (Catuneanu *et al.,* 1998). The sedimentary fill was predominantly sourced from uplift-induced erosion of the Cape Fold Belt (Catuneanu *et al.,* 1998; Johnson *et al.,* 2006).

The tectonic setting of the main Karoo Basin is described in Section 2.3. The basin stratigraphy reflects an overall trend from marine environments to lacustrine/terrestrial environments, commencing with the glacio-marine basal Dwyka Group and pelagic sediments of the lower Ecca Group. The upper Ecca Group was associated with shallow marine sedimentation and was followed by fluvial sedimentation of the Beaufort Group and overlying lower Stormberg Group (Molteno and Elliot Formations). Aeolian environments dominate the upper Stormberg Group (Clarens Formation; Catuneanu *et al.,* 2005). Johnson *et al.* (2006) mentioned that the end of sedimentation in the main Karoo Basin is marked by the Drakensberg Group. The Drakensberg Group is described in Section 2.2. The Karoo stratigraphy west of longitude 24° E only includes the Dwyka, Ecca and Beaufort Groups (**Figure 2-3**). The stratigraphy relevant to the study area was updated with recently approved modifications by the South African Committee for Stratigraphy (SACS) published by Viglietti *et al.* (2017), SACS (2019) and Cole *et al*. (2016a).

2.1.1 Dwyka Group

The Karoo Supergroup deposition commenced with the Dwyka Group, which was deposited during the Late Carboniferous to Early Permian. During this time, Gondwana was situated within the polar latitudes covered by glaciers and continental ice sheets (Smith, 1990). These glaciers form thick sequences of diamictites that are

dominated by silt. The diamictites attain a thickness of 800 m in the foredeep (Visser, 1991). The Dwyka Group rests on Precambrian bedrock in the northern margin of the basin, unconformably or paraconformably overlies the Cape Supergroup rocks in the south, and unconformably overlies the rocks of both the Natal Group and Msikaba Formation east of the basin (Johnson *et al.,* 2006).

2.1.2 Ecca Group

The Permian Ecca Group consists of a clastic sequence of mudstone, sandstone, siltstone, minor conglomerate and coal outcrops in the northern parts of the basin (Johnson *et al.,* 1996; Catuneanu *et al.,* 2005). The Ecca Group is thinner elsewhere in southern Africa; in the main Karoo Basin, it attains a thickness of 3000 m particularly in the foredeep (Catuneanu *et al.,* 2005). With the retreat of ice sheets, Ecca deposition started with the Prince Albert Formation, which is dominated by well laminated olive-grey mudrock attaining a thickness of approximately 300 m in the western part of the basin (Wickens, 1994). This was followed by the Whitehill Formation, which is characterised by pyrite-bearing black shale dominated by clay minerals near its base and which is associated with dolomite concretions (Visser, 1992). The Whitehill Formation is thickest in the south (approximately 80 m) and thins northward, with a thickness of approximately 20 to 30 m recorded in the central-western Karoo Basin (Cole and McLachlan, 1994). These formations in the basin crop out in the southern, western and northwestern parts of the basin.

Johnson *et al*. (2006) mentioned that the Ecca Group is further subdivided into several formations (excluding Prince Albert and Whitehill Formations). They identified distinct geographic areas (southern, western, northwestern and northeastern characterised by different packages). Collingham Formation overlies the Whitehill Formation. The Collingham Formation outcrops in the southern and western parts of the basin. In the southern part of the basin, the Collingham Formation is overlain by Vischkuil, followed by Laingsburg, Ripon, Fort Brown and Waterford formations. The western and northwestern regions are characterised by the Tierberg, Skoorsteenberg, Kookfontein and Waterford formations, while the northeastern region is characterised by the Pietermaritzburg, Vryheid, and Volksrust formations.

The Collingham Formation is composed of continuous, thin beds of siliceous mudrock that range in thickness from 30 to 70 m (Woodford and Chevallier, 2002aa). The formations that lie west of longitude 24° E will be briefly discussed.

2.1.2.1 Western and northwestern regions

In the western and northwestern regions of the Karoo Basin the Tierberg Formation is dominated by an argillaceous succession. It reaches an overall thickness of about 700 m in the western part of the basin and thins northeastwards to approximately 350 m. The Skoorsteenberg Formation, which has a thickness of 250 m, has been identified as a lens-shaped arenaceous unit between the Tierberg and the Kookfontein formations (Johnson *et al.,* 2006). Johnson *et al.* (2006) reported that with a sharp contact Kookfontein Formation overlies Skoorsteenberg Formation. The Kookfontein Formation has a thickness of approximately 350 m. The base of the formation is characterised by horizontally laminated dark-grey shales that alternate with clastic rhythmites, and alternating siltstones and thin sandstones are found at the top of the formation (Johnson *et al.*, 2006). The Waterford Formation overlies the Kookfontein and Tierberg formations in the western region. The formation is dominated by arenaceous sediments and alternate with mudrock or rhythmite units and is approximately 130 m thick (Woodford and Chevallier, 2002a).

2.1.2.2 Southern region

In the southern region, the Vischkuil Formation overlies the Collingham Formation. This formation is composed dominantly of argillaceous strata and has a varying thickness that ranges between 200 and 400 m (Catuneanu *et al.,* 2002). The Vischkuil Formation is overlain conformably by the Laingsburg Formation. The Laingsburg Formation consists of four sandstone-rich units that are divided by shale units making up a total thickness of about 400 m (Catuneanu *et al.,* 2002). The Ripon Formation overlies the Laingsburg Formation. It is similar to the Laingsburg Formation and appears to have been deposited as a submarine fan system mainly consisting of poorly sorted, fine-grained sandstone that alternates with mudrock and rhythmite (Johnson *et al.,* 1996). The Fort Brown Formation is composed predominantly of

rhythmites and mudrock. The rhythmites of the Fort Brown Formation are part of marine shelf shales and are also pro-delta deposits (Catuneanu *et al.,* 2005). This formation has an average thickness of approximately 1 000 m (Woodford and Chevallier, 2002a).

2.1.3 Beaufort Group

The Beaufort Group is composed of the lower, Lopingian, Adelaide and the upper, Lower Triassic, Tarkastad Subgroups (Johnson *et al.,* 2006). It attains a thickness of about 3 500 m in the foredeep with a fining-upward succession of sandstones and mudstones deposited by overbank flooding of meandering rivers (Johnson *et al.,* 2006).

The Adelaide Subgroup comprises alternating mudrocks and lithofeldspathic sandstones (Johnson *et al.,* 2006). The mudrocks are generally blocky and massive. The Abrahamskraal and Teekloof formations make up the Adelaide Subgroup west of longitude 24° E and are considered as equivalent to the Abrahamskraal Formation - known previously as Koonap Formation and Middleton formation - east of longitude 24° E (Woodford and Chevallier, 2002a; Cole *et al.,* 2016a; Johnson *et al.,* 2006). The Abrahamskraal Formation has a varying thickness in the southwest of the basin. South of Beaufort West, it is thinner (approximately 2150 m) but thickens to 2575 m between 33°2.0' S and 33°5.0' S (Day and Rubidge, 2014).

Cole and Wipplinger (2001) divided the Teekloof Formation into the Poortjie, Hoedemaker, Oukloof and Steenkampsvlakte Members; however, based on biostratigraphic correlation, Smith (1993) and Viglietti *et al.* (2017) correlated the Oukloof and Steenkampsvlakte members with the Balfour Formation to the east of longitude 24° E. Both the Middleton Formation (east of longitude 24° E) and Teekloof Formation (west of longitude 24° E) are dominated by red mudstone but the boundaries are linked by the sandstone-rich unit at their respective bases, the Poortjie Member is at the base of the Teekloof Formation and the Oudeberg Member at the base of the Balfour Formation.

2.1.4 Stormberg Group

The Molteno, Elliot and Clarens formations previously known as the Stormberg Group (SACS, 1980) form part of the upper stratigraphy of the Karoo Supergroup. The Upper Triassic Molteno Formation overlies the Beaufort Group and consists of alternating medium- to coarse-grained sandstones and mudstones (Woodford and Chevallier, 2002a). Sedimentation of the Elliot Formation began during the Upper Triassic and ended in the Lower Jurassic; it is dominated by red mudstones (Woodford and Chevallier, 2002a). The Lower to Middle Jurassic Clarens Formation forms the youngest Karoo sedimentary sequence and consists of well-sorted, medium- to fine-grained sandstone. The formation rests conformably over the red mudstones of the Elliot Formation.

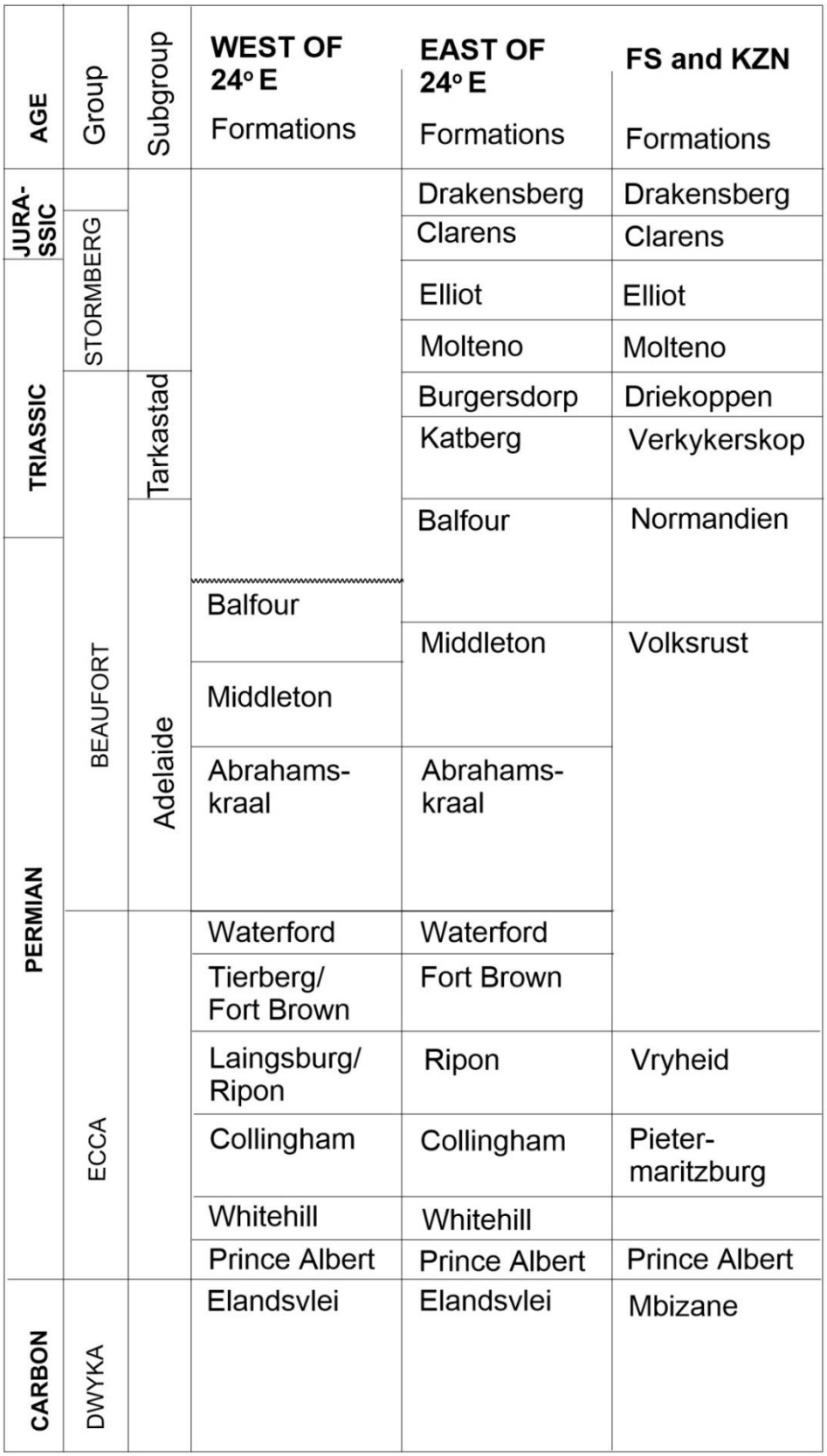

Figure 2-3 Stratigraphy of the Karoo Basin either side of longitude 24° E (from Bamford, 2016, with modifications from Cole *et al.,* 2016a; Smith, 1993; Viglietti *et al.,* 2017; SACS, 2019).

2.2 Karoo Dolerite Suite and Drakensberg Group

2.2.1 Karoo Dolerite Suite

Jurassic age dolerite sills and dykes, commonly known as the Karoo Dolerite Suite (Duncan and Marsh, 2006), form an important component in the Karoo Basin stratigraphy. These are linked to the continental flood basalts of the extrusive Drakensberg Group (Eales *et al.,* 1984) and together comprise the Karoo Large Igneous Province (LIP) (Johnson *et al.,* 2006). This volcanism effectively terminated the deposition of the Karoo Supergroup sediments (Smith, 1990). The Karoo LIP is linked to the breakup of Gondwana in the Middle Jurassic (Smith, 1990; Catuneanu *et al.,* 2005), which involved, inter alia, dextral shear displacement between southern Africa and the Falkland Plateau associated with the opening of the Atlantic Ocean (Johnston, 2000).

The dolerites form a three-dimensional interconnected network of dykes and sills, with local variations in orientation (**Figure 2-4**) (Duncan and Marsh, 2006), making it challenging in many cases to identify individual sheets and magmatic systems. The majority of the dolerite intrusions are characterised by poor surface exposure, making it challenging to accurately delineate them. The dolerite intrusions occur predominantly in the upper Ecca Group and the Beaufort Group but they do occur in the earlier stratigraphy of the Karoo Supergroup (Woodford and Chevallier, 2002a).

The near-vertical dykes in many instances branch into sills and, less commonly, cut across them (Woodford and Chevallier, 2002a). The dykes typically range in width from 2 to 10 m, but widths of up to 70 m have been recorded in the Western Karoo Domain (Woodford and Chevallier, 2002a). The length of the dykes ranges from 5 to 30 km long but there are cases of dykes that are 80 km long (Duncan and Marsh, 2006). The interconnectivity of the dolerite dykes and sills, with only limited cross-cutting relationships, suggests that magma intruded relatively rapidly into a large number of fractures and resulted in the formation of a dolerite network.

Du Toit (1920) suggested that the emplacement of the dolerite sills was controlled by the country-rock lithology. Drilling in the Karoo provided proof of the preferential horizons along which the dolerites intruded (de la Rue Winter and Venter, 1970), such as along the contacts between the Dwyka and Ecca groups, between the Prince Albert and Whitehill formations and also between the Ecca and Beaufort groups. Dolerites also intruded into the Beaufort Group lithologies (**Figure 2-4**). The thickness of the sills differs: in the Dwyka Group the thickness is approximately 130 m and in the Ecca Group it is up to 200 m. The Beaufort Group is dominated by saucer-shaped sill complexes of different sizes, from 30 to 60 km in diameter (Duncan and Marsh, 2006; Nengovhela *et al.,* 2016).

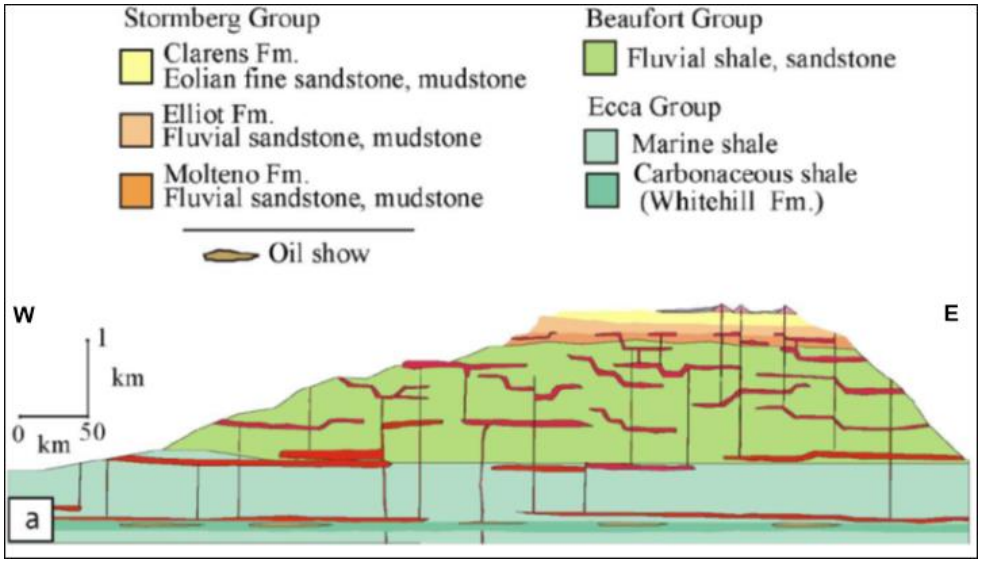

Figure 2-4 Schematic cross-section of the Karoo Basin showing the vertical and lateral distribution of the Karoo intrusive network in the Karoo stratigraphy (Galerne, 2009).

Woodford and Chevallier (2002b) identified five major ring and sill complex systems in the main Karoo Basin, namely, Sutherland, Victoria West, Middelburg, Queenstown and Umtata. The study area falls partially within the Victoria West major ring and sill complex system on Rosedene and Renosterkop farms (**Figure 2-5**).

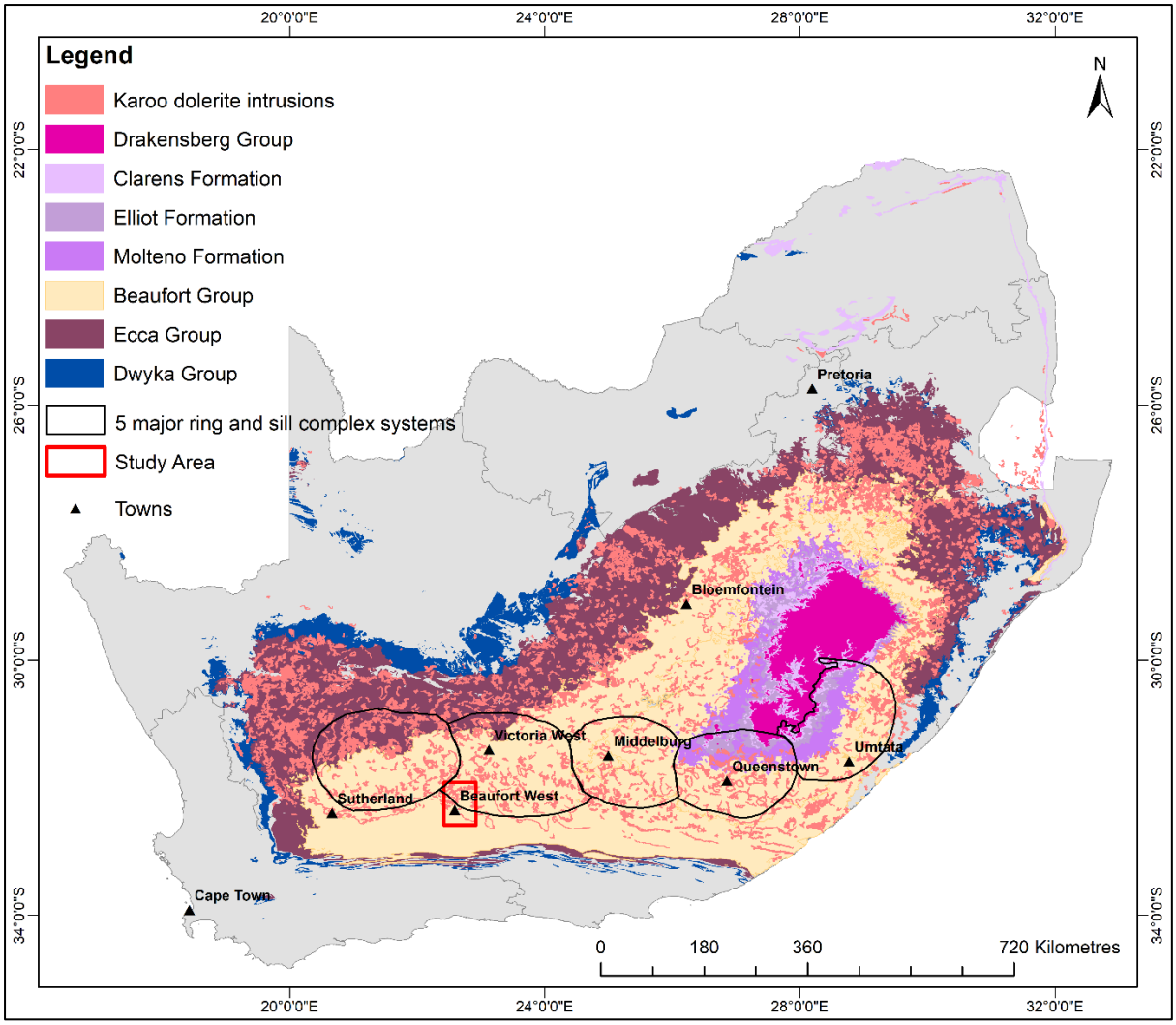

Figure 2-5 The 5 major sill and ring complex systems (mega-basins) found in the western to eastern Karoo (modified from Woodford and Chevallier (2002b) overlain over simplified geological map. The study area is located southwest of Victoria West major sill and ring complex system.

The sills in these ring complexes form different shapes, from coalescing circular structures to kidney-shaped and oval structural units, and may be composed of several smaller sills resulting in 'ring-within-ring arrangement (Woodford and Chevallier, 2002a). Chevalier *et al*. (2004) pointed out that, in places, the sills make up >30% of the stratigraphic thickness and have a cumulative volume of approximately 340 000 km³. Chevallier and Woodford (1999) recognized five morphological and structural features of a dolerite sill and ring system (**Figure 2-6**):

- Horizontal flat-lying inner sill that forms the saucer bottom, with thicknesses ranging from 60 to 100 m reflected clearly in the geomorphology of the particular area.
- Inclined sheet and links the lower inner sill and the upper outer sill. These inclined sheets commonly form a topographic high with an uneven shape and range in thickness from 30 to 100 m. Initial geological mapping led to the suggestion that inclined sheets can have dips up to 60°. However, mapping of inclined sheets using seismic data have let to the suggestion that dips are much less, between 5 and 20° (Scheiber *et al.,* 2014b).
- Outer sill is a widespread sill, up to approximately 100 km in diameter and positioned approximately 100 m higher than the inner sill. These sills have commonly been removed by erosion.
- Minor secondary ring structures/sills are found within larger sill-ring complexes.
- Sub-vertical dykes usually form the rim of the ring structure. They range between 10 and 30 m in width. On a regional scale, the NNW-trending dykes are considered as the major feeder conduits to the Karoo ring complexes (Chevallier and Woodford, 1999).

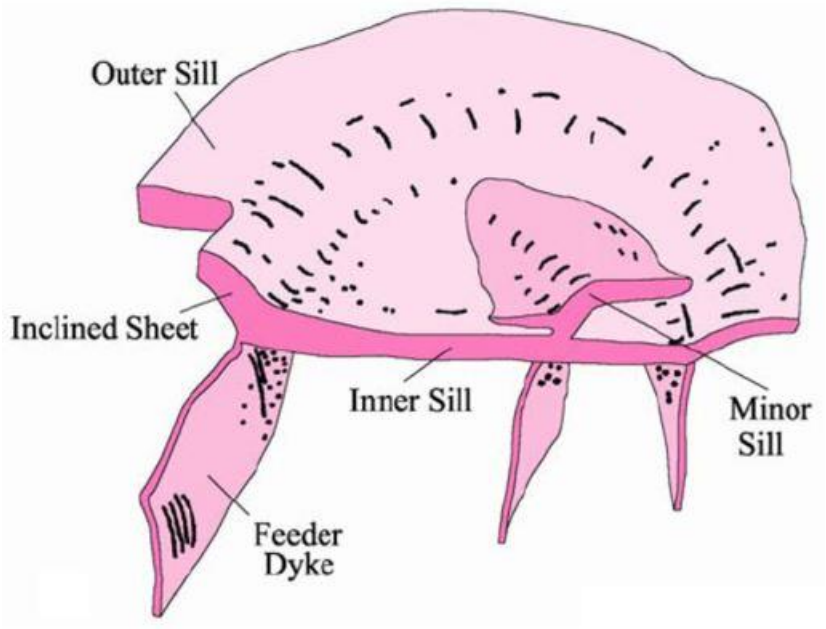

Figure 2-6 The conceptual saucer-shaped model of a dolerite dyke-sill-ring complex. The model is characterised by an inner sill that forms the saucer bottom; an inclined

sheet that connects the lower inner sill and the upper outer sill; the outer sill situated approximately 100 m above the inner sill; minor secondary sills/ring structures found within larger sill-ring complexes, and sub-vertical dykes usually found where ring structures are well developed (Chevallier and Woodford, 1999).

In the Victoria West sill and ring complex (**Figure 2-7**), the ring-like structures (inclined sheets) are established along western and southern parts of the complex. A cross-section in **Figure 2-7,** shows the topographic expression of the inclined dolerite sheets connecting the inner sill to the outer sill (Chevallier and Woodford, 1999).

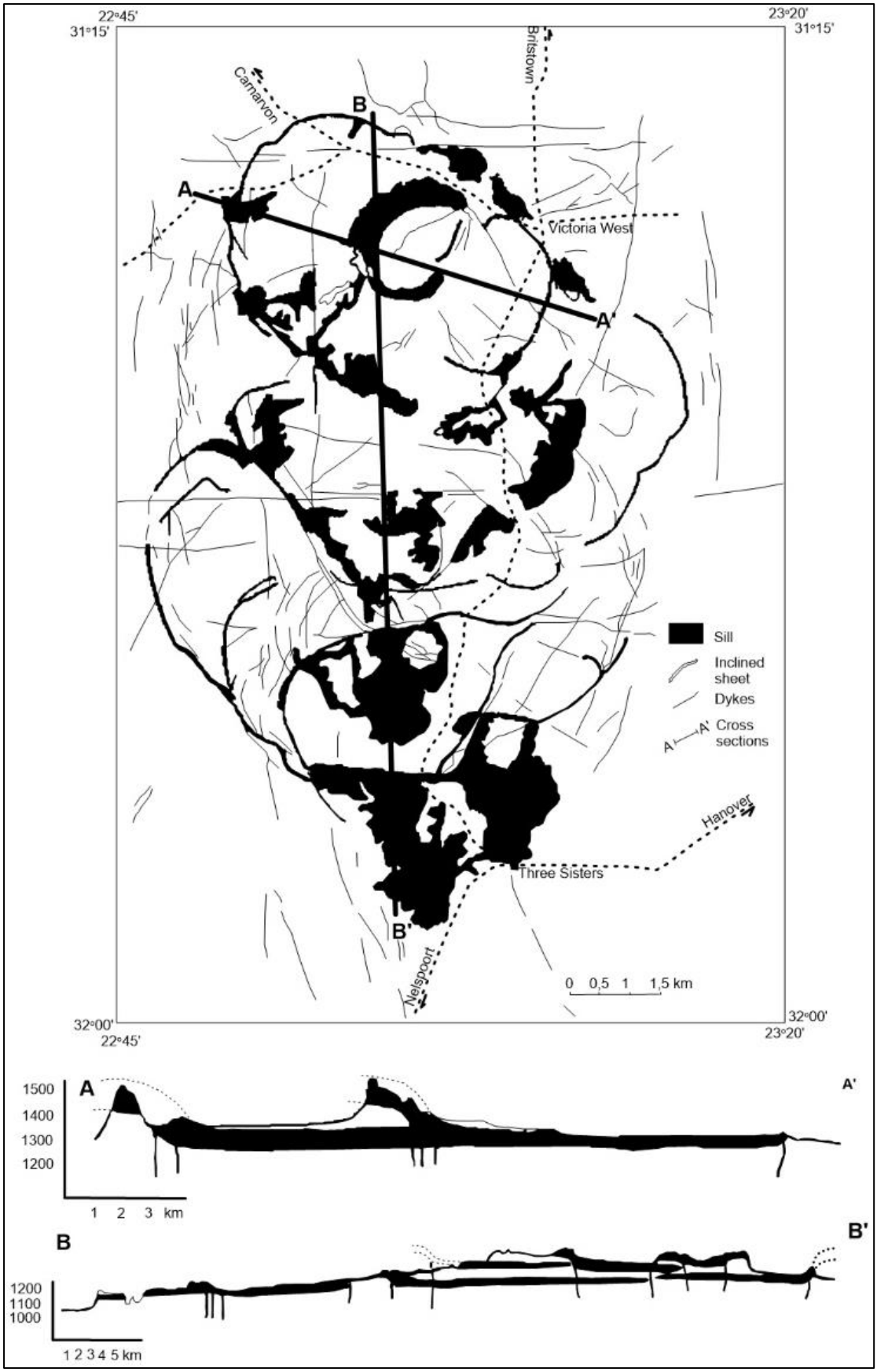

Figure 2-7 Victoria West sill and ring complex (Chevallier and Woodford, 1999).

The South African Petroleum Exploration Company (SOEKOR) drilled deep boreholes during the 1960s and 1970s, two of which (boreholes AB1/65 and KW1/67) are located close to the study area (**Figure 2-8**). Muedi (2019) re-logged some of the SOEKOR boreholes (OL1/69, QU1/65, AB1/65, SP1/69, LA1/68 and MA1/69) and showed that individual dolerite sill thicknesses range from 5 m to 280 m and that the total thickness of the sills in the boreholes is between 206 m and 500 m. In the western Karoo Basin, the numerous sills are preserved and crop out closer to the surface (Muedi, 2019) while thicker dolerites are common in the eastern Karoo Basin within the Ecca and Beaufort Groups at greater depths (Muedi, 2019).

Borehole AB1/65 is located approximately 83 km north-northeast of Beaufort West, with a total depth of 2281 m, and KW 1/67 is located 73 km south-southeast of Beaufort West, with a total depth of 5555 m (Rowsell and De Swardt, 1976). Muedi (2019) recorded 556.67 m of dolerite in AB1/65 during re-logging and recorded the highest percentage (24 %) of dolerites intersected compared to the other re-logged boreholes (OL1/69, QU1/65, SP1/69, LA1/68 and MA1/69). Borehole KW1/67 intersected no dolerite because it lies south of the so called ‘dolerite line’ (Rowsell and De Swardt, 1976). South of this “line” no dolerites are said to have intruded. Or at least, the volume of dolerite is significantly less and so none are intersected by the limited boreholes in this area.

The SOEKOR boreholes show more than 150 m of dolerite in the northwest (QU1/65 and AB1/65) and east/northeast (WE1/66 and SE1/66) regions of the basin, with sills distributed at all stratigraphic levels, whereas in the centre of the basin they show less than 150 m of dolerite that is restricted to the upper levels of the basin stratigraphy (Roswell and de Swart, 1976).

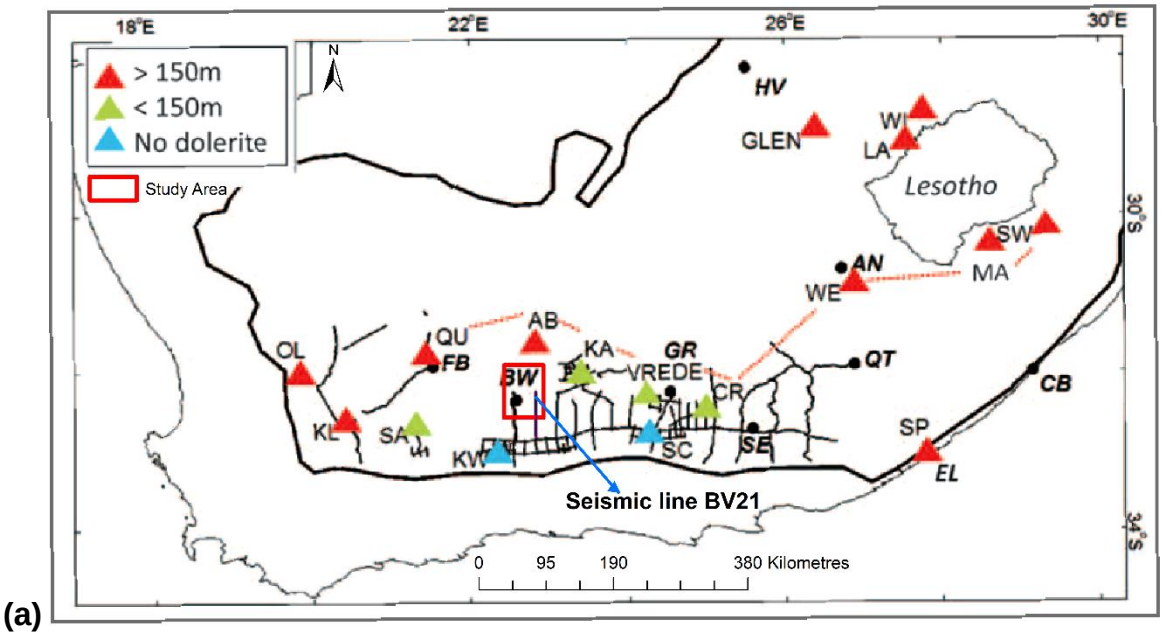

(a)

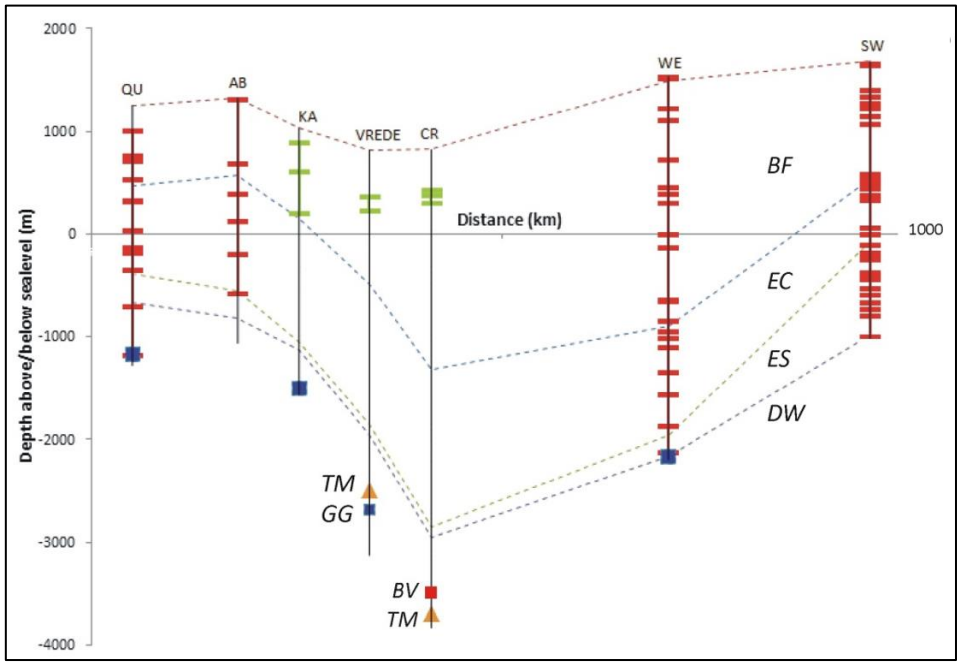

(b)

Figure 2-8 (a) Map showing the locations of SOEKOR boreholes, dolerite thickness greater than 150 m (red triangles), dolerite thickness less than 150 m (green triangles) and zero dolerite south of dolerite line (blue triangles). SOEKOR seismic lines are marked (black lines), including one that passed through the study area (BV21). The surveys (including wells) are divided into regions: northwest region around Fraserburg (FB), southwestern region around Graaff-Reinet (GR) and two regions in the southeast around Somerset-East (SE) and Queenstown (QT). Additional wells are in Aliwal North (AN) and East London (EL). (b) Broadly west-east profile through the main Karoo Basin showing the dolerite distribution (horizontal lines) in SOEKOR deep wells;

location of the profile shown by dotted line in (a). Stratigraphic boundaries are marked with dotted lines: BF – Beaufort Group, EC – upper Ecca Group, ES – Ecca shales, DW – Dwyka Group, BV – Bokkeveld (red square), TM – Table Mountain Group (orange triangle), GG – Granite-gneiss basement (blue square). Solid black lines indicate the total well depth. Above 400 m of dolerite occurs in each well in the east/southeast and northwest while <150 m of dolerite is found in the southwest wells (modified after Rowsell and De Swardt, 1976; Scheiber-Enslin *et al.,* 2014b).

2.2.2 Drakensberg Group

The Drakensberg flood basalts were extruded during the Upper Triassic to Lower Cretaceous and have been grouped into two formations (Barkley East and Lesotho formations; Eales *et al.,* 1984; Catuneanu *et al.,* 2005). The Karoo Dolerite Suite represents a shallow feeder system to the basalt eruptions (Walker and Poldervaart, 1949). The erosional remnant of the flood basalts is centred in Lesotho (Woodford and Chevallier, 2002a). The basalts form the upper parts of the Drakensberg Mountain Range along the border between KwaZulu-Natal Province and Lesotho and cover the northern section of the Eastern Cape Province (Duncan and Marsh, 2006). The volcanic activity initially occurred alternating with the Clarens Formation sandstone units (**Figure 2-9**). In South Africa and Lesotho, the Drakensberg basalts reach an average thickness of 1.8 km (Muedi, 2019).

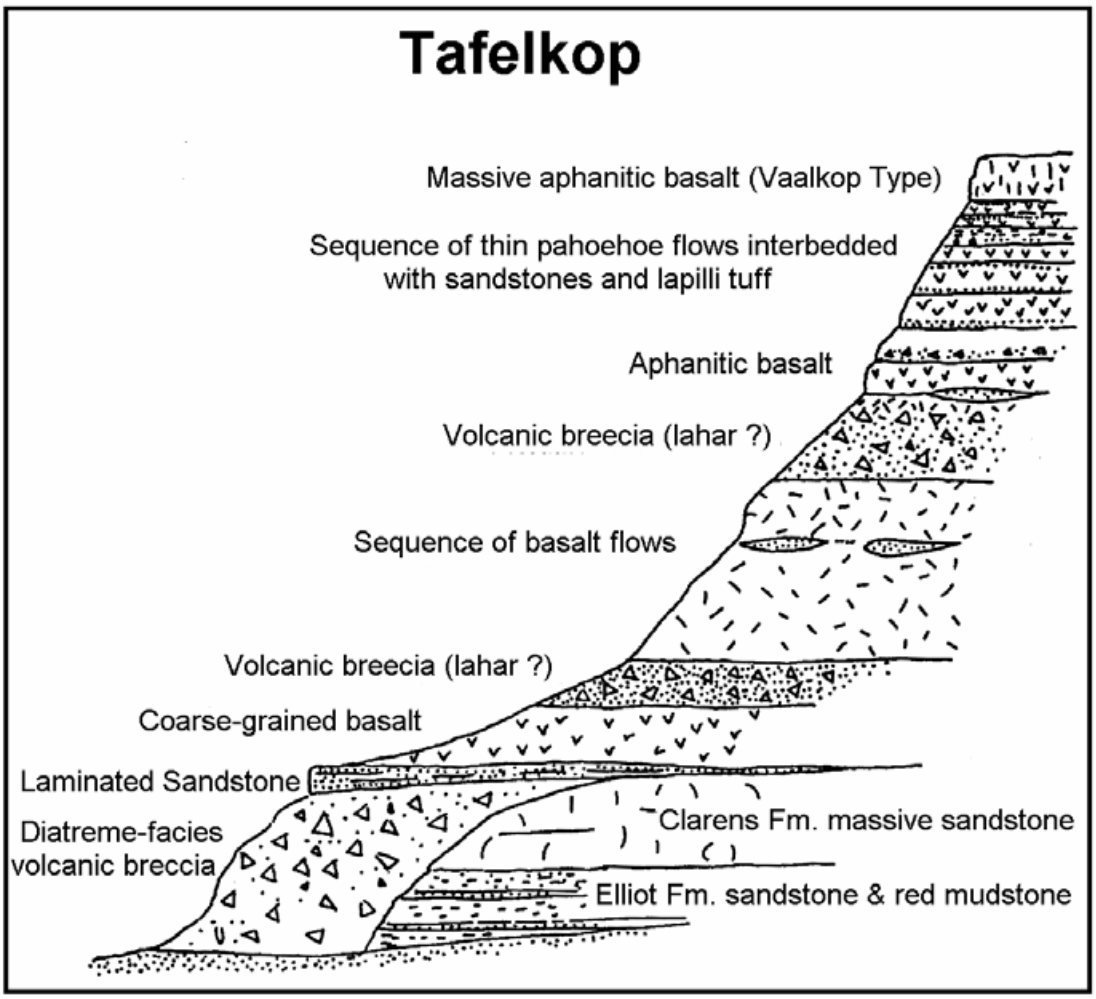

Figure 2-9 Stratigraphy of the Barkley East Formation and its relation with the Clarens Sandstone at Tafelkop (Eastern Cape Province) (Marsh, 1991).

2.3 Tectonic setting

Two tectonic regimes operated during Karoo-age sedimentation (Catuneanu *et al.,* 2005; Angielczyk *et al.,* 2014). Along the northern (Tethyan) Gondwana margin, basins formed in an extensional regime (Hälbich *et al.,*1983; Catuneanu *et al.,* 1998; Angielczyk *et al.,* 2014); these arere not discussed further in this study. The tectonic regime along the southern margin of Gondwana where the main Karoo Basin is located was dominated by north-south compression related to subduction, accretion and orogenesis. This took place along the Panthalassan (palaeo-Pacific) margin of Gondwana. The compression formed a Pan-Gondwanian fold-thrust belt with a series of foreland basins during the Permian and Triassic. The Cape Fold Belt forms one of

these E-W-trending fold-thrust belts, with the main Karoo Basin as a foreland basin to its north.

The Cape Fold Belt (CFB) comprises an E-W-trending southern branch and a NNW-trending western branch that meet at a syntaxis inland of Cape Town, which is a domain of intense folding and faulting (Söhnge, 1983). Catuneanu *et al*. (2004) theorised that tectonic loading caused by the Cape Fold Belt would have caused flexural subsidence as far as 1350 km northwards of the belt front, thus creating the accommodation space for the sediments of the main Karoo Basin.

The CFB folding is characterised by sinusoidal, upright mega-folds restricted immediately south of latitude 32°30'0″ S, while north of latitude 32°30'0″ S, Karoo sediments are almost undeformed (Woodford and Chevallier, 2002a). Faults in the main Karoo Basin are also dominantly related to the Cape Fold Belt. Faults are well documented in the southern branch of the Cape Fold Belt and occur throughout the Cape Supergroup and into the Beaufort Group (Booth and Goedhart, 2004). Major faults within the Cape Fold Belt have a complex displacement history (Hälbich *et al.,* 1983; Tankard *et al.,* 2009), having been reactivated as normal faults during the Jurassic breakup of Pangea.

Various tectonic models have been proposed for the Cape Fold Belt. A northward-directed subduction zone from the southern margin was proposed by Johnson (1991) and Pankhurst *et al*. (2006). However, Lindeque *et al*. (2011) proposed a southward-directed subduction zone south of the belt, based on seismic reflection data (geophysics data) and also supported a thin-skinned deformation model for the CFB. De Beer (1992) and Newton *et al.* (2006) proposed a mostly thick-skinned model and suggested that the CFB formed by reactivation of pre-existing crustal fabrics such as the Colenso and Piketberg faults.

Conversely, Johnston (2000), Booth (2009) and Tankard *et al.* (2009) proposed the Cape Orogeny as a strike-slip orogenic belt. Tankard *et al.* (2009) highlighted features associated with the Worcester and Cango faults, specifically the east-trending

anticlinoria of the Swartberg and Langeberg ranges, which are rooted in these faults. The Swartberg mountains are located approximately 130 km south of Beaufort West while the Langeberg range is located further southwest. Tankard *et al*. (2009) proposed that features in the Worcester and Cango shear zones, namely (1) en-echelon faults and folds, (2) uplift along a restraining bend on Worcester fault, and (3) flower structures, are consistent with dominant sinistral displacement. The strain in the orogeny was partitioned between transpression along with the Worcester and Cango fault systems and the northward-directed thrust-fold belt.

2.3.1 Karoo foreland basin phase

A 30 Ma depositional hiatus exists between the Cape Supergroup and the overlying Karoo Supergroup, from approximately 330 to 300 Ma (Catuneanu *et al.,* 2005; Tankard *et al.,* 2009). Different models have been proposed to explain this hiatus, both independent of the foreland system model and in the context of the foreland system model. Visser (1987) proposed that the basal Karoo unconformity could correspond to a period of no deposition owing to the Dwyka ice sheet that covered the entire southern Africa before the foreland system developed. On the other hand, Catuneanu *et al.* (2004) interpreted the hiatus as a basal unconformity of the foreland system resulting from the earliest stages of tectonic loading and of forebulge uplift.

The common tectonic model for the main Karoo Basin is that it represents a retro-arc foreland basin situated north of the magmatic arc linked to a north-dipping subduction zone (Dickinson, 1974; Johnson, 1991 and Catuneanu *et al.,* 1998). However, alternative tectonic models have been proposed, including a Jura-type foreland basin related to a southward-dipping subduction zone (Lindeque *et al.,* 2011) and a flexural foreland basin (Tankard *et al*., 2012).

Catuneanu *et al.* (2004) divided the basin into a foredeep, forebulge (peripheral bulge) and a backbulge basin resulting from supracrustal loading by the fold-thrust belt (**Figure 2-10**). In the main Karoo Basin, the foredeep accommodated the full basin stratigraphy (Veevers *et al.,*1994; Catuneanu *et al.,* 2005). Stratigraphic patterns and

thicknesses indicate that all sedimentation occurred during the flexural episode related to the compressional stresses (Catuneanu *et al.,* 2005).

Further support for the synchronous development of the basin and the belt comes from $^{40}Ar/^{39}Ar$ dating of micas on cleavage planes from the southern Cape Fold Belt. This dating has revealed four compressional deformation episodes, at 278, 258, 247 and 230 Ma, which were followed by uplift and horizontal extension at approximately 215 Ma that deformed southern part of the Karoo Basin (Hälbich *et al.,* 1983, **Table 2-1)**. The first Cape Fold Belt movement or pulse is recorded in the Swartberg folding, dated at 278 ± 2 Ma in cleavage in the Cederberg Formation. The Swartberg folding has been correlated with the end of Dwyka Group sedimentation by Veevers *et al.* (1994) and Cole (1992); however, Tankard *et al*. (2009) used U-Pb zircon dating to propose that the Dwyka Group was deposited from 302 to 290 Ma and, thus, that the first tectonic pulse should correlate with Ecca Group deposition.

The second pulse at ca. 258 ± 2 Ma, associated with Outeniqua folding, has been correlated with the deposition of the lower Beaufort Group. The third pulse, at ca. 247 Ma, correlates with the deposition of the middle Beaufort strata (Hälbich *et al.,*1983).

There are different views on the fourth orogenic pulse: (1) Hälbich *et al*. (1983) proposed that the fourth orogenic pulse, at ca. 230 ± 3 Ma, correlated to the uppermost Beaufort Group deposition (**Table 2-1**), whereas (2) Veevers *et al*. (1994) proposed that sedimentation of the Molteno, Elliot and Clarens Formations was facilitated by the fourth pulse that created more accommodation space in the basin. Based on current geochronological constraints, the fourth pulse occurred during the early stage of Molteno Formation deposition, where the Cape and Karoo Supergroup were deformed by listric thrusting and folding (Veevers *et al.,* 1994). The age of the retrogressive metamorphism in the metabasic rocks of the Kango Group has been attributed to uplift and horizontal extension in the Cape Fold Belt which is, in turn, correlated with the last phase of braidplain deposition at the base of the Clarens Formation (Hälbich *et al.,*1983).

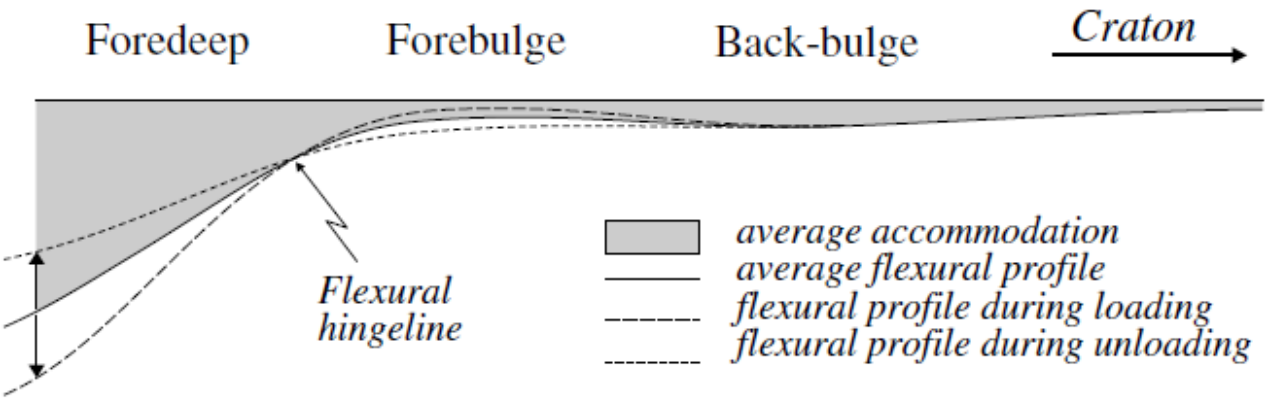

Figure 2-10 Model for the deposition of the main Karoo Basin as a retro-arc foreland basin. Accommodation space was created during phases of loading and unloading of the crust by the Cape Fold Belt, which caused the crust to flex. Renewed thrusting caused orogenic loading that gave rise to foredeep subsidence and uplift in the forebulge. The reverse occurred during orogenic quiescence where the foredeep undergoes uplift as a result of isostatic rebound, compensated by subsidence of the forebulge. The study area is located within the foredeep (Catuneanu, 2004).

Table 2-1 Tectono-sedimentary history summary of both Cape Fold Belt and Karoo Supergroup (Hälbich *et al.,* 1983).

Time	**Deformational event**	**Erosion/sedimentation**
Early Permian 278 ± 2 Ma	Swartberg Folding S_1 forms	Deformation of the southern Ecca Facies
Mid to Late Permian 258 ± 2 Ma	Outeniqua folding S_2 forms	Deposition of lower Beaufort Group
Late Permian to Early Triassic 247 ± 3 Ma	Increase of Outeniqua folding Mega-folding of southernmost Ecca and Beaufort Groups	Deposition of middle Beaufort Group
Mid to Late Triassic 230 ± 3 Ma	Kinking of S_1 and S_2 Listric thrusting of Beaufort Group	Deposition of uppermost Beaufort Group
Late Triassic 215 ± 5 Ma	Uplift and horizontal tension	Deposition of Molteno, Elliot and Clarens Formations

2.3.2 Terminal-phase rifting and magmatism

Intracontinental rifting is assumed to have started at approximately 185-177 Ma linked to the Karoo LIP, as Antarctica split from southern Africa (Veevers *et al.,* 1994). The breakup was triggered by a large mantle plume off the present-day east coast of South Africa (Storey and Kyle, 1997; Catuneanu *et al.,* 2005; Woodford and Chevallier, 2002a) (**Figure 2-11**). Separation of East Gondwana (Antarctica, Madagascar, India) from West Gondwana (South America, Africa) is estimated to have only taken place at approximately 165-150 Ma (Veevers *et al.,* 1994).

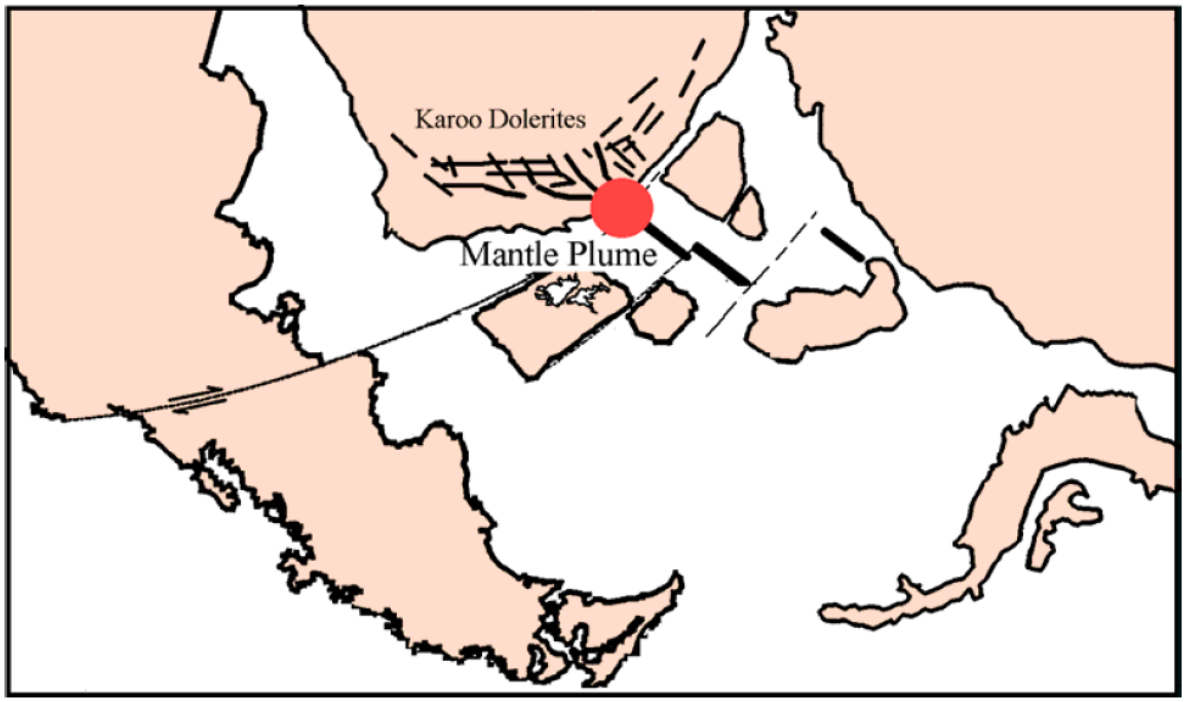

Figure 2-11 Plate tectonic reconstruction for breakup of East and West Gondwana (Storey and Kyle, 1997; Woodford and Chevallier, 2002a). Mantle plume (red circle) positioned off the east coast of South Africa gave rise to the Karoo flood basalts and dolerites.

Chevallier and Woodford (1999) proposed that the main Karoo Basin is subdivided into three structural domains based on dyke orientation (**Figure 2-12**). In the Western Karoo Domain very long dykes show a strong E-W trend, with shorter NNW-trending dykes, which Chevallier and Woodford (1999) interpreted as consistent with intrusion

during right-lateral (dextral) shear. Such E-W right-lateral (dextral) shear would be expected to be accompanied by NE-SW P fractures and NW-SE Riedel shears. Riedel shears would develop at an acute angle to the main E-W shear zone while Conjugate Riedel (R') shears would be oriented at a high angle (Woodford and Chevallier, 2002b). P fractures are described as minor faults and would be oriented anticlockwise to the main dextral fault.

The northern part of the study area (latitude 32°15'0″ S) forms the southern margin of Western Karoo Domain. The Eastern Karoo Domain is dominated by a curvi-linear dyke swarm, with orientations swinging from E-W along the coast to NNW-SSE inland. Secondary dyke orientations vary from NW-SE along the coast to NNE-SSW further inland. Dykes in the Transkei-Lesotho-Northern Karoo Domain also display a curvilinear major trend, curving from NW-SE in the coastal region to E-W in the Free State Province, with NE-SW dykes found within and alongside the basalt plateau (Woodford and Chevallier, 2002a).

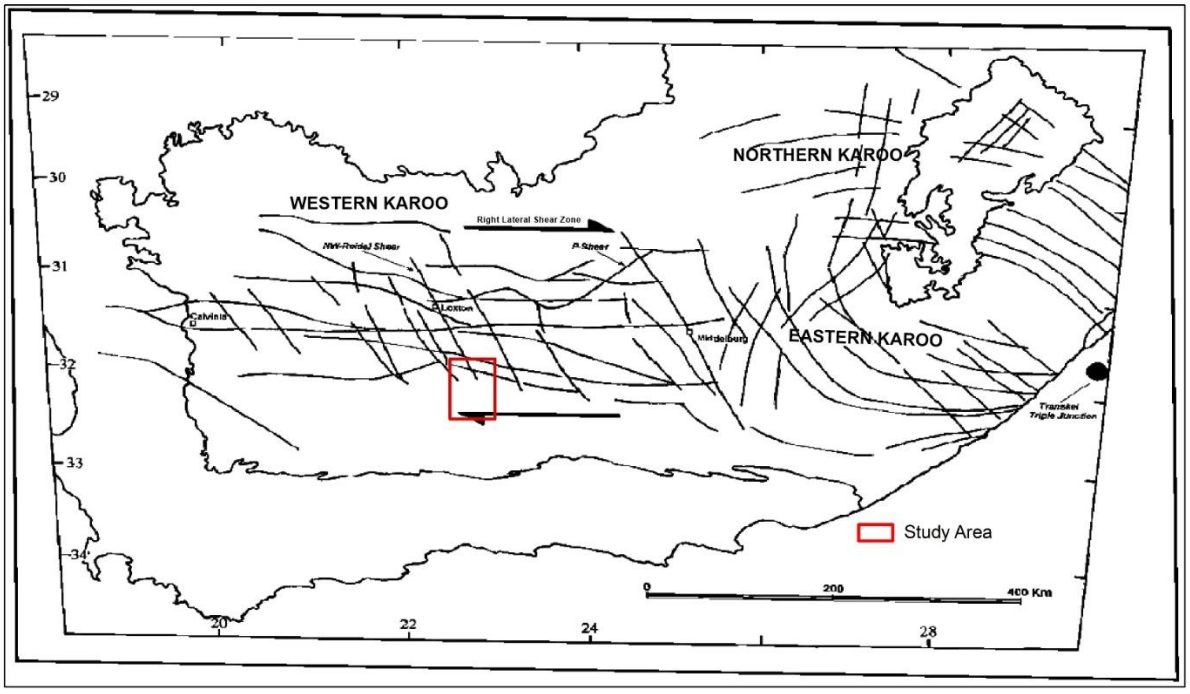

Figure 2-12 Structural map of the main Karoo Basin showing the three principal structural domains (Western Karoo Domain, Eastern Karoo Domain and Transkei-Lesotho-Northern Karoo Domain) defined by Woodford and Chevallier (2002b). The

study area is located south of Loxton town where the northern part of the study area forms the southern edge of the Western Karoo Domain.

The main E-W and secondary NNW dyke orientations in the Western Domain (**Figure 2-13b)** are features found in transform fault systems established between two rifts (Woodford and Chevallier, 2002b, **Figure 2-13a**). Chevallier and Woodford (1999) interpreted the Western Karoo Domain as a failed transform fault that was replaced by the Agulhas Fracture Zone during the Early Cretaceous.

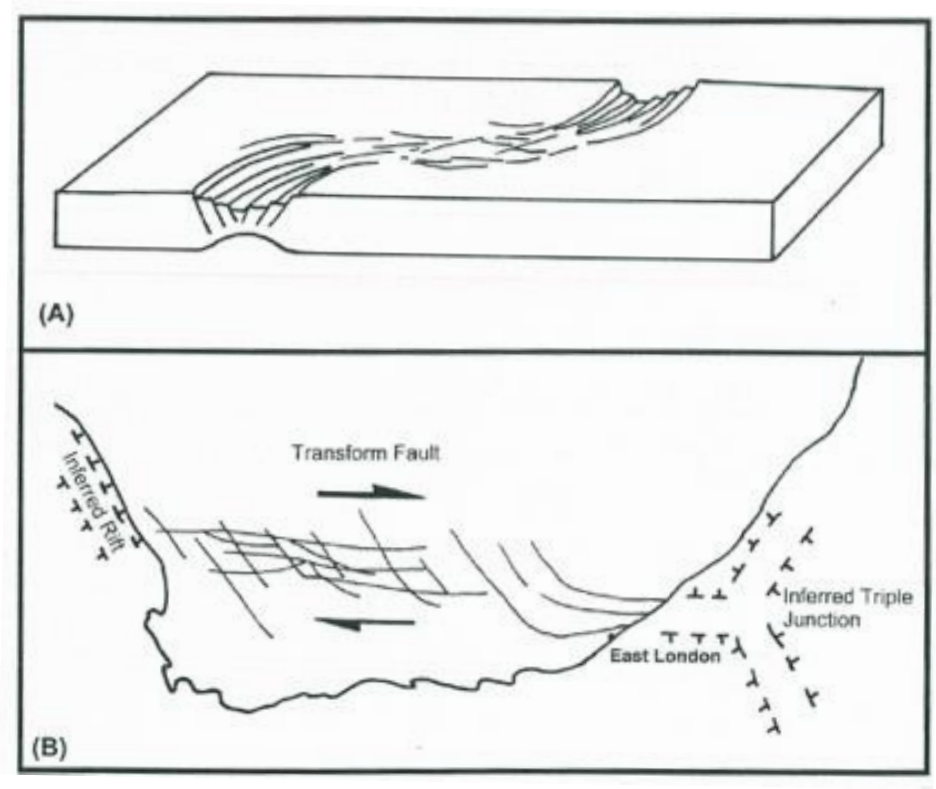

Figure 2-13 (A) Block diagram of a transform fault between two rift systems compared with (B) Simplified map of Karoo dyke orientations in the main Karoo Basin interpreting them as an E-W right-lateral shear zone transform fault between two rift systems off the east and west coasts of South Africa (Woodford and Chevallier, 2002b).

The tectonic evolution and stress field over southern Africa from the Cape Orogeny up to Gondwana rifting are summarised by Woodford and Chevallier (2002b) and are shown in **Figure 2-14**:

- A is related to the Cape Fold Belt where E-W fold axes were accompanied by N-S and E-W conjugate joints as a result of N-S compressional stress regime.
- B is related to the early stages of Gondwana break-up, which was accompanied by the formation of NNW faulting and jointing along existing zones of crustal weakness.
- By stage C dolerite dykes intruded along both the E-W shear zone and NNW fractures. The stress field that dominated during this time was a NW-SE compressive stress field.

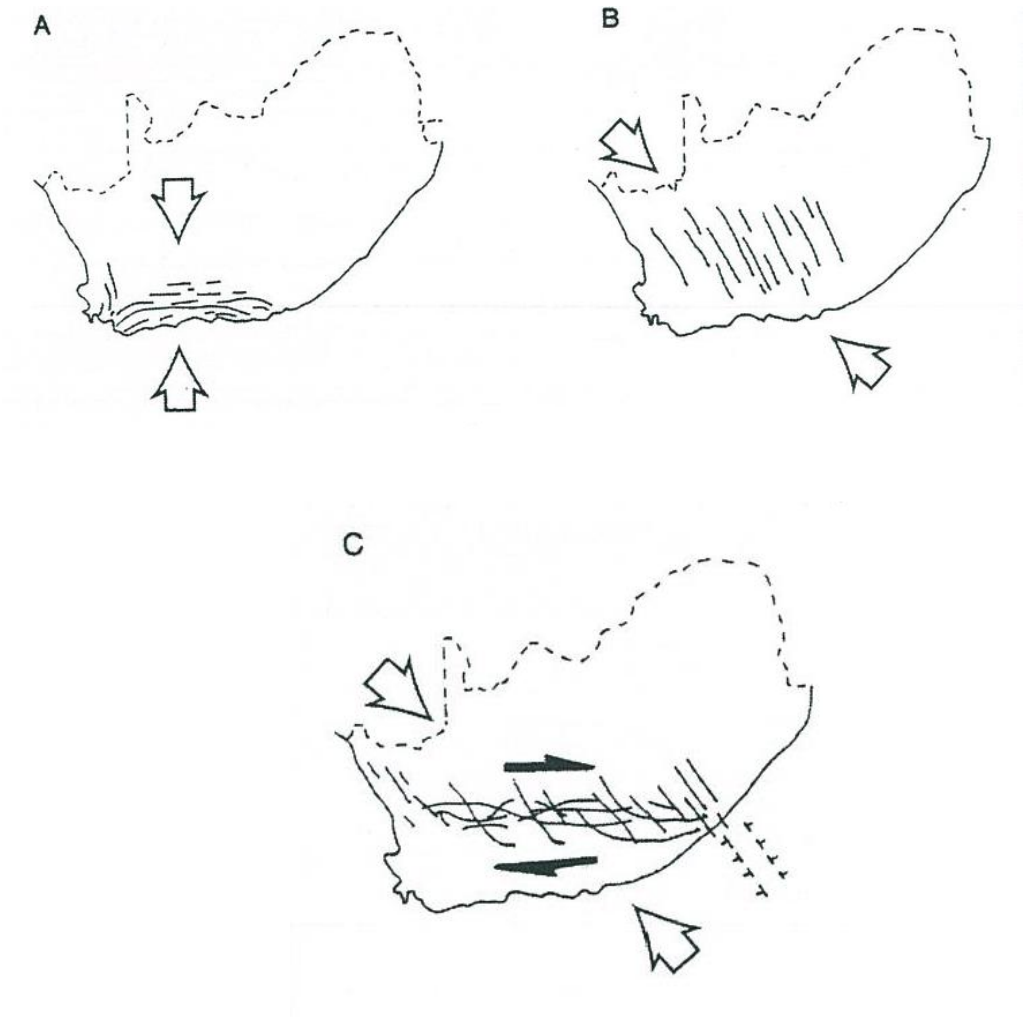

Figure 2-14 Tectonic and stress field history of the main Karoo Basin from Permian to Jurassic times: A. east-west fold axes of the Cape Fold Belt developed under north-south compressive stress regime; B. Early phase of Godwanaland break-up associated with the formation of NNW jointing and faulting along existing zones of crustal weakness; and C Rifting phase of Gondwanaland break-up where dolerites intruded along NNW fractures and on E-W shear/dislocation zones (Woodford and Chevallier, 2002b).

2.4 Fossil fuel resources of the Karoo Basin

The deposition of Karoo Supergroup sediments occurred during the explosive colonisation of land by plants between approximately 300 to 183 Ma (Catuneanu *et al.,* 2005). Rocks in the basin are characterised by a range of palaeoenvironments from glacial to desert, however, both the fossil record and the presence of numerous

coal seams in the Ecca and Beaufort Group indicate that conditions ideal for the development of fossil fuel resources were present during at least part of this history.

The main Karoo Basin has long been exploited for its coal, particularly in the east of the basin within rocks of the Ecca Group. Basin deepening towards the south precluded coal development, however, palaeo-environmental models suggest that, during Ecca times, the broader basin became cut off and anoxic, leading to the deposition of carbon-rich black shales, typified by the Whitehill Formation. Exploration has shown that it is a potential source of shale gas. This resource could be exploited as another energy source in South Africa using the process of 'fracking' which increases the recovery of the tightly-bound gas within shale horizons (de Kock *et al.,* 2017). Shale formations act as both the source and the reservoir for the gas (Sunjay *et al.,* 2014). de Kock *et al.* (2017) outline the shale gas resource (dotted black line) in the Karoo Supergroup (**Figure 2-15**). The black shales of the Prince Albert Formation underlying the Whitehill Formation are also considered to contain shale gas (Moorcroft and Tonnelier, 2016).

In the central parts of the basin, the Whitehill Formation shales are approximately 30 m thick with local depocentres (reaching thicknesses of approximately 72 m) near Calvinia, Laingsburg and Graaff Reinet (Rowsell and De Swardt, 1976; Cole and McLachlan, 1994). Boreholes AB1/65 and KW 1/67 intersected the Whitehill Formation at depths of over 2 000 m and 4000 m, respectively. These boreholes are approximately 150 km apart. Based on the borehole results, the Whitehill Formation deepens from north to south.

Although initial estimates by Kuuskraa *et al.* (2011) suggested that the total gas reserve in the Karoo Basin could have been as much as ~18 x 10^9 m^3 resource estimate, subsequent studies (e.g. de Kock *et al.,* 2017) drastically reduced this estimate to 0.4–11 x 10^9 m^3 (13–390 Tcf). The abundance of dolerite dykes and sills in the main Karoo Basin may be a critical factor in reserve estimates; however, Cole *et al.* (2016b) suggested from the observed geographic and stratigraphic distribution patterns that dolerite material is limited toward the escarpment.

Previous studies have noted that when the Karoo Large Igneous Province (KLIP) magmas were emplaced, substantial volumes of gases such as carbon dioxide, carbon monoxide and hydrogen sulfide hydrochloride acid) and water would have escaped into the atmosphere; over 2000 Gtonnes of carbon dioxide alone is estimated to have escaped from the sedimentary strata (Svensen *et al*., 2007; Svensen *et al*., 2006; Nengovhela, 2018).

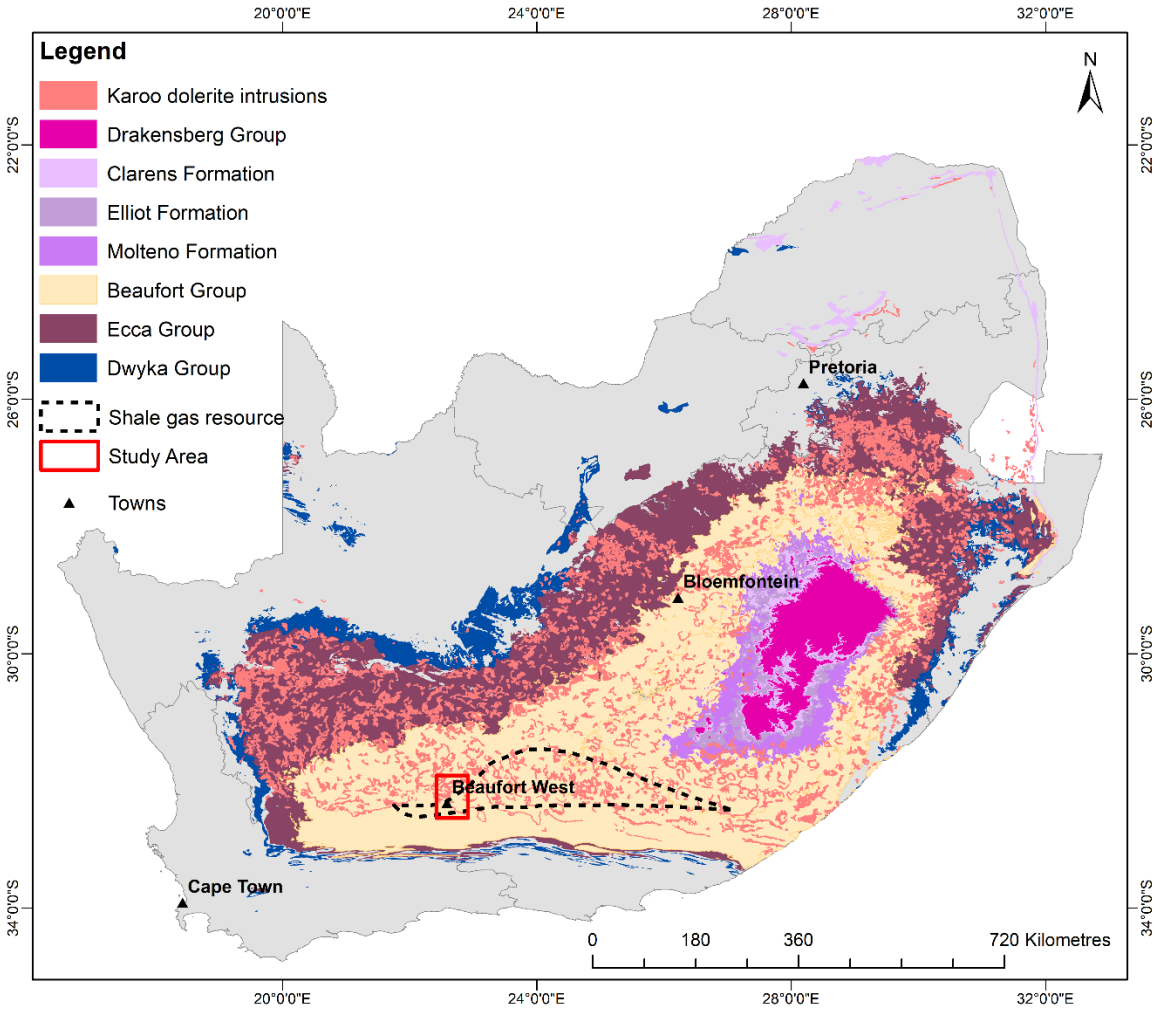

Figure 2-15 A simplified geological map displaying the study area (red outline). The shale gas resource is shown as a dotted black line and was outlined by de Kock *et al.* (2017).

2.5 Summary

- The main Karoo Basin is commonly interpreted as a retro-arc foreland basin situated north of the magmatic arc related to northward subduction beneath southern Africa.
- Sedimentation and stratigraphic thicknesses are closely linked to tectonism and loading in the CFB along the basin's southern margin. The deepest part of the basin is in the foredeep north of the Cape Fold Belt.
- The Karoo Large Igneous Province (LIP) (Karoo Dolerite Suite and Drakensberg basalts) terminated the deposition of the Karoo Supergroup sediments during the Middle Jurassic, linked to the breakup of Gondwana. The dolerite distribution occurs predominantly in the upper Ecca and Beaufort groups. The dolerites form a complex interconnected network at depth, making it challenging to accurately delineate them.
- The northern part of the study area falls within the southern part of the Western Karoo Domain of main Karoo Basin (Chevallier and Woodford, 1999) associated with two distinct structural features: E-W dykes intruded along a major E-W right-lateral shear zone and dolerite dykes intruded along NNW fractures.
- The black shales of mainly the Whitehill Formation and Prince Albert Formation (Lower Ecca Group) are considered to contain gas. During the Karoo Large Igneous Province (KLIP) emplacement, gas and water escaped into the atmosphere, though there may still be gas available within the shales (Holness *et al.,* 2016; de Kock *et al.,* 2017).

3 CHAPTER THREE - LOCAL GEOLOGY

The surface geology of the study area comprises Lopingian (268 to 264 Ma, Lanci *et al.,* 2013) Beaufort Group sediments, Lower Jurassic (185-177 Ma, Veevers *et al.,* 1994) Karoo dolerites, Kimberlites swarms and Quaternary unconsolidated sediments (**Figure 3-1**).

The geological maps of the study area were originally compiled from unpublished 1:50 000 scale hard copy mapsheets, monochromatic aerial photos and fieldwork in the 1970/80's. Recent geological maps were generated from additional fieldwork, digitising structures and geology from hard copy 1:50 000 scale mapsheets, and interpretations of recent remote sensing data and high-resolution satellite imagery, which have provided better constraints on lithological distinctions and boundaries. Several modifications are recorded on these newer maps, such as delineation of member-level geological units and also the geometric relationships between dolerite intrusions and the sedimentary strata (Cole *et al.,* 2016b).

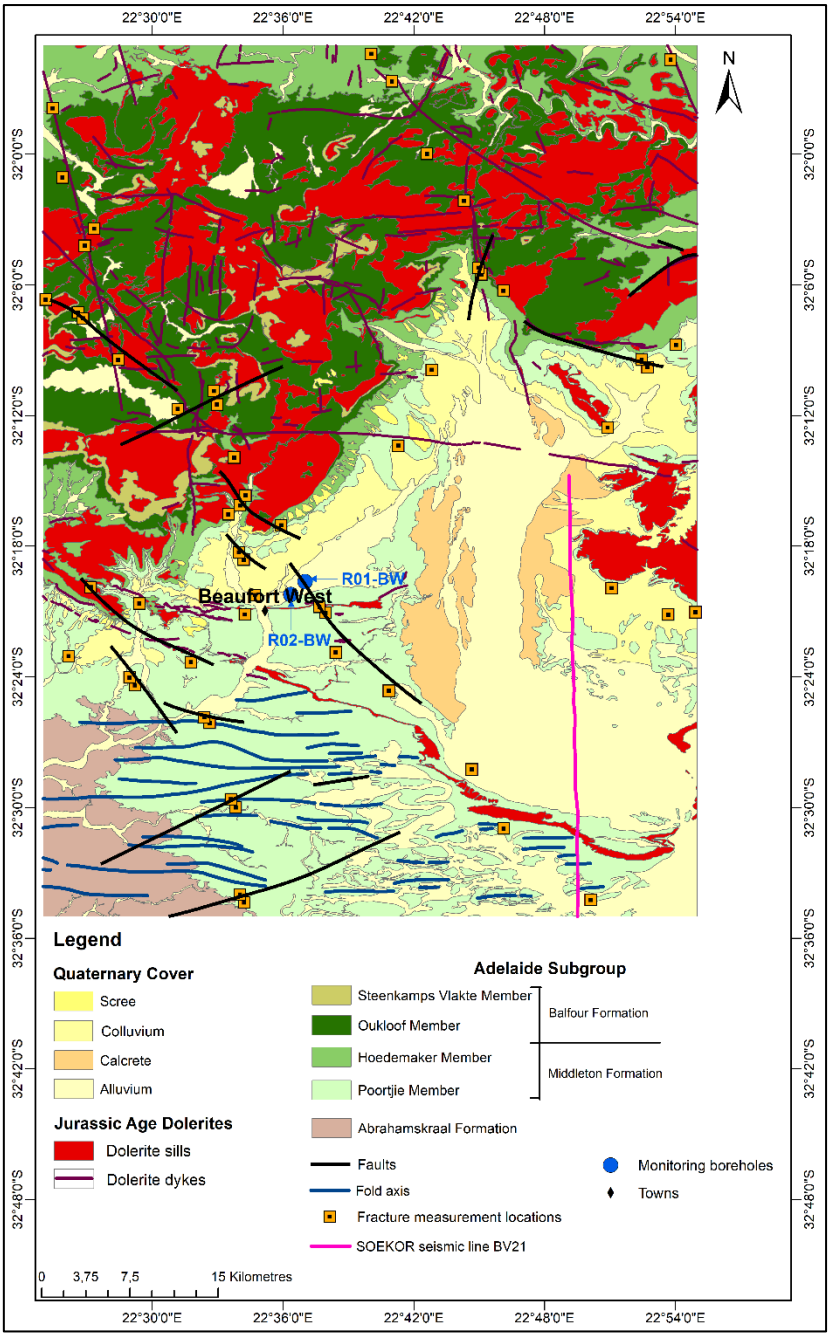

Figure 3-1 1: 50 000 geological map of the study area. The dolerite sills and dykes were digitised from SPOT 5 satellite images at a scale of 1: 10 000 by Cole *et al*. (2016b). Faults and fracture measurement locations are shown. The SOEKOR seismic line BV21 is shown in pink and the monitoring boreholes are shown as blue markers.

The Beaufort Group is subdivided into the lower Adelaide and upper Tarkastad Subgroups (Johnson *et al.,* 2006). East of 24°E, the Adelaide Subgroup is subdivided into the Abrahamskraal, Middleton and Balfour formations; however, west of longitude 24°E, the subgroup is subdivided into the Abrahamskraal and Teekloof formations

(SACS, 1980, Johnson *et al.,* 2006). The local geology of the area was re-mapped at 1:50 000 scale as part of the geo-environmental baseline study (Cole *et al.,* 2016b), resulting in several modifications to the stratigraphic interpretation of the area. SACS-approved changes based on correlation of lithological units west of longitude 24°E are: (1) the Poortjie and Hoedemaker members were originally part of the Teekloof Formation and are now under the Middleton Formation (SACS, 2019; Cole *et al.,* 2016b), and (2) the Oukloof and Steenkamps Vlakte Members were originally part of the Teekloof Formation according to SACS (1980) and are now part of Balfour Formation, as shown in **Figure 3-2** (Smith, 1993; Viglietti *et al.,* 2017).

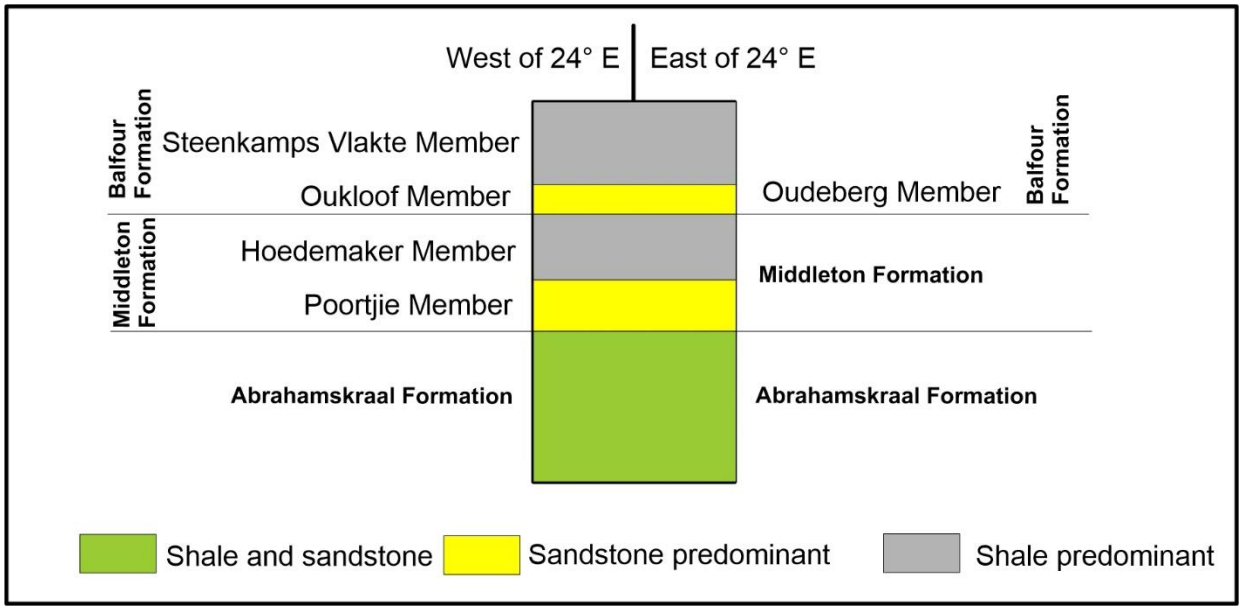

Figure 3-2 Lithostratigraphy of the Beaufort Group showing updated terminology for stratigraphic subdivisions. The Teekloof Formation has been replaced by the Middleton Formation (Poortjie and Hoedemaker Members) and the Balfour Formation (Oukloof and Steenkamps Vlakte Members) west of longitude 24° E, and the Koonap Formation) east of longitude 24° E has been replaced by the Abrahamskraal Formation (SACS, 2019; Viglietti *et al.,* 2017; Cole *et al.,* 2016b).

3.1 Lithostratigraphy

3.1.1 Abrahamskraal Formation

The Abrahamskraal Formation is restricted to the southwestern parts of the study area, (**Figure 3-1**). The Abrahamskraal Formation attains an estimated maximum thickness of 300 m and is gently folded towards its southern outcrop limits (Cole *et al.,* 2016b). The formation is composed of approximately 40 m of mudstone, approximately 6 m of sandstone and approximately 15 m of siltstone (Cole *et al.,* 2016b). It is divided into lithostratigraphic members located outside the study area and information on them can be found in Day and Rubidge (2014).

3.1.2 Middleton Formation

The Middleton Formation consists of the Poortjie and Hoedemaker Members (**Figure 3-2**). The Poortjie Member forms the lower unit and is composed of a series of sandstone bodies between 5 m and 15 m thick interbedded with subordinate siltstone and mudstone (Cole *et al.,* 2016b). It is exposed south of the Great Escarpment (**Figure 3-1**) but is largely covered by Quaternary sediments (Cole *et al.,* 2016b). The upper unit of the Middleton Formation is marked by the mudstone-rich Hoedemaker Member that ranges in thickness from 160 m at De Jagers Pass (gravel road about 30 km NNE of Beaufort West) up to 285 m within the Karoo National Park (Cole *et al.,* 2016b). The Hoedemaker Member is exposed along the slope face of the Great Escarpment.

3.1.3 Balfour Formation

The Balfour Formation involves the Oukloof and Steenkamps Vlakte members and is characterised by abundant dolerite intrusions (**Figure 3-2**, Cole *et al.,* 2016b). The Oukloof Member marks the base of the Balfour Formation and is composed of a series of thick (5-15 m) sandstone bodies interbedded with subordinate siltstone and mudstone (Cole *et al.,* 2016b). In the western part of the Karoo National Park and in De Jagers Pass, the Oukloof Member attains a thickness of approximately 145 m and 150 m, respectively (Cole *et al.,* 2016b). The member outcrops in the north of the study

area but is overlain by the Steenkamps Vlakte Member, which is dominated by mudstone in the study area (Cole *et al.,* 2016b). The Steenkamps Vlakte Member ranges in thickness from 80 m at the top of De Jagers Pass (gravel road about 30 km NNE of Beaufort West) to 150 m within the Karoo National Park (northwest of Beaufort West) (Cole *et al.,* 2016b).

The Oukloof Member correlates with a sandstone-rich unit east of 24° E named the Oudeberg Member, while the Steenkamps Vlakte Member correlates with the Daggaboersnek Member east of longitude 24° E (Cole *et al.,* 2016b). The upper stratigraphic contact of the Steenkamps Vlakte Member is not mapped in the study area.

3.1.4 Jurassic Age Dolerites

The dolerite dykes and sills in the study area were digitised from SPOT 5 satellite imagery at a scale of 1:10 000 (Cole *et al.,* 2016b; **Figure 3-1**). The Karoo dolerites in South Africa were mapped first by Rogers and Schwarz (1902).

- Dykes

The dykes in the study area correspond to the two main trends (E-W to ESE-WNW, and SSE-NNW) identified within the Western Karoo Domain by Chevallier and Woodford (1999). Chevallier and Woodford (1999) referred to an E-W trending dyke southwest of Renosterkop as the Tweeling-Brandwag dyke (**Figure 3-1**). 208 boreholes along an 11 km part of the Tweeling-Brandwag dyke were drilled by the Department of Water Affairs and confirm the dyke has a width between 5 to 11 m with a dip angle of 82-90° to the south or north. Campbell (1975) suggested that the Tweeling-Brandwag dyke intruded into a fold-hinge of a low amplitude syncline. Chevallier and Woodford (1999) pointed out that the major E-W dykes such as the Tweeling-Brandwag dyke show an en échelon segmentation or lateral displacement (**Figure 3-3**). The attitude of this dyke changes rapidly along strike and has an offset of approximately 250 m on the Tweeling Farm. Chevallier and Woodford (1999) pointed out that the dyke defines the major southernmost limit of the main E-W dyke

system in the Western Karoo Domain. However, there are E-W dykes around Beaufort West (south of the Tweeling-Brandwag dyke) that Dhansay (2018a) described as having a complex anastomosing geometry trending E-W and that are associated with an inclined dolerite sheet.

Dykes with a NNW trend are evenly spaced and can be very long such as the dyke that passes west of longitude 22°30'0″ E and which extends for >29 km across the northwest of the study area but continues beyond the study area boundary (**Figure 3-1**).

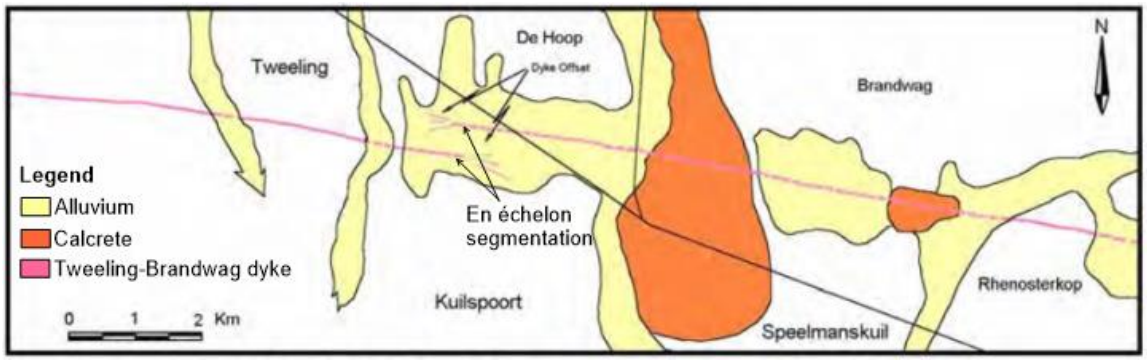

Figure 3-3 Morphology of the Tweeling-Brandwag Dyke, Beaufort West (Campbell, 1975; Woodfordand Chevallier, 2002a). The dyke offset is observed in Tweeling Farm.

- Sills and ring complexes

The dolerite sills are a dominant feature of the escarpment in the study area. The thickness of the sills vary and they are interconnected by the up-stepping dolerite inclined sheets. The lowermost sill attains a thickness of approximately50 m and the uppermost sill a thickness of up to 150 m (Cole *et al.,* 2016b). In De Jager's pass off-road (NE of Beaufort West), these inclined sheets are dipping north (**Figure 3-4**). East of Beaufort West, along a vertical road cutting, a sharp contact is observed between the sill and the sedimentary rocks. In the vicinity of the contact, the sediments are baked and commonly form hornfels (**Figure 3-5**). On the surrounding host rock along the contact, extreme fragmentation and fracturing is observed but far from contact, fracturing becomes less intense.

The dolerite outcrops near the drilling site east of Beaufort West comprise a complex anastomosing network of dykes trending in the E-W direction and inclined sheets that have a shallow dip of between 10° and 45° north. At a quarry exploiting the western part of the inclined sheet, the mudstones are baked to hornfels with calcareous nodules. Fine-grained sandstones cap the dolerite sill in the area.



Figure 3-4 Inclined dolerite sheet cutting through the sub-horizontal Beaufort Group sediments in De Jager's Pass (off-road NE of Beaufort West).

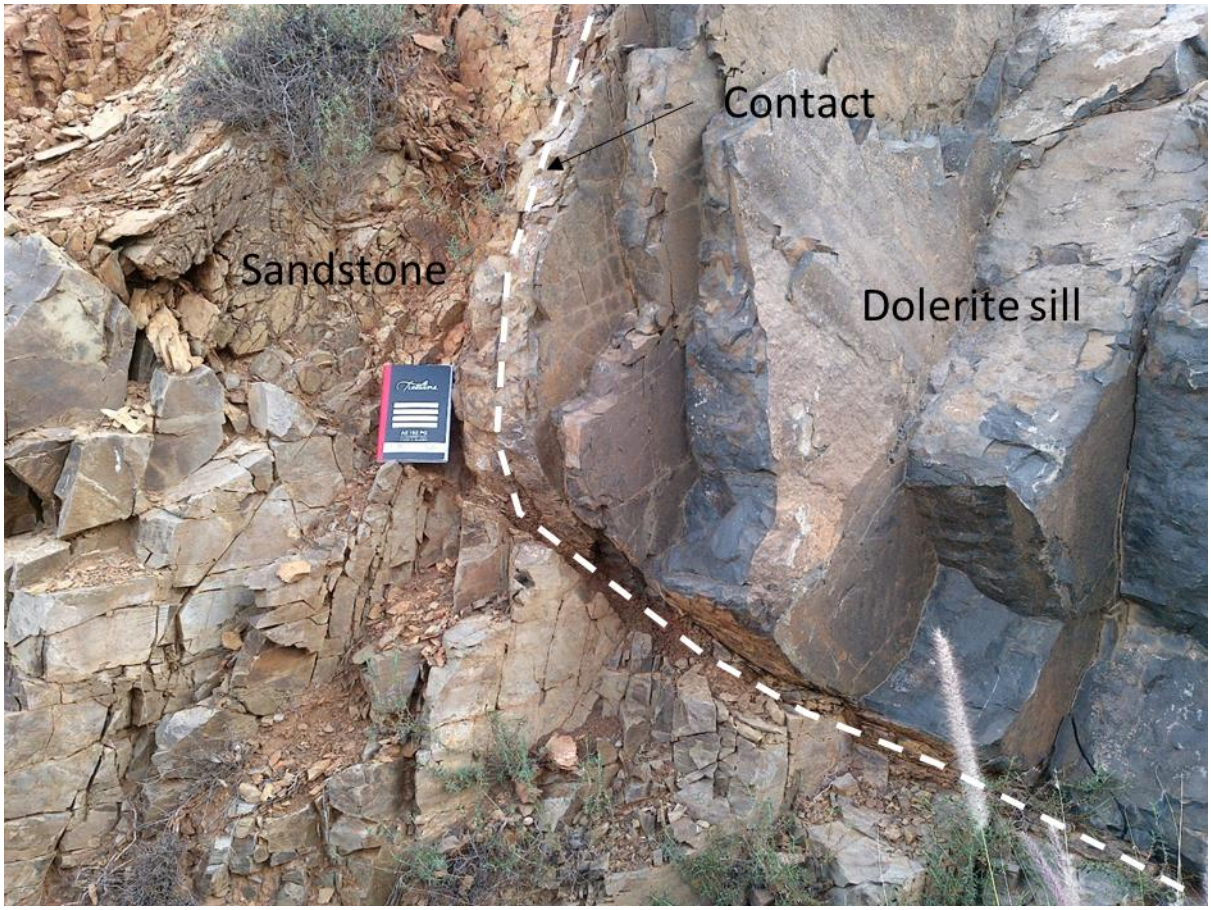

Figure 3-5 Contact between Poortjie Member and Karoo dolerite sill where baking of the country-rock is evident.

3.1.5 Kimberlites

Kimberlite swarms were mapped in the study area although are predominantly in the north, northeast, and west of the study area. The Kimberlites dykes intruded from 170 Ma to 80 Ma (Woodford and Chevallier, 2002b). The Kimberlite dyke swarms intruded into similar trends to the Karoo dolerite dykes (NNW and NNE) but can be identified with a regular pattern characterized by thin sub-parallel linear features.

3.1.6 Quaternary sediments

The Quaternary sediments are composed dominantly of alluvium with subordinate colluvium, eluvium, calcrete, and scree (Cole *et al.,* 2016b). The alluvium is deposited on river and stream beds and composed dominantly of silt- to pebble-size rock fragments. The alluvium thickness varies from a few metres to approximately 9 m in the Gamka River valley located northeast of Beaufort West. The rock fragments amongst the silt matrix consist of sandstone, mudstone, siltstone, calcrete and dolerite (Cole *et al.,* 2016b).

Colluvium is found on gentle slopes, mainly at the foot of the Great Escarpment and can be calcareous in places. Eluvium is composed of angular to sub-angular rock fragments that are set in a matrix composed of sand, clay and/or silt. Calcrete is found east of Beaufort West on the peneplain and it contains fragments of mudstone, sandstone and siltstone. Scree is found on the mountain slopes and steep hills in the study area, particularly the slopes of the Great Escarpment, and consists of unconsolidated sediments with rock fragments set in a finer clayey to sandy matrix.

3.2 Structural geology

The oldest structural features in the Karoo Supergroup are related to the Cape Fold Belt folds predominant south of the basin that resulted from a N-S compressive stress field during the Late Palaeozoic (300-250 Ma). Younger structures are related to the early phase of Gondwana break-up, which was dominated by a NW-SE compressive stress field. Chevallier and Woodford (1999) suggested that the E-W long dykes intruded along a major right-lateral E-W shear/dislocation zone lying mostly north of the study area, and that these dykes were accompanied by Riedel shears (NW) and NE-trending P-type fractures.

3.2.1 Folds

The Cape Fold Belt is characterised in the south by east-west trending folds. Rocks in the southern part of the study area, located over 150 km north of the fold belt also display E-W trending folds. Folding style in the Cape Fold Belt is diverse but folds in the study area are characterised by gentle folding with approximately 170° interlimb angle (Woodford and Chevallier, 2002a).

3.2.2 Faults

Faults found in the basin are linked to the Cape Fold Belt formation, they take place throughout the Cape Supergroup and into the Beaufort Group (Booth and Goedhart, 2004). In the study area, the Beaufort Group strata and the dolerites are cut by brittle faults, (Dhansay *et al.,* 2017, **Figure 3-1**).

Between latitude 32˚30'0″ S (within the study area) and 32°45'0″ S, where the sediments are folded, the sandstone strata are cut by numerous E-W-trending listric thrusts (fractures oblique to the bedding) that are filled with quartz, as well as conjugate joints and quartz-filled shears and tension gashes (Woodford and Chevallier, 2002a). Listric thrusts are localised south of the study area; however, the most dominant faults are strike-slip and normal faults attributed to both Cape Fold Belt and rifting phase during Gondwana break-up (Dhansay, 2018a, **Table 3-1**).

Large faults structures were observed in the area with a strike length ranging from 1 to 30 km for all the fault types (Dhansay, pers. comm., 2020). Mineralised slickensides in the area resulted from movement along shear fractures and along shallow and moderately-dipping fault planes (**Figure 3-6**). In **Table 3-1**, the mineralised slickensides are shown by 11 and 12 fault-slip measurements (Cole *et al.,* 2016b). Movement was localised between shallow to moderately dipping fault planes within these shear fractures.

a)  b) 

Figure 3-6 Slickenside development on fault plane sub-parallel to bedding. (a) Slickensides are associated with calcite mineralization (location: 22,563° E; -32,493° S) and (b) Groove surfaces associated with quartz mineralization (location: 21,911° E; -32,696° S).

3.2.3 Fractures

The lithologies of the study area have been subjected to brittle deformation as evidenced by fractures. In the Karoo, fractures are significant for groundwater flow and recharge (Botha and Cloot, 2004) and can also influence natural gas movement (Cole *et al.,* 2016b). Different mechanisms may lead to fracture development in the Karoo (Woodford and Chevallier, 2002a):

- Magma activities from both intrusive and extrusive events. The fracturing of the country-rock can occur during and after dolerite emplacement (Chevallier *et al.,* 2001);
- Non-intrusive tectonic structures which include folding, bedding-plane fracturing, regional lineaments, faulting, vertical jointing;
- Diagenesis, thermo-metamorphism; and
- Mechanical weathering

Dhansay *et al.* (2017) measured 365 fractures in and around the study area, which were combined with fault-slip field data and fracture measurement locations (**Figure 3-1)**. The fractures were measured on both country rock and on dolerites. Dhansay *et al*. (2017) observed that the fault-slip field information in the study area is poorly

developed. **Table 3-1** shows the fault-displacement data for both fault types within the study area. Dhansay *et al*. (2017) used this information to calculate the paleo-stress axes orientations within the study area. Results were compared with the current stress axes from World Stress Map (Heidbach *et al.,* 2016) and earthquake focal mechanisms outside the study area (Brandt and Saunders, 2011). Based on the findings of slip and dilation analysis by Dhansay *et al.* (2017), fractures that are susceptible to reactivation are E-W and NW-SE trends and particularly those that are steeply inclined over 70°.

Table 3-1 Fault-slip field measurements in the study area measured by Dhansay *et al.* (2017).

ID	**Measurement location**		**Fault plane**		**Fault Slip lineation**		
	Lon	Lat	Dip direction	Dip	Fault Slip	Plunge	Movement
1	22.566	-32.230	334	74	323	74	Normal
2	22.529	-32.383	0	9	2	9	Normal
3	22.564	-32.493	121	13	182	6	Normal
4	22.529	-32.382	353	11	358	11	Normal
5	22.553	-32.455	346	19	346	19	Normal
6	22.450	-32.101	222	14	248	13	Normal
7	22.529	-32.383	219	84	308	9	Dextral
8	22.564	-32.493	164	82	253	10	Dextral
9	22.570	-32.565	174	86	263	12	Dextral
10	22.487	-32.400	359	85	86	32	Dextral
11	22.631	-32.345	194	71	280	11	Dextral
12	22.752	-32.087	258	85	169	12	Sinistral
13	22.448	-32.122	231	82	318	20	Dextral
14	22.529	-32.382	171	86	82	14	Sinistral
15	22.448	-32.122	72	86	161	9	Dextral
16	22.456	-32.071	59	83	332	26	Sinistral
17	22.877	-32.158	338	12	256	2	Sinistral

In the study area above the escarpment, the dolerites show fracture sets that could relate to cooling. These fractures are referred to by Chevallier et al. (2001) as the post-emplacement fractures common in the Karoo Basin. Rose diagram plots in **Figure 3-8** show the combined fracture orientation measurements on both country rock and dolerites in the study area. The earthquake focal mechanism located around the study area is shown in **Figure 3-8**. The focal mechanisms of the earthquake show seismic events nearby the study area having a strike-slip component possibly related to the tectonic discontinuities. These discontinuities include the Cape Fold Belt towards both north and south of the study area and the Namaqua-Natal boundary. There is a correlation between the seismic events from the E-W oriented faults and the E-W fractured that are found within the area and also around the study area (Dhansay, 2018a).

Four rose diagram plots in **Figure 3-8** relate to outcrops above the escarpment. In the northwestern and northeastern parts of the area, ENE-WSW to NE-SW trends dominate over NNW-SSE to NW-SE trends. Both NE-SW and NW-SE fracture trends could be associated with the NE-oriented P shear type fractures and NW-oriented Riedel shear fracture accompanying the right-lateral E-W shear zone that Woodford and Chevallier (2002b) mapped in the Victoria West area. The middle part of the escarpment is dominated by E-W to ESE-WSW fracture trends. Along the edge of the escarpment, three trends are dominant: E-W, NE-SW and NW-SE. East of Beaufort West, E-W and NE-SW trends are observed. The dominant trends south of Beaufort West, where there is scant dolerite outcrop, are NW-SE to NNW-SSE, NE-SW and E-W to ESE-WNW. These trends will be compared with the structural trends delineated from the high-resolution magnetic data in Chapter Seven (section 7.1.2).

3.2.4 Foliation

In the study area, foliation occurred in response to shearing that is associated with minor fault surfaces, particularly on the low-angle normal faults (Cole *et al.,* 2016b, **Figure 3-7**). Fine-grained Beaufort Group lithologies in the area were possible preferred localities for strain partition. Also, foliation occurs in the dolerite rocks and is commonly associated with fracture planes that have experienced various levels of

shearing (Cole *et al.,* 2016b). The fabrics in the dolerites suggest that foliations formed both syn- and post-dolerite intrusion (Dhansay, pers.comm., 2020).



Figure 3-7 Foliation development around Beaufort West in response to discrete shearing (co-ordinates: 32.0745 S; 22.7474 E, Cole *et al.,* 2016b).

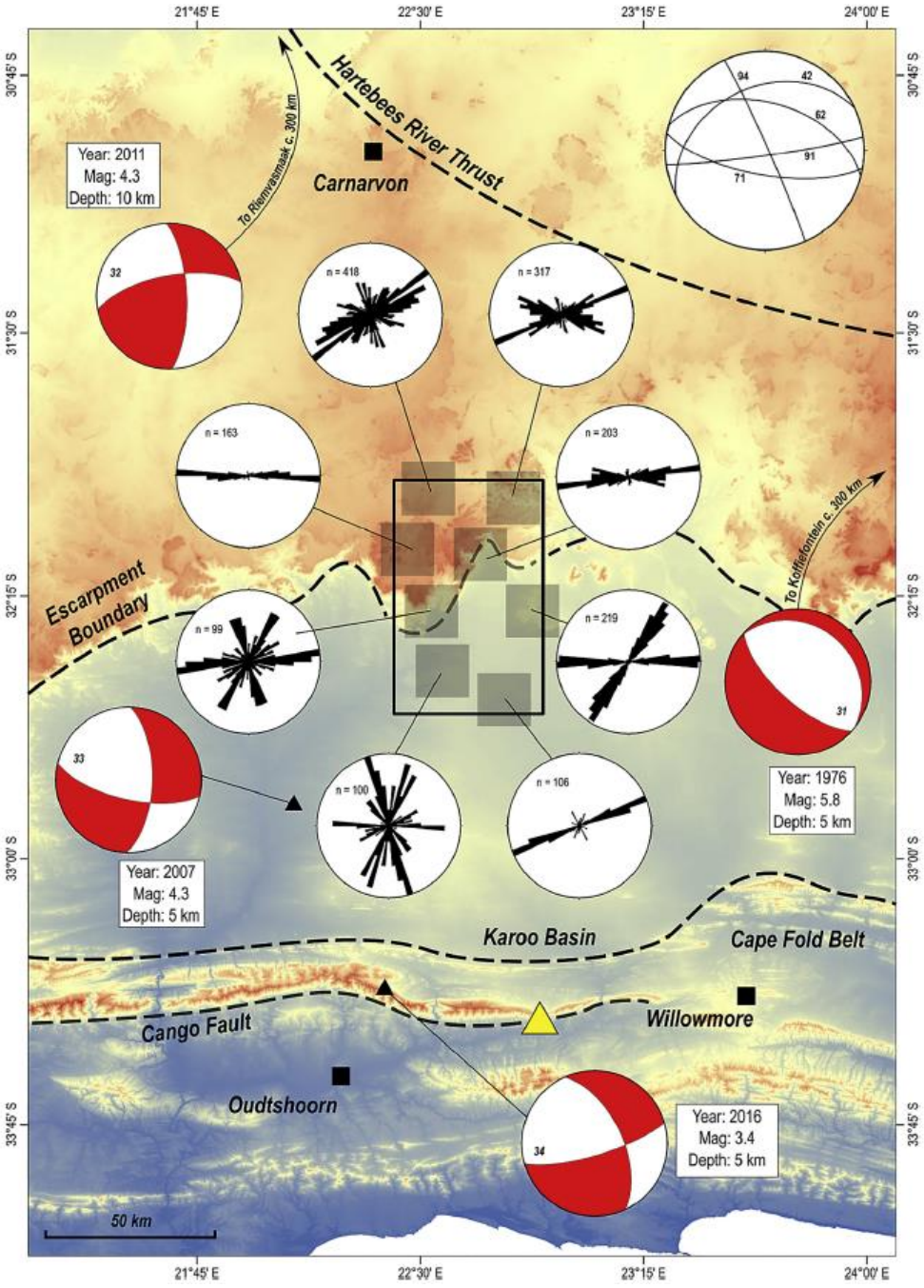

Figure 3-8 Stereo-diagrams of fracture orientations mapped from remote sensing throughout the study area (black rose diagrams) from Dhansay *et al.* (2017). Current stress axes from earthquake focal mechanisms are shown around the study area (red beach balls), the location of the large paleo-seismic event (yellow triangle). Orientations of fracture sets that could be reactivated at hydraulic pressures above hydrostatic pore fluid pressures, e.g. 32 MPa up to approximately 10 MPa, shown by top right insert.

3.3 Monitoring boreholes

Two boreholes were drilled in the study area and both intersected a dolerite intrusion. The boreholes (R01-BW and R02-BW) were drilled by Torque Africa Exploration using air rotary percussion (Nxokwana *et al.,* 2018, **Figure 3-1**). R01-BW is located at 22.61693° E and 32.326602° S, was drilled to a depth of 1402 m. R02-BW is located at 22.60614° E; 32. 33712° S and was drilled to 516 m. **Table 3-2** shows the thicknesses of the geological units intersected by the boreholes and the graphic presentation of these boreholes is shown in **Figure 3-9.**

In R01-BW, a fine- to medium-grained dolerite showing a crystalline matrix intruded the Abrahamskraal Formation at depths of ~492 m to ~508 m and no other dolerite intrusion was recorded from percussion chips (Nxokwana *et al.,* 2018). Downhole geophysics was performed and recorded dolerite rock at depths of 489 to 508 m and depths of 690 to 692 m recognised by high resistivity, high density and very low gamma-ray values (Nxokwana *et al.,* 2018). In borehole R01-BW, Abrahamskraal Formation has a total thickness of 677 m.

In the R02-BW borehole, the dolerite also intruded into the Abrahamskraal Formation between depths of 161 to 178 m and is described as a fine- to medium-grained dolerite with calcite veins (Nxokwana *et al.,* 2018). Downhole geophysics was performed and dolerite rock was recorded at depths between 159.5 to 176.5 m. In the R02-BW borehole, the Abrahamskraal Formation has a thickness of 434 m intersected during drilling but this may not be the total thickness of the formation because drilling was stopped at 516 m.

Table 3-2 Boreholes drilled within the study area that intersected the Karoo dolerite showing logs and total thicknesses (Nxokwana *et al.,* 2018).

Borehole name	Depth of unit (m)	Thickness (m)	Stratigraphy
R01-BW	0-57	57	Poortjie Member (Middleton Formation)
	57-492	435	Abrahamskraal Formation
	492-508	16	Karoo dolerite
	508-750	242	Abrahamskraal Formation
	750-919	169	Waterford Formation
	919-1402	483	Tierberg Formation
R02-BW	0-1	1	Eluvial and soil
	1-65	64	Poortjie Member (Middleton Formation)
	65-161	96	Abrahamskraal Formation
	161-178	17	Karoo dolerite
	178-516	338	Abrahamskraal Formation

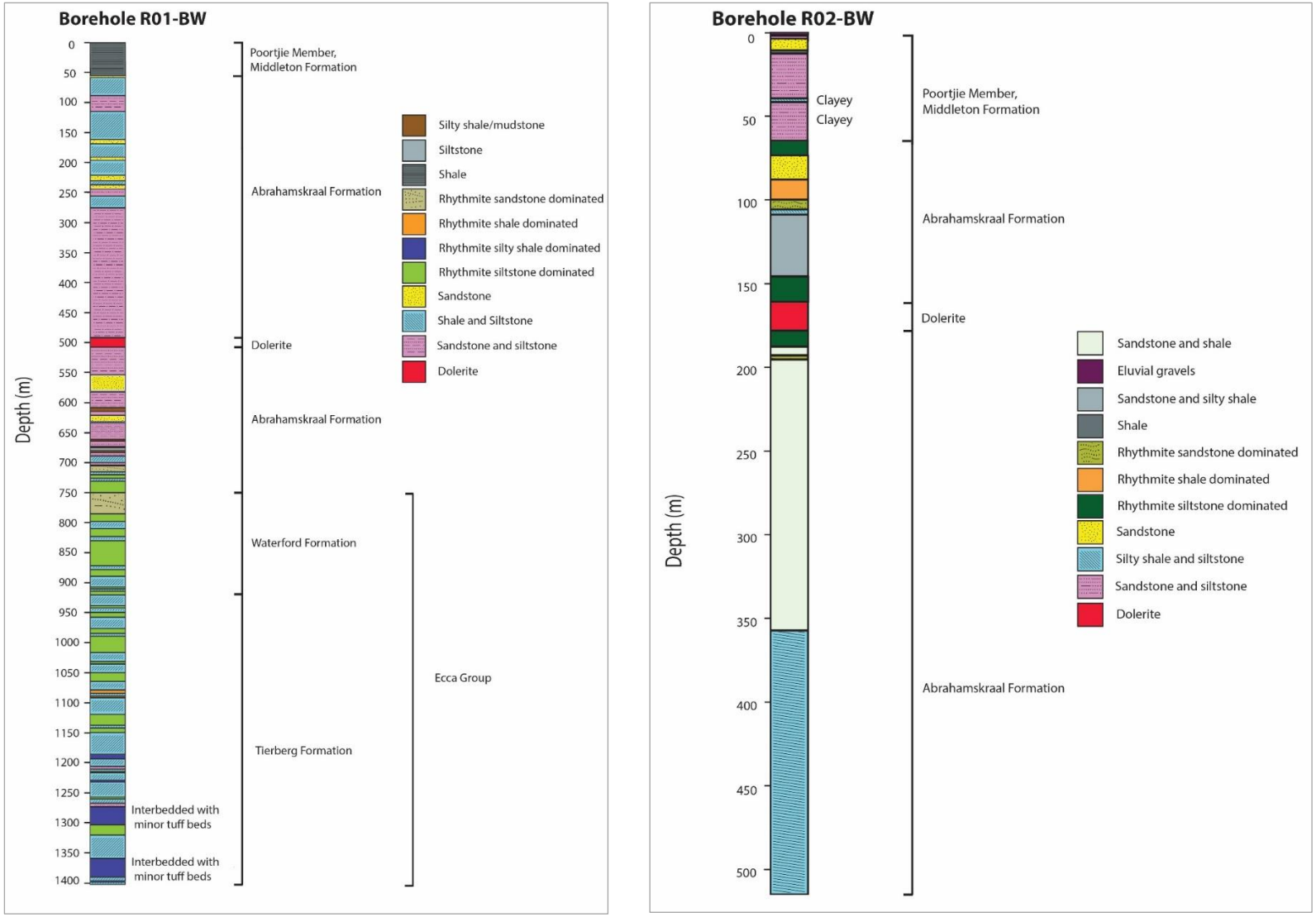

Figure 3-9 Graphical borehole logs of R01-BW and R02-BW (Nxokwana *et al.,* 2018).

3.4 Summary

- Observations in the chapter are largely based on the study by Cole *et al*. (2016b) and Dhansay *et al*. (2017). Geological mapping by Cole *et al.* (2016b) at a scale of 1:50 000 resulted to several modifications to stratigraphy. Changes made west of longitude 24° E were as follows: (1) lower members of Teekloof Formation (Poortjie and Hoedemaker) are grouped under Middleton Formation, and (2) upper members of Teekloof Formation (Oukloof and Steenkamps Vlakte) are grouped under Balfour Formation (Cole *et al.,* 2016b).
- Two main dolerite dyke trends were identified through this mapping: E-W to WNW-ESE, and NNW-SSE. The observed dolerite trends correlate well with the E-W and NNW-trending dykes in the Victoria West area that Chevallier and Woodford (1999) observed. A right-lateral shear zone was identified on the E-W dykes by Chevallier and Woodford (1999), and similar strike-slip arrangement is mapped on the dykes in the study area. SSE-NNW dykes are long, in Middelburg (approximately 300 km from Beaufort West) the dyke is 200 km long. In the study area, the NNW-SSE dyke west of longitude 22°30'0″ E **(Figure 3-1)** is approximately 29 km but extends further outside the study area.
- Dolerite sills dominate the escarpment in the study area and the rims are usually topographically accentuated. Five levels of sills were mapped with varying thicknesses and are interconnected via up-stepping inclined sheets such as the one seen in De Jager's pass (Cole *et al.,* 2016b). Other inclined sheets include one that outcrops near Beaufort West town and the large inclined sheet found in the south of the study area. Along the dolerite contacts fracturing and baking of sediments are observed. The major E-W dyke northeast of Beaufort West cuts through the dolerite sills in the west, similar to the situation observed in the Victoria West sill-ring complex (Chevallier and Woodford, 1999).
- Two dominant faults are found in the study area, strike-slip and normal faults (Cole *et al.,* 2016b). These faults cut through the Beaufort Group sediments. Shearing occurred shown by the development of mineralised slickensides along shallow and moderately-dipping fault planes and shear fractures.
- Dhansay *et al*. (2017) measured 365 fractures in and around the study area and combined these with fault-displacement data for all fault types in the study

area. Paleo-stress axis orientations were calculated and compared with current stress axis orientations from both the World Stress Map and nearby earthquake focal mechanisms. Slip and dilation analysis showed that E-W and NW-SE fractures, and particularly those that are steeply inclined over 70°, are susceptible to reactivation. Rose diagram plots performed on the fractures showed the following trends: NE-SW to ENE-WSW, E-W to ESE-WNW and NW-SE to NNW-SSE, which could be a result of the NW-SE compressive stress regime during Gondwanaland break-up.

- Foliation in the study area has occurred in response to shearing that is associated with minor fault surfaces and also fracture planes in the dolerite.
- Both monitoring boreholes drilled by air rotary percussion R01-BW and R02-BW located east of Beaufort West intersected a dolerite intrusion and this was confirmed by downhole geophysics (Nxokwana *et al.,* 2018). R01-BW showed two dolerites delineated by downhole geophysics at depths ranging from 489 to 508 m and 690 to 692 m. Dolerite rock was delineated at depths of 161 to 178 m in R02-BW borehole. Both dolerites intruded the Abrahamskraal Formation.

4 CHAPTER FOUR – MAGNETIC METHOD

4.1 Introduction

The magnetic method is a potential field method used to determine the subsurface geology anomalies in the earth's magnetic field produced by rocks with contrasting magnetic properties in subsurface (Mariita, 2007). The Karoo sediments are non-magnetic while the Karoo dolerites are magnetic, therefore the magnetic method is a suitable method to delineate the Karoo dolerite sills and dykes in the study area. Other common causes of magnetic anomalies are folded magnetic rock units or faulted magnetic rock units. Magnetic rock units are those that contain magnetite.

Magnetic surveys can be conducted on land or at sea, and can either be ground-based, airborne or satellite. Airborne surveys have lower resolution compared to ground magnetic surveys, but ground surveys are usually collected over a small survey area.

These magnetic anomalies are caused by induced and remanent magnetism of crustal rocks. The magnitudes of induced and remanent magnetisation rely on the composition, quantity and size of magnetic mineral grains (Hoover *et al.,* 1993).

4.1.1 Induced magnetism

Induced magnetism is a component of magnetisation that is generated in response to an applied field in the direction of the Earth’s magnetic field and disappears when the applied field is removed (Gunn and Dentith, 1997). Induced magnetism is more common than remanent magnetism. Mariita (2007) defined the induced magnetic anomaly’s shape, size and amplitude as a function of geometry, depth, orientation, size, and also magnetic susceptibility of the particular body together with surveyed area’s inclination and intensity of the Earth’s magnetic field.

4.1.2 Natural Remanent Magnetism (NRM)

The NRM is a permanently recorded remanent magnetism in rock even after the inducing field is switched off and often contributes to the total magnetization (Telford *et al.,* 1976). NRM includes thermal remanent magnetization (TRM), detrital magnetization (DRM), chemical remanent magnetization (CRM), isothermal remanent magnetization (IRM) and viscous remanent magnetization (VRM) (Isles and Rankin, 2013). The most common way for rocks with high magnetic susceptibility to acquire NRM would be during cooling of magma through its Curie temperature. This thermal remanent magnetization (TRM) is therefore acquired in the geomagnetic field direction at that time of cooling (Telford *et al.,* 1976).

4.1.3 Magnetic susceptibility

The physical property of the magnetic method is magnetic susceptibility, which describes the ability of lithology to be magnetised. The results are useful for geophysical interpretation and modelling purposes. Magnetic susceptibility (*K*) is defined by **Equation 4-1**:

$$M = k * H \qquad \textbf{4-1}$$

where H is the inducing magnetic field and M represents the induced magnetization of the material. Both M and H are specified in amperes per meter (A/m) and the volumetric susceptibility k is dimensionless, sometimes expressed as “SI”. The magnetic response is reliant on the amount of the magnetic material and the susceptibility of the rocks and minerals (Telford *et al.,* 1976).

Magnetic material can be subdivided into three groups: (1) diamagnetic material that has negative magnetic susceptibility, (2) paramagnetic material that has positive magnetic susceptibility but low in absolute value and (3) ferromagnetic material that has positive magnetic susceptibility and very high in absolute value, and also can have magnetism even when the external field is removed (**Figure 4-1**). The susceptibility of

ferromagnetic material will vary as the field strength of the external field varies. Magnetic susceptibility is normally measured in a low-field strength of ≤ 1 nT, the reason is that this allows high sensitivity, rapid measurements, making the procedure is easier (Rochette *et al.,* 1992).

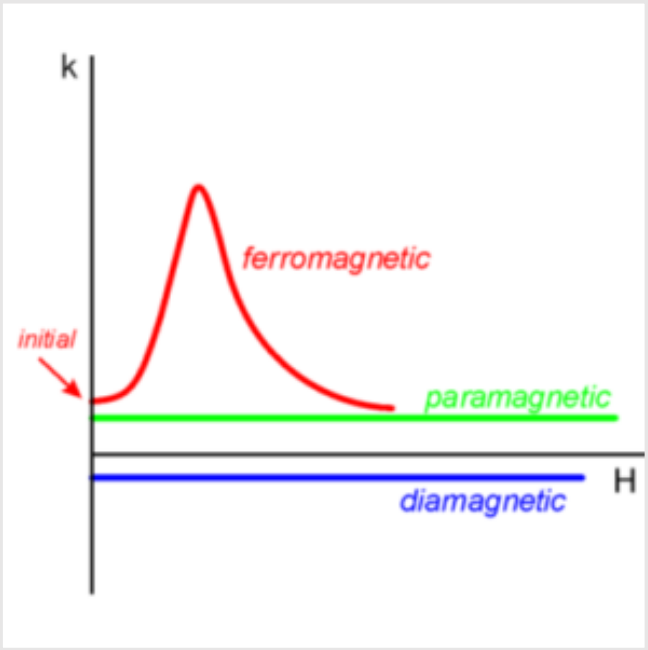

Figure 4-1 Field variation of susceptibility for ferromagnetic, paramagnetic and diamagnetic substances (Hrouda *et al.,* 2009).

4.1.4 Magnetic survey instrumentation

Magnetic surveys measure the variations in the earth's magnetic field caused by differences in the magnetic properties of the lithology underneath the surface. This measurement consists of a combination of remanent and induced fields in the crustal rocks and the earth's core field (such as International Geomagnetic Reference Field, IGRF) (Isles and Rankin, 2013).

A magnetometer is used to measure the strength and orientation of the magnetic field, whilst some measure only the strength of the magnetic field. Commonly used magnetometers are fluxgate, proton precession, gradiometer and caesium vapour

systems. Fluxgate, caesium vapour and proton magnetometers are commonly used for airborne surveys. The fluxgate and the gradiometer vector magnetometers measure both the strength and orientation of the magnetic field.

4.2 Magnetic standard processing

The following standard steps are taken in the reduction of aeromagnetic data, some of which also apply to marine and ground data. These include diurnal variations, levelling, removal of the International Geomagnetic Reference Field (IGRF), and then finally the data is gridded (Luyendyk, 1997).

4.2.1 Diurnal variations

The magnetic field of the earth has day-night variations due to variations in solar activity. During survey, this activity is measured by a base station on the ground at a fixed location. Survey readings are then corrected using these measurements. The correction is never larger than 40 nT. If the variation is larger due to solar flares then the survey is put on hold.

4.2.2 Levelling

The survey flight lines for both the regional and high-resolution aeromagnetic data were oriented north-south. Tie lines are flown at right angles to the flight lines and the intersection between the flight lines and tie lines are called crossover points. Crossover points are measured at different times during the survey and therefore the magnetic field values at the same crossover point will differ. Levelling corrects for these differences between the readings at the crossover points.

4.2.3 International Geomagnetic Reference Field (IGRF)

The purpose of this correction is to remove the background geomagnetic field from the surveyed magnetic data and remain with the residual magnetic field that is related to the subsurface geology of the area being investigated (Regan and Cain, 1975).

Spherical harmonic analysis shows that above 99% of the main geomagnetic field comes from convection in the liquid outer core of the earth. Corrections are conducted by the applications of magnetic reference models to calculate magnetic declination with other components of the magnetic field.

The reference field model is a mathematical algorithm that is based on the analysis of the magnetic monitoring satellites. These satellites orbit partially or the whole world. The common method used to observe the magnetic field and create these global models is the spherical harmonic analysis. The most commonly used models are International Geomagnetic Reference Field (IGRF) and the World Magnetic Model (WMM). Both are traditionally updated every five years. The IGRF model was used in this study as Regan and Cain, (1975) refers to it as being useful for magnetic survey reductions. The IGRF's inception was during International Association of Geomagnetism and Aeronomy (IAGA) symposium that took place in 1968 (Regan and Cain, 1975).

The correction is done by calculating the IGRF value for every point the magnetometer took a reading and from the observed value, subtract the IGRF value to provide an anomaly due to subsurface bodies (Reeves, 2005). The correction was done to the levelled magnetic data.

4.3 Magnetic data filtering techniques

4.3.1 Sunshading

Sunshading is regularly applied mainly to potential field data to enhance linear features (faults, dykes, and other lineaments) or suppress linear features depending on the elevation and azimuth of the light source in the filter. It is applied to gridded data. The interpreter will choose the elevation and azimuth of a source of illumination such as the sun or light source and the resulting reflectance from topographic data surface will be calculated. Reflectance is calculated for all data/gridded points.

Lambertian reflector is given by **Equation 4-2** (Horn, 1982):

$$R = \frac{1 + p_0 p + q_0 q}{\sqrt{1+p^2+q^2}+\sqrt{1+p^2{}_0+q^2{}_0}} \qquad \textbf{4-2}$$

where *p and q* are the horizontal gradients of the data which can be calculated from both frequency and space domains, p_0 = -cos θ tan θ, q_0 = -sin θ tan θ, θ is the sun elevation (measured from vertical), θ represents the azimuth (measured in an anticlockwise direction from East (Horn, 1982).

Cooper, (2003) demonstrates sunshading of linear features in **Figure 4-2**. Shown in **Figure 4-2a** is data composed of intersecting linear features at the same point. Sunshading from the East with a sun elevation of 30° from horizontal is shown in **Figure 4-2b**, where N-S linear features are identified. **Figure 4-2c** and **d** are also sun shaded similar to **Figure 4-2a** with different orders where order 1 is shown in **Figure 4-2c** and order 5 is shown in **Figure 4-2d**.

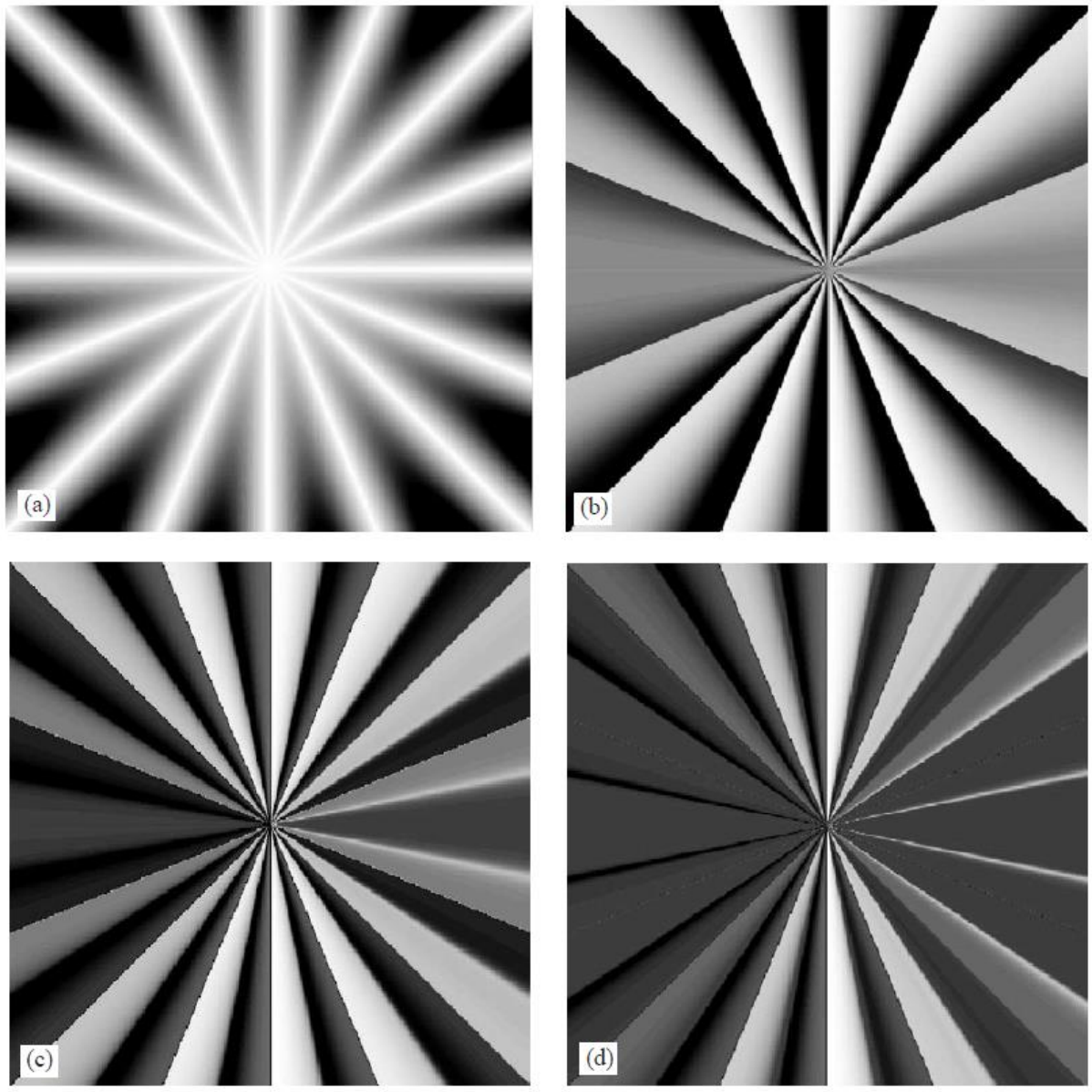

Figure 4-2 Sun shading linear features (a) presented data; (b) sun shaded data azimuth 0, inclination 30°, order 0; (c) sun shaded data azimuth 0, inclination 30°, order 1 and (d) sun shaded data azimuth 0, inclination 30°, order 5 (Cooper, 2003).

4.3.2 Vertical derivative

The first vertical derivative method is a filter that enhances shallow geologic sources while suppressing deeper geological sources (Telford *et al.,* 1990). It is applied to the IGRF corrected TMI data. It also enhances the noise in the data. In the wavenumber domain, the nth order vertical derivative is shown in **Equation 4-3** (Telford *et al.,* 1976 ; Sakala *et al.,* 2017):

$$A'(k) = A(k)|k|^n \qquad \textbf{4-3}$$

where A'(k) is the amplitude at a wavenumber k, k=2π/λ and **λ** is the wavelength.

4.3.3 Analytic signal

The analytic signal is useful in locating the edges of the bodies for shallow sources or at a regional scale (Li, 2006). The curve of the analytic signal over a body has a tendency of being wider than the TMI curve but it can resolve sources that are closely-spaced because it is a function of derivatives.

Equation 4-4 is used to derive the three orthogonal gradients of the total magnetic field at a location (x,y) (MacLeod, *et al.,* 1993):

$$|A(x,y)| = \sqrt{\left(\frac{dT}{dx}\right)^2 + \left(\frac{dT}{dy}\right)^2 + \left(\frac{dT}{dx}\right)^2} \qquad \textbf{4-4}$$

where A(x,y) is the amplitude of analytic signal at location (x,y) and T is the observed total magnetic field at (x,y). The x and y derivative of the magnetic data are calculated sometimes using a 3 x 3 filter while the z derivative is calculated using the Fast Fourier Transform (FFT) system (MacLeod, *et al.,* 1993).

Li (2006) highlights misleading statements about the analytic signal, that: (1) magnitude of the analytic signal is not dependent on both the magnetization direction and direction of the Earth's field, (2) total magnetic intensity data entails both normal and remanent magnetization. Analytic signal will transform both magnetizations into a single response because it is insensitive to the direction of magnetization. Therefore the results will not be accurate for bodies with high remanent magnetization.

Li (2006) elaborated that the method depends on the burial depth, body's magnetization direction, earth's magnetic-field direction, extent and the angle of dip of a source body.

4.3.4 Wavenumber domain

In order to apply filters to the IGRF corrected TMI data, the grid must first be converted from space domain to the wave/frequency domain by the application of Fourier Transform in MAGMAP (Oasis Montaj Geosoft software). Step by step filtering is used. These filters can be used to remove or to enhance the information of interest. Then once the filter has been applied in the wave domain, the grid is converted back into the space domain for ease of visualization. The Fourier transformation is, therefore, the connection between space domain and wavenumber domain (Reeves, 2005).

Bhattacharyya (1966) divided filtering and the Fast Fourier Transformation (FFT) into the three steps below and shown in **Figure 4-3**:

- the grid is transformed to two-dimensional (2D) spectrum in the wavenumber domain;
- the spectrum is multiplied with a filter in the wavenumber domain and
- filtered spectrum is converted back to space domain using reverse transformation

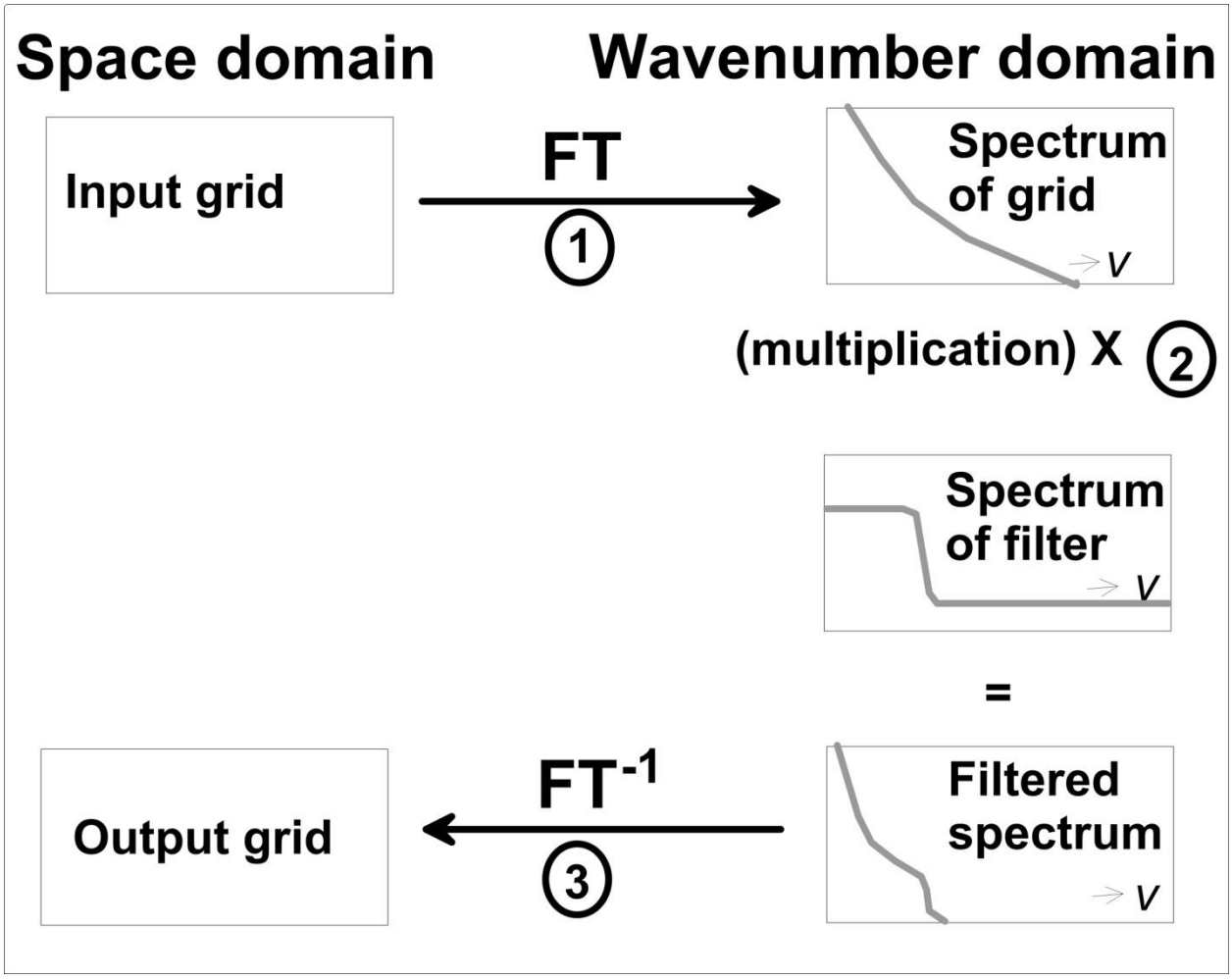

Figure 4-3 Stages for filter data from space to wavenumber domains (Reeves, 2005). 1. The input grid is transformed from space to 2D spectrum in the wavenumber domain; 2. 2D spectrum is multiplied with a filter. 3. Filtered 2D spectrum is converted back to space domain through reverse transformation.

4.3.5 Reduce to the pole

The Reduce to the Pole (RTP) technique is applied to the IGRF corrected magnetic data. The method is useful in low magnetic latitudes and it changes magnetic anomalies to appear as if they are located at the north magnetic pole which makes the interpretation easier (**Figure 4-4**). The RTP filter is useful in aligning highs and gradients of magnetic anomalies over their sources and minimising the polarity effect on the data (Zahra and Oweis, 2016), for example, an east-west dyke in South Africa is characterised by a magnetic high located north and magnetic low in the south with the dyke running between the high and low; while at the magnetic pole the positive will

be over the dyke making it easier to interpret. Interpretation of the RTP filtered magnetic data becomes easier and more accurate. The method is reliant on the shape, susceptibility, also to magnetization and regional field directions (Zahra and Oweis, 2016).

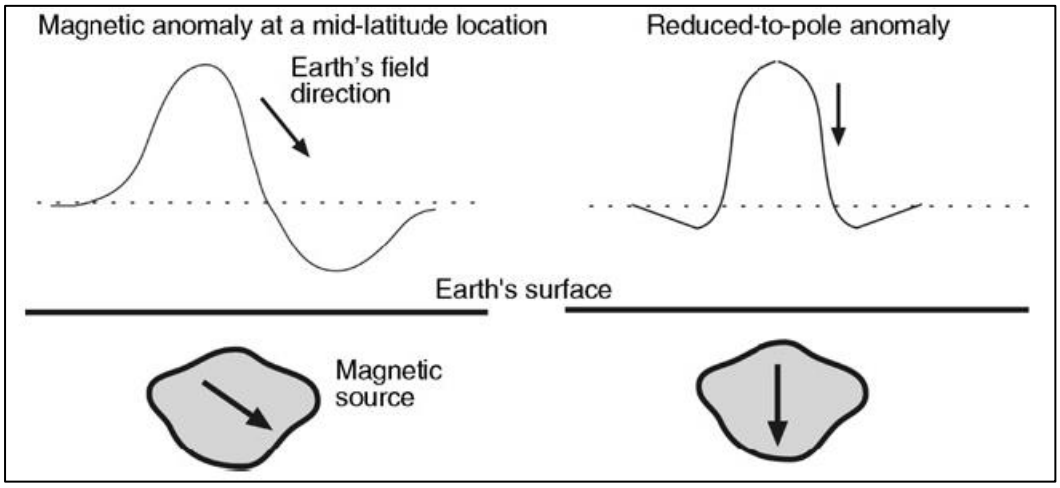

Figure 4-4 Skewness of a magnetic anomaly due to a uniform arbitrarily magnetized source below Earth's surface in an obliquely oriented Earth's magnetic field (left) and its reduced-to-pole expression in the vertical magnetization and vertical field conditions (right) (Ravat, 2007).

The RTP is calculated in the frequency domain using **Equation 4-5** (Grant and Dodds, 1972):

$$\boldsymbol{L(\theta) = \frac{1}{sin\,(I)Cos\,(I)Cos(D-\theta)}} \qquad \textbf{4-5}$$

Where **θ** is the wave number, *I* is the magnetic inclination and D is the magnetic declination.

4.3.6 Power spectrum transformation

The Fast Fourier Transformation (FFT) filters are applied to RTP data to isolate deep regional and shallow residual components of the data. Power spectrum transformation was performed using interactive filtering in MAGMAP Geosoft software. Fast Fourier

Transformation is the second step after the grid has been prepared. Radial Average Spectrum is then performed using the transform grid file (generated from Fast Fourier Transformation) as input grid. A result of this process is a two-dimensional (2D) radially averaged power spectrum plotted against wavenumber (**Figure 4-5**). The radially-averaged power spectrum is based on energy logarithms, hence if the spectrum is plotted on a semi-logarithmic scale it will plot as several linear segments (Khalil *et al.,* 2016). The slope of each segment is used to determine average depth estimates of the ensemble of sources lying at different depths in the subsurface (Spector and Grant, 1970; Khalil *et al.,* 2016). The cut-off wavelength in the filter corresponds to different linear segments that assist in isolating the regional component, residual component and noise in the data located at the shallow part of the curve with very high frequencies (Khalil *et al.,* 2016).The power spectrum shows a decaying curve with increasing frequency and the depth of the magnetic source (h) is determined by **Equation 4-6**:

$$h = -\frac{S}{4\pi} \qquad \textbf{4-6}$$

where S is the slope of the log power spectrum.

Based on the two-dimensional (2D) radially averaged power spectrum curve, the cut-off wavelengths can be defined from the energy power spectrum curve using an appropriate filter. The application of the filter form is the last steps of interactive filtering (MAGMAP). The Butterworth band pass filter was used in the study area because it introduces less ringing to the data (Allen and Mills, 2004). Output maps for regional and residual components are produced after the filter has been applied.

4.3.6.1 Limitations power spectrum transformation

The power spectrum transformation method has limitations, such as grid spacing, precise linear plot on the spectra and window size (Spector and Grant, 1970; Poudjom-Djomani *et al.,*1995; Ranganai, 2012). These limitations could produce incorrect depth estimation. To eliminate the shortcomings of the method the following was suggested: Johnson and Macleod (2016) suggested that a larger area should be used to delineate

low wavenumbers associated with basement anomalies and Ranganai (2012) suggested that the data length should be six times the maximum source depth.

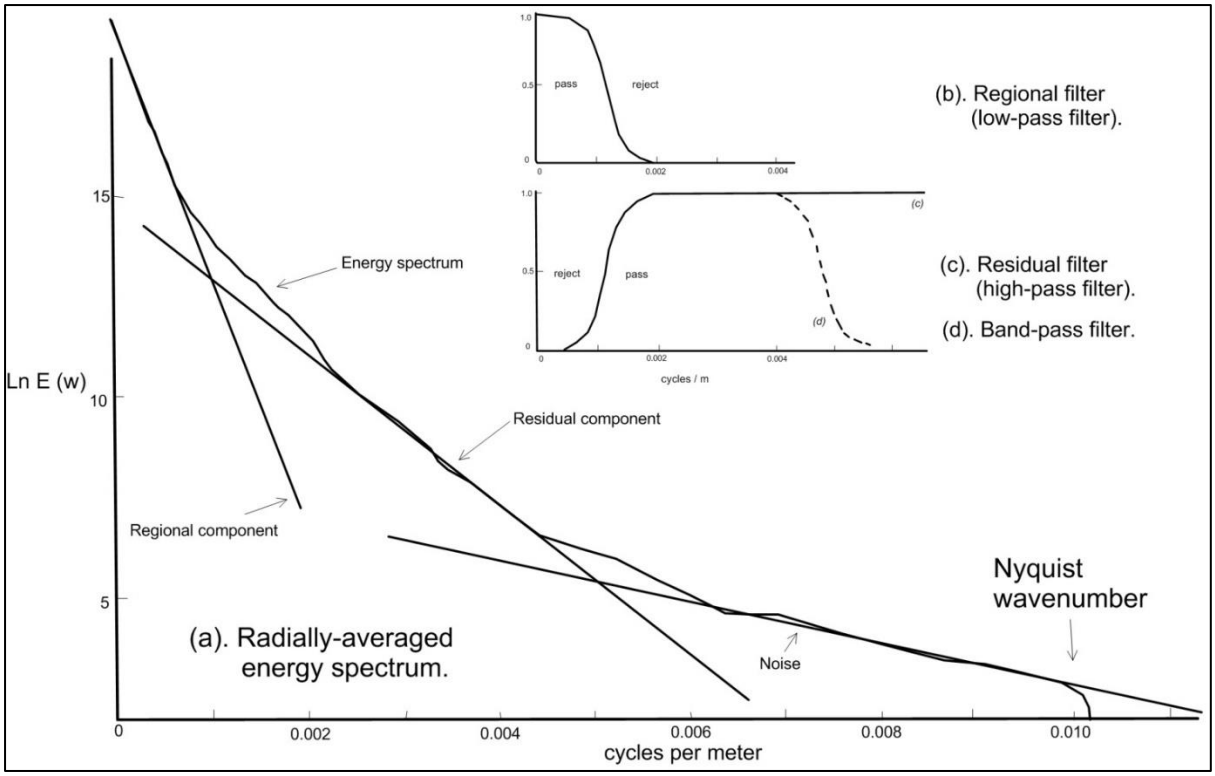

Figure 4-5 Depth estimation technique using the energy spectrum in the wavenumber domain (Reeves, 2005). (a) The radial averaged power spectrum curve after spectrum calculation. (b) Band pass filter was applied to separate the deep magnetic component associated by allowing the low frequencies to pass through and rejecting the higher frequencies. (c) A Butterworth filter was applied by allowing the high frequencies to pass associated with the near-surface magnetic component and rejecting the low frequencies. (d) represents the noise component of the data and it is usually rejected.

4.4 Summary

- The magnetic method is an appropriate tool to map the Karoo dolerite sills and dykes because of their high magnetic susceptibility values when compared to the Karoo sediments known to contain low or no magnetic susceptibility values. Magnetic susceptibility is a physical property of the magnetic method (Telford *et al.,* 1990). However, the method also depends on other parameters such as the size, shape, orientation of remanent or induced magnetisation bodies, and their depth.
- Total Magnetic Intensity (TMI) data contains both short wavelength (associated with shallow bodies) and long wavelength (associated with deep magnetic bodies). In the study, the first vertical derivative and analytic signal filters described in this chapter were used to map the shallow magnetic bodies related to the Karoo dolerites.
- Two-dimensional (2D) radial averaged power spectrum was performed in the wavenumber domain. The energy power spectrum plot is used to determine average depth estimates of magnetic sources lying at different depths in the subsurface. Several linear segments can be drawn from the curve related to magnetic sources. In the study area, output maps for regional and residual components were generated after the Butterworth band pass filter was applied. However, the power spectrum transformation has limitations result in incorrect depth estimations, such as: grid spacing, precise linear plot on the spectra, window size (Spector and Grant, 1970; Poudjom-Djomani *et al.,*1995; Ranganai, 2012). To determine low wavenumbers (related to basement anomalies), a larger area should be used (Johnson and Macleod, 2016).

5 CHAPTER FIVE – DTM, MAGNETIC AND SEISMIC DATA

5.1 Introduction

This chapter focuses on the collection of the geophysics methods (mainly the magnetic method), which was analysed to understand the Karoo dolerite dykes and sills. Filtering of these datasets is briefly discussed and the results are shown.

High-resolution Digital Terrain Model (DTM), airborne magnetic and radiometric surveys (not reported in this study) were flown in November 2017 covering 18 full 1: 50 000 topographic map sheets (**Figure 5-1**). The survey was flown in an N-S direction and tie-tines were in an E-W direction shown in **Figure 5-2**.

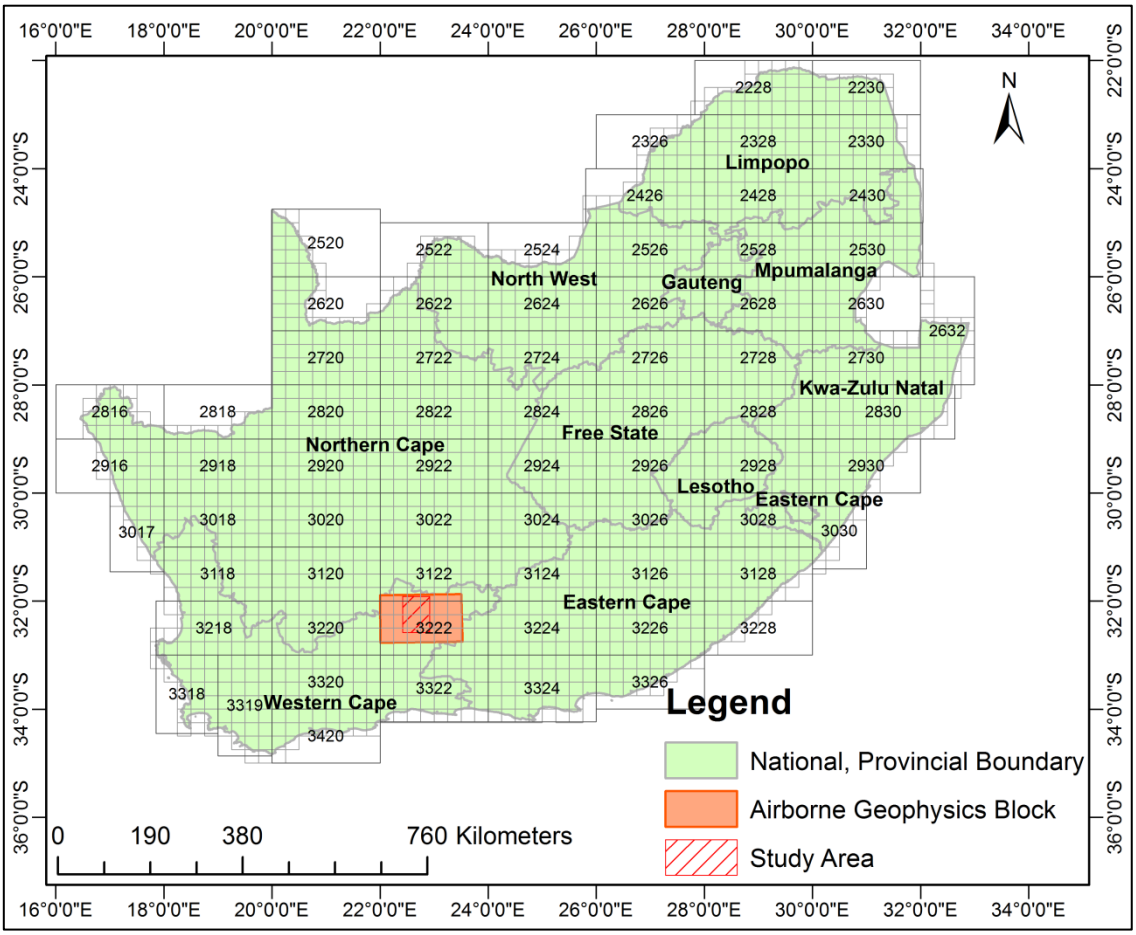

Figure 5-1 Study area in the Western Cape (hatched block) within the high resolution aeromagnetic and radiometric survey block (larger shaded red block). The small and big square boxes represent 1: 50 000 and 1: 250 000 map sheets respectively.

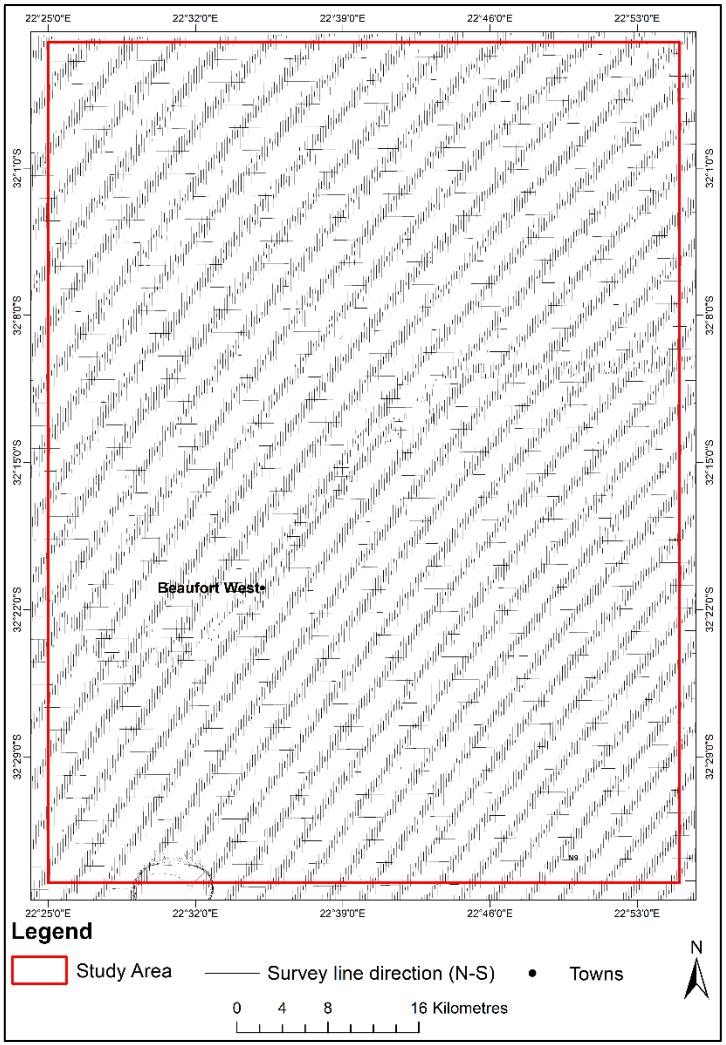

Figure 5-2 Study area (red outline block) within the high-resolution aeromagnetic and radiometric survey block superimposed with N-S survey line direction and E-W tie line direction. This is a zoomed image to show the line path.

5.2 Digital Terrain Model (DTM) data

The topography data was used for extraction of terrain parameters for the study area. Digital Terrain Model data (DTM) was acquired together with magnetic and radiometric data during the survey (AeroPhysX, 2017). The elevation for the study area starts below 900 m in the south of the study area and increases up to 1 700 m above sea level in the northern part of the study area.

The highest elevations correspond to the escarpment in the north capped by the dolerite sills. The lowest elevation zones stretch just below latitude 32°15'0″ S to below 32°33'0″ S. Several rivers namely; Doringhoek, Kuils, Gamka, Spitskop, Krom, Skaapfontein se, Sak, Kwagga, Platdoring, Boeteka, Stols and Ongeluks run through the study area and are superimposed on the elevation map (**Figure 5-3**).

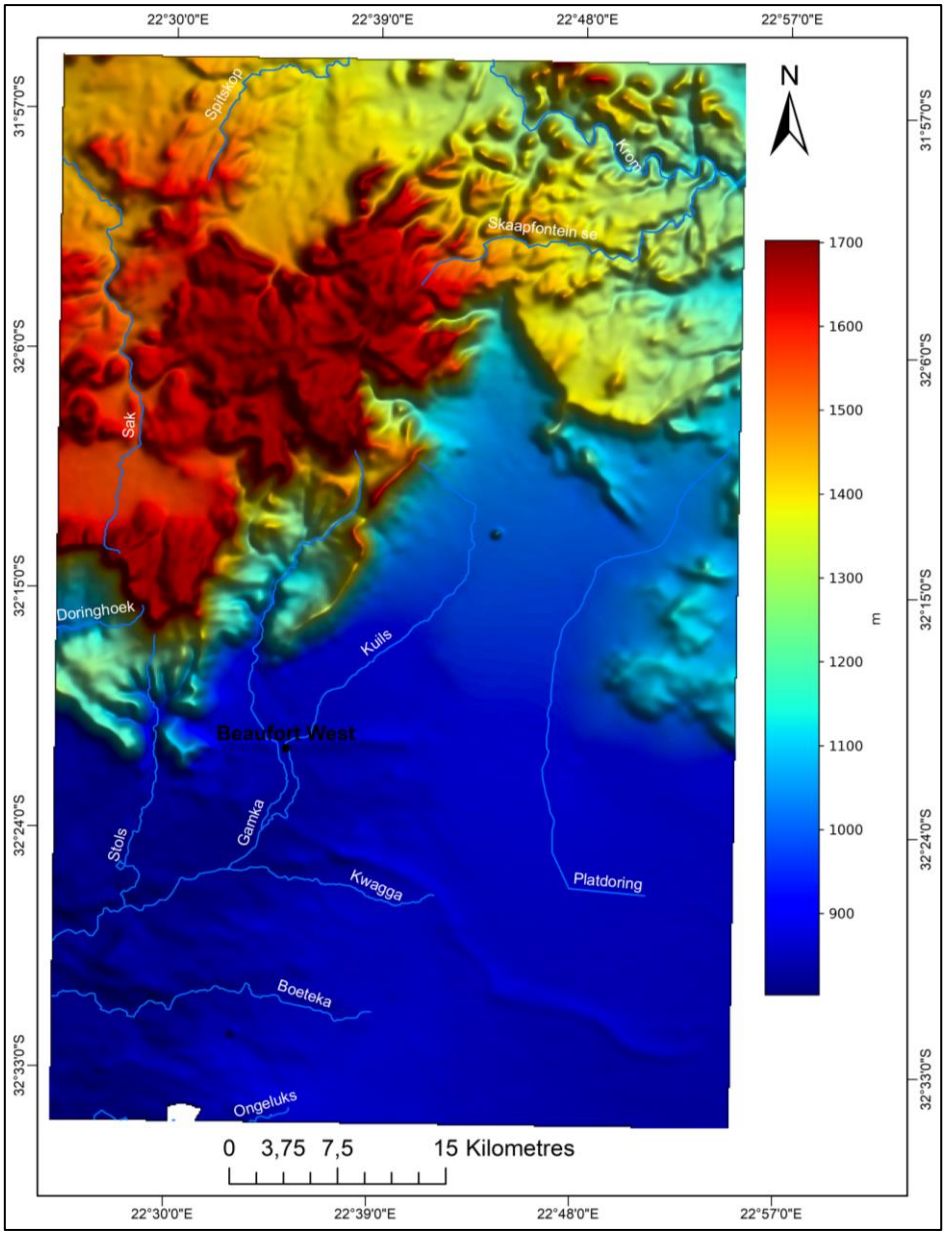

Figure 5-3 Digital Terrain Model (DTM) of the study area with superimposed towns and rivers.

5.3 Magnetic Data

5.3.1 Survey specifications

The regional airborne magnetic data covers the whole of South Africa and was acquired during the latter part of the 20th century (Stettler *et al.,* 2000). Geosearch

(Pty) Ltd was awarded the contract in 1976 to survey the study area (Stettler *et al.,* 2000; **Figure 5-6b**).

Table 5-1 shows the summary of the type of aircraft used to fly the high-resolution magnetic and radiometric data and geophysical equipment on-board are shown in **Figure 5-4** (AeroPhysX, 2017). Aeromagnetic parameters for both high-resolution and regional data for this study are listed in **Table 5-2** and **Table 5-3**.

Table 5-1 Aircraft type and on-board geophysical equipment (AeroPhysX, 2017).

Item	**Specification**
Aircraft	Cessna 210 and 206
Operator	AeroPhysX
Registration	ZS-BTS, ZS-OZC and ZS-MXF
Survey Speed	110 knots = 203 km/h
Magnetometer (x4): Sensitivity Sampling frequency Dynamic range	Scintrex CS-3 Cesium vapour 0.0006 nTHz1/2 10 Hz 15000 to 105000 nT
Magnetometer base station:	Geometrics G829 Caesium vapour
Radar Altimeter	Acuity Laser Altimeter, sensitivity = 1 cm, accuracy = 5 cm.
Electronic Navigation	Satloc-M3 navigation system with E-diffTM DGPS.

Table 5-2 Survey Specifications for high-resolution airborne magnetic and radiometric data (AeroPhysX, 2017).

Item	Specification
Line spacing	200 m
Tie line spacing	2000 m
Line direction	N/S
Tie line direction	E/W
Total line kilometres	~72 300 km
Sensor clearance	~ 80 m (subject to safety consideration)

Table 5-3 Survey specifications for regional magnetic data.

Item	Specification
Contractor	Geosearch (Pty) Ltd
Line spacing	1 000 m
Tie line spacing	10 000 m
Line direction	N/S
Tie line direction	E/W
Sensor clearance	100 ± 15 m

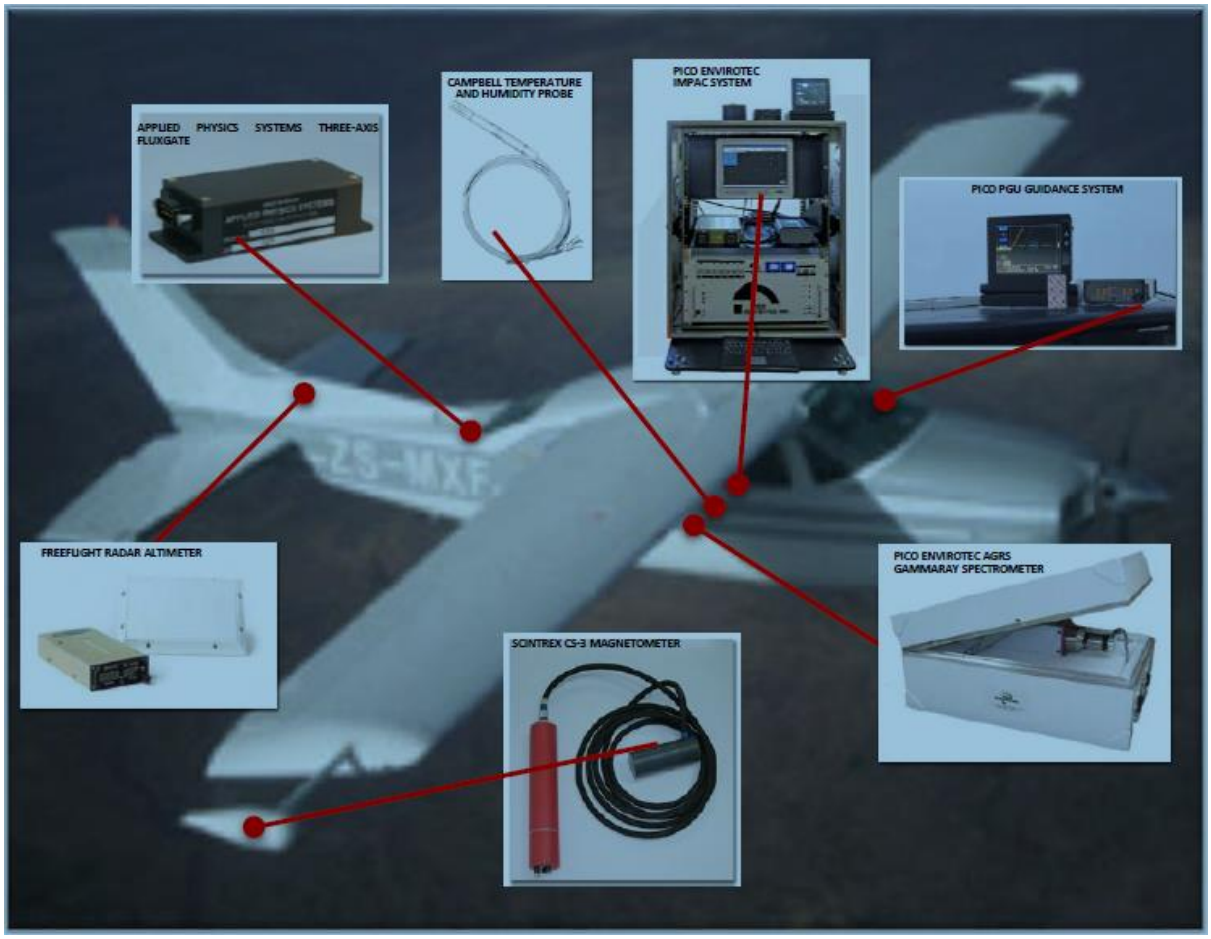

Figure 5-4 Image showing positioning of instrumentation on aircraft (AeroPhysX, 2017).

5.3.2 Processing

5.3.2.1 Standard magnetic processing

The processing of the existing regional and high-resolution airborne magnetic data was performed by the contractor who collected the data. The main processing described in Chapter Four involves diurnal variation correction, levelling of the data, and Regional Magnetic Field (GRF) correction (Luyendyk, 1997):

5.3.2.2 Advanced processing

The magnetic intensity data was provided as grids from the contractor and was sun shaded to make magnetic features more identifiable. This is done by simulating the

sun illuminating the “topography” of the magnetic data from different angles, thereby enhancing anomalies with different strike directions. The sun-shading of 45° NE was chosen as the best inclination angle for the study area because it highlighted most of the linear features especially those that lie perpendicular to the illumination direction (**Figure 5-5a**). Sun-shading from the NE direction led to the suppression of lineaments oriented in a NE direction since the lineaments lie parallel to the illumination angle. To highlight these linear features, the magnetic data was sun-shaded from a 315°(NW) illumination angle (**Figure 5-5b**).

Additional processing that was applied to the total magnetic intensity (TMI) data included advanced filtering to enhance images making interpretations simple. These methods were discussed in chapter four and they are common practise for magnetic interpretations, namely; (1) International Geomagnetic Reference Field (IGRF); (2) reduction to the pole (RTP) which arranges anomalies above their appropriate sources; (3) the first vertical derivative (1VD) to delineate shallow linear structures and (4) analytic signal (AS) to delineate magnetic bodies.

5.3.2.3 Preparation of datasets for interpretation

The magnetic datasets were processed and interpreted using the following software packages: PyGMI, Geosoft Oasis Montaj and ArcMap. The PyGMI software was used for displaying the gridded data, sun shading and creating georeferenced images for interpretation. The Geosoft Oasis Montaj software was used to perform advanced filtering of the collected magnetic data and ArcMap was used for map creation.

5.3.3 Results

5.3.3.1 Airborne magnetic data

The high-resolution magnetic data over the study area has a total magnetic intensity that ranges from approximately 26100 to 26350 nT (**Figure 5-5**). The IGRF was removed from the TMI data resulting in the residual magnetic data with magnetic anomalies associated with local geological structures.

The existing IGRF corrected regional aeromagnetic data collected with 1 km line spacing (**Figure 5-6b**) are compared with the IGRF corrected high-resolution aeromagnetic data from this study collected with 200 m line spacing (**Figure 5-6a**). High frequency/short wavelength anomalies are visible on the high-resolution magnetic data and are “missing” on the regional data.

The long-wavelength and short-wavelength features are seen on the high-resolution data in **Figure 5-6a**. The positive long-wavelength anomaly is present in the northern part of the area over the escarpment with an amplitude of 305 nT. The central part (around Beaufort West) is characterised by a large negative long-wavelength anomaly with an amplitude of about 74 nT. Another positive long-wavelength anomaly lies in the southern part of the study area, with an amplitude of approximately 185 nT. Short-wavelength anomalies are superimposed over the long-wavelength anomalies mainly in the northern part of the study area.

Generally, there is a good correlation between the mapped geology and magnetic signatures in the area. The magnetic high over the escarpment corresponds to the Karoo Dolerite Suite owing to their strong magnetic susceptibility. As expected, the high-resolution data delineates these short-wavelength dolerites in much more detail.

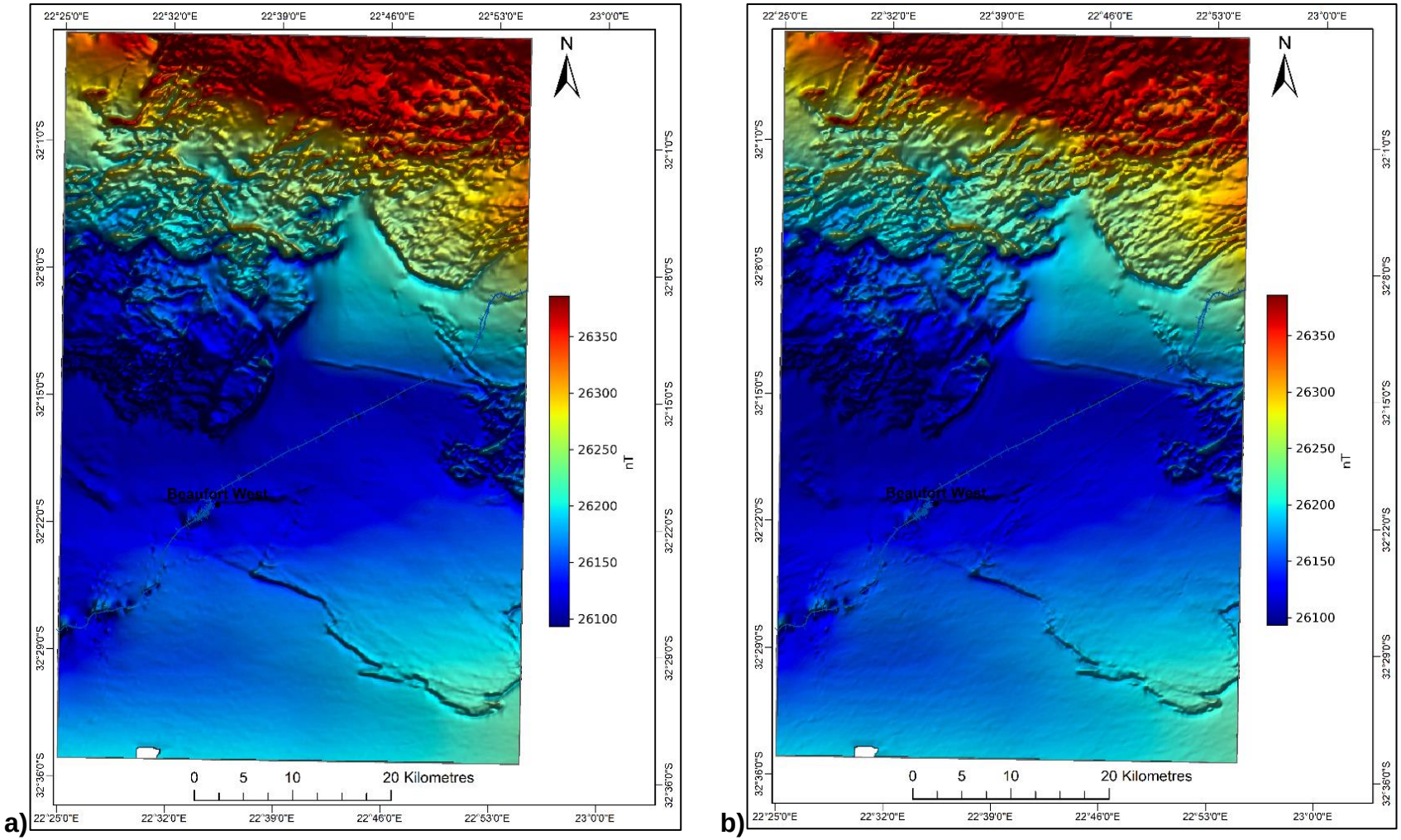

Figure 5-5 Original TMI data with IGRF. (a) Sun-shaded to 45° (NE) and (b) Sun-shaded to 315° (NW) to highlight NE striking anomalies.

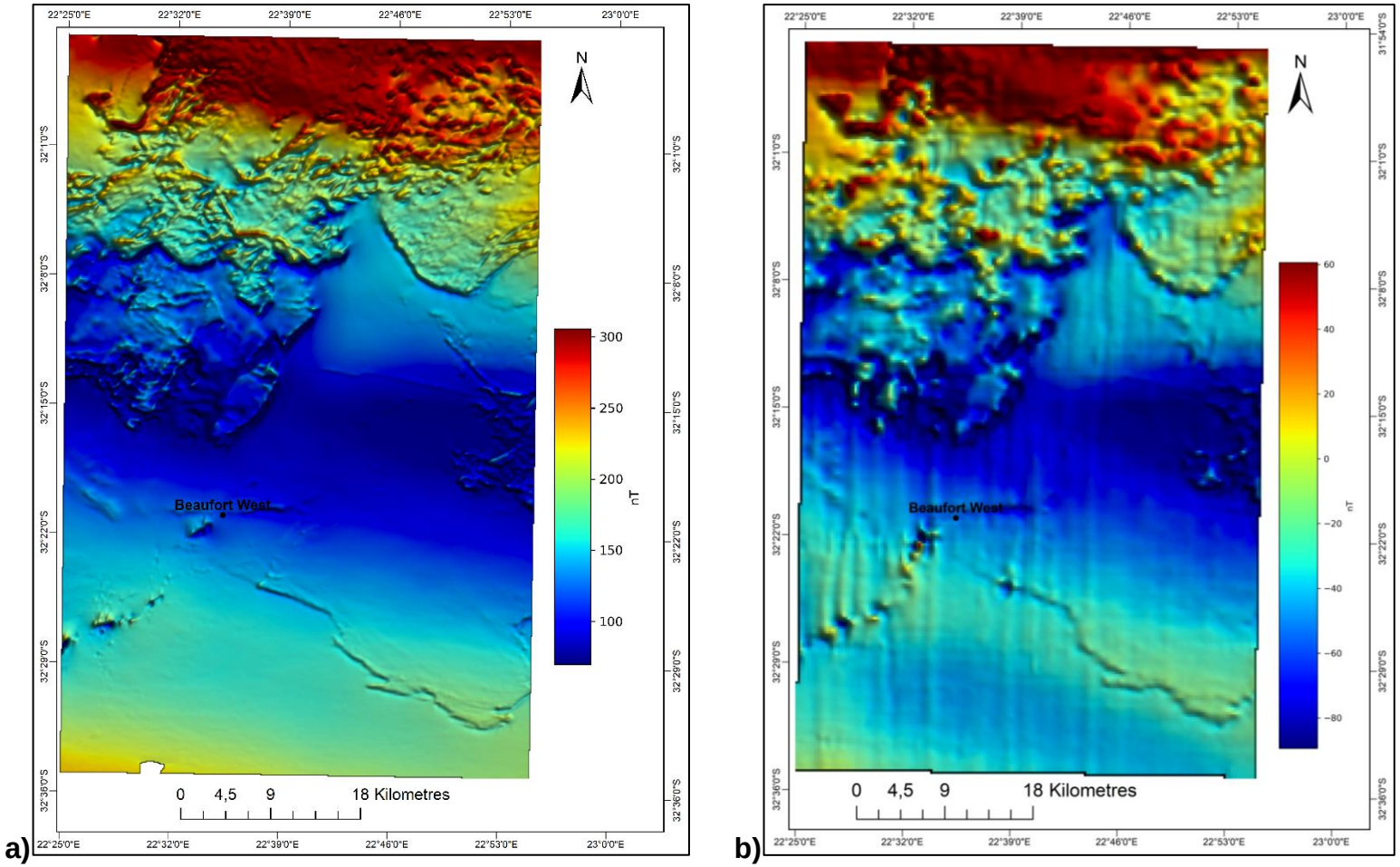

Figure 5-6 (a) IGRF corrected high-resolution Total Magnetic Intensity (TMI) data image for the study area acquired at 200 m line spacing (b) IGRF corrected regional Total Magnetic Intensity (TMI) data image for the study area acquired at 1 km line spacing. High frequency/short wavelength anomalies are clearly visible on the high-resolution magnetic data in (a) compared to (b).

Filtering was performed on the IGRF corrected TMI data to map the lineaments and subsurface bodies in the area. The Reduce to Pole (RTP) filter was performed to ensure the magnetic anomalies are centred over their causative bodies (**Figure 5-7**), except when there is the significant remanent magnetisation of the body. The first vertical derivative filter was used to map shallow linear structures and shows the geological structures more clearly than the TMI data (**Figure 5-8a**). The analytic signal amplitudes were calculated as this filter enhances the edges of magnetic bodies which are near the surface and gives the best results when the contacts are vertical (**Figure 5-8b**). These filtered images were used to outline magnetic bodies in Chapter Seven.

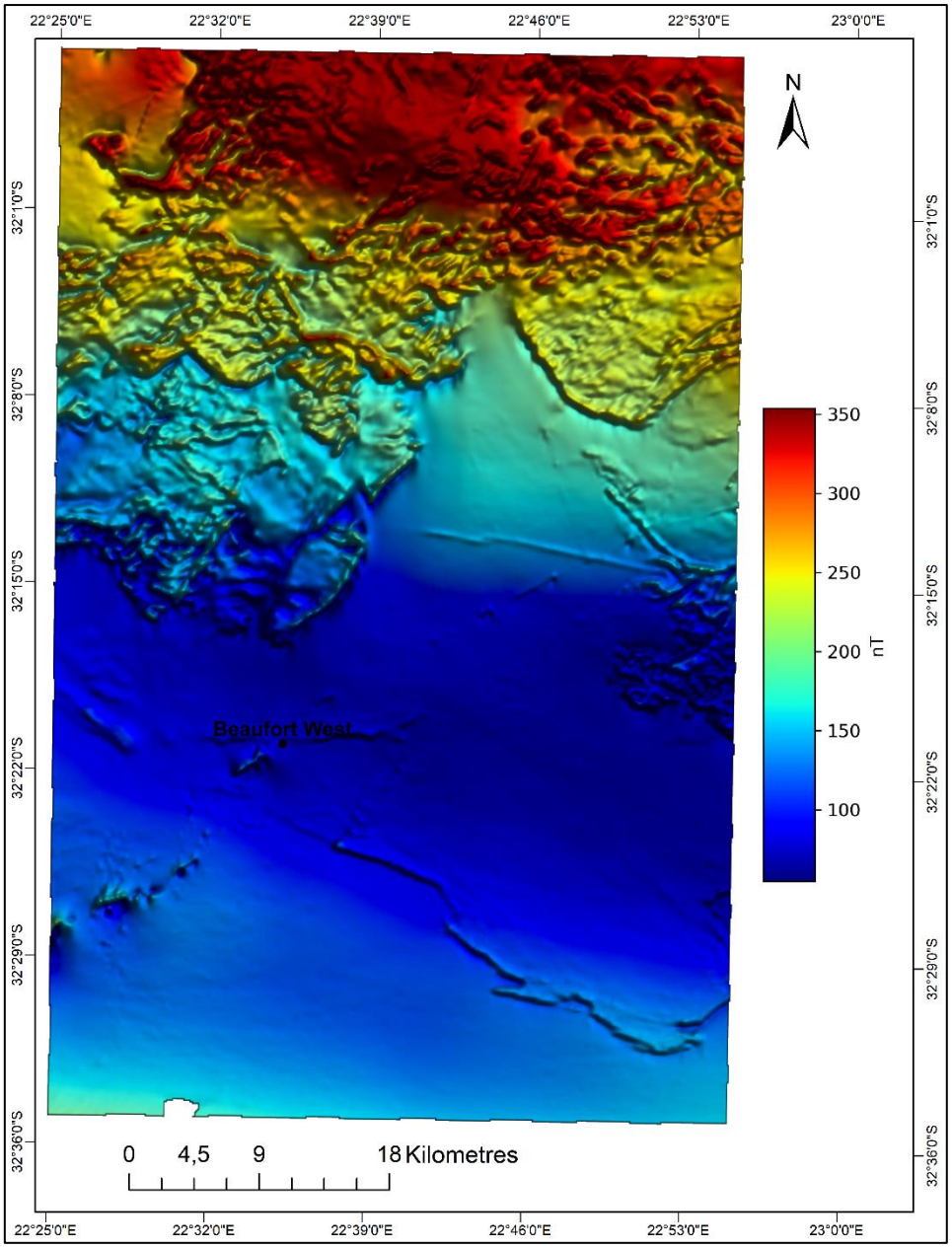

Figure 5-7 Total magnetic intensity data reduced to the pole (RTP) resulting in magnetic anomalies that are aligned with their causative bodies.

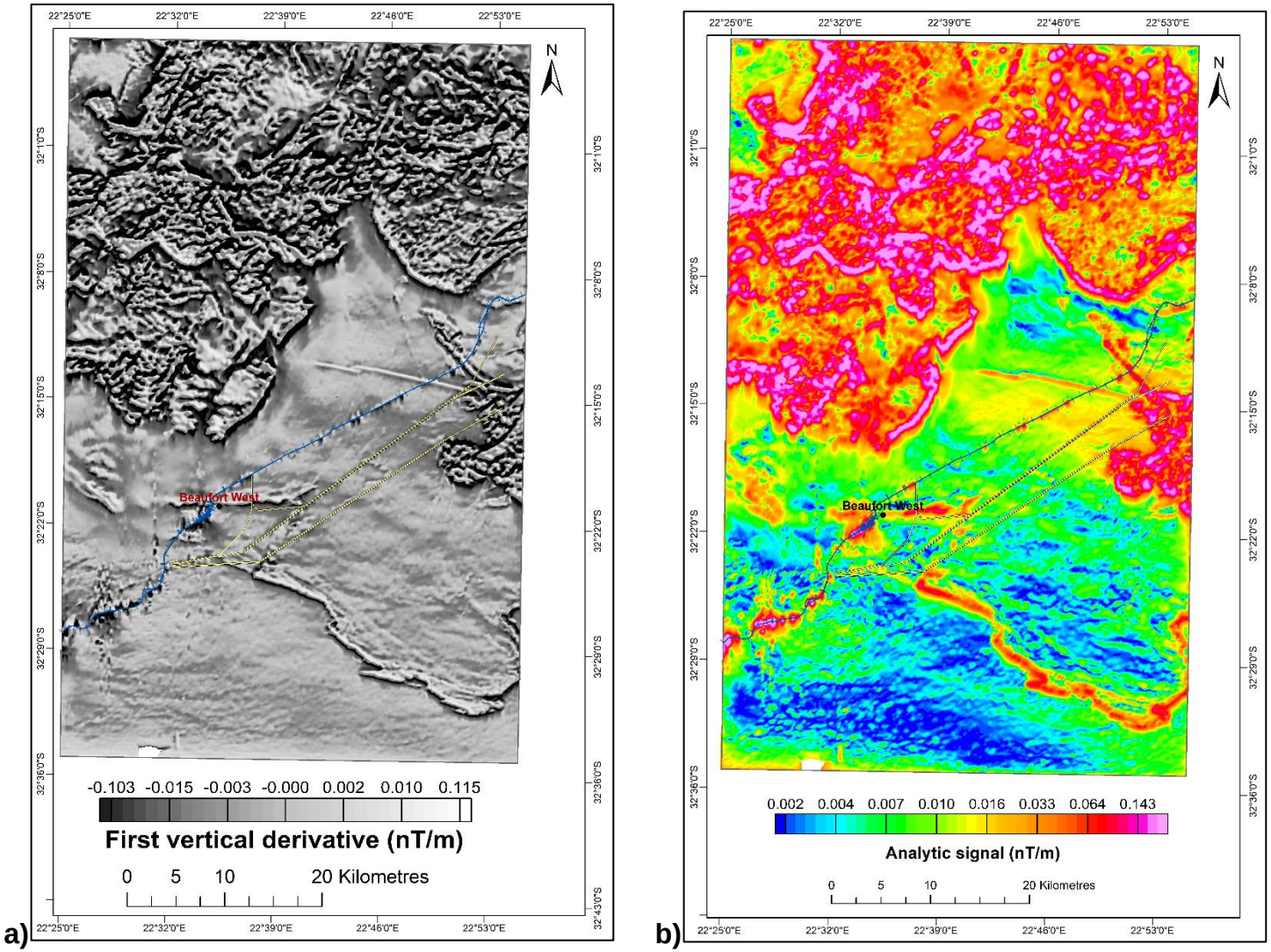

Figure 5-8 Filtering of the TMI data to better highlight shallow magnetic sources: (a) First vertical derivative and (b) Analytic signal.

5.4 Seismic Data

A state oil company SOEKOR collected about 13, 000 line-kilometres of 2D seismic data during the 1970s and 1980s in the southern Karoo and one of the seismic lines (line BV21) runs through the study area (Scheiber-Enslin *et al.,* 2014b). The analogue data was scanned and digitised by Falcon Oil and Gas. The acquisition and processing parameters for the survey are outlined in **Table 5-4**.

Table 5-4 Acquisition and processing parameters for Karoo Basin SOEKOR seismic surveys (Fatti and Du Toit, 1970).

Item	Parameter
Source	Dynamite (50 lbs/20 kg) used in 15-18 m deep holes
Fold	Single
Traces per shot point	24
Processing	Corrected for low-velocity layer (2130 m/s) at the surface
	Corrected to elevation datum using velocity of 4570 m/s)
	NMO correction
	CDP stacking (where available)
	Band-pass filtering
Dominant Frequency	40 Hz
Dominant half wavelength/resolution	70 m (assuming a velocity for dolerites of 5.55 km/sec)

Two continuous strong reflectors are visible on the seismic section, the upper limits of both the Whitehill Formation and the basement (**Figure 5-9**).

The Whitehill Formation shows up as a strong reflector due to its lower velocity (~4000 m/s) compared to the surrounding rock (~5000 m/s) (Fatti and Du Toit, 1970). The high-velocity dolerites also show up as strong reflectors. Often it is difficult to image below them due to “ringing”. The top of the Bokkeveld Group and Table Mountain Group show up as weak reflectors. The original interpretation of these data was carried out by (Fatti, 1970; Fatti and Du Toit, 1970 and Fatti 1987).

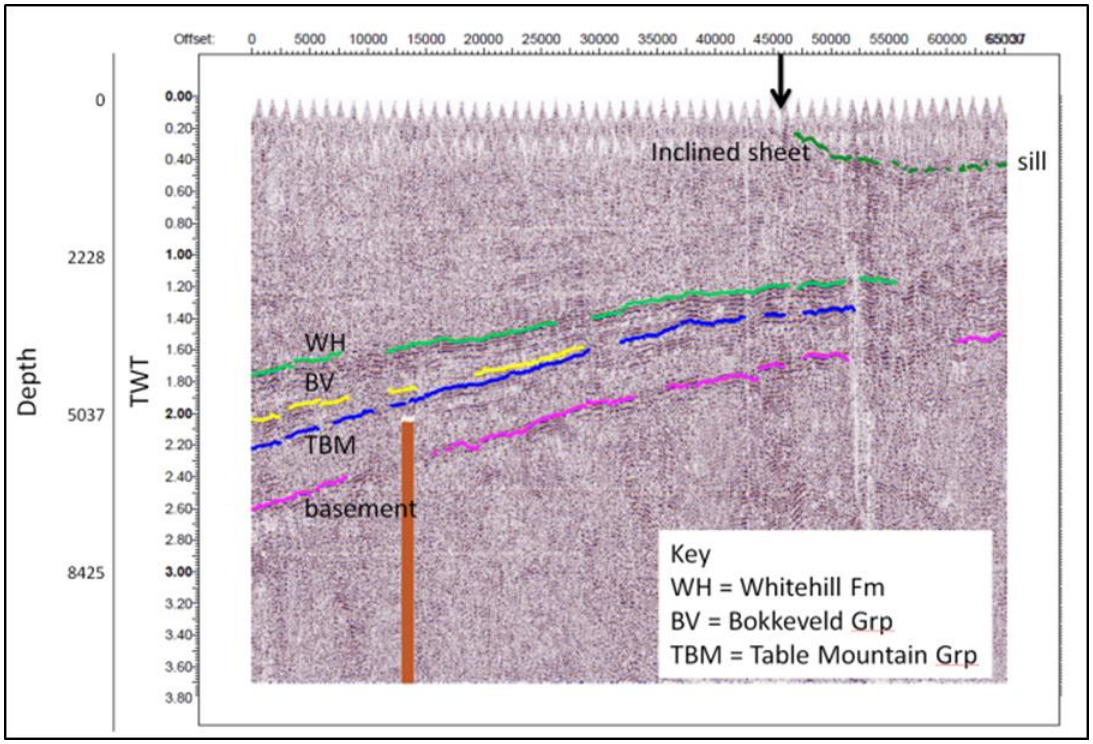

Figure 5-9: Seismic section BV21 showing the inclined sheet (dark green) and Karoo (WH – Whitehill Formation, light green), Cape Supergroup sediments (BV – Bokkeveld Group, yellow; TBM – Table Mountain Group, blue) and basement (pink).

Scheiber-Enslin *et al.* (2014b) and Scheiber-Enslin *et al.* (2015) performed more recent interpretations. Two-way time (TWT) to depth conversions (**Equation 5-1)** from these recent studies, was used in this study, such as:

$$\boldsymbol{Measured\ Depth = 231.5\ TWT^2 + 2022.6\ TWT} \qquad \textbf{5-1}$$

5.5 Summary

- The highest elevation values from the Digital Terrain Model data (DTM) corresponded to the escarpment lying in the north capped by the dolerite sills and elevation values are the lowest south of the area.
- Noticeable high frequency/short wavelength anomalies related to the dolerites are observed on the high-resolution airborne magnetic data and are “missing” on the low-resolution airborne magnetic data. However, both low- and high- resolution airborne magnetic datasets showed the low frequency/long-wavelength anomalies related to deep-seated basement magnetic bodies.
- Shallow-based filters (first vertical derivative and analytic signal) were applied on the Total Magnetic Intensity (TMI) data and delineated linear structures and shallow-seated magnetic source bodies related to the Karoo dolerite sills and dykes.
- In this study, the seismic line BV21 is shown on the geology map (**Figure 3-1**) in chapter 3 and is amongst the 13, 000 line-kilometres of 2D seismic data collected by SOEKOR in the 1970s and 1980s. Processing of these datasets was performed by Fatti and Du Toit (1970). Seismic line BV21 will be used in chapter Seven to correlate with the magnetic data and in Chapter Eight to constrain the 2D magnetic model.

6 CHAPTER SIX - PHYSICAL PROPERTIES DATA

6.1 Introduction

This chapter deals with measurements of the physical properties of rock samples from the study area. These measurements are performed to understand the physical properties of the rocks in the area and some of these measurements particularly the magnetic susceptibility will be used for the 2D magnetic model. The samples were collected along the N1 national road in Beaufort West. The following rock samples were collected from the outcrops: a dolerite sill located at latitude -32.38003° S and longitude 22.52300° E, sandstone and mudstone both located at the base of the Poortjie Member at latitude -32.43517° S and longitude 22.42311° E.

The Karoo dolerite sill has a dark grey colour, medium to coarse-grained, fractured and contains quartz veins. The sandstone has an olive grey colour, fine-grained and buff-weathered. The sandstone was also fractured and horizontally laminated. Grey colour in sandstone was due to clay material and greenish colour due to chlorite material. The mudstone was characterised by the mottling texture of dark red colour and green grey colours, and breaks off easily. The rock samples were cut according to required dimensions (2 cm x 2 cm x 2 cm) for physical properties. Three physical property measurements were conducted; magnetic susceptibility, Natural Remanent Magnetism (NRM) and bulk density. The physical properties measured are briefly discussed below.

6.1.1 Sample preparation

The rock samples were cut using a Struers Labotom-5 cutting machine (**Figure 6-1**) which comes with a flushing system that rinses the cutting chamber of any debris released from the cutting process. More details on

the cutting process can be found in the Labotom-5 instruction manual (Struers, 2014).

All rock samples were subdivided into three or four smaller specimens for bulk magnetic susceptibility. The sandstone was labelled MP1, dolerite labelled MP2 and mudstone labelled MP3 and for each label provided, an alphabetic notation was given to separate the specimens from the others from the same rock sample.

a)

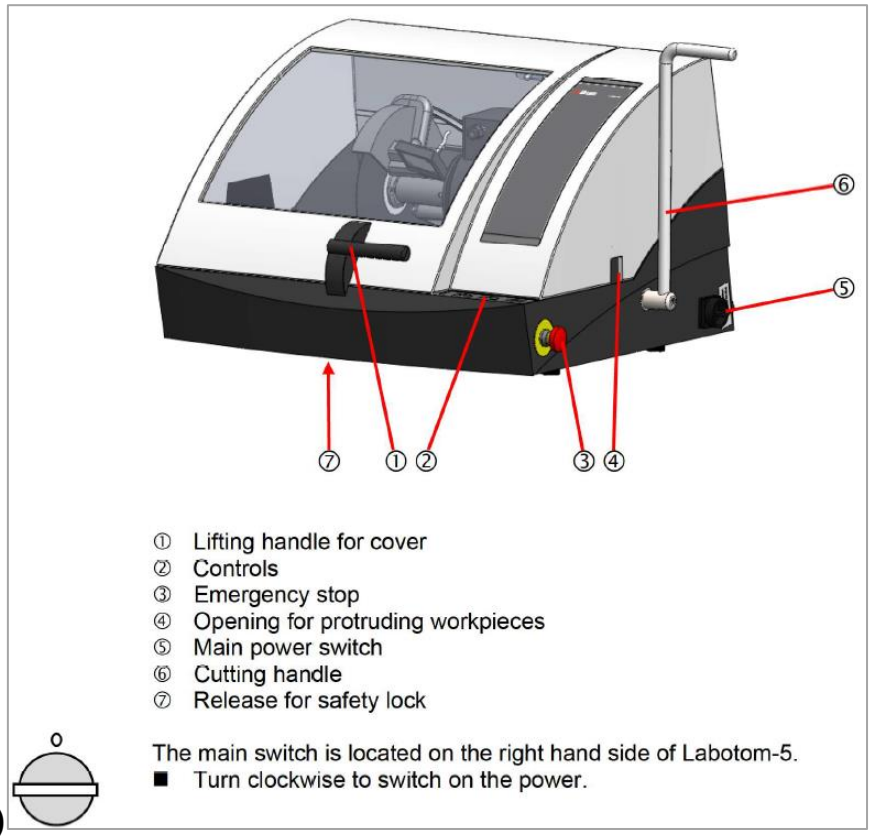

b)

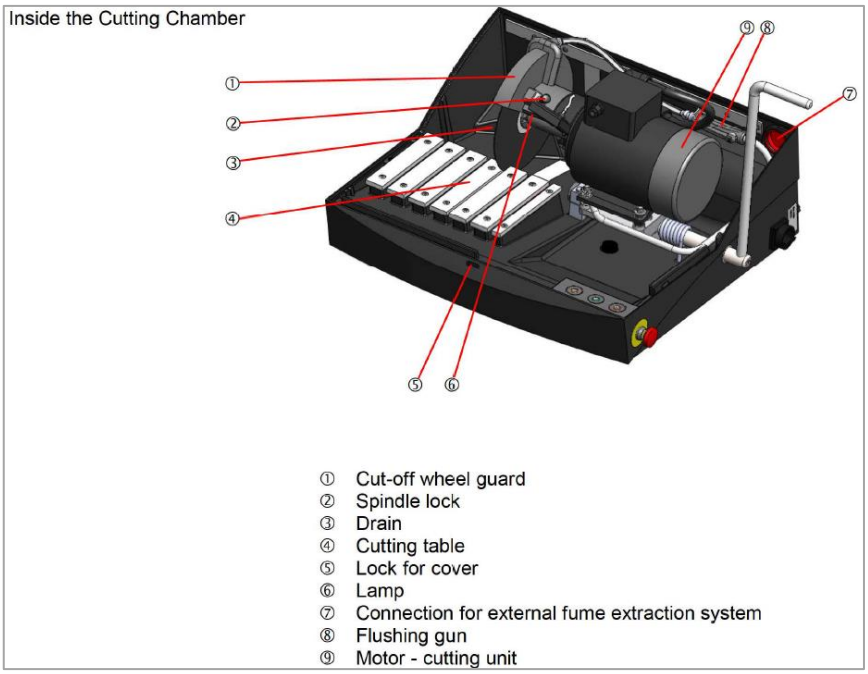

Figure 6-1 Struers Labotom-5 cutting machine: (a) Labelled exterior of the equipment and (b) interior of the equipment (Struers, 2014).

6.1.2 Magnetic susceptibility measurement

Magnetic susceptibility measurements were carried out within a low-field cage. The instrument used for magnetic susceptibility measurements was the MFK1-FA multi-function kappabridge (**Figure 6-2**) instrument connected and operated by a computer using the SAFYR7 software. Bulk magnetic susceptibility measurements were conducted on the specimens using the default settings of 200 A/m field intensity, 976 Hz frequency and each specimen was measured three times. Before measurements, the calibration of the instrument was done using the factory-supplied calibration standard. The steps followed for bulk magnetic susceptibility measurement are described by AGICO (2018b). **Table 6-1** summarizes the magnetic susceptibilities of the measured specimens.



Figure 6-2 MFK1-FA multi-function kappabridge instrument setup was used to measure bulk magnetic susceptibility (AGICO).

Table 6-1 The magnetic susceptibility measurements of the samples using a MFK1-FA multi-function kappabridge, with three repeats.

Lithology	**Sample name**	**Susceptibility 1 (x10 $^{-3}$ SI)**	**Susceptibility 2 (x10 $^{-3}$ SI)**	**Susceptibility 3 (x10 $^{-3}$ SI)**	**Average (x10 $^{-3}$ SI)**
Sandstone	MP1A	1.284	1.284	1.284	1.284
	MP1B	1.399	1.399	1.399	1.399
	MP1C	1.383	1.383	1.383	1.388
	MP1D	1.152	1.151	1.152	1.152
Dolerite	MP2A	19.187	19.188	19.187	19.187
	MP2B	18.513	18.514	18.514	18.514
	MP2C	21.378	21.376	21.377	21.377
	MP2D	18.922	18.922	18.921	18.922
		(x10 $^{-6}$ SI)			
Mudstone	MP3A	196.100	196.130	196.270	196.167
	MP3B	194.010	193.970	193.900	193.960
	MP3C	195.970	195.940	195.970	195.960

A comparison between the average magnetic susceptibility documented by Telford *et al.* (1976) and the average measured magnetic susceptibility of the lithology samples (sandstone, dolerite and mudstone) is shown in **Table**

6-2). The values compare well with the dolerite having the highest magnetic susceptibility and the sandstone and mudstone having low magnetic susceptibilities.

Table 6-2 Comparison of average measured magnetic susceptibility values and those from Telford *et al.* (1976).

Rock type	**Measured value average range (x10 $^{-3}$ SI)**	**Telford et al. (1976) (x10 $^{-3}$ SI)**
Sandstone	1.152 to 1.399	0 to 20
Dolerite	18.513 to 21.377	1 to 35
Mudstone/Shale	0.193900 to 0.196130	0.01 to 15 ***

***Shale not mudstone value

6.1.3 Natural Remanent Magnetisation (NRM)

JR-6A dual-speed spinner magnetometer (**a**) was used to measure the remanent magnetism. The measurement process is controlled by a desktop computer and all the functions of the JR-6 spinner magnetometer are controlled by REMA6 software (AGICO, 2018a). The measurement results are automatically saved as *.jr6 format and as a text file (*.txt) format. Measurements can be performed manually, semi-automatic or automatic. The semi-automatic measurement was chosen for this study. An automatic holder is used for the semi-automatic measurement but the position of the specimen is set manually.

The instrument was calibrated based on the type of measured specimen and for this experiment; a cubic calibration standard was used. The volume (cm^3) and the magnetization (A/m) are written on the side of each calibration standard and can be entered on the calibration standard values window under settings/calibration standard item in the REMA 6 software. The volume for the cubic calibration standard is 8 cm and the magnetization is 7.78 A/m. The calibration was performed as follows (AGICO, 2018a): The NRM measurements were conducted in three measurement positions: P1, P2 and P3 (**b**) and the results are shown in **Table 6-3**. Only the NRM measurement was performed, declination and inclination were not measured because these were un-orientated hand samples.

a)

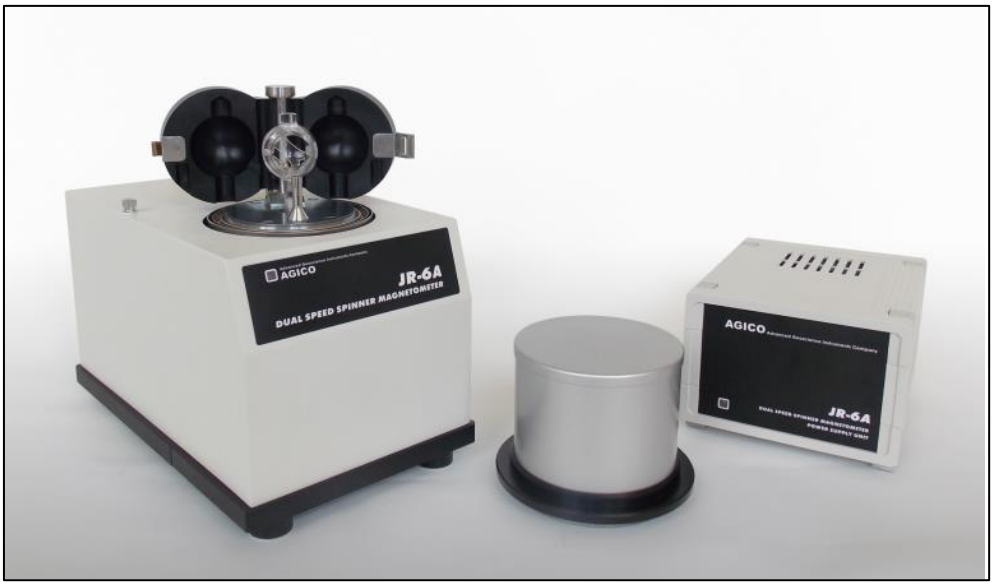

b)

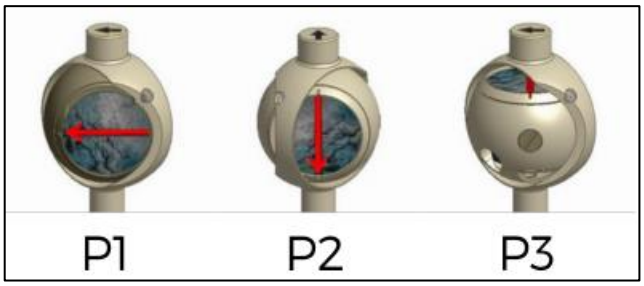

Figure 6-3 (a) JR-6A spinner magnetometer. (b) Measuring positions for semi-automatic mode: P1 represents x direction, P2 represents z-axis of the specimen coordinate system and P3 horizontal in y direction (AGICO, 2018a).

Table 6-3 Natural Remanent Magnetism measurements for the specimens.

Lithology	Sample name	NRM (A/m)
Sandstone	MP1A	0.034
	MP1B	0.036
	MP1C	0.038
	MP1D	0.031
Dolerite	MP2A	0.699
	MP2B	0.728
	MP2C	0.624
	MP2D	0.650
Mudstone	MP3A	0.008
	MP3B	0.002
	MP3C	0.002

As expected the NRM of a dolerite would be higher than that of the clastic rocks because the dolerite normally has relatively large magnetic susceptibility and even when the inducing field is removed a portion of the induced magnetization remains.

6.1.4 Density measurement

The density of a material is defined as its mass per unit volume (g/cm^3). The local changes in densities of the rocks cause minute changes in the gravity field (Telford *et al.,* 1976). Density provides a direct proxy for the degree of mineralization since most ore minerals are denser than silicates, which dominate un-mineralized rocks. Besides, permeability and weathering influence porosity which affects density (Enkin *et al.,* 2012). However, mineral composition and the anisotropy of a sample also affect the measured density (Paananen, 2004). High-density bodies are associated with positive gravity anomalies while low-density bodies are associated with gravity lows (Hoover *et al.,* 1993).

The specimens were measured for bulk density using two types of equipment for comparison purposes. The demagnetizer instrument (**Figure 6-4**) was used to dry the samples for 24 hours at 110 °C to remove trapped

moisture from the sample and to ensure the correct dry mass was measured. The difference in dry sample mass and saturated sample mass indicates the porosity of the sample. The samples were cooled to room temperature before carrying out the dry bulk density measurements. The bulk density measurement was measured using the Mettler Toledo (**Figure 6-5**) and the Sartorius equipment (**Figure 6-6**).

The bulk densities measured using the Mettler Toledo instruments were conducted in air and in an auxiliary liquid (water). The density is automatically calculated by the balance by taking into account the density of air (0.0012 g/cm³), the density of the water (0.99732 g/cm³ at 24°C).

The bulk densities measured using the Sartorius equipment were conducted in air and suspended in water with a thin copper wire of 1.034 g known mass. The densities were calculated manually and therefore the density of water was approximated to 1 g/cm³ at 24°C. The temperature of the water was measured with a thermometer to ensure that the temperature was at 24 °C.

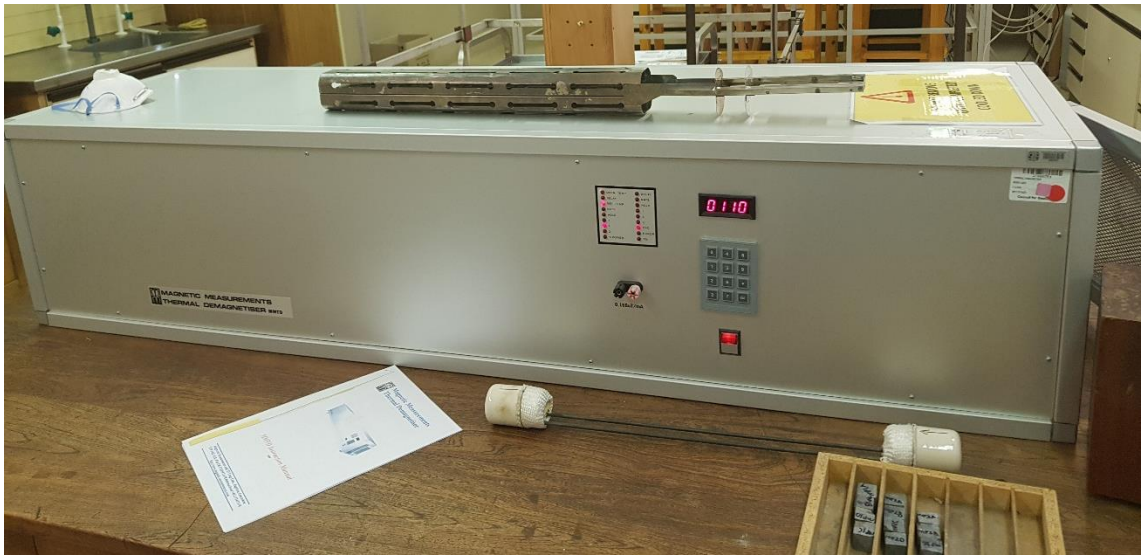

Figure 6-4 Demagnetizer instrument used to dry the specimen for a period of 24 hours at 110 °C.

a) 

b) 

Figure 6-5 Mettler Toledo instrument used for density measurements. (a) Measuring mass/weight of the sample in the air and (b) measuring the mass/weight of the sample in the beaker with water.



Figure 6-6 Sartorius equipment used for density measurements. The bucket contains water to immerse the suspended sample with a copper wire.

The density of the sample measured using the Sartorius equipment is calculated using the mass and volume of the sample (**Equation 6-1**), assuming the mass of the wire is negligible (Cole and Maré, 2004):

$$\rho_{sample} = \frac{Mass\ in\ Air_{sample}}{Volume\ in\ Air_{sample}} \qquad \textbf{6-1}$$

Porosity (Φ in %) measurement is given by **Equation 6-2** (Lin *et al.,* 2015):

$$(\boldsymbol{\Phi}) = \frac{\boldsymbol{Mass\ in\ Water_{sample} - Mass\ in\ Air_{sample}}}{\boldsymbol{Bulk\ Volume}} \boldsymbol{x\ 100} \qquad \textbf{6-2}$$

The density results from both the Mettler Toledo and Sartorius methods are shown in **Table 6-4** and **Table 6-5**. The observed difference between the two methods is due to the simplification of the formula used with the Sartorius balance where the density of air was not taken into account and that of water was rounded to 1 g/cm³.

Table 6-4 Dry bulk density measurement measured with Mettler Toledo equipment.

Rock Type	Sample name	Mass in air (g)	Mass in liquid (g)	Volume of solid (cm^3)	Density (g/cm^3)	Density (Mean) (g/cm^3)	Density (Minimum) (g/cm^3)	Density (Maximum) (g/cm^3)
Sandstone	MP1A	19.548	12.206	7.369	2.653	2.649	2.646	2.653
	MP1B	18.712	11.665	7.073	2.646			
	MP1C	20.746	12.935	7.840	2.647			
	MP1D	16.453	10.260	6.216	2.648			
Dolerite	MP2A	19.598	13.191	6.431	3.048	3.040	3.036	3.048
	MP2B	21.733	14.600	7.160	3.036			
	MP2C	22.499	15.119	7.408	3.038			
	MP2D	19.900	13.368	6.556	3.036			
Mudstone	MP3A	19.834	12.464	7.398	2.682	2.770	2.679	2.682
	MP3B	20.562	12.921	7.670	2.682			
	MP3C	18.460	11.593	6.8903	2.679			

Table 6-5 Dry bulk density measurements measured with Sartorius equipment.

Rock Type	Sample name	Mass (dry) (g)	Mass (saturated) (g)	Mass in water (g)	Volume sample (cm^3)	Density (g/cm^3)	Density (Mean) (g/cm^3)	Density (Minimum) (g/cm^3)	Density (Maximum) (g/cm^3)	Porosity (%)
Sand-stone	MP1A	19.481	19.581	13.115	7.4	2.633	2.645	2.633	2.660	1.351
	MP1B	18.670	18.774	12.621	7.083	2.636				1.468
	MP1C	20.708	20.855	13.935	7.807	2.652				1.883
	MP1D	16.423	16.566	11.283	6.174	2.660				2.316
Dolerite	MP2A	19.595	19.607	14.118	6.511	3.010	3.013	3.003	3.032	0.184
	MP2B	21.727	21.740	15.527	7.234	3.003				0.180
	MP2C	22.496	22.499	16.048	7.482	3.007				0.040
	MP2D	19.896	19.905	14.299	6.562	3.032				0.137
Mudsto ne	MP3A	19.827	19.838	13.398	7.463	2.657	2.658	2.656	2.660	0.147
	MP3B	20.554	20.573	13.861	7.727	2.660				0.246
	MP3C	18.448	18.484	12.537	6.945	2.656				0.518

A comparison was made with the standard density documented by Telford *et al.* (1976) for lithologies similar to those measured in the study area. Results are shown in **Table 6-6**. The values are in good agreement. The ranges from Telford *et al.* (1976) are larger as they measured a larger number of samples.

Table 6-6 Comparison of average measured density values and those from Telford *et al.* (1976).

Rock type	Measured value in this study (g/cm^3)	Telford et al. (1976) (g/cm^3)
Sandstone	2.63 to 2.66	1.61 to 2.76
Dolerite	3.00 to 3.03	2.50 to 3.20
Mudstone/Shale	2.66	1.77 to 3.2 ***

***Shale not mudstone value

6.2 Summary

- The physical property measurements measured in this chapter were magnetic susceptibility, Natural Remanent Magnetisation (NRM) and density.
- The magnetic susceptibility and density measurements were comparable to measurements from Telford *et al.* (1976).
- Two pieces of equipment were used for density measurements to ensure the data quality and the density measurements were comparable. Sartorius equipment was able to measure both wet and dry densities of the samples; the results from these measurements were used for porosity calculations. As expected, the sandstone samples had high porosity values compared to the dolerite and mudstone. The dolerite samples had the lowest porosity values.
- Magnetic susceptibility will be used mainly in Chapter Eight as part of input data for the magnetic model.

7 CHAPTER SEVEN – INTERPRETATION

7.1 Mapping using Filtered Magnetic Data

The results generated from filtered aeromagnetic data is interpreted in this chapter. The interpretation includes separating deep and shallow magnetic sources (lineaments and bodies), and depth estimations through Radially Averaged Power Spectrum method.

Measured magnetic susceptibility of Karoo dolerites in the area is high, ranging from 18.513 to 21.377 x10^3 SI (discussed in Chapter Six) and is therefore easy to detect compared to the country rocks characterised by low magnetic susceptibilities.

7.1.1 Separating Deep Sources

Figure 7-1 shows a bandpass filtered image of the regional aeromagnetic data delineating the deep east-west trending magnetic anomaly that crosses the study area. A bandpass filter (cutoff wavelength of 4000 m) was applied to the regional aeromagnetic data.

The study area lies on Namaqua-Natal Mobile Belt basement rocks. The boundary between the Namaqua and Natal Belts based on borehole data to the north of the study area is marked in **Figure 7-1** (Eglington and Armstrong, 2003), showing the study area lies on the Natal terrane. The Natal terrane is characterized by several east-west magnetic anomalies (Thomas *et al.,* 1992; Scheiber-Enslin *et al.,* 2014a). The strongest anomaly is the east-west Beattie Magnetic Anomaly that is easily identified on the TMI map of South Africa and passes south of the study area. The source of the Beattie anomaly is not clear as the anomaly is covered by younger Cape and Karoo Supergroup rocks.

The Williston Anomaly occurs north of the Beattie. It is associated with outcropping Natal rocks on the east coast of South Africa. The continuity of the anomaly to the

west is “swamped” by the larger Beattie Anomaly, and therefore the Williston anomaly can only be identified clearly when the data is low-pass filtered (Thomas *et al.,* 1992; Scheiber-Enslin *et al.,* 2014a). The Williston Anomaly passes through an area in the southern part of the study area (**Figure 7-1**).

Thomas *et al.* (1992) suggest that the Beattie Magnetic Anomaly, Williston Anomaly and Mbashe Anomaly (south of the Beattie Anomaly, only evident on the east coast) are the results of magnetised shear zones that form part of the Natal basement rocks. The depth of the source bodies in the western Karoo Basin are estimated from seismic data at 5-15 km for the Williston Anomaly and 7-15 km for Beattie Magnetic Anomaly (Lindeque *et al.,* 2011).

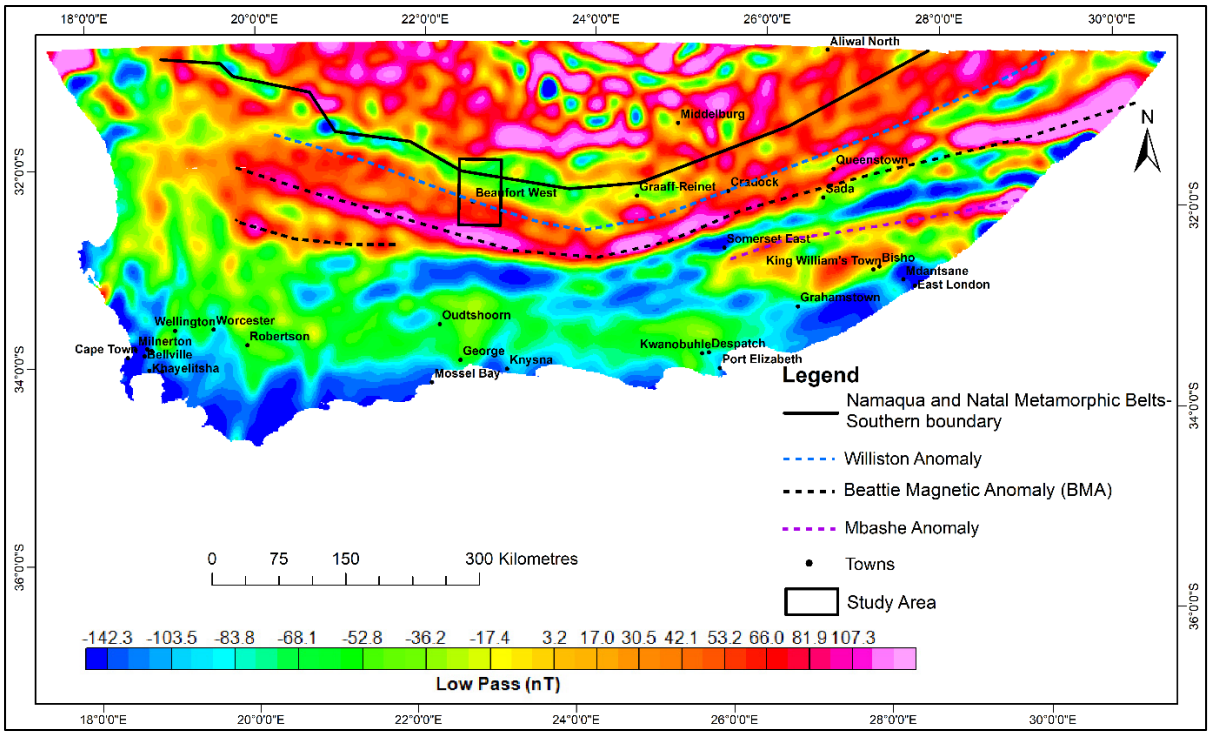

Figure 7-1 Low-pass filtered image of the regional TMI data for South Africa used to highlight deep magnetic anomalies. The edge of the Namaqua and Natal Belts (black line), and the Beattie and Williston Magnetic Anomalies (dashed black and blue lines) are marked.

7.1.2 Shallow magnetic lineaments

The first vertical derivative filter of the magnetic data (**Figure 7-2a**) was used to map lineaments with five main directions: E-W to ESE-WNW, NNW-SSE, NW-SE, NE-SW and NNE-SSE (**Figure 7-2b**). These lineaments dominate above latitude 32°15'0″ S in the study area, and consists of a large number of outcropping sills.

By comparing these lineaments to mapped geology and to Google Earth imagery, they seem to associate to dykes (Karoo dolerites and kimberlites) and joints. The longest mapped dyke in the field area trends east-west and shows an en-échelon segmentation in the magnetic data north of latitude 32°15'0″ S (black arrow, **Figure 7-2b)**. Woodford and Chevallier (2002a) referred to this dyke as the Tweeling-Brandwag dyke. Marsh and Mndaweni (1998) also observed similar en-échelon segmentation in a long Karoo dyke in the Eastern Cape Province. The dolerite dykes either branch into sills or cut through them. The NNW-SSE dykes are also long such as the dyke located on latitude 32°1'0″ S, which is approximately 29 km long within the study area and extends outside the study area boundary. North of latitude 32°15'0″ S in **Figure 7-2a**, there are also short, closely spaced lineaments that have short wavelength/high-frequency anomalies associated with the dolerite sills.

Several faults were mapped in the field area by Dhansay *et al.* (2017). Faults can be recognised on magnetic data if the following occurs: an offset of similar magnetic units and a sudden change in depth of magnetic sources; rocks on either side of the fault have similar susceptibilities, but the fault plane itself either has a high magnetic susceptibility due to the precipitation of magnetic minerals or a narrow linear magnetic low due to weathering along the fault plane where magnetic minerals are oxidized to non-magnetic minerals (Gunn *et al.,* 1997). An example of a Strike-slip fault is shown in **Figure 7-2b** (coordinates 32°8'0″ S and 22°39'0″ E). If these scenarios do not apply, it cannot be detected.

Additional faults were inferred from the magnetic data. The majority of these faults were interpreted as strike-slip faults as they laterally displace magnetic units such as

west of the study area (32°15'0″ S). Dip-slip faults were also identified such as the fault that lies in the far NE of the area (32°8'0″ S). The dip-slip fault was identified by a downthrown block with weak magnetic country rocks south of the fault. Faults mapped on surface are not always clear on magnetic data. There could be many reasons for this, (1) such as the host rock could be made up of low magnetic susceptibility materials and therefore there is no susceptibility contrast across the fault (such as the faults southern part of the study area); (2) the anomaly due to the offset of the surface faults could be below the resolution of the magnetic data. A reason why a fault may be evident on magnetic data but not mapped on surface is that the magnetic fault may be too deep to be mapped on the surface.

South of 32°29'0″ S in **Figure 7-2**, the geologically mapped fold axis of the Cape Fold Belt folds were superimposed on the magnetic data striking approximately east-west. The signal is weak due to the low magnetic susceptibility of these sedimentary rocks hence they were not mapped from the magnetic data. Local geology mapping conducted by Cole *et al.* (2016b) observed these E-W fold axes or hinges. No dolerite dykes or sills were mapped south of the study area at this scale. Scheiber-Enslin *et al.* (2014b) suggested that the absence of outcropping dolerites could be the result of tectonic activity in the Cape region that lead to earlier northward tilting of Karoo rocks in the south which later dolerites could not intrude through. Due to the shallow focus of the vertical derivative filter, cultural noise such as power lines and railway line were also detected and are shown in **Figure 7-2b**.

Rose diagrams were generated from the high-resolution magnetic data (**Figure 7-3a**) and were compared to the rose diagrams generated from remotely-sensed fracture orientations (**Figure 7-3b**). Dhansay *et al.* (2017) generated these diagrams for sections of the study area, a similar approach was used for the rose diagram plots generated from the high-resolution magnetic data in this study for the sake of comparison. In general, there is a correlation between both the surface and shallow sub-surface geology (<200 m, from magnetic data) mainly related to the dolerites. There is a significant decrease in magnetic lineaments from the magnetic data south of the Beaufort West town and that is related to the absence of dolerite dykes, linked to the proximity to the dolerite line. A similar decrease in dolerites is observed south

of Beaufort West town from the surface geology mapping and majority of lineaments were mapped from host rocks (**Figure 3-1**).

While the two rose diagrams compare well, there are also some discrepancies. In the eastern part of the lower half of the rose diagrams, the trend determined from the magnetic data is only NE-SW, but the geological mapping rose diagram shows two additional directions: a prominent E-W and an ENE-WSW direction. These additional trends could be due to lineaments in non-magnetic rocks. Similarly, in the western part of the lower half of the study area, the magnetic trend is only E-W, whereas the geological mapping rose diagram has two additional prominent directions: NNE-SSW and NNW-SSE.

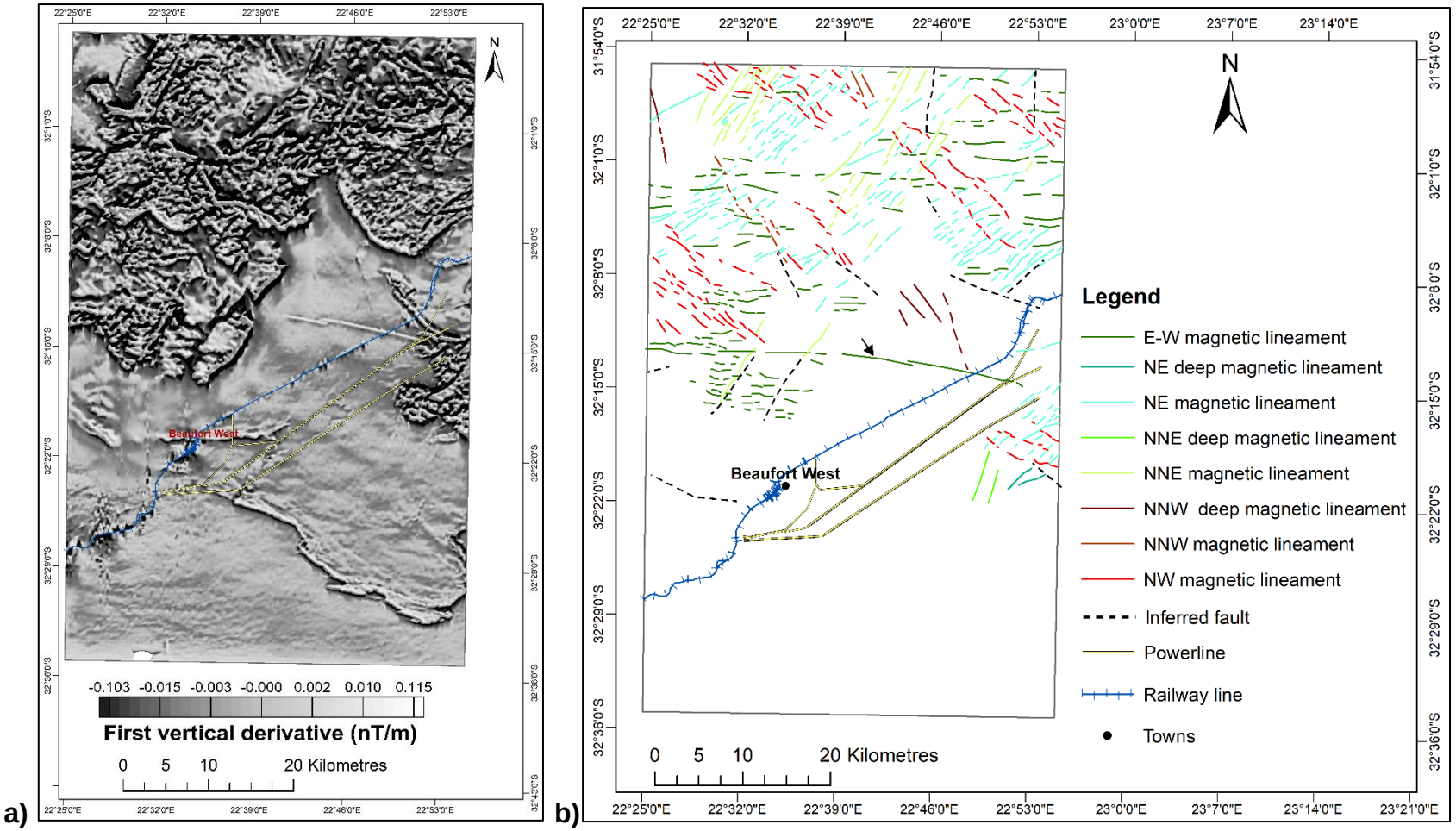

Figure 7-2 (a) First vertical derivative of the TMI data and (b) Inferred magnetic lineament interpretation derived from the first vertical derivative. The major E-W dyke known as Tweeling-Brandwag dyke is shown by a black arrow on (b) (Campbell, 1975; Woodford and Chevallier, 2002a).

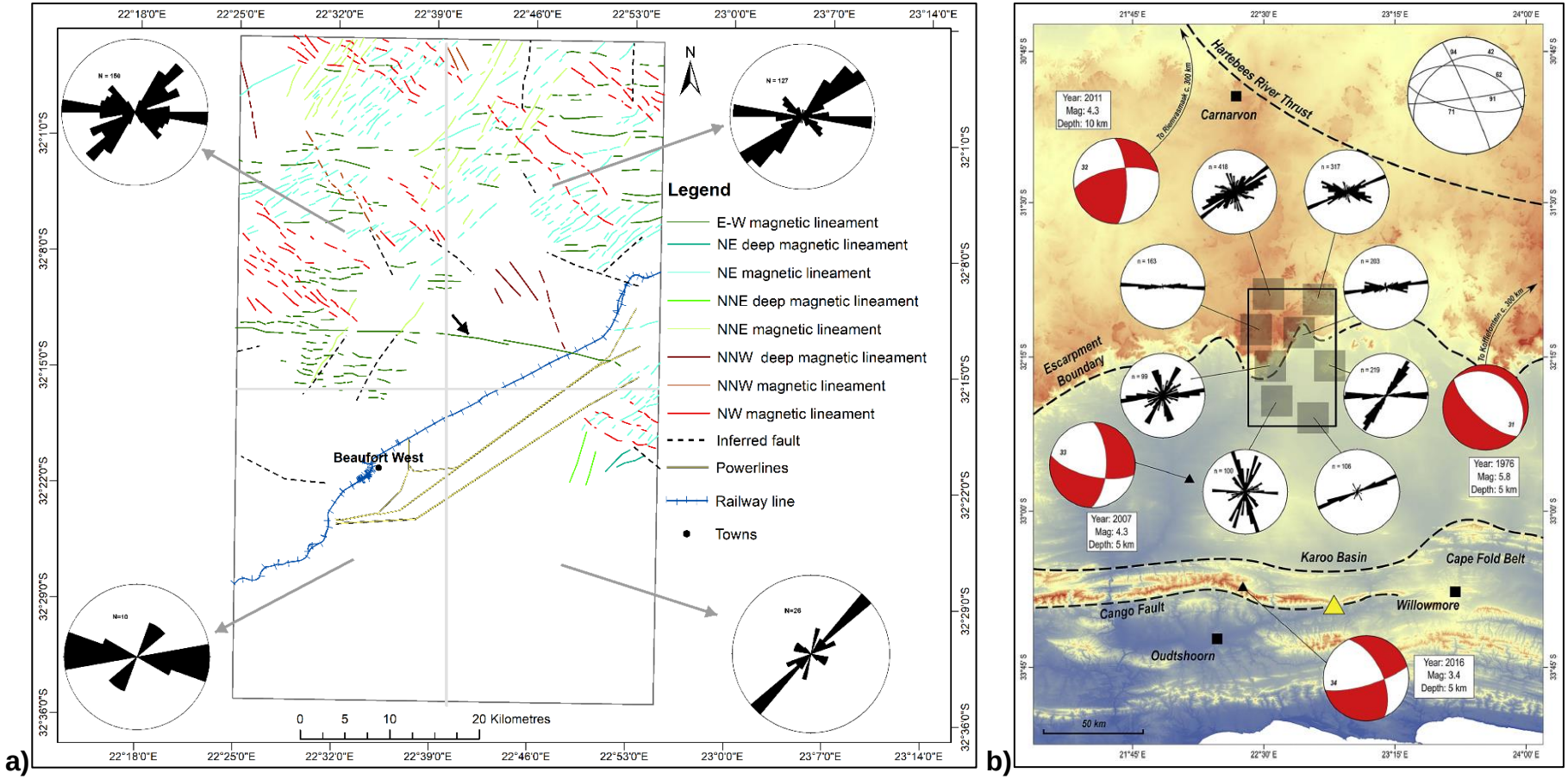

Figure 7-3 A comparison of rose diagram plots generated from (a) high-resolution airborne magnetic data and (b) the surface geology by Dhansay *et al.* (2017). There is a correlation between surface geology north of Beaufort West and shallow sub-surface geology (<200 m).

7.1.3 Shallow Magnetic Bodies

The analytic signal filter of the magnetic data (**Figure 7-4a)** corroborated with TMI data, was used to map the magnetic bodies (**Figure 7-4b**) which are interpreted as Karoo dolerite sills and an inclined sheets in **Figure 7-5b**. The sills cap the escarpment whereas the inclined sheet outcrops in the south of the study area (south of 32°22'0″ S). The outcropping sills display variable horizontal extent from the magnetic data.

The edges of the sills (dark red, **Figure 7-5b**) were delineated from the analytic signal. The edges or rims of the sills are topographically heightened such as the rim parallel to latitude 32°2'0″ S. The rim of the sill has an elevation of approximately 1696 m and the centre of the sill has an elevation of approximately 1680 m. This is common for the sills outcropping in the Beaufort Group (Chevallier and Woodford, 1999). In some areas, there are smaller sills within the larger sills. The interconnected network of sills is similar to that mapped by Galerne *at al.* (2011) at the Golden Valley Sill Complex of the Karoo Basin near Queenstown.

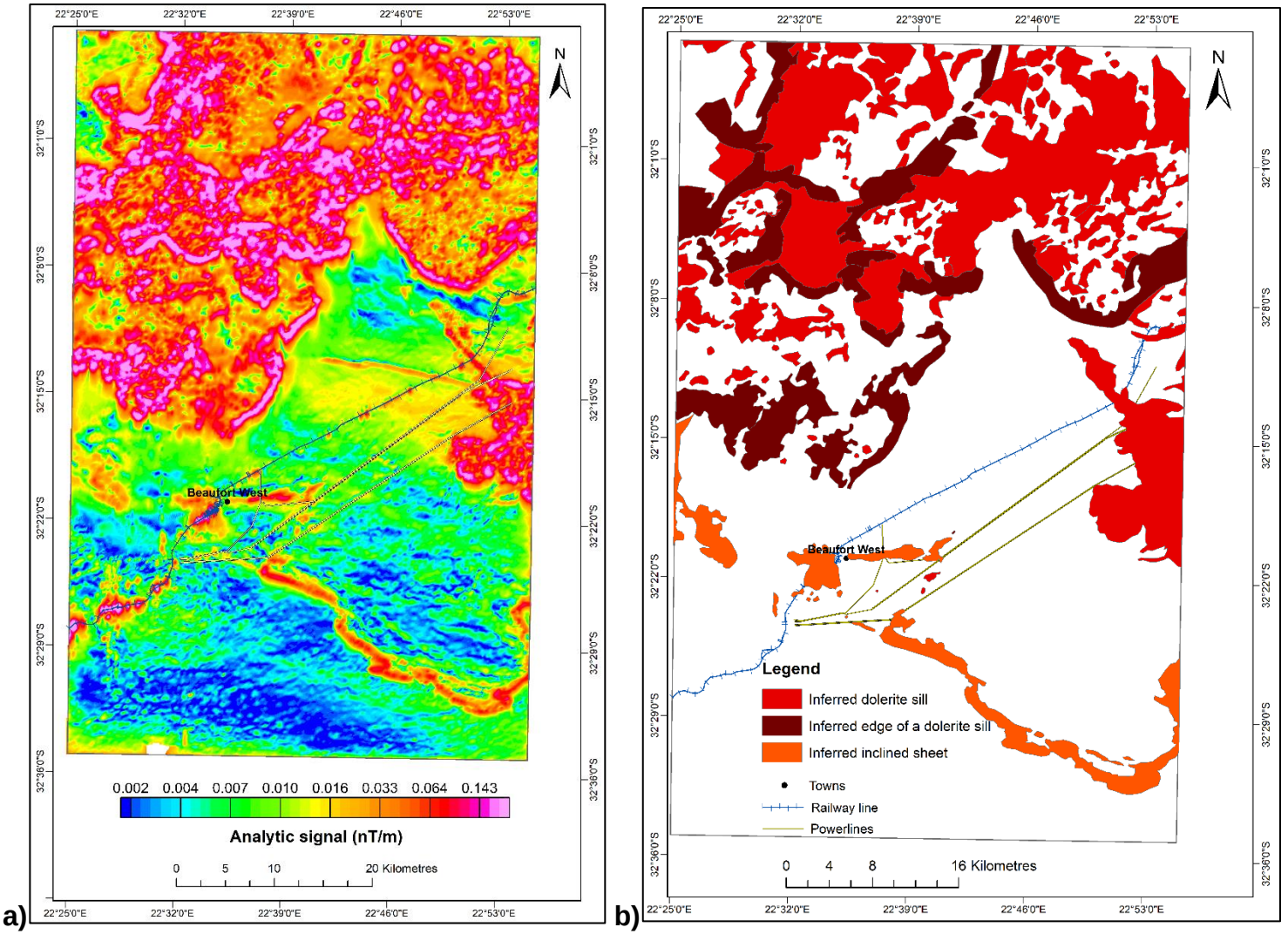

Figure 7-4 (a) Analytic signal of the TMI data and (b) Inferred magnetic bodies (sills and inclined sheet) derived from the analytic signal image in (a).

7.2 Mapping using Seismic Data

The historic SOEKOR seismic line BV21 runs through the study area (**Figure 7-5a**). These seismic data were collected by the state oil company SOEKOR in the 1970s and 1980s.The inclined sheet south of 32°22'0″ S is imaged on the seismic data, as well as a deep sill (~1000 m depth below surface) (**Figure 7-5b**). The Karoo and Cape Supergroup sediments and basement rocks are delineated on the seismic section due to strong acoustic impedance contrasts at each interface; namely the top of the Whitehill Formation of the Karoo Supergroup, and Bokkeveld and Table Mountain Groups of the Cape Supergroup and Natal granite-gneiss basement. The inclined sheet can be distinguished from a sill by a cross-cutting relationship with layered sedimentary sequences (Planke *et al.,* 2014). On the seismic image, the deep sill continues horizontally for approximately 10 km to the edge of the section. This shows the significant lateral extent of these sills at depth.

Two SOEKOR boreholes near the study area (KW1/67 and AB1/65) are summarized in **Table 7-1**. Borehole AB1/65 is 83 km north-northeast of Beaufort West while KW1/67 is 73 km south-southwest of Beaufort West. The boreholes show how the Whitehill Formation deepens by over 3 km over a north-south distance of approximately 150 km. Seismic section BV21 shows the Whitehill Formation deepens from approximately 2.2 km to 2.8 km over a distance of 65 km.

Table 7-1 Deep boreholes located close to the study area (Roswell and de Swart, 1976).

Borehole Number	Longitude	Latitude	Overall Depth (m)	Thickness of dolerite (m)	Top of Whitehill Formation (m, below sea-level)
AB1/65	22.6164	-31.8020	2281	622	466
KW1/67	22.3350	-32.9847	5555	0	3391

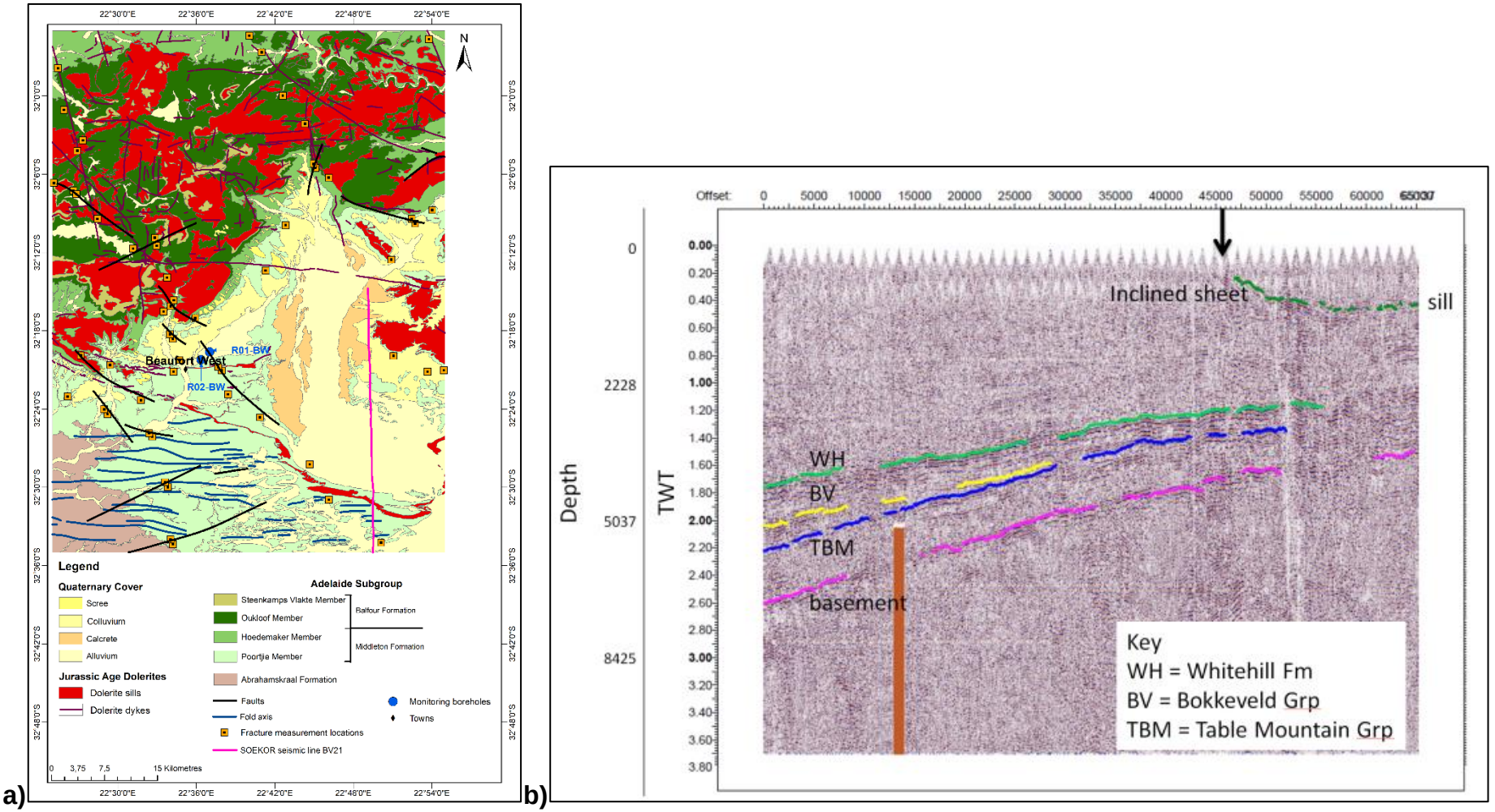

Figure 7-5 (a) 1:50 000 geology of the study area. SOEKOR seismic line (BV21) is indicated (pink line) and extends off the map to the south; (b) Seismic section BV21 showing the inclined sheet (dark green) and Karoo (WH – Whitehill Formation, light green), Cape Supergroup sediments (BV – Bokkeveld Group, yellow; TBM – Table Mountain Group, blue) and basement (pink).

7.3 Estimating Depths using the Radial Averaged Power Spectrum Method

In **Figure 7-6** the study area is divided into 20 blocks to investigate the depth of magnetic sources. The Radial Averaged Power Spectrum (RAPS) method was calculated for each block. This was accomplished through Fast Fourier Transform (FFT) in the MAGMAP menu in Oasis Montaj Geosoft software.

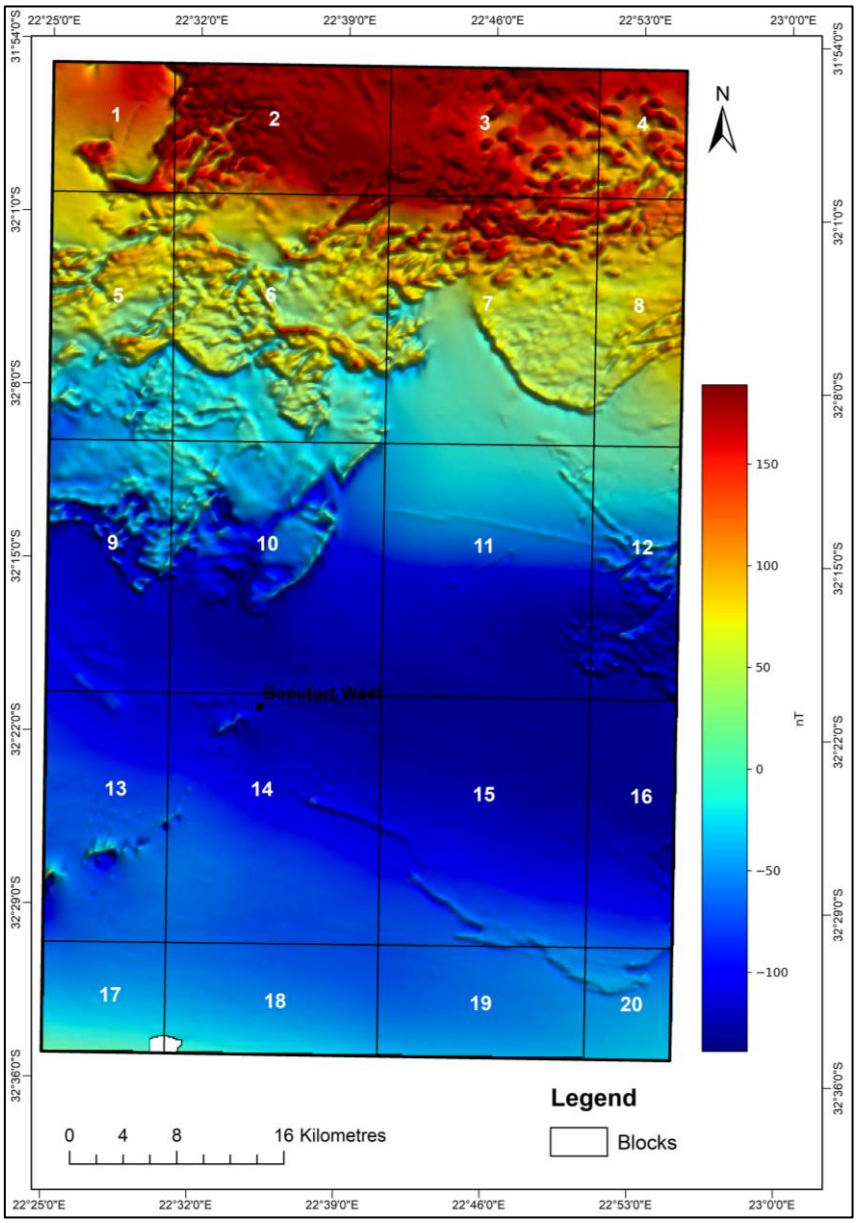

Figure 7-6 Reduced to the pole (RTP) data divided into 20 blocks so that the Radially Average Power Spectrum Method could be applied to each block.

The Radially Averaged Power Spectrum was performed over the seismic line BV21, to compare the results with the depths from the seismic data. Spector and Grant (1970) determined that the depths to magnetic sources directly correlate with the slope of radially averaged power spectrum plot. Hence the depth estimates were inferred from the slope of the line segment. **Figure 7-7a** shows intermediate sources at approximately 1 km, corresponding to the dolerite sill mapped on the seismic data. Shallow sources are observed at 0.3 km and link to outcropping dolerite outcrops. Deep sources are >3 km and are associated with bodies in the basement. It is a standard practice not to plot the line segment with very high wavenumber values as these are usually associated with noise in the data.

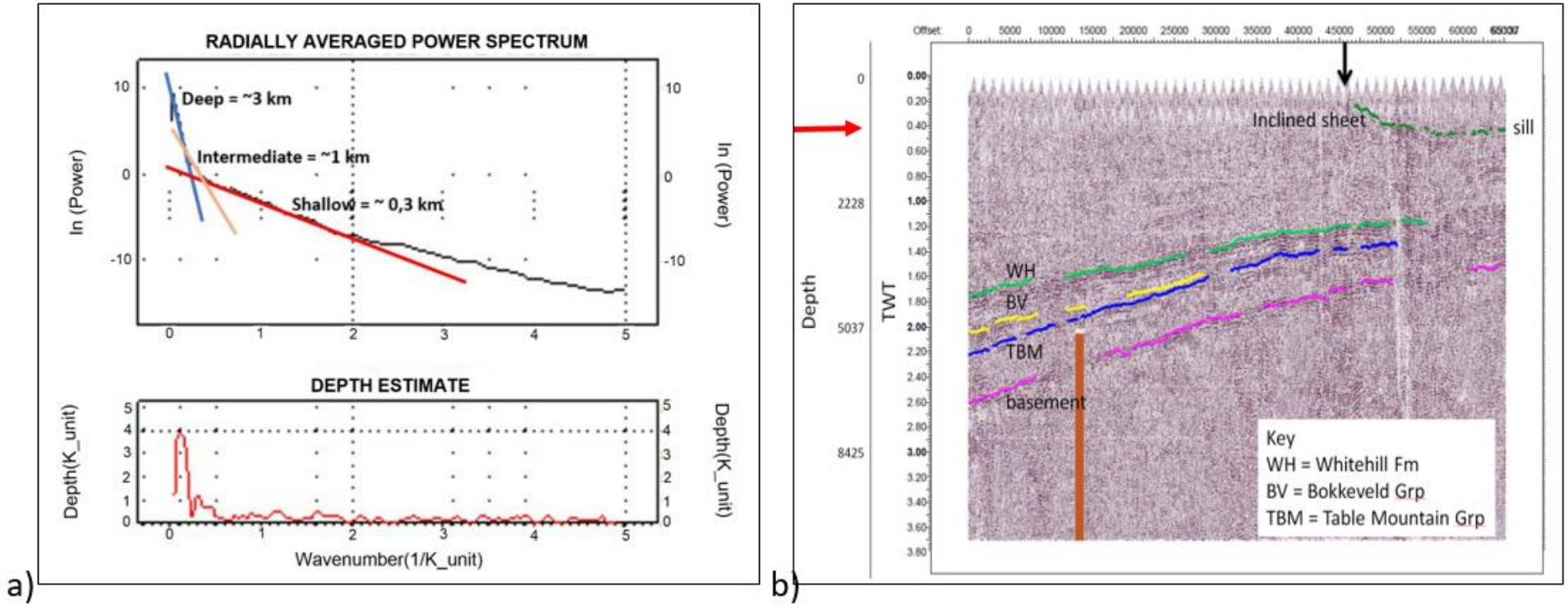

Figure 7-7 (a) Radial averaged power spectrum of the RTP TMI data over seismic line BV21. The depth to the magnetic sources are estimated from the slope of the curve. The deep magnetic sources (blue line) are at approximately 3 km, intermediate sources at approximately 1 km and shallow magnetic sources (red line) are at approximately 0.3 km. (b) the inner sill depth (~1 km) estimated from radial averaged power spectrum is shown by a red arrow on the seismic data (profile line BV21).

The Radially Averaged Power Spectrum (RAPS) was performed on all the blocks to determine depths to the magnetic sources. Block 14 is chosen as an example (**Figure 7-8**). The Radially Averaged Power Spectrum for block 14 with two linear segments correspond to sources at different depths (**Figure 7-8)**.

Shallow sources are estimated at 0.24 km while deeper sources are at 1.6 km (**Figure 7-8**). The shallow source relates to the E-W dolerite inclined sheet in Beaufort West town. This sheet is intercepted at varying depths by several boreholes: 161 to 178 m in R02-BW borehole and 498 to 508 m and 690 to 692 m in R01-BW borehole (located over 1 km NE of R02-BW in **Figure 7-9a**.

Magnetic data over block 14 was filtered in order to understand the signal of the shallow and deep sources. The regional/deep component was separated out by passing the low frequencies associated with deep magnetic sources and rejecting the high frequencies. The shallow component was separated out by allowing the high frequencies to pass. **Figure 7-9c and d** show the shallow and deep sources in block 14, respectively. The anomalies on the high pass data for block 14 are linear and semi-circular, with magnetic values ranging from -6.5 to 3.3 nT (**Figure 7-9c**). Magnetic values for deep-seated magnetic sources range from 59 to 115.1 nT (**Figure 7-9d**). The deep source determined from the RAPS analysis at 1.6 km is not the true depth of the deep sources in the region. The depth estimates are affected by the size of the block, which is a limitation of the method.

The results of the other blocks are summarised in **Table 7-2** and their Radially Averaged Power Spectrum (RAPS) graphs are presented in Appendix A. The shallow sources for these blocks are about 0.3 km depth related mainly to dolerite sills and dykes. Depths to the basement anomalies (e.g. Beattie and Williston Anomalies) were not resolved because the Radial Average Power Spectrum (RAPS) was performed on smaller blocks.

Window size is one of the limitations of the Radial Average Power Spectrum (RAPS) and is discussed in Chapter Four (section 4.3.6.1). Therefore the deep magnetic sources listed in the table are not a true reflection of the deep sources in the region.

To map the realistic depths to deep magnetic sources, the RAPS was performed on regional magnetic data for the whole study area and delineated deep sources at depths of about 11 km (**Figure 7-10**). The deep magnetic anomalies are shown on the low pass map (**Figure 7-11**). The deep magnetic source anomalies estimated from the RAPS are within the depths proposed for the source of the Beattie Magnetic Anomaly and the Williston Anomaly within the basement by Lindeque *et al.* (2011) in the western Karoo Basin from seismic data.

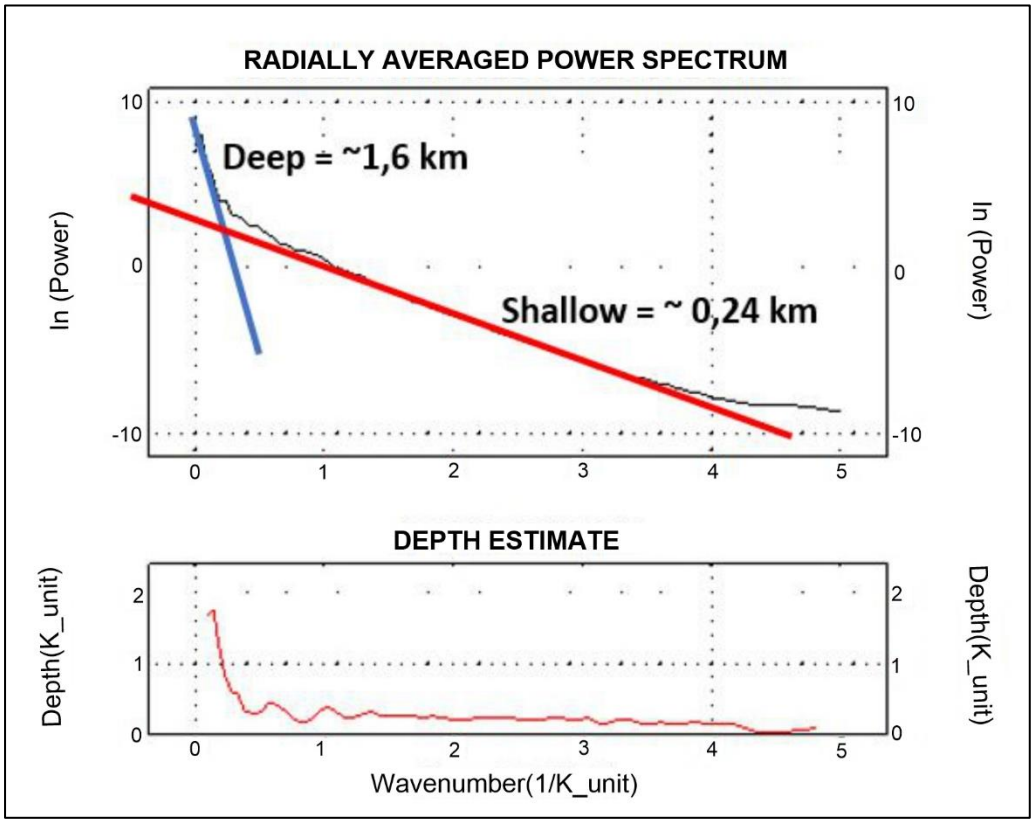

Figure 7-8 Radially averaged power spectrum performed from RTP TMI dataset for block 14. Depth to magnetic sources are estimated from the slope of the curve. The deep magnetic sources (blue line) are at approximately 1.6 km and shallow magnetic sources (red line) are at approximately 0.24 km. Due to the fact that the region was divided into smaller blocks, this means that the “deep” source is not a true reflection of the much deeper basement sources expected in the region.

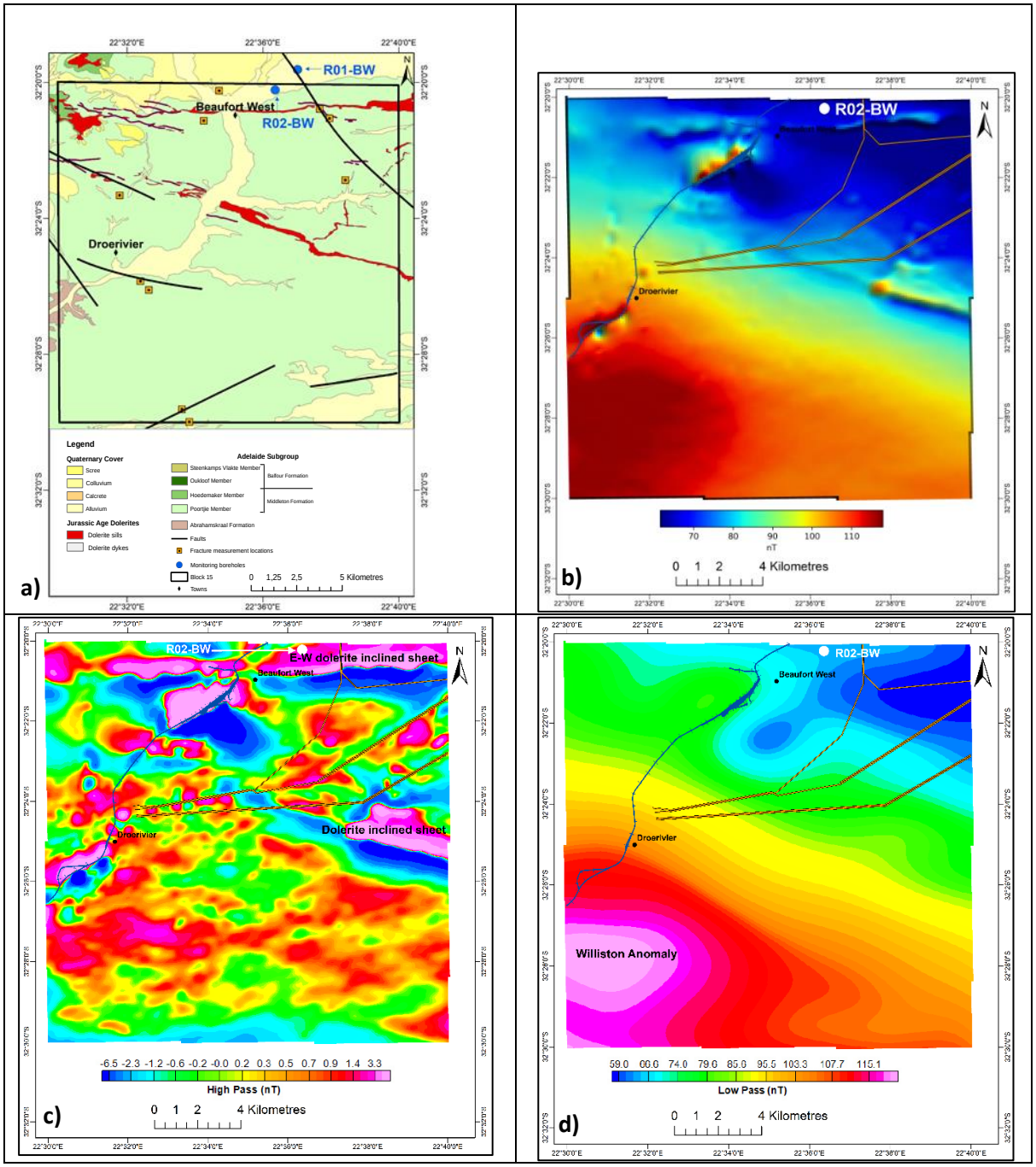

Figure 7-9 Understanding the shallow and deep magnetic sources in the southern portion of the study area (block 14, Figure 7-6): (a) 1:50 000 geological map showing the recently drilled boreholes R01-BW and R02-BW; (b) Reduce to the pole of the TMI data; (c) High-pass filtered magnetic component of the RTP (shallow sources); (d) Low-pass filtered magnetic component of the RTP data (deep sources).

Table 7-2. Depth Estimations for remaining blocks using Radially Averaged Power spectrum (RAPS). Deep magnetic sources were not resolved due to a small window size used (a limitation of the method), however the shallow sources were delineated.

Block	Deep magnetic sources (km)	Shallow magnetic sources (km)
1	-	0.3
2	1.3	0.3
3	1.2	0.3
4	-	0.3
5	1.4	0.3
6	1.4	0.3
7	1.1	0.3
8	0.7	0.26
9	1.5	0.3
10	1.4	0.3
11	1.4	0.57
12	1.3	0.27
13	1.3	0.3
15	2.3	0.3
16	0.67	0.23
17	1.4	0.3
18	1.6	0.26
19	1.6	0.28
20	0.8	0.3

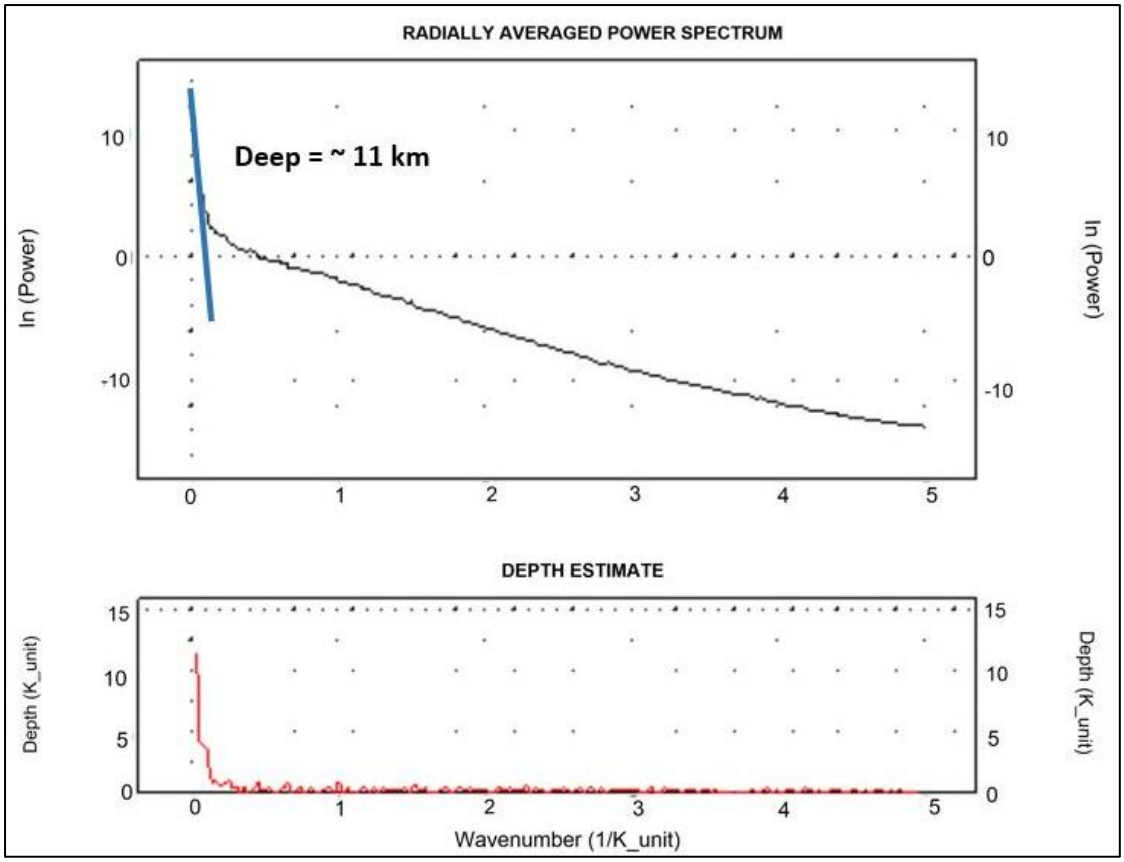

Figure 7-10. Radially averaged power spectrum performed on regional RTP TMI data for entire study area. Depth to magnetic sources are estimated from the slope of the curve. The deep magnetic sources (blue line) are at approximately 11 km.

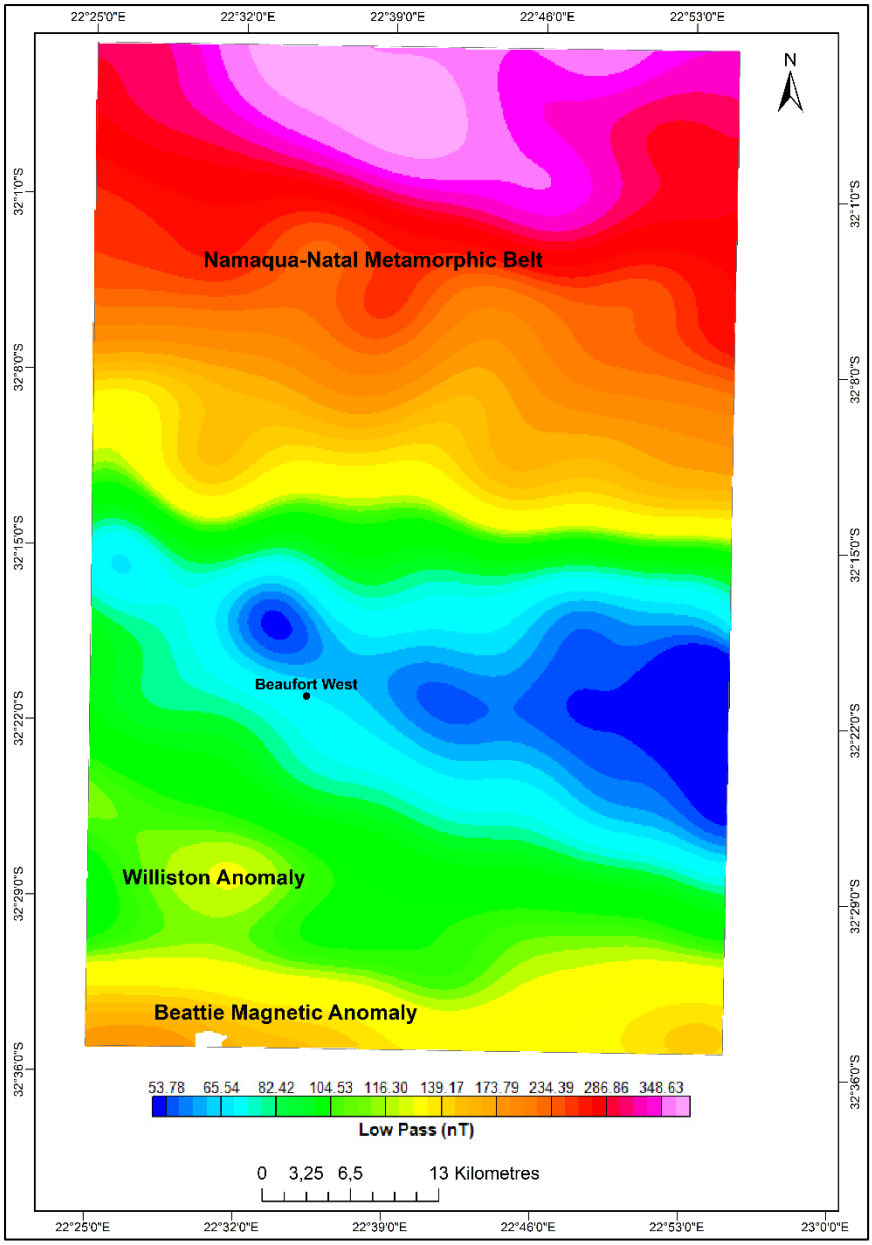

Figure 7-11. Low-pass filtered magnetic component of the RTP data used to highlight deep magnetic sources such as edge of the Namaqua and Natal Belts, and the Beattie and Williston Magnetic Anomalies.

7.4 Summary

- Deep magnetic anomalies characterised by long-wavelength are related to the Beattie Magnetic Anomaly (BMA), Williston Anomaly in the central and the positive anomaly over the Escarpment corresponding to the Namaqua and Natal Belts. Beattie anomalies lie outside of the study area. The Karoo dolerites are located at shallow depths characterized by short wavelengths. The short-wavelengths are superimposed over the long-wavelengths on the Total Magnetic Intensity (TMI) data, hence shallow features should be separated.
- Five linear features mapped from the magnetic data: E-W to ESE-WNW, NNW-SSE, NW-SE, NE-SW and NNE-SSE interpreted as dolerite dykes, kimberlite dykes, fractures and faults. The E-W to ESE-WNW and NNW-SSE structural features correspond to the structural features in the Western Karoo Domain. Some other structural features in the area were observed on the dolerite sills and they could be related to shearing.
- Most of the inferred sub-surface faults from the magnetic data do not correlate with the surface faults. The surface faults further south of the study area cut through the country rock known to have low magnetic susceptibility values. These faults could not be mapped because sedimentary rocks usually have low magnetic susceptibilities (discussed in Chapter Six); hence, no contrast was observed from the magnetic data that these faults were cutting.
- The Karoo dolerite sills with their edges were delineated from the filtered magnetic data. The rims of these sills contain high magnetic signature that could result from the concentration of magnetic material on the rims. The rims are topographically accentuated and this is common for the sills mapped by Chevallier and Woodford (1999). A seismic line BV21, (part of the SOEKOR seismic data collected) cut through an outcropping dolerite inclined sheet southeast of Beaufort West. The seismic data mapped the inner sill that connects to the inclined sheet at approximately 1000 m below the surface. The seismic data was used to map the depth of the inner sill.
- Borehole AB1/65 located northeast of Beaufort West intersected the Whitehill Formation at 466 m while borehole KW1/67 located south-southwest of Beaufort West intersected the Whitehill Formation at 3 391 m. The

interpretation drawn from these boreholes is that the Whitehill Formation becomes shallow towards the north of the study area. The depth of the formation in the study area is deeper than 466 m as borehole R02-BW had a total depth of 1402 m which was still in the Tierberg Formation and seismic line BV21 mapped it to a depth of over 2 000 m.

- Depth estimations were performed for the study area. The Karoo dolerites intruded at shallow depths and the shallowest depths related to the dolerites estimated from the Radial Averaged Power Spectrum (RAPS) were located at shallow depths around 0.3 km. The deep magnetic sources anomalies were only delineated from the RAPS performed on the entire study area. The deep sources were about 11 km and are within the depths mapped by Lindeque *et al.* (2011) in the western Karoo Basin from seismic data.

8 CHAPTER EIGHT - FORWARD MODELLING

8.1 Magnetic Modelling

Magnetic modelling over an interesting feature in the area forms part of the objectives of the study. This is done to understand the geometry, depth and thickness of the modelled feature, particularly the dolerites of which this study aims to investigate.

A 2D magnetic model was created over the seismic line BV21 cutting through the study area. Before modelling, profile data was investigated along the seismic line. The Digital Terrain Model (DTM) was compared with the high-resolution airborne magnetic data before modelling. The filtering of the magnetic data was performed including the removal of the International Geomagnetic Reference Field (IGRF) and high pass filtering to better understand the signal due to the shallow subsurface geology (dolerites).

Figure 8-1 shows the TMI and filtered magnetic data along the profile. The TMI signal is a combination of both deep-seated and shallow magnetic anomalies. The TMI data shown in **Figure 8-1a** shows a minor shift when the IGRF field is removed. The magnitudes on TMI before IGRF is removed range from 26 200 to 26 120 nT and changes to -60 to -180 nT after IGRF is removed. The IGRF is removed to highlight the anomalies related to subsurface bodies (Reeves, 2005). The TMI curve after IGRF is removed in **Figure 8-1a**, highlights deep-seated bodies related to the Beattie and Williston Magnetic Anomalies.

In this study, the aim was to model the Karoo dolerite bodies, which are associated with shallow magnetic anomalies. A high-pass filter was therefore used to remove anomalies due to deep-seated magnetic bodies. Several high-pass filtering were applied to get the best fit high pass data. Data obtained after applying a high pass filter with a cut-off of 2000 m, 400 m, 150 m are plotted with the TMI in **Figure 8-1b** and **c**. It is evident from the profile lines that the 2000 m cut-off value preserves a portion of deeper sources and the 150 m cut-off introduces a lot of noise to the data. The cut-off

value of 400 m was selected as the best cut-off to display shallow magnetic sources. Geophysics methods are usually sensitive to cultural noise such as railway line and power lines. Overhead power lines generate magnetic and electric fields which can co-exist or exist individually (Pretorius, 2006). The high-pass filtered magnetic data highlighted two power lines that cross the northern part of the profile (**Figure 8-1a**).

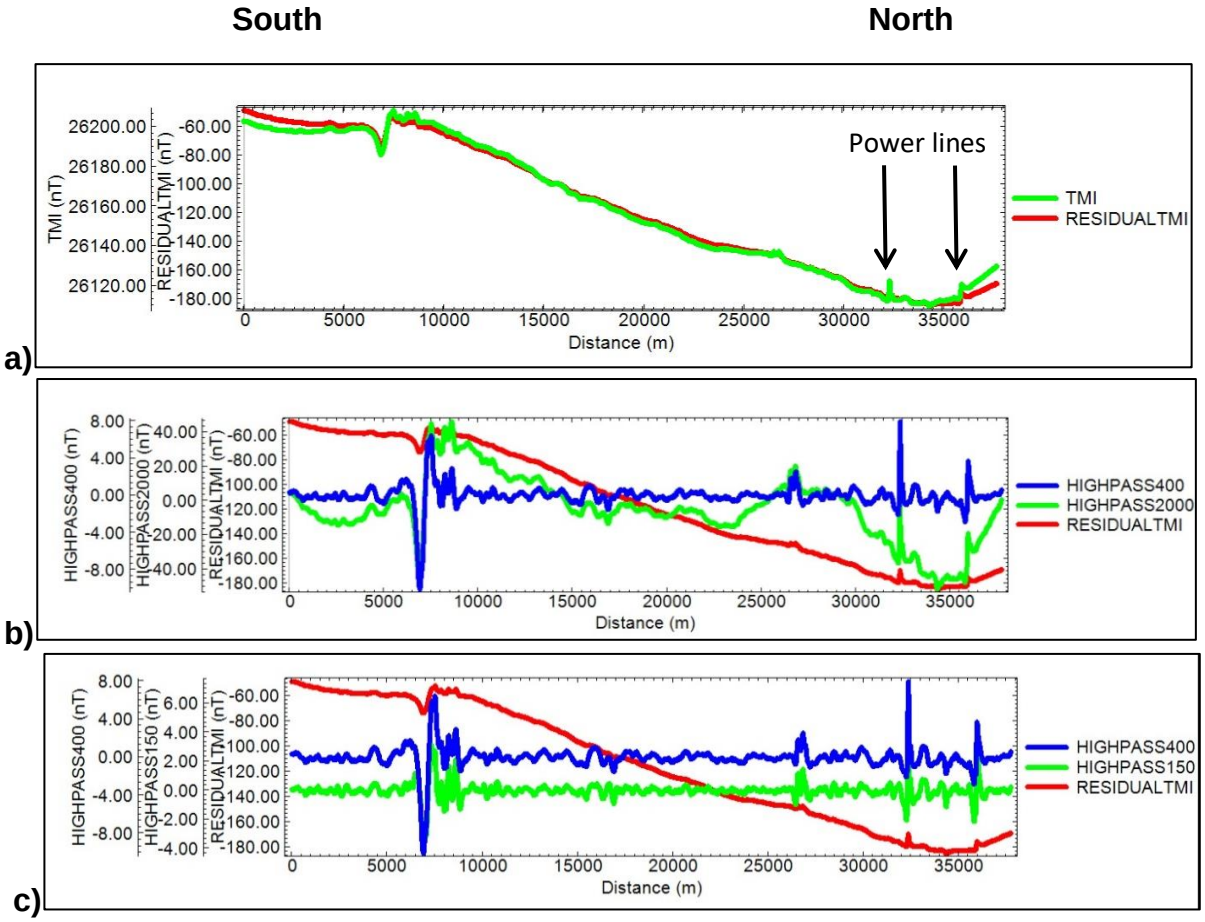

Figure 8-1 TMI and filtered magnetic data: (a) TMI before IGRF is removed (green) and residual TMI after IGRF was removed (red) showing a change in amplitude and slight shift; (b) Residual TMI (red) compared with high pass filtered data with a cutoff of 2000 m (green) and 400 m (blue). The cutoff of 2 000 m still shows regional features compared to a cutoff of 400 m, which highlights shallow features. The long-wavelength magnetic response in the south of the profile on the residual TMI data compared to the high-pass data with a cutoff of 400 m, is related to deep bodies such as those causing the Beattie and Williston Anomalies; (c) Residual TMI (red) compared with high pass filtered data with a cutoff of 400 m (blue) and 150 m (green). The cutoff of 150 m enhances noise in the data, and therefore a cutoff of 400 m was selected. The

cultural noise due to two power lines represented by sharp peaks north of magnetic data profile.

The ground elevation values generally decrease from north to south especially along seismic line BV21. The elevation values can sometimes be associated with geological bodies such as where the inclined dolerite sheet outcrops, elevation data values increase and correlate with a magnetic anomaly (**Figure 8-2a**).

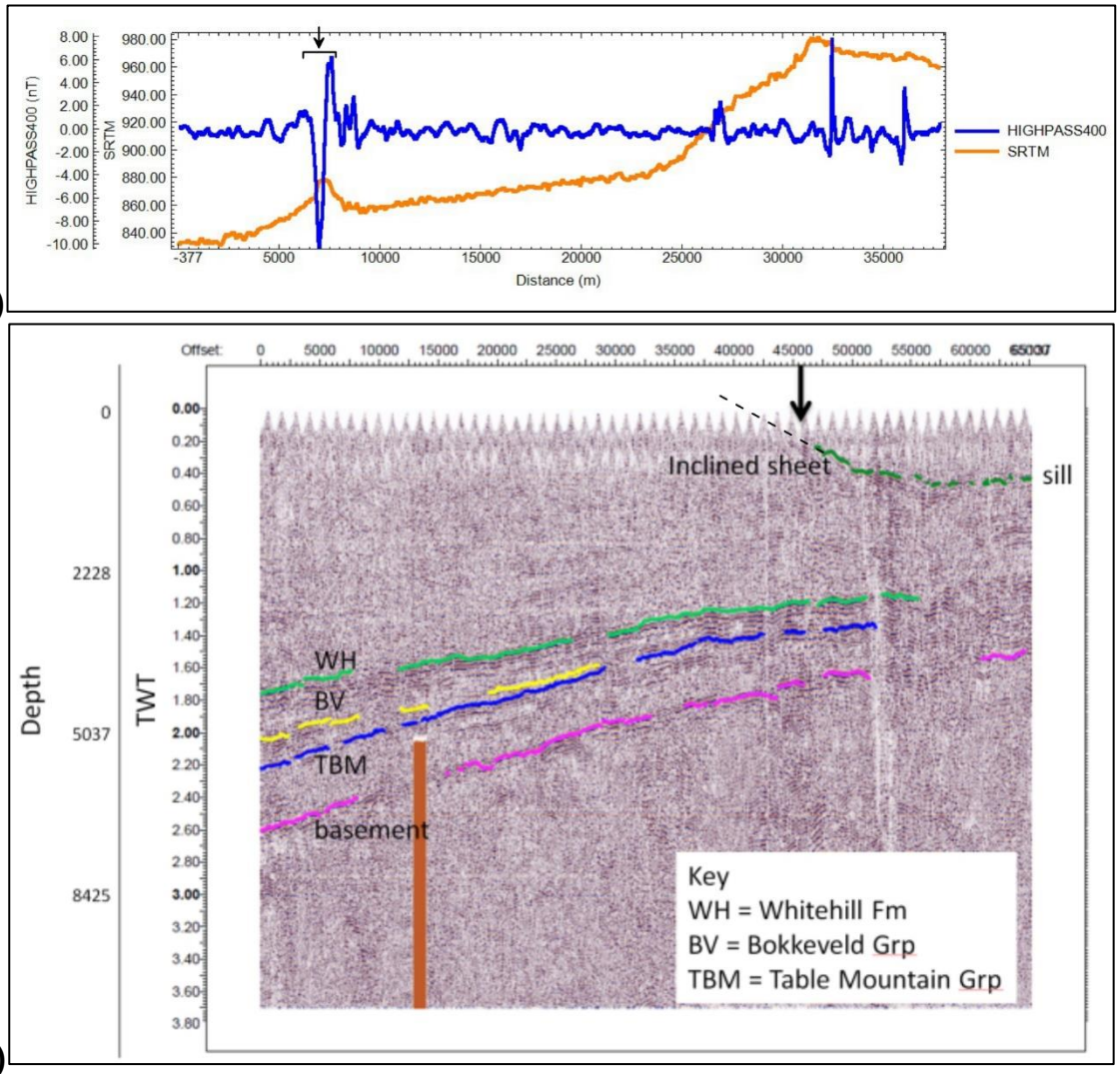

Figure 8-2 Comparison of (a) Space Shuttle Radar Topography Mission (SRTM) data (orange), high-pass filtered magnetic data with a cutoff of 400 m (blue), and (b) seismic section BV21 showing location of the inclined sheet. The outcropping inclined sheet (black arrow) shows up as a topographic high and magnetic anomaly on (a).

8.2 Forward modelling interpretation

Forward modelling was carried out using mag2dc, an open-source software (Cooper, 1997). The program uses a 2.5 D Talwani algorithm to calculate the magnetic field over a body (Talwani and Heirtzler, 1964).

The magnetic susceptibility used for the dolerite sills and dykes is 0.02 SI, measured from the rock samples and discussed in Chapter Six. The magnetic susceptibility of the dolerite was used because dolerites are highly magnetic and sedimentary rocks, especially the Karoo sediments generally consist of low-magnetic susceptibilities.

Seven magnetic anomalies identified in **Figure 8-3** will be discussed below from south to north of the profile line and were included in the model. The magnetic method delineated power lines north of the magnetic profile line. The high pass filtering technique applied to the TMI data also enhanced these power lines and are avoided on the model. All magnetic bodies are related to the Karoo dolerite sills and dykes.

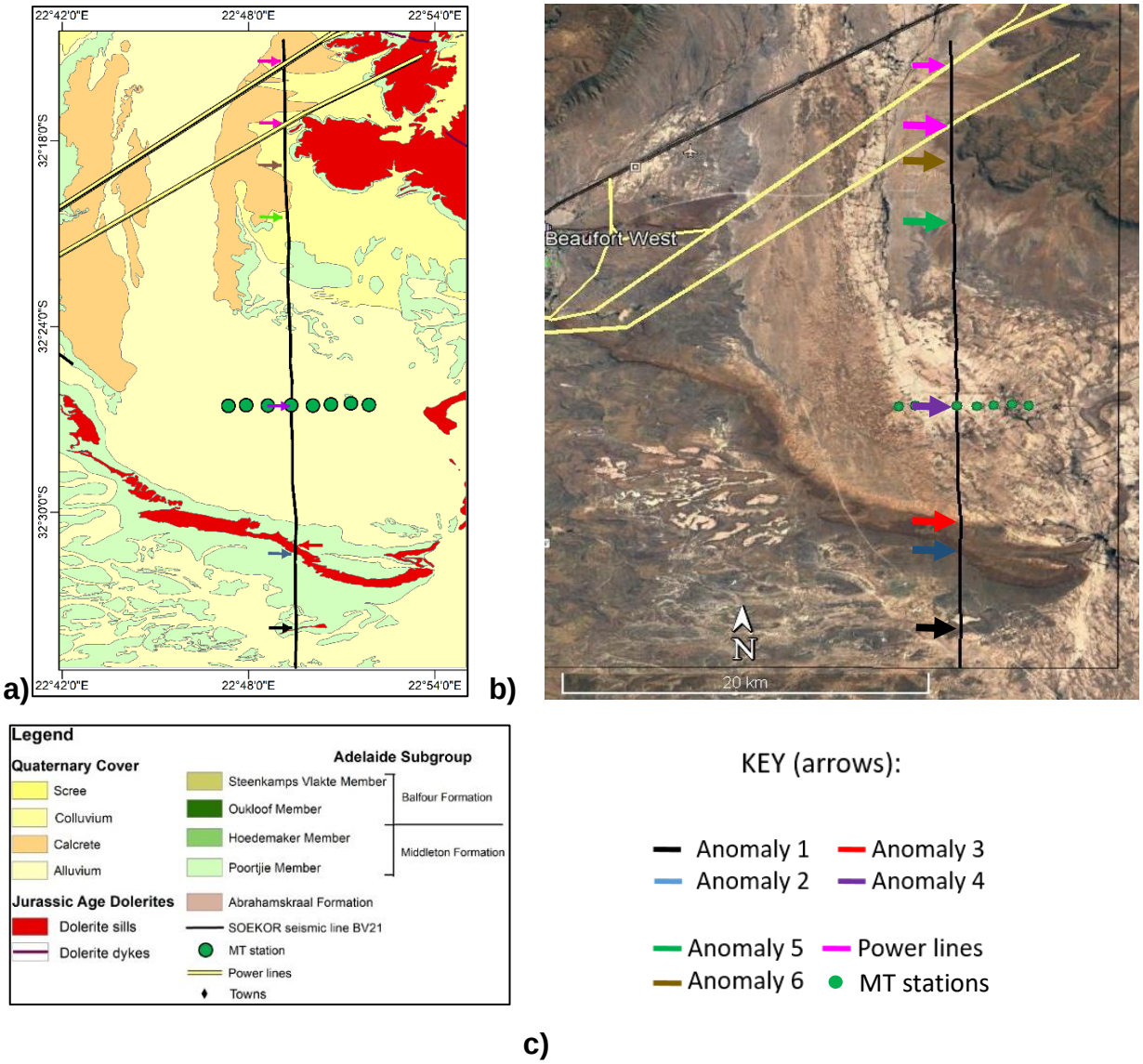

Figure 8-3 Investigation of magnetic anomalies along seismic profile BV21: (a) 1:50 000 scale geology map with seismic profile (black line) (modified after Cole *et al.*, 2016b). (b) Google Earth image. (c) Profile with TMI, high pass filtered data (cutoff of 400 m) and elevation data. The location of magnetic anomalies of interest (coloured arrows, labelled 1-6) are marked in a, b and c.

Anomaly 1

Anomaly 1 in the south of the profile is linked to a small mapped dolerite outcrop that is interpreted as a dolerite sheet joining the main exposed sheet north of this body. This dolerite sheet was mapped as an outcropping body on the 1:50 000 geology mapsheet but was not mapped on the 1:250 000 geology mapsheet. The magnetic response of the outcropping dolerite sheet over the seismic line BV21 is 184 nT. The seismic line cuts through the narrow part of the dolerite sheets with much more outcrop observed east of the seismic line (shown by black arrow, **Figure 8-4**). The thickness of the body from the magnetic response is approximately 10 m, which is in line with mapping throughout the Karoo (Duncan and Marsh, 2006).

Anomaly 2 and 3

Anomaly 2 is due to the inclined sheet mapped on seismic line BV21 that outcrops. The outcropping sheet forms a topographic high (elevation of approximately 878 m). The inclined sheet meets the dolerite sill at depth as seen on the seismic data at depth of about 1000 m below the surface or 120 m above sea level. This will be referred to as the inner sill. Woodford and Chevallier (2002) mentioned that these inclined sheets tend to be the feeder to both outer- and the inner- sills (**Figure 8-5**). The dolerite sill that the sheet is connected to intruded into the lower Beaufort Group or Ecca Group stratigraphy, where there was sufficient overburden to force the sill to intrude over a long distance. Inclined sheets form on the edges of sills when overburden pressure is exceeded. The upper Beaufort Group strata instead are dominated by saucer-shaped sill due to a smaller overburden thickness (Woodford and Chevallier, 2002a, Polteau *et al.,* 2008).

Anomaly 3 is a possible extension of the Anomaly 2 inclined sheet that does not outcrop, but to the west and east, there is an “indent” in the outcropping sheet and could be connected and result in a body below anomaly 3 (**Figure 8-4**). This body could be considered a “minor sills/sheet” as shown in **Figure 8-5**.

Based on previous studies, sills, sheets and dykes form a complicated interconnected network (Scheiber-Enslin *et al.,* 2014b, Hansen *et al.,* 2004). Multiple inclined sheets can be connected to a dolerite sill at depth (Du Toit, 1920). This was demonstrated from a cross-section in Victoria West (Chevallier and Woodford, 1999, **Figure 8-6**). Cartwright and Hansen (2006) propose a model of sill-feeding-sill due to the connection of the inner sill and inclined sheets (**Figure 8-5**).

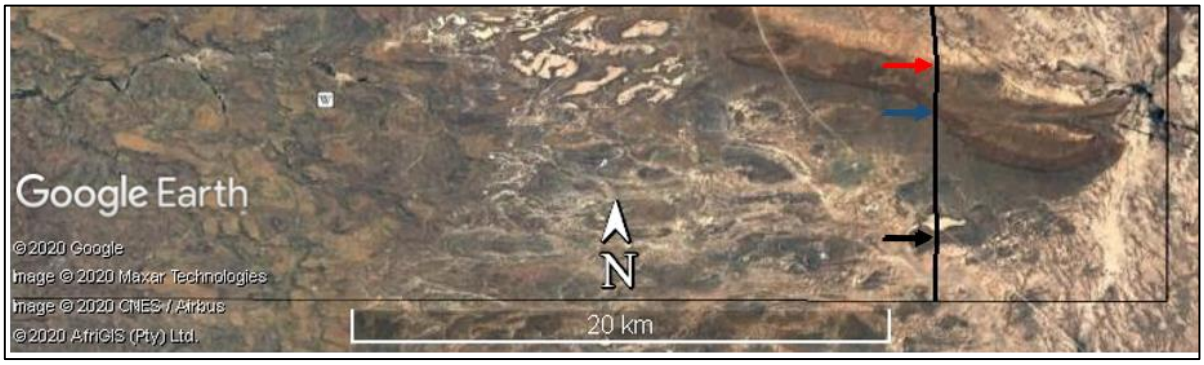

Figure 8-4 Outcropping inclined sheet (Anomaly 2, dark blue arrow) on Google Earth with seismic profile BV21 (black line), dolerite sill (black arrow) and minor sill (Anomaly 3, red arrow).

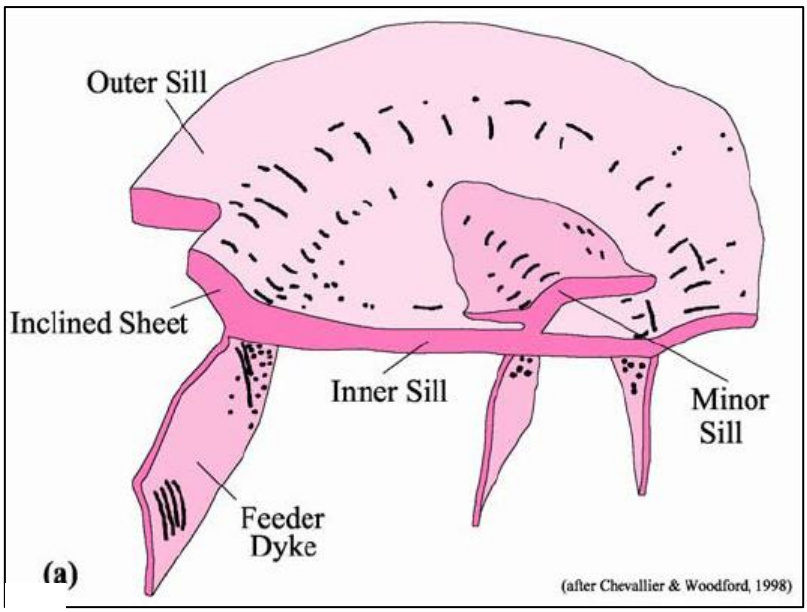

Figure 8-5 A 3-D model showing five common morphological and structural features associated with Karoo sills (Chevallier and Woodford, 1999).

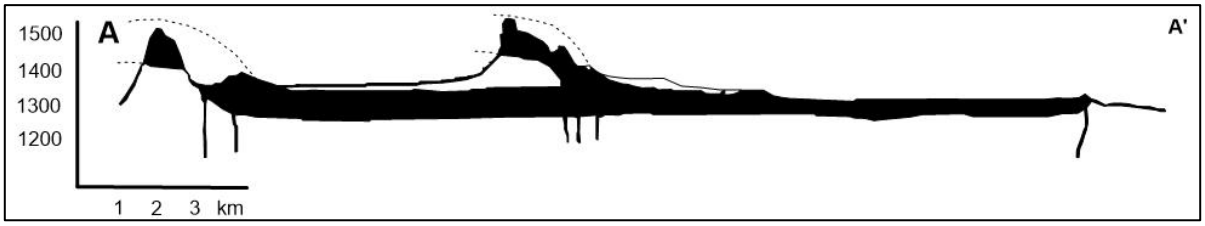

Figure 8-6 Victoria West sill and ring. Inclined sheet linking the lower inner sill to the upper outer sill and two inclined sheets are connected to an inner sill (Chevallier and Woodford, 1999). The location of the cross-section line is found in Chapter 2, Figure 2-8.

Anomaly 3 could therefore be due to another inclined sheet coming off from the 1 000 m deep inner sill (**Figure 8-7a**) or a minor sill/sheet coming off from the known inclined sheet (Anomaly 2) (**Figure 8-7b**). The sheet appears to be 10 to 20 m thick on Google Earth. Recently drilled boreholes in the study area, R01-BW (drilled up to 1 400 m deep) and R02-BW (drilled up to 516 m deep) intersected the Beaufort West inclined sheet at 498-508 m and 161-178 m respectively. The thickness of Beaufort West inclined sheet from R01-BW was about 10 m and about 17 m from R02-BW.

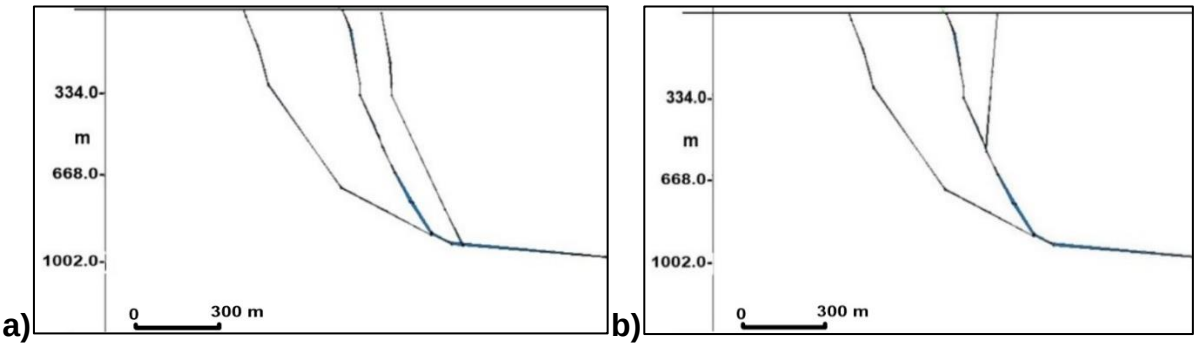

Figure 8-7 Model along seismic profile BV21. In (a) Anomaly 3 is modeled as a separate inclined sheet coming off from the 1 km deep sill. The inclined sheet does not outcrop. In (b) Anomaly 3 is modeled as an offshoot from the main inclined sheet.

Anomaly 4

There is no outcrop below Anomaly 4, but inclined sheets are mapped further west and east (shown by yellow arrows, **Figure 8-8**), that are linked with the inclined sheet that outcrops further south and is mapped on the seismic image (Anomaly 2 on the magnetic model). Magnetotelluric (MT) data parallel to anomaly 4 was collected and interpreted by Integrated Geoscience Solutions (2018) (station location shown by green markers, **Figure 8-8**). The data show a sill just deeper than 1 km to the east with the Whitehill Formation at 2 km depth below it and shows another dolerite intrusion that could possibly be a dyke at the centre of **Figure 8-9**. This depth estimate for the sill fits in well with the depth estimated on the BV21 seismic profile.



Figure 8-8 Anomaly 4 location (purple arrow) on Google Earth image with seismic profile BV21 marked (black line) and MT stations (green markers). The anomaly could be due to a buried inclined sheet linking the outcropping sheet to the west and east (shown by yellow arrows).

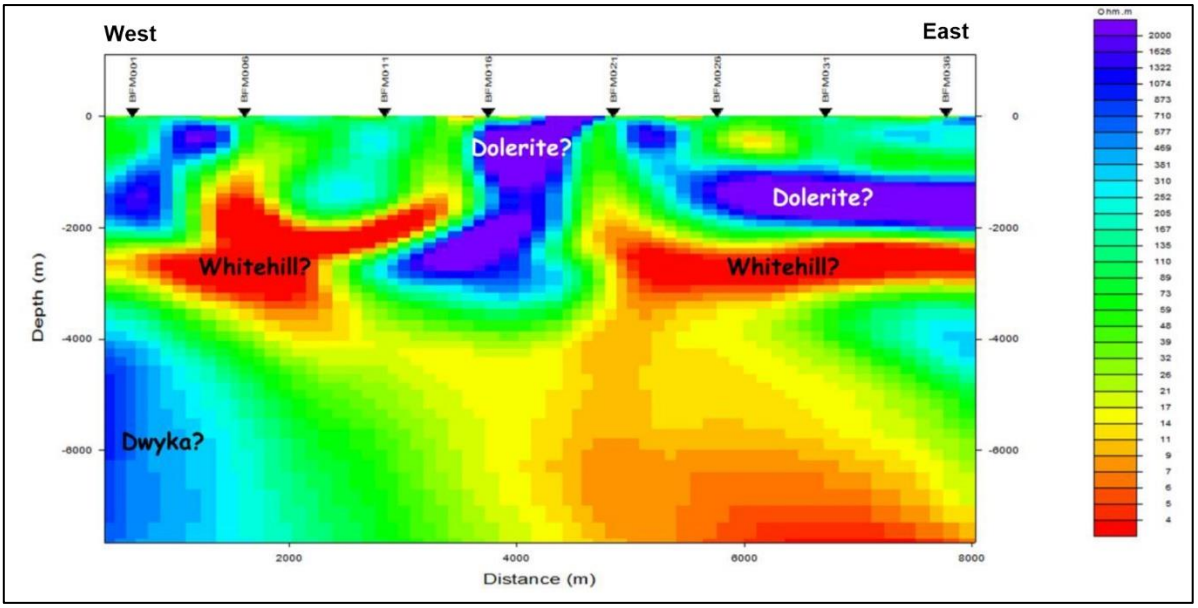

Figure 8-9 Magnetotelluric (MT) data (bottom image) collected where seismic line BV21 crosses, location of both surveys are shown on Google Earth in Figure 8-8. The conductive Whitehill Formation is mapped around 2 km depth with a shallower resistive sill above it around 1 km depth from around 6 km distance along the profile. What appears to be a dyke or inclined sheet cross-cutting the Whitehill Formation is mapped at 4 km distance (Integrated Geoscience Solutions, 2018). The dyke appears wider than expected due to the resolution and spacing of the MT data.

Anomaly 5

From the magnetic profile, anomaly 5 is seen as two anomalies close together, which are interpreted as two NE-SW dykes that are close to each other based on the first vertical derivative of the TMI data (**Figure 8-10**). The dykes are covered by thick alluvium and do not outcrop on surface and therefore have a weak magnetic response.

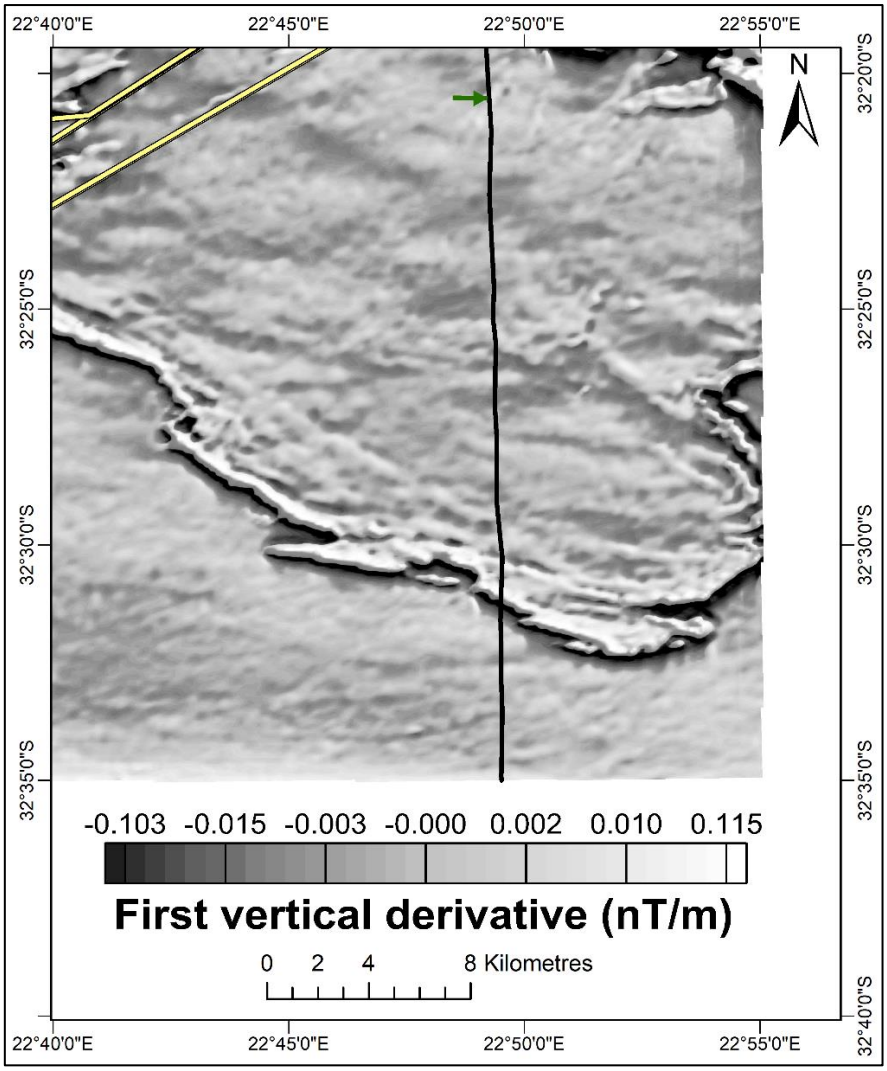

Figure 8-10 Anomaly 5 location on first vertical derivative image (green arrow in the north of the image). The anomaly could be due to two buried dykes that are very close to each other and have a smooth magnetic signal which could indicate that they are not very close to surface.

Anomaly 6

Anomaly 6 (brown arrow) is located close to the power lines and is modeled as a dolerite dyke at a depth striking E-W (**Figure 8-11**).

Anomalies 7 and 8

Anomalies 7 and 8 (pink arrows) are due to power lines which are classified as cultural noise (**Figure 8-11**).

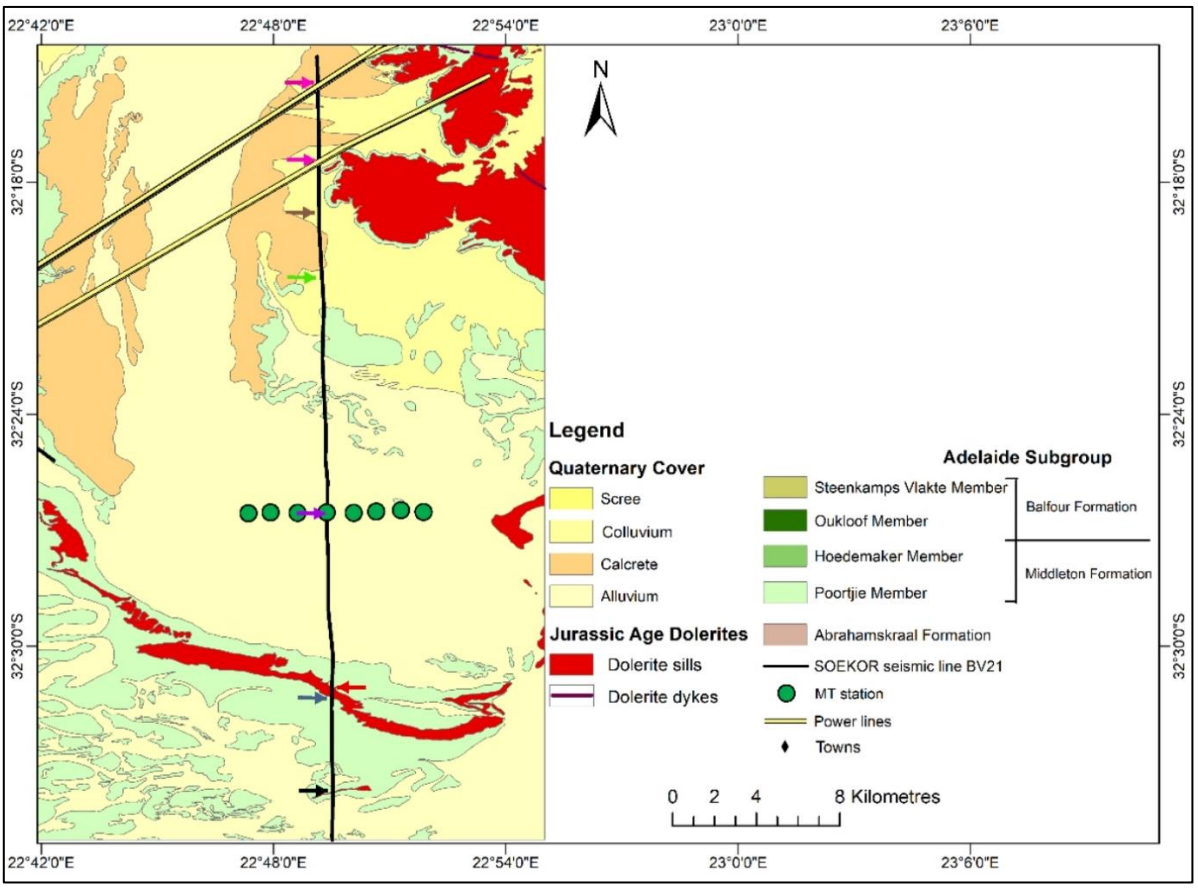

Figure 8-11 Anomaly 5 and 6 locations (green and brown arrow) on 1:50 000 geology image with seismic section BV21 marked (black line). Anomaly 7 and 8 are due to power lines (pink arrows).

The final 2D magnetic model is shown in **Figure 8-12**. **Figure 8-12a** shows anomaly 4 presented as a dolerite dyke, while **Figure 8-12b** models anomaly 4 as an inclined sheet connected to the inner sill. Both interpretations fit the observed curve.

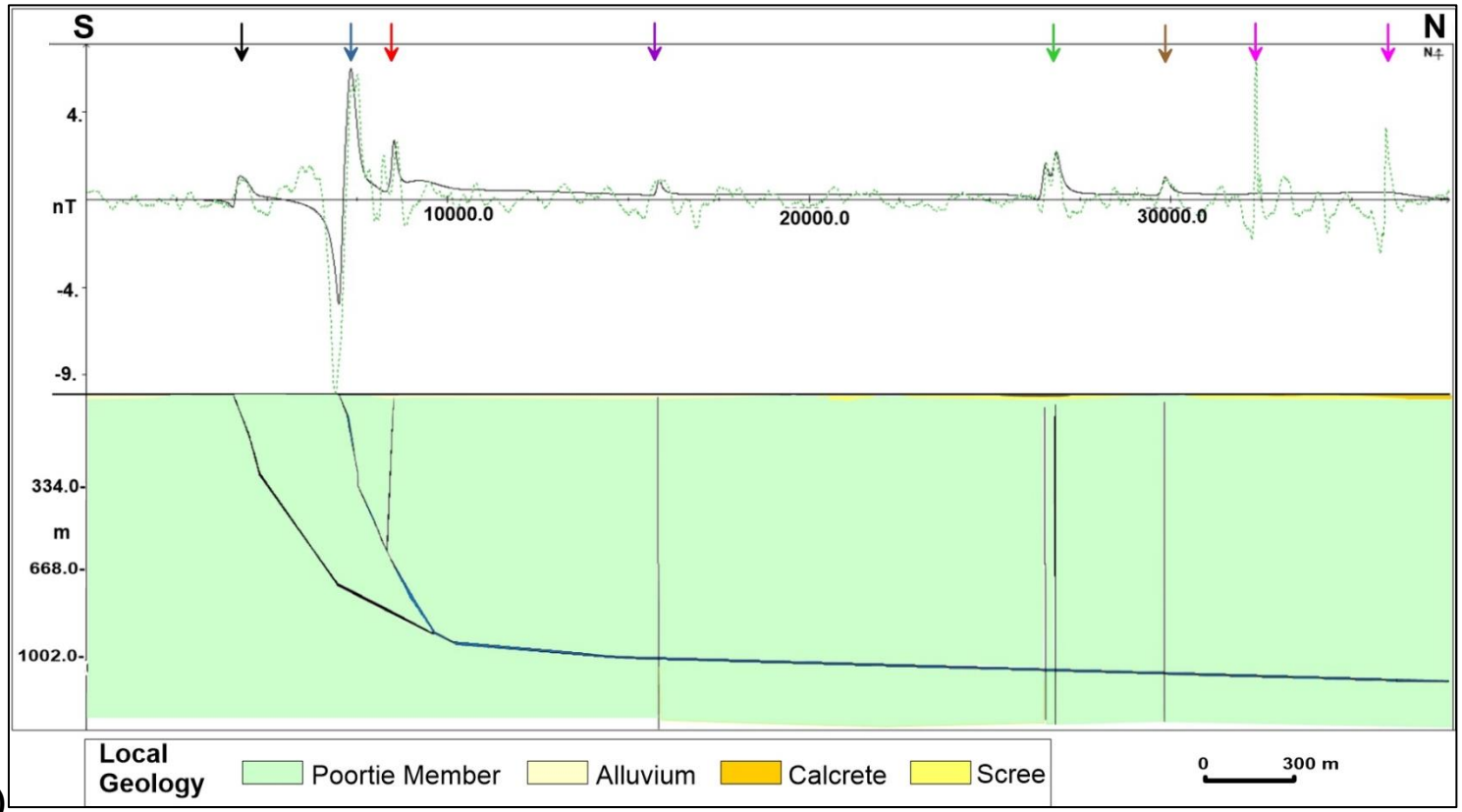

a)

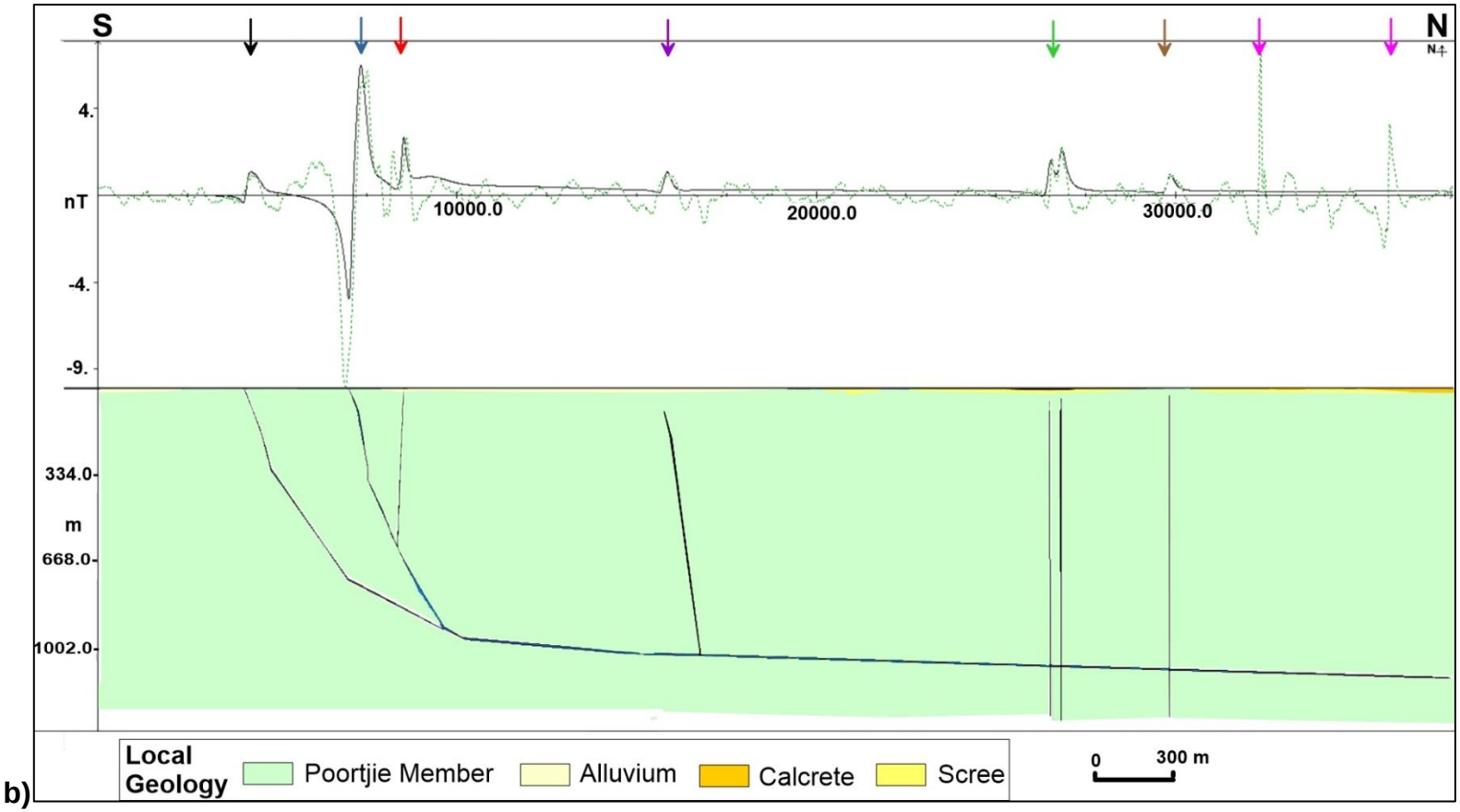

b)

Figure 8-12 Final 2D magnetic model over SOEKOR seismic line BV21 showing dolerite sills, sheets and dykes. Magnetic models are non-unique and therefore, anomaly 4 shown by puple arrow is modelled as dyke (a) dyke and (b) an inclined sheet due to a lack of outcropping data to constrain the model.

The resolution of the data was tested by comparing a 10 m and 20 m thick inner sill (for example., sill at 1 km depth running from about 10 km to 40 km along the profile). Increasing the thickness of the sill by 10 m increased the magnetic curve by around 1 nT (**Figure 8-13** compared to **Figure 8-12**). This is a very small change and therefore we cannot definitely say how thick the sill is. Throughout the model we chose to use a thickness of 10 m.

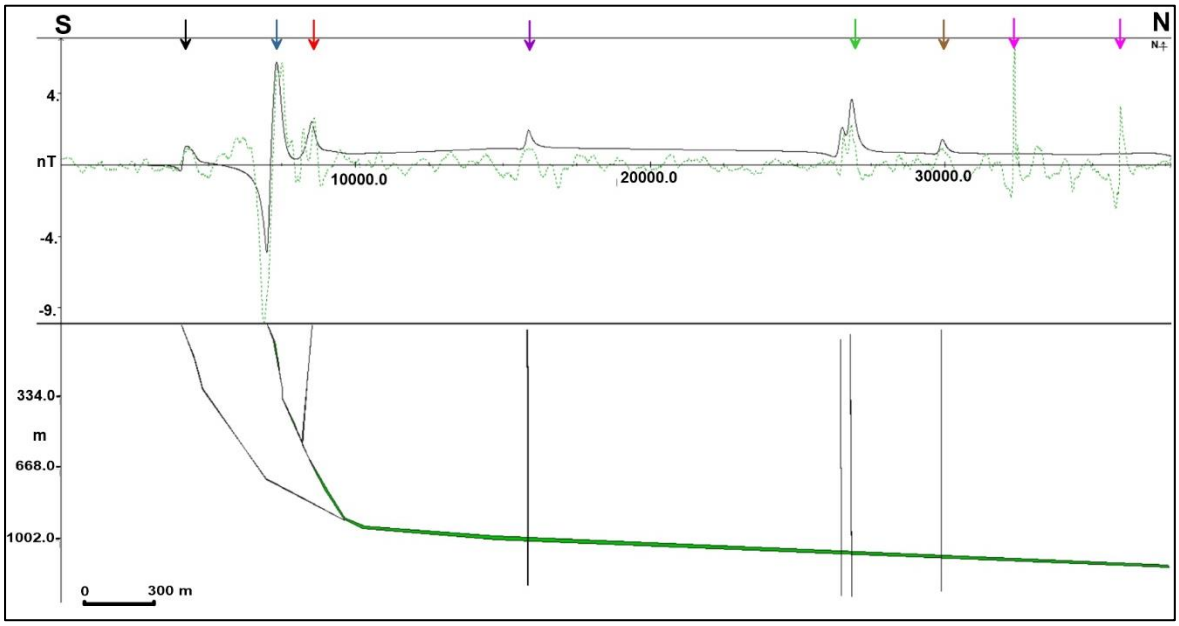

Figure 8-13 Mag2dc model showing a thicker inner sill. The thicker inner sill did not fit the observed magnetic curve suggesting that the sill is thinner.

A 30 m sill thickness was used at 2 000 m (close to the depths of the Whitehill Formation) (**Figure 8-14a**). The magnetic field response of approximately 3 nT was observed on the calculated curve. Multiple sills with 10 m thickness that lie at different depths (1 000 m, 1 500 m and 2 000 m) were used to determine if the magnetic method will be able to map multiple sills at different depths. **Figure 8-14b** shows the calculated curve response at 2 nT. The difference between the 10 m sill used in **Figure 8-12** and multiple sills in **Figure 8-14b** is 1 nT. Therefore, the sills from either multiple sills or thick sill at greater depths cannot be resolve by the magnetic data. Hence the magnetic model was constrained with the seismic section.

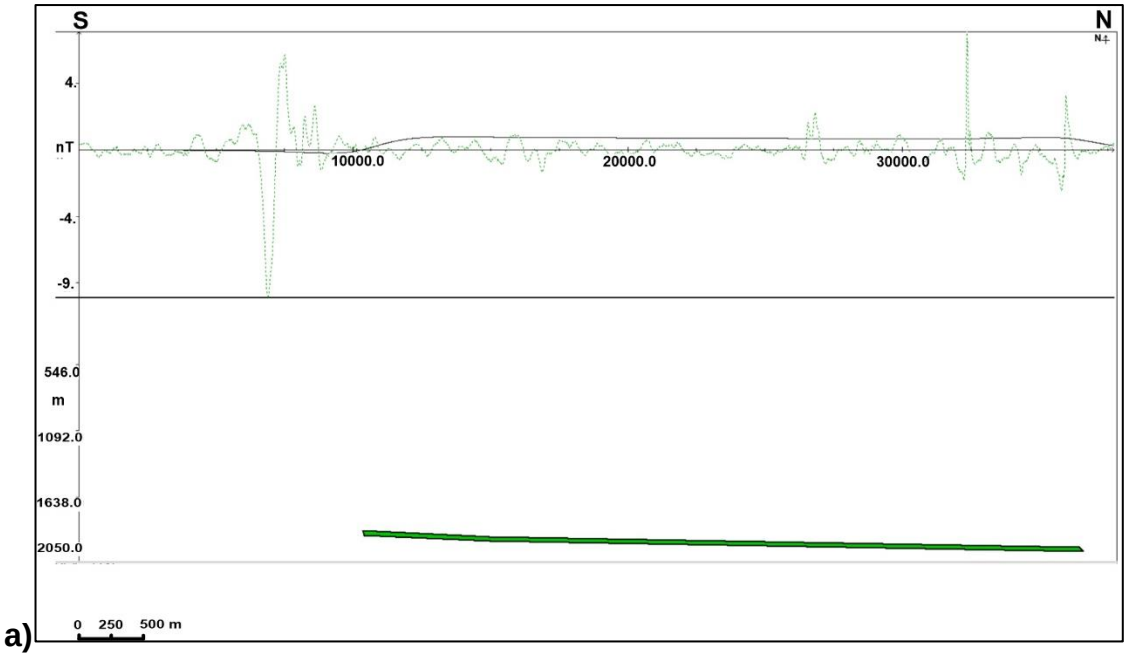

a)

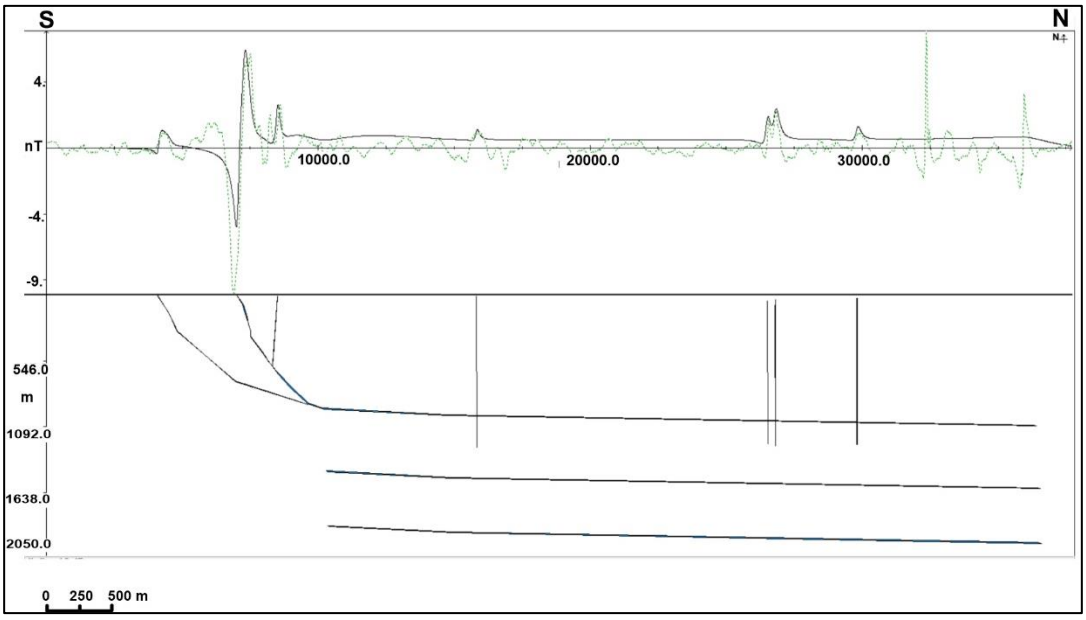

b)

Figure 8-14 A 2D magnetic model, (a) showing a thick sill of 30 m at 2 000 m (b) shows multiple sills of 10 m thickness at different depths (1 000 m, 1 500 m and 2 000 m). Both models shows small magnetic field response and cannot be relied on to map a thick sill at greater depths or multiple sills.

8.3 Summary

- A 2D magnetic model was created for an area in the southern part of the study area where an inclined dolerite sheet outcrops. The magnetic model was created over seismic profile BV21. The inclined sheet is connected to an inner sill at depth (~1000 m below surface) as imaged on the seismic data, similar to the Victoria West sill-ring complex (Chevallier and Woodford,1999).
- Six anomalies delineated from the magnetic data are associated with dolerite sheets and dykes, and two other anomalies are related to the cultural noise (anomaly 7 and 8). Multiple inclined sheets are assumed to be connected to the same inner sill at depth. The inner sill appears to be thin (about 10 m) because when a thicker sill was modelled, the calculated curve did not fit the observed magnetic curve. North of Beaufort West, recently drilled boreholes R01-BW and R02-BW recorded the dolerite sheet thickness at 10 and 17 m, respectively. This shows that the sills are thinner at depth.
- One of these dolerite sills was mapped using Magnetotelluric (MT) data. The Magnetotelluric (MT) data mapped the dolerite at approximately 1 km depth and the Whitehill Formation at approximately 2 km.
- Magnetic data is useful in delineating magnetic bodies that are not exposed. Magnetic models can then be used to understand the shape and thickness of the bodies. However, the method works best when constrained with other geophysical methods and correlated with mapped geology.

9 CHAPTER NINE – DISCUSSION AND CONCLUSION

This chapter discusses and correlates geological and geophysical results. The tectonic history is determined from these results (such as geometry, type, spatial and temporal variation of structures associated with tectonic events in the area).

9.1 Summary of geology results

The surface geology of the area was mapped at 1: 50 000 geology mapsheet scale by Cole *et al.* (2016b) and resulted in several modifications to the stratigraphy west of longitude 24°, though some were done by other authors (Viglietti *et al.,* 2017; SACS, 2019; Cole *et al.,* 2016b). The 1:50 000 geology mapsheet scale is shown in **Figure 3-1.** These changes are that Middleton Formation include both Poortjie and Hoedemaker Members, and that the Oukloof and Steenkamps Vlakte Members are now grouped under Balfour Formation. Cole *et al.* (2016b) study also involved digitising of dolerite dykes and sills from SPOT 5 imagery at a scale of 1:10 000 and mapping of structures in the area. A study done by Dhansay *et al.* (2017) focused more on the structural geology of the area.

Two dolerite dyke trends identified through mapping are E-W to WNW-ESE and NNW-SSE which both were trends identified by Woodford and Chevallier (2002b) in the Western Karoo Domain (**Figure 3-1)**. These dykes are very long, for instance, the NNW-SSE dyke at latitude 32°1’0″ S, which is approximately 29 km long within the study area but extends outside the study area boundary. Five levels of sills were mapped by Cole *et al.* (2016b) in the study area with varying thicknesses, connected via up- stepping inclined sheets such as the one observed in De Jager’s pass. Other inclined sheet outcrops include the large one south east of the study area and another near Beaufort West (**Figure 3-1)**. The dolerite sills dominate the escarpment and are topographically accentuated.

Dhansay *et al.* (2017) measured 365 fractures in and around the study area (**Table 3-1)**; these measurements were combined with fault-movement data. Eight rose

diagram plots were performed on these data and the following trends were identified: NE-SW to ENE-WSW, E-W to ESE-WNW and NW-SE to NNW-SSE (**Figure 3-8**). These structural trends are compared in this study with structures interpreted from the magnetic data.

9.2 Summary of geophysical results

The magnetic method was used to understand the rocks in the study area particularly rocks that carry magnetic minerals in them. The data was used in two ways: to delineate subsurface geological structures and to provide depth estimations for magnetic bodies. It is vital therefore to understand the wavelengths in the TMI data associated with different source depths.

9.2.1 Deep sources

The extent of deep magnetic sources was mapped using low pass filtered regional magnetic data (1 km line spacing). The Beattie and Williston Anomalies were mapped from the east coast of South Africa to the western Karoo. Lindeque *et al.* (2011) mapped the Beattie Anomalies and Scheiber-Enslin *et al.* (2014a) mapped both the Beattie and Williston Anomalies. In the study area, the Williston Anomaly was clearly identified after the 1 km spacing regional magnetic data was low-pass filtered. The rocks associated with these strong magnetic anomalies are buried approximately between 5 and 15 km below the Cape and Karoo sediments in the western Karoo (Lindeque *et al.,* 2011).

9.2.2 Shallow magnetic component

9.2.2.1 Lineament

The structural trends were mapped extensively from the higher resolution magnetic data. These trends include the following directions E-W to ESE-WSW, NNW-SSE, NW-SE, NE-SW and NNE-SSE associated with the Karoo dolerite dykes, kimberlites and fractures. The results showed that not all lineaments from remote sensing imagery

(SPOT 5) correlate well with magnetic lineaments but some lineaments were picked by both datasets (such as Tweeling-Brandwag dyke shown by a black arrow and NNW-SSE dyke intruded in the northwest corner of the study area (purple arrow, **Figure 9-1)**. The remaining shorter lineaments occurring mainly over the sills were mapped from the magnetic data.

Woodford and Chevallier (2002b) observed en-echelon segmentation on the E-W dolerite dykes in Victoria West area and similar en-echelon segmentation is observed on the E-W to ESE-WSW dolerite dykes in the study area. Based on this study, it can be concluded that the magnetic method can also map structures that are buried below sediments and the interpretations can add value to the understanding of tectonic events that have occurred in the area.

The magnetic method does, however, have limitations: Magnetic data relies on the magnetic susceptibility of the rocks. If there is no difference in magnetic susceptibility values, the method may not be able to differentiate between rock types. For instance in the study area, kimberlite dykes also intruded Karoo sediments mapped by Woodford and Chevallier (2002b) in the Victoria West area. The magnetic susceptibility of a kimberlite measured outside the study area ranged from 43 x 10^{-5} to 3267 x 10^{-5} SI and were sourced from the Council for Geoscience Petro-physical Database. The magnetic susceptibility values of a dolerite sample from the study area ranges from 19 x10^{-3} to 2138 x 10^{-3} SI and falls within the kimberlite range. The two dykes can therefore not be differentiated based on magnetic signature, but rather on the description by Woodford and Chevallier (2002b) that the dolerite dykes are irregular, single bodies and thick while the kimberlites are thin, sub-parallel with a regular pattern (**Figure 9-2**). Future work for this project could entail returning to the field area and collecting samples from one of these kimberlite dykes to make measurements on and confirm the magnetic susceptibility and whether the dykes are able to be mapped using the magnetic method.

An additional limitation is the direction of the flight line, which was in north-south orientation. Any lineaments in the north-south direction will not be detected. The flight

line spacing was 200 m, this means that narrow lineaments between the flight lines will not be easily detected such as lineaments smaller than 50 m. However, along the flight lines, 10 m wide dykes are resolvable.

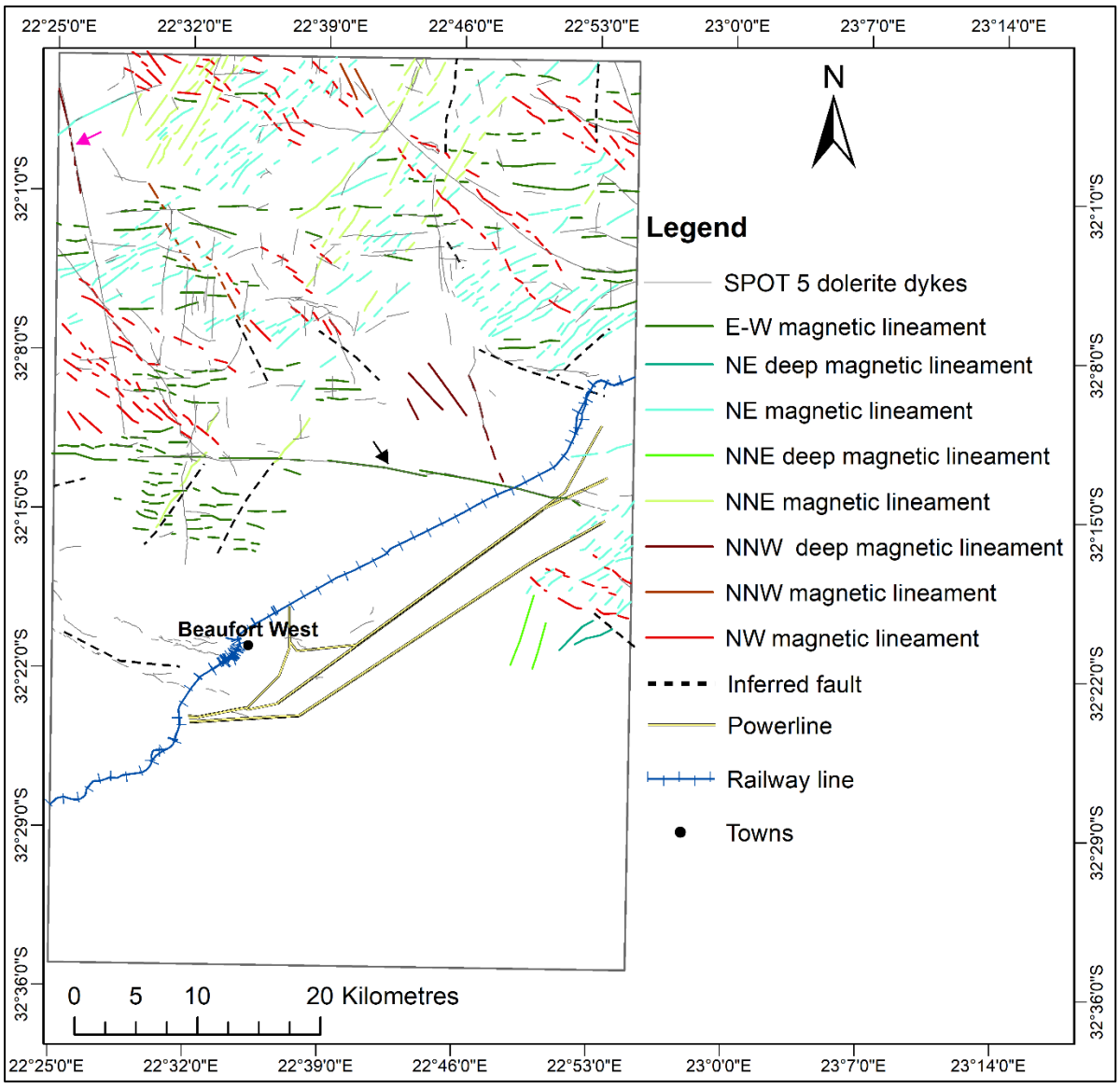

Figure 9-1 Lineament interpretation derived from first vertical derivative magnetic data overlain with SPOT 5 interpreted lineaments. Black and pink arrows show some of the lineaments that correlated well from both datasets. The remaining lineaments (shorter lines) were mapped from the magnetic data.

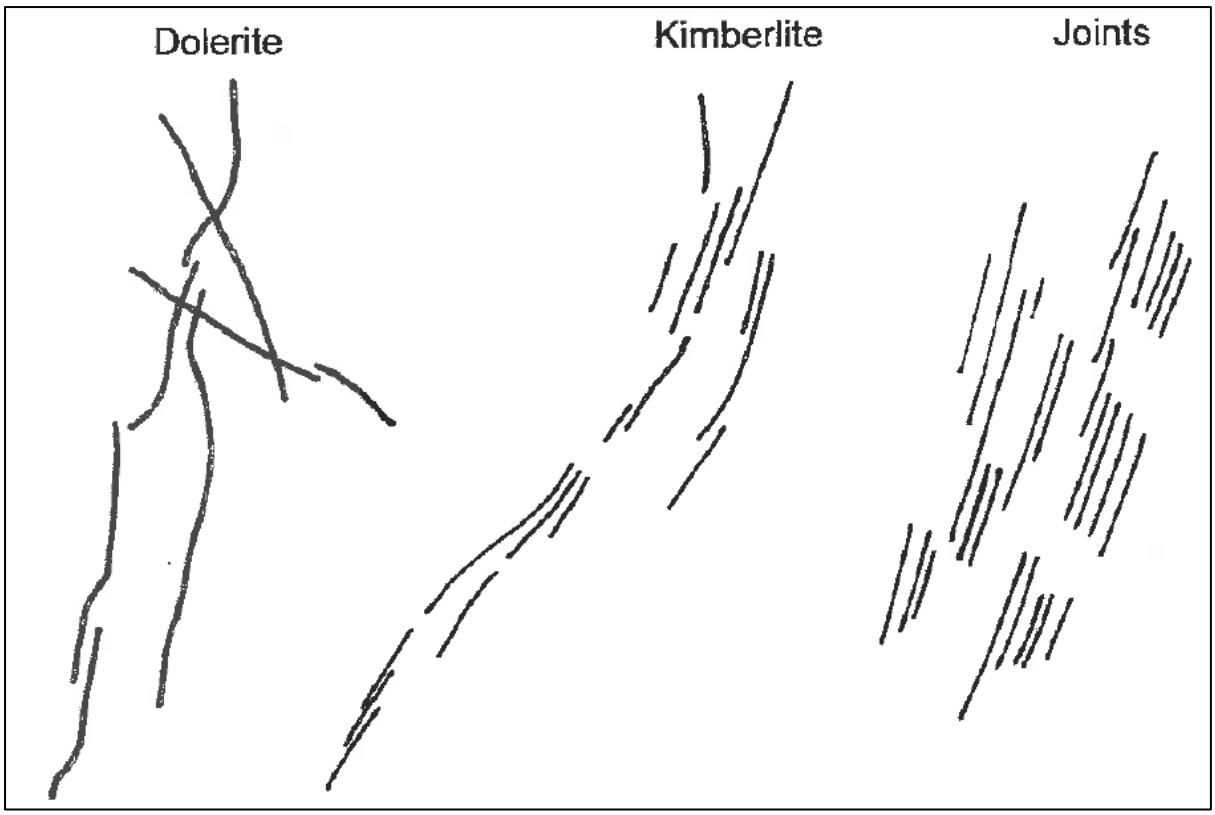

Figure 9-2 Diagram showing three major structural features in the Western Karoo Domain Woodford and Chevallier (2002b) Similar features are delineated in the study area from the airborne high-resolution magnetic data. Dolerite dykes are, in general, thick, single and irregular lineaments. Kimberlites are swarms of regular, thin, sub-parallel lineaments. Master joints are dense swarms of evenly spaced, parallel and straight fractures.

9.2.2.2 Magnetic bodies

Another component of the shallow features that were mapped using magnetic data are the Karoo dolerite sills. The sills derived from the magnetic data cover a larger area than those from SPOT 5 imagery because magnetic data also map the buried part of the sills (**Figure 9-3**). Due to resistance to weathering, the entire sill is associated with high elevations as seen on the DTM. The higher sill edges are associated with a strong magnetic signature which made it easy to delineate their boundaries.

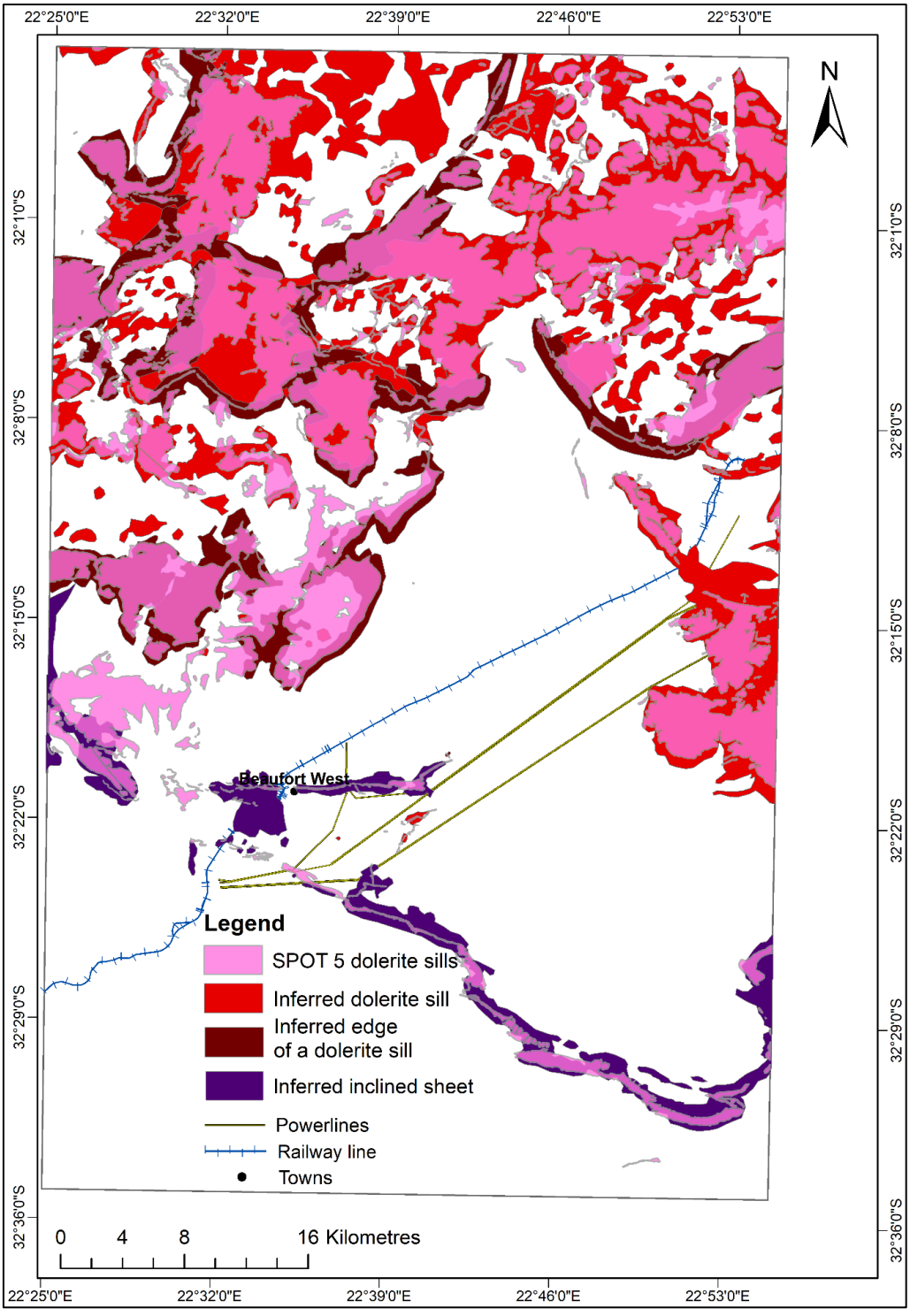

Figure 9-3 Magnetic bodies interpreted from analytic signal magnetic data overlain with SPOT 5 interpreted dolerite sills. The magnetic data allow for differentiation of individual sills, and confirm their circular to elliptical shape. The shallow subsurface extent of the sills can be mapped using magnetic data, while SPOT 5 data is limited to outcrop. The magnetic data therefore highlights the connected and extensive nature of the dolerite sills.

9.2.2.3 Depth estimation

The study area is partially located on the projected shale gas resource area (de Kock *et al.,* 2017). It is therefore important to estimate the depths to major dolerites (**Figure 9-4**). These dolerites will either have heated up surrounding shale layers, resulting in gas escape; or the fractures associated with these dolerites could have trapped and be hosting this gas (Holness *et al.,* 2016; Svensen *et al.,* 2007; de Kock *et al.,* 2017). There are deep wells drilled in the main Karoo Basin that intersected dolerite intrusions recorded by Rowsell and De Swardt (1976). However, the wells are scattered and none are located in the study area. Hence, the depth estimations from magnetic data are important.

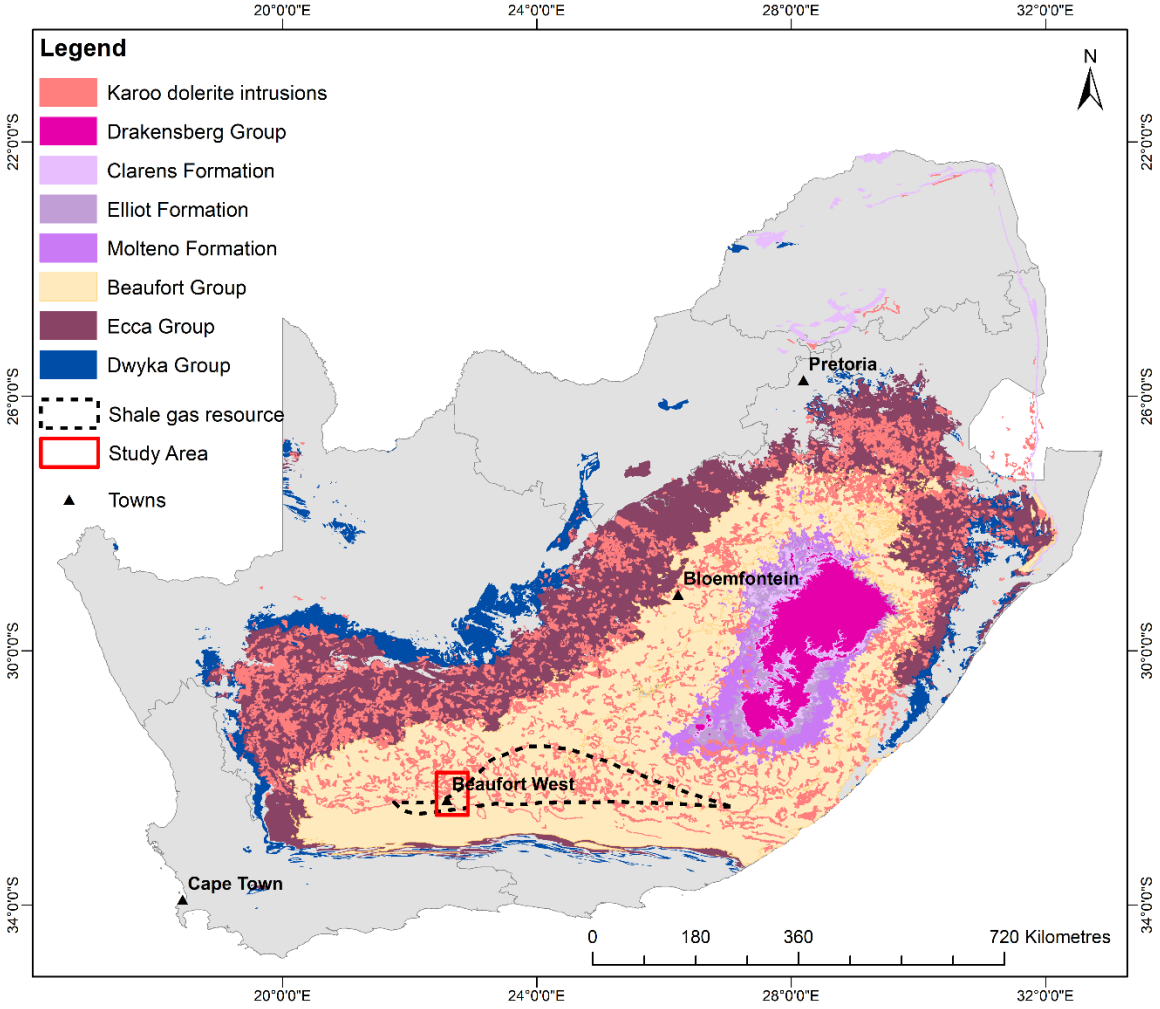

Figure 9-4 Simplified geological map showing the study area (red outline) partly located on the shale gas resource outlined by de Kock *et al.* (2017) (dotted black outline).

In the study area, the radial averaged power spectrum (RAPS) method was used to estimate the depths of magnetic sources. In the study area, depths to shallow magnetic sources are around 0.3 km. Other methods conducted in the area confirmed that dolerites are located at shallow depths, such as recently drilled boreholes. Borehole R01-BW and R02-BW intersected the Beaufort West inclined sheet at 498-508 m and 161-178 m respectively. Intermediate depths are estimated at around 1 km such as the dolerite sill connected by the inclined sheet southeast of Beaufort West (**Figure 9-3**). The depth correlates with sills mapped on magnetotelluric (MT) and seismic data. Magnetotelluric (MT) data shows a sill at just over 1 km depth (see **Figure 8-9,** Integrated Geoscience Solutions, 2018). Seismic data mapped an inner dolerite sill at approximately 1 km depth southeast of Beaufort West.

However, the power spectrum transformation method has limitations, discussed in Chapter Four (section 4.3.6) such as grid spacing, precise linear plot on the spectra, window size (Spector and Grant, 1970; Poudjom-Djomani *et al.,*1995; Ranganai, 2012). The limitation that affected the results generated using the power spectrum transformation method was the window size. The depth to low wavenumbers (related to deep anomalies) were not resolved.

9.2.2.4 2D magnetic modelling

Magnetic models are used to understand the subsurface geology in displaying the geometry (Likkason, 2014). Several anomalies were detected on the higher resolution data that were not mapped by the regional data. This higher resolution data with 200 m line spacing will only be able to detect features clearly that are larger than ¼ of the spacing, i.e., 50 m. The magnetic model was therefore generated over a survey line L3870 instead of using the gridded data as the resolution is higher. Magnetic susceptibility of dolerite samples was 0.02 SI and was used for the model. This value correlates well with the documented magnetic susceptibility of dolerite (Telford *et al.,* 1976).

The 2D magnetic model created using the high resolution TMI data over the seismic profile line BV21, lies southeast of Beaufort West. However, magnetic models are ambiguous such that multiple models can fit the same magnetic anomaly (Likkason, 2014). Therefore, the seismic data was used to constrain the magnetic model. In their study, Scheiber-Enslin *et al.* (2014b) observed that seismic data has a resolution of 70 m, features smaller than this value, as well as vertical structures, cannot be detected. The seismic data mapped the depth of the inner dolerite sill at ~1000 m below the surface, which was the main feature of interest. This sill is connected to the surface by an inclined sheet. Mapped geology was also used to constrain the model at shallow depths. Other anomalies from the model were narrow structures related to dolerite dykes and the edge of a dolerite sill.

9.3 Tectonics history and stress field based on magnetic data

9.3.1 Regional tectonics

The study conducted by Woodford and Chevallier (2002b) summarised the major tectonic evolution and stress field that occurred in southern Africa up to the beginning of the Karoo rifting phase, as shown in **Figure 2-14**.

- N-S compressional stress regime gave rise to Cape Fold Belt formation identified by E-W fold axes which are accompanied by N-S and E-W conjugate joints ca. 300 and 230 Ma (Hälbich *et al.,*1983).
- NNW faulting and jointing along pre-existing zones of crustal weakness accompanied the early stages of Gondwana break-up.
- NW compressional stress regime dominated the rifting stage and resulted in dolerite dykes intruding along an E-W shear zone and along the NNW fractures ca. 190-180 Ma Woodford and Chevallier (2002b).

9.3.2 Stress field analysis

Structural orientations from the magnetic data are shown by the rose diagrams in **Figure 9-5** and are taken from **Figure 7-3b**. These include dolerite and kimberlite dykes, texture patterns in the sills linked to fractures and faults.

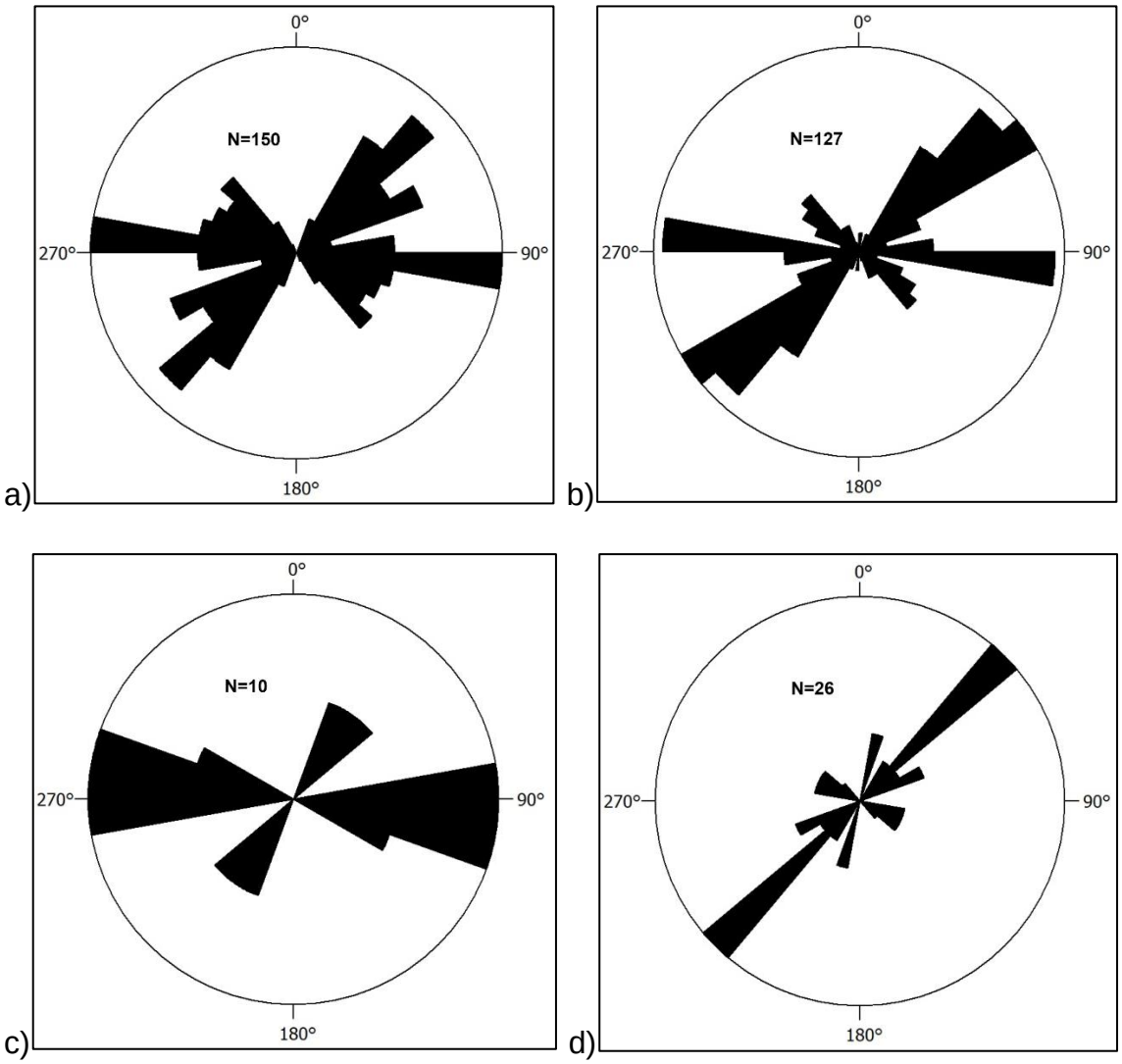

Figure 9-5 Rose diagram plots generated from magnetic lineaments mapped. (a) and (b) are from the northwest and northeast of the field area (on the escarpment). These two plots are similar to E-W to ESE-WNW and NE-SW trends. (c) shows E-W to ESE-WNW and NE-SW trends that are located at the edge of the escarpment, and (d) shows a dominant NE-SW trend. All trends are related to Karoo dolerite dykes, kimberlite dykes and fractures and faults.

9.3.2.1 N-S compressional stress regime

The N-S compression stress field is regarded as the dominant stress field that existed and gave rise to Cape Fold Belt formation (**Figure 9-6**). Existence of N-S compression in evident in the main Karoo Basin and in the study area through fold axis or hinges observed with listric thrusts south of Beaufort West around latitude 32˚30'0″ S (Woodford and Chevallier, 2002a). The N-S compression also resulted in an east-west fold axis south of the escarpment into which the E-W trending Tweeling-Brandwag dyke later intruded (shown by black arrow on **Figure 9-1**) (Campbell, 1975). Therefore, pre-existing structures in this orientation may have been re-activated and opened during the NW compressional stress regime.

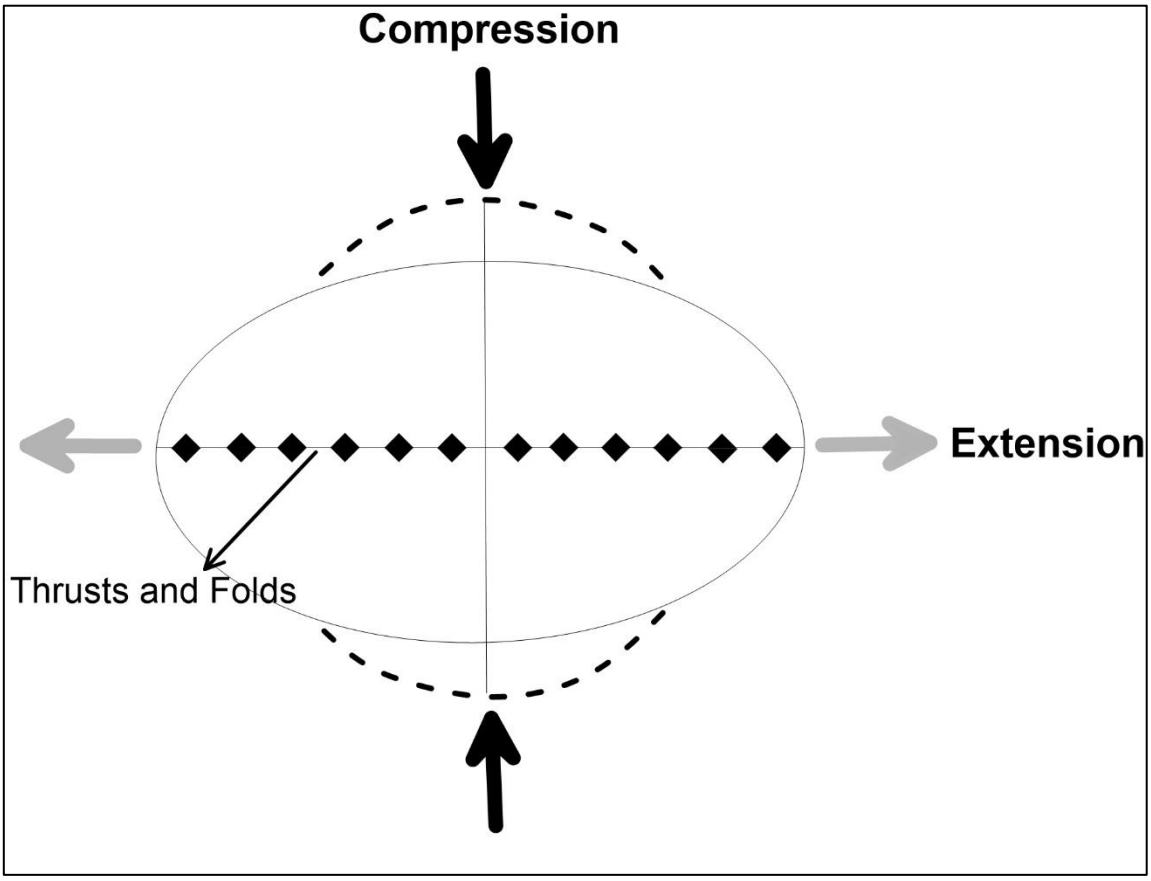

Figure 9-6 A N-S compressional stress regime resulted in structural features in the study area such as fold axis/hinges and thrusts (Cape Fold Belt). This stress regime dominated during the Late Palaeozoic time.

9.3.2.2 NW compressional stress regime

Woodford and Chevallier (2002b) identified an E-W dextral shear zone in the southern Karoo Basin based on dolerite dyke orientations (**Figure 2-12** and **2-13**). This shear zone is thought to be the result of a NW-SE compressional and NE-SW extensional stress field that initiated the rifting phase of Gondwana break-up (**Figure 9-7**). In the NW compressional stress field, principal displacement would occur in the E-W direction, and be dextral i.e., simple shear deformation with transtension.

NNW trending dykes are observed on the magnetic data. They are cut by younger structures, as seen in an example located in the northwest corner of the study area where a NE-SW dolerite dyke is observed cutting through the NNW dolerite dyke (shown by pink arrow on **Figure 9-1**). There is a correlation of these dykes to those mapped by SPOT 5 imagery. These dykes were more prominent outside the study area observed from regional airborne magnetic data (1 km line spacing) covering the whole of South Africa. Another observation from the magnetic data was that the edges of the Karoo dolerite sills seem to align NW (**Figure 9-3**).

Faults from both magnetic data and Dhansay *et al.* (2017) were trending NE-SW and NW-SE. These faults could be related to the NW Riedel shears and NE P fractures and some of the dolerites were mapped along these orientations from the magnetic data. Riedel shear and conjugate Riedel shears (R') are associated with the principal displacement zone (**Figure 9-7**). Both Riedel shears and P fractures are present in the Western Karoo Basin (Woodford and Chevallier, 2002b).

Based on the rose diagram plots in **Figure 9-5**a-b, a schematic diagram of a simple shear system **(Figure 9-7)** was generated and correlates with the stress field during the rifting phase of Gondwanaland break-up ca. 190-180 Ma.

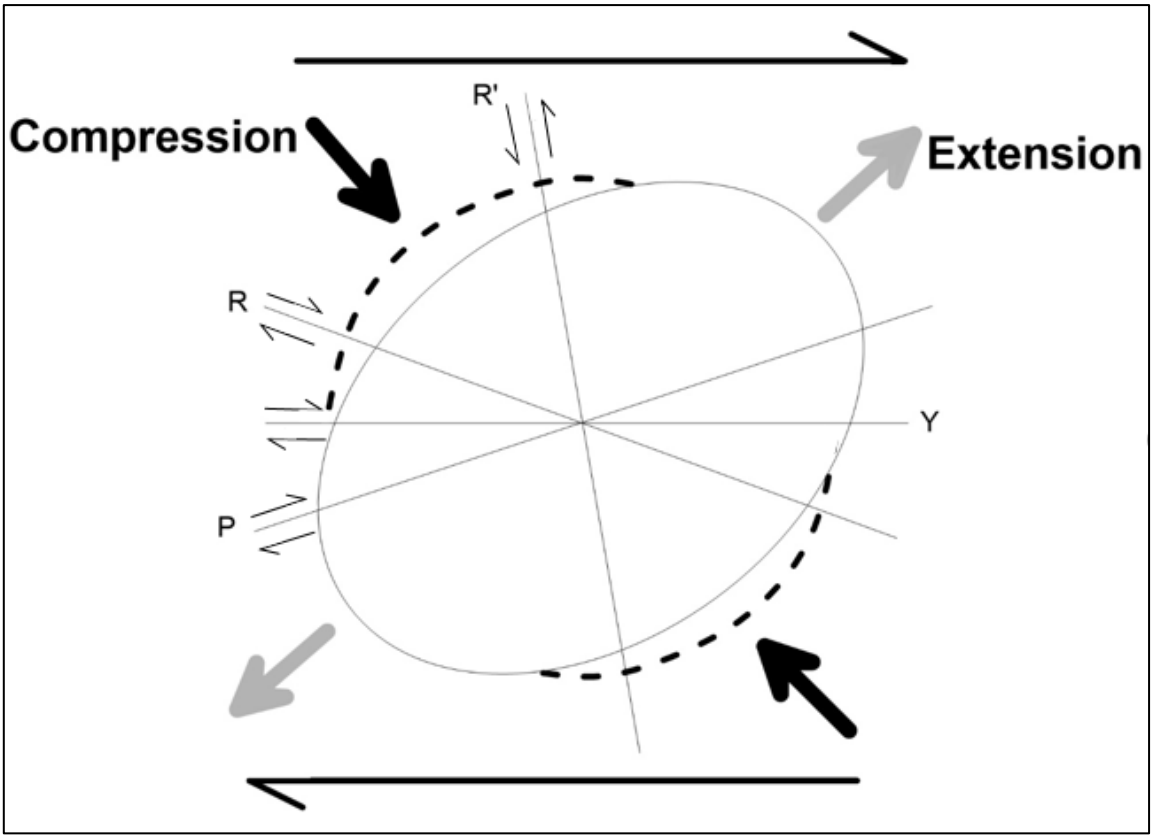

Figure 9-7 The stress regime that dominated in Southern Africa during the Jurassic, when the dolerite emplacement took place. A NW compressional stress regime resulted in majority of structural features e.g. dolerite dykes and texture within dolerite sills in the study area being oriented NW.

9.3.2.3 NE-SW linear features

NE-SW to NNE-SSW linear features are presumed to be related to dolerite dykes, kimberlite dykes and master joints. In Loxton town northeast of the study area, NE-SW dolerite dykes are reported and one of these dykes was drilled into for groundwater exploration (Woodford and Chevallier, 2002b). The dolerite dykes in this orientation may not be related to any of the historic major tectonic stress regimes that existed in the area discussed above because (1) NE-SW orientation is orthogonal to the NW sigma 1 (σ_1) direction that dominated during Gondwana break-up, and fractures in this orientation are mainly closed for a NW compressional stress regime (Woodford and Chevallier, 2000) and (2) the NE-SW orientation isn't related to the dominant N-S compressional stress regime that gave rise to the Cape Fold Belt.

The NE-SW to NNE-SSW dolerite dykes could be possible if σ_1 was ENE to WSW to E-W sinistral strike-slip deformation but there is no evidence that suggests σ_1 is in this direction in the study area, even though Tankard *et al.* (2009) suggested sinistral strike-slip deformation further south of the study area approximately 250 Ma.

NE-SW kimberlite dykes are seen north and northeast of the study area (such as in Loxton town). Kimberlite dykes intruded along pre-existing structures and are post-Karoo events because they intruded between the Upper Jurassic to the Upper Cretaceous with associated master-jointing. In the study area, predominant NNE trend associated with kimberlites is observed and suggests that a principal extensional stress (σ_1) was NNE-SSW direction. Kimberlite age data in Victoria West cluster located north of the study area are summarised in **Table 9-1.** Woodford and Chevallier (2002b) suggested that early kimberlite fissures intruded coeval to the dolerite dykes and NNW structures were reactivated. Jelsma *et al.* (2008) suggest that kimberlites are also linked with Gondwana break-up (and may have contributed to shale gas release).

Table 9-1. Kimberlite ages for Victoria West cluster north of the study area.

Kimberlite ages				
Latitude	**Longitude**	**Orientation**	**Age (Ma)**	**Sourced**
-31.2650	22.5600	NNE	74	Smith *et al.,* 1994
-31. 0342	22.5394	NNW	82	Moore *et al.,* 2008
-31.1017	22.7156	NNW	103	Smith *et al.,* 1994
-31.6472	22.2697	N-S	174	Smith *et al.,* 1994
-31.5019	22.7397	N-S	143	Smith *et al.,* 1994

9.4 Application of results

The results from the study can be applied to both shale gas and groundwater investigations.

9.4.1 Shale gas resource

Depending on how far the sills are from the potential source of shale gas, the sill can affect and 'burn off' the gas. Magma intrudes at temperatures of about 1200 °C while the highest temperature the gas could withstand is about 250 °C. Thus, above these temperatures, the gas will be 'burnt off' (Cawthorn, 2015). The surrounding rocks that lie within half the thickness of the dolerite sill will be affected (Maré, 2015). If the shale gas layer is in the vicinity of a thick sill, the gas will be removed. Therefore, it is important to map the location of the sills within the shale gas resource, using data such as magnetic data. The magnetic data revealed that the sills are extensive in the subsurface while SPOT 5 imagery mapped the outcropping part of the sills.

Beaufort West lies on an E-W oriented dolerite sill. The recently drilled boreholes discussed in Chapter Three (**Figure 3-1)** immediately north of Beaufort West revealed that the dolerites are thin (approximately less than 20 m) and intruded into the Abrahamskraal Formation. Also, the inclined sheet south of Beaufort West where the 2D magnetic model was generated also recorded thicknesses of less than 10 m. Therefore, if dolerite sills intruded proximal to Whitehill Formation in this area, then approximately 10 m of shale will be affected.

The magnetic method, however, is unable to resolve sill thickness at the depth of the Whitehill Formation, or resolve multiple sills compared to one thick sill. Other datasets such as boreholes and seismic surveys are needed to resolve the sill and inclined sheet geometry at such depth. The benefit of the magnetic method is mapping the shallow geometry of the dolerites which will help planning during fracking operations. This planning would help avoid any problems when the fractures associated with the dolerites are intersected during drilling. These problems can include leakage of gas out if well casing fails, and movement of the gas along these fractures. These fractures

can also host gas that has been “burnt off” of the shale layer and migrated into these fractures and been trapped in a stratigraphic or structural trap. Mapping the dolerites would allow for the identification of these traps.

9.4.2 Groundwater

The study area has water shortages and the Karoo dolerites dykes are normally targeted for groundwater because the country rock is usually fractured closer to dolerite dykes contact, which increases the permeability of the country rock (Enslin, 1950). Enslin (1950) suggested that dolerite dykes are vertically jointed and fractured closer to their contacts at depth and high yields can be expected. Woodford and Chevallier (2002b) suggested the E-W lineaments gave high yields during drilling conducted on different sites in the Western Karoo Domain. Moderate to low yields were found on other lineament orientations (NNW, NW, NE and NNE) in the same study. The linear features delineated from the magnetic data can be used to locate new structures hosting groundwater.

9.5 Conclusion

The main Karoo Basin hosts rocks of the Karoo Supergroup. A common tectonic model suggests that the main Karoo Basin represents a retro-arc foreland basin that is located north of the magmatic arc associated with the north-directed subduction (Catuneanu *et al.,* 1998).

The Jurassic aged dolerite dykes and sills are linked to the Karoo Large Igneous Province (KLIP) that intruded into the Karoo stratigraphy mainly in the Upper Ecca and Beaufort Groups. The dolerite intrusion is sometimes buried under thick sediments, making it challenging to accurately delineate them from surface outcrops. The Karoo Basin is recognised as shale gas source because it hosts the appropriate shale gas rock formations.

The study is partly located on the projected shale gas resource. Previous studies suggest that dolerites will either have heated up surrounding shale layers, resulting in

gas escape or fractures associated with the dolerites may have trapped and are hosting the gas (Holness *et al.,* 2016; de Kock *et al.,* 2017; Svensen *et al.,* 2007). Therefore, mapping the location of the dolerite material is crucial. Equally, Karoo dolerite dykes are usually targeted during groundwater exploration and information inferred from this study can be useful to locate good groundwater targets.

Magnetic linear features, magnetic bodies, depth estimations, 2D forward magnetic model and stress field analysis were carried out using magnetic data. Five linear features generated from the magnetic data: E-W to ESE-WSW, NNW-SSE, NW-SE, NE-SW and NNE-SSE associated with the Karoo dolerite dykes, kimberlites, fractures. In the study area, there was no magnetic susceptibility contrast between the Karoo dolerite dykes and kimberlite dykes so dolerite dykes were identified assuming they have an irregular pattern, and are usually single bodies and very long (Woodford and Chevallier, 2002b). The buried part of the dolerite sills were mapped from the magnetic data and SPOT 5 imagery mapped the dolerite outcrops.

Deeper magnetic sources associated with to the Beattie Magnetic and Williston Anomalies associated with the Natal Mobile Belt were mapped using low pass magnetic filters. Power spectrum transformation was used to estimate the depth of the magnetic sources particularly shallow sources related to the dolerites. The depth estimations revealed that the dolerites dominate depths of 0.3 km. However, some of the dolerites were mapped at depths over 1 km such as the dolerite sill connected by the inclined sheet southeast of Beaufort West through the use of seismic and magnetotelluric data. A 2D forward magnetic model was created over the flight line where seismic profile BV21 is located. The limitation of the magnetic data, however, is that it can only be used to map deeper sills if other data like seismic and borehole data are available to help constrain it. Otherwise, the benefit of the magnetic method is mapping the shallow dolerite geometry to aid with safe fracking operations, and for finding gas that has migrated and been trapped.

Rose diagram plots plotted from the magnetic data and rose diagram plots generated by Dhansay *et al.* (2017) have similar trends. The trends from magnetic data were

used to determine the regional tectonics using stress and strain analysis. The stress field analysis in the area correlated with the tectonic evolution and stress field proposed by Woodford and Chevallier (2002b) up to Karoo rifting phase in southern Africa.

The interpretations inferred from the magnetic data shows the importance of aeromagnetic surveys for the mapping of anomalous subsurface rocks. Interpretations from aeromagnetic surveys should be included in tectonic history interpretations because they are usually associated with regional trends.

10 REFERENCES

AeroPhysX. (2017) Council for Geoscience Karoo Magnetic and Radiometric Field Survey Final Report. 1-37.

AGICO. (2018a) JR-6A/JR-6 Spinner magnetometer for measurements of remanent magnetization. AGICO Inc. Advance Geoscience Instruments Company, Czech Republic. 1–46. https://www.agico.com/downloads/documents/manuals/jr6-man.pdf (2 April 2019).

AGICO. (2018) SAFYR7 Kappabridge Control Software User Manual. AGICO Inc. Advance Geoscience Instruments Company, Czech Republic. 1–85. https://www.agico.com/downloads/documents/manuals/safyr7-man.pdf (2 April 2019).

AGICO. Multi-function kappabridges magnetic susceptibility- anisotropy systems. AGICO Inc. Advanced Geoscience Instruments Company, Czech Republic: 1–2. http://paleomag-ifz.ru/sites/default/files/docs/mfk1.pdf (2 April 2019).

Allen, R.L. and Mills, D.W. (2004) Signal Analysis, Time, Frequency, Scale, and Structure. United States of America: Institute of Electrical and Electronics Engineers, Inc. 1-407.

Angielczyk, K. D., Steyer, J., Sidor, C. A., Smith, R. M. H., Whatley, R. L and Tolan, S. (2014) Permian and Triassic Dicynodont (Therapsida: Anomodontia) faunas of Luangwa Basin, Zambia: Taxanomic Update and Implication for Dicynodont Biogeography and Biostratigraphy. In: Kammerer, C. F., Angielczyk, K. D. and Fröbisch, J. eds. Early Evolutionary History of the Synapsida. Springer International Publishing: 93-138.

Bamford, M.K. (2016) Fossil Woods from the Upper Carboniferous 16 to Lower Jurassic Karoo Basin and Their Environmental Interpretation. In: de Wit, M. J. and Linol B. eds. Origin and Evolution of the Cape Mountains and Karoo Basin. Springer International Publishing: 159–167.

Bhattacharyya, B.K. (1966) Continuous spectrum of the total magnetic Field anomaly due to the rectangular prismatic body. Geophysics, 31(1), 97–121.

Booth, P.W.K. and Goedhart, M.L. (2004). Thrust faulting in the northernmost foreland zone of the Cape Fold Belt, Fort Beaufort, Eastern Cape, South Africa. South African Journal of Geology, 117: 301–315.

Booth, P.W.K. (2009) A review of the structural geology of the Cape Fold Belt and challenges towards future research. In Swaziland Geophysical Association 11th SAGA Biennial Technical Meeting and Exhibition: 481–485.

Botha, J. F. and Cloot, A.H. (2004) Karoo Aquifers-Deformations, Hydraulic and Mechanical Properties. In Water Research Council Report 936/1/04. http://www.wrc.org.za.

Brandt, M. and Saunders, I. (2011) New regional moment tensors in South Africa. Seismology Research Letters, 82: 69–80.

Campbell, G.D.M. (1975) Groundwater Investigation at Beaufort West. Technical Report Gh3235. Directorate: Geohydrology, Department Water Affairs and Forestry, Pretoria.

Cartwright, J. and Hansen, D.M. (2006) Magma transport through the crust via interconnected sill complexes. Geology, 34 (11): 929–932.

Catuneanu, O., Hancox, J., Cairncross, B. and Rubidge, B.S. (2002) Foredeep submarine fans and forebulge deltas: orogenic off-loading in the underfilled Karoo

Basin. Journal of African Earth Sciences, 35: 489–502.
Catuneanu, O. (2004) Basement control on flexural profiles and the distribution of foreland facies : The Dwyka Group of the Karoo Basin , South Africa. Geological Society of America, 32(6): 517–520.
Catuneanu, O., Hancox, P.J. and Rubidge, B.S. (1998) Reciprocal flexural behaviour and contrasting stratigraphies: a new basin development model for the Karoo retroarc foreland system, South Africa. Basin Research, 10: 417–439.
Catuneanu, O., Wopfner, H., Eriksson, P.G., Cairncross, B., Rubidge, B.S., Smith, R.M.H. and Hancox, P.J. (2005) The Karoo basins of south-central Africa. Journal of African Earth Sciences, 43(1–3): 211–253.
Cawthorn, G. (2015) Unpacking the secrets of South Africa's dolerite sills. The Conversation Africa, Inc. https://theconversation.com/unpacking-the-secrets-of-south-africas-dolerite-sills-43123 (03 March 2021).
Chevalier, L., Gibson, L.A., Nhleko, O.L., Woodford, A.C., Nomquphu, W., and Kippie, I. (2004) Hydrogeology of fractured-rock Aquifers and related ecosystems within the Qoqodala dolerite ring and sill complex, Great Kei catchment, Eastern Cape. In Water Research Commission, Report. 1238/1/04. 1-126
Chevallier, L., Goedhart, M. and Woodford, A.C. (2001) Influence of dolerite ring-structures on the occurrence of groundwater in Karoo Fractured Aquifers: a morpho-tectonic approach. In Water Research Commission, Report 937/1/01. 1-146.
Chevallier, L and Woodford, A. (1999) Morpho-tectonics and mechanism of emplacement of the dolerite rings and sills of the Western Karoo. South African Journal of Geology, 102 (1): 13-54.
Cole, D. I., Johnson, M. R. and Day, M.O. (2016a) Lithostratigraphy of the Abrahamskraal Formation (Karoo Supergroup), South Africa. Geological Society of South Africa, 119: 415–424.
Cole, D.I., Mosavel, H., Browning, C., Chevallier, L., Mitha, V. Dhansay, T., Musekiwa, C., and Maya, M. (2016b) Environmental baseline modelling and observed changes during drilling of a deep stratigraphic borehole in the Karoo: Results of a geological investigation around Beaufort West. In Council for Geoscience Report 2016-0093. 1-61.
Cole, D.I. and McLachlan, I.R. (1994) Oil shale potential and depositional environment of the Whitehill Formation in the main Karoo Basin. Publication (unedited), Geological Survey of South Africa, Library book no 553283COL (Volume I Text; Volume II Tables and Appendixes) In Council for Geoscience Report 1994-0213.
Cole, D.I and Wipplinger, P. (2001) Sedimentology and molybdenum potential of the Beaufort in the main Karoo Basin, South Africa. Memoir, Council for Geoscience, South Africa, 80, 225.
Cole, J. and Maré, L.P. (2004) A Geophysical investigation of the regional potential field data over the south eastern limb of the Bushveld Complex. Pretoria.
Cole, D.I. (1992) Evolution and development of the Karoo Basin. In: De Wit, M.J and Ransome, I. G. D. eds. Inversion Tectonics of the Cape Fold Belt, Karoo and Cretaceous Basins of Southern Africa. Rotterdam: Balkema: 87–99.
Cooper, G.R.J. (2003) Feature detection using sun shading. Computers and Geosciences, 29: 941–948.
Cooper, G.R.J. (1997) Forward modeling of magnetic data. Computers and Geosciences, 23(10): 1125–1129.
Day, M.O. and Rubidge, B.S. (2014) A brief lithostratigraphic review of the Abrahamskraal and Koonap formations of the Beaufort Group, South Africa:

Towards a basin-wide stratigraphic scheme for the Middle Permian Karoo. Journal of African Earth Sciences, 100: 227–242.
De Beer, C.H. (1992) Structural evolution of the Cape fold belt syntaxis and its influence on syntectonic sedimentation in the SW Karoo Basin. In: De Wit M. J. and Ransome, I. G. D. eds. Inversion Tectonics of the Cape Fold Belt, and Karoo and Cretaceous Basins of Southern Africa. Rotterdam: Balkema: 197–206.

De la Rue Winter, H. and Venter, J.J. (1970) Lithostratigraphic correlation of recent deep boreholes in the Karoo - Cape sequence. In Proceedings of the 1970 Gondwana Symposium. 395–408.
De Kock, M. O., Beukes, N. J., Adeniyi, E.O., Cole, D., Götz, A.E., Geel, C. and Ossa, F. (2017) Deflating the shale gas potential of South Africa's main Karoo Basin. South African Journal of Science, 113 (9): 1–12.

Dhansay, T. (2018a) On the evolution and mechanics of the brittle upper crust below South Africa: Implications toward the sustainable transformation of exploration/exploitation in the Earth's Critical Zone. Nelson Mandela University.
Dhansay, T. (2018b) Structural mapping assists in targeting groundwater aquifers. Council for Geoscience *GEOclips*: 3. https://www.geoscience.org.za/images/GeoClips/CGS2018-Geoclips-Vol52.pdf.
Dhansay, T., Navabpour, P., de Wit, M. and Ustaszewski, K. (2017) Journal of African Earth Sciences Assessing the reactivation potential of pre-existing fractures in the southern Karoo, South Africa : Evaluating the potential for sustainable exploration across its Critical Zone. Journal of African Earth Sciences, 134: 504–515.
Dickinson, W.R. (1974) Plate tectonics and sedimentation. In: Dickinson, W. R. ed. Tectonics and Sedimentation. Special Publication Geological Society of South Africa: 1–27.
Duncan, A.R. and Marsh, J.S. (2006). The Karoo Igneous Province. In: Johnson, M. R., Anhaeusser, A. C. R. and Thomas, R. J. eds. Geology of South Africa. Johannesburg/Pretoria: Geological Society of South Africa and Council for Geoscience: 501–519.
Du Toit, A.L. (1920). The Karoo Dolerites- a study in Hypabyssal Intrusion. Transactions Geological Society of South Africa, 23: 1–42.

Eales, H.V., Marsh, J.S. and Cox, K.G. (1984). The Karoo igneous province: an introduction. Special Publication 13, Geological Society of South Africa, 13: 1–26.
Eglington, B.M. and Armstrong, R.A. (2003). Geochronological and isotopic constraints on the Mesoproterozoic Namaqua – Natal Belt : evidence from deep borehole intersections in South Africa. Precambrian Research, 125: 179–189.
Enkin, R.J., Cowan, D., Tigner, J., Severide, A., Gilmour, D., Tkachyk, A., Kilduff, M. and Baker, J. (2012) Physical property measurements at the GSC paleomagnetism and petrophysics laboratory, including Electric Impedance Spectrum methodology and analysis. Geological Survey of Canada: 38.
Enslin, J.F. (1950) Geophysical methods of tracing and determining contacts of dolerite dykes in Karoo sediments in connection with the siting of boreholes for water. Transactions Geological Society of South Africa, 53: 193–204.
Fatti, L. and Du Toit, J.J.L. (1970) A regional reflection-seismic line in the Karoo basin near Beaufort West. Geological Society of South Africa - Transactions and Proceedings, 73: 17–28.
Fatti, L. (1987) Reflection Seismic Surveys in the Karoo Basin by Soekor. In South

Africal Geophysics Association (SAGA) Yearbook. 22–30.
Fatti, L. (1970) The use of seismic reflection techniques in the Karoo Basin, MSc. University of the Witwatersrand. South Africa, Johannesburg.
Frankel, J.J. and Kent, L.E. (1948) Intrusion of glass in dolerite. Transactions Geological Society of South Africa, 51.
Galerne, C. (2009) Emplacement Mechanisms and Magmatic Differentiation Induced by Magma Flow in Sill Intrusions in Sedimentary Basins, PHD, University of Oslo.
Grant, F. S. and Dodds, J. (1972) MAGMAP FFT processing system development notes. Paterson, Grant and Watson Limited.
Gunn, P.J and Dentith, M.C. (1997a) Magnetic responses associated with mineral deposits. AGSO Journal of Australian Geology and Geophysics, 17(2): 145–158.
Gunn, P.J., Maidment, D.E. and Milligan, P.R. (1997b) Interpreting aeromagnetic data in areas of limited outcrop. AGSO Journal of Austrlian Geology and Geophysics, 17(2): 175–185.
Hälbich, I.W., Fitch, F.J. and Miller, J.A. (1983) Dating the Cape orogeny. In Söhnge, A. P. G. and Hälbich, I.W. eds. Geodynamics of the Cape Fold Belt. Geological Society of South Africa Special Publication: 149–164.
Hansen, D. M., Cartwright, J. A. and Thomas, D. (2004) 3D Seismic Analysis of the Geometry of Igneous Sills and Sill Junction Relationships. Geological society of London, Memoirs, 29: 199–209.
Heidbach, O., Rajabi, M., Reiter, K., Ziegler, M. and W.T. (2016) World Stress Map Database Release 2016. GFZ Data Services. https://doi.org/10.5880/WSM.2016.001
Holness, S., Driver, A., Todd, S., Snaddon, K., Hamer, M., Skowno, A., Daniels, R.D., Bragg, C., Alexander, G., Bazelet, C., Bills, R., Branch, B., Coetzer, W., Conradie, W., Edge, D., Lyle, R., Mansell, M., Mecenero, S., Mlambo, M., Simaika, J., Staude, H., Underhill, L., Brittingham, M., Esler, K., Hoffman, T. and Dean, S. (2016) Shale Gas Development in the Central Karoo: A Scientific Assessment of the Positive and Negative Consequences. Summary for policy makers (SPM), Council for Scientific and Industrial Research (CSIR) Research Space. 1-47.
Hoover, D.B., Klein, D.P. and Campbell, D.C. (1993) Geophysical methods in exploration and mineral environmental investigations. In: du Bray, E. A. ed. Preliminary compilation of descriptive geoenvironmental mineral deposit models. United States Geological Society, Preliminary Report 95-831, 19–27.
Horn, B.K.P. (1982) Hill shading and the reflectance map. Geo-Processing, 2: 65–146.
Hrouda, F., Chlupáčová, M and Chadima, M. (2009) The use of magnetic susceptibility of rocks in geological exploration. Terraplus Geophysical Equipment Supplier, Brno, Czech Republic. 1-27.
Integrated Geoscience Solutions. (2018) Magneto-telluric baseline study in the Ceres and Beaufort West Areas. Report for the Council of Geoscience 1-31.
Isles, D.J. and Rankin, L.R. (2013) Geological Interpretation of Aeromagnetic Data. The Australian Society of Exploration Geophysicists. CSIRO Publishing, Collingwood, Australia. 4, 35.
Jelsma, H., Barnett, W., Richards, S. and Lister, G. (2008) Tectonic setting of kimberlites. In 9th International Kimberlite Conference: Extended Abstracts, 9. https://doi.org/10.29173/ikc3298
Johnson, M.R., van Vuuren, C.J., Hegenberger, W.F., Key, R. and Shoko, U. (1996) Stratigraphy of the Karoo Supergroup in southern Africa: an overview. Journal of African Earth Sciences, 23(1): 3–15.
Johnson, M.R., van Vuuren, C.J., Visser, J.N.J., Cole, D.I., de V. Wickens, H., Christie,

A.D.M., Roberts, D.L. and Brandl, G. (2006) Sedimentary rocks of the Karoo Supergroup. In: Johnson, M. R., Anhaeusser, A. C. R. and Thomas, R. J. eds. Geology of South Africa. Johannesburg/Pretoria: Geological Society of South Africa and Council for Geoscience: 461–499.

Johnson, A. and Macleod, I. (2016) Using Power Spectra for Potential Field Data Interpretation : Challenges and cautions. Journal of Geophysics, 37: 187–190.

Johnson, M.R. (1991) Sandstone petrography, provenance and plate tectonic setting in Gondwana context of the southeastern Cape-Karoo Basin. South African Journal of Geology, 94(2/3): 137–154.

Johnston, S.T. (2000) The Cape fold belt and syntaxis and the rotated Falkland Islands: dextral transpressional tectonics along the southwest margin of Gondwana. Journal of African Earth Sciences, 31: 51–63.

JR-6A. (2018) Spinner magnetometer for measurements of remanent magnetization. User Manual, version 3.1. AGICO

Khalil, A., Hafeez, T. H., Saleh, H.S. and Mohamed, W.H. (2016) Inferring the subsurface basement depth and the structural trends as deduced from aeromagnetic data at West Beni Suef area, Western Desert, Egypt. NRIAG Journal of Astronomy and Geophysics, 5(2): 380–392.

Kuuskraa, V., Stevens, S., Van Leeuwen, T. and Moodhe, K. (2011) World Shale Gas Resources : An Initial Assessment of 14 Regions Outside the United States. Advanced Resources International, Inc. Arlington,Washington, DC. https://www.eia.gov/analysis/studies/worldshalegas.

Lanci, L., Tohver, E., Wilson, A. and Flint, S. (2013) Upper Permian magnetic stratigraphy of the lower Beaufort Group, Karoo Basin. Earth and Planetary Science Letters, 375: 123–134.

Li, X. (2006) Understanding 3D analytic signal amplitude. Geophysics, 71(2): 13. https://doi.org/10.1190/1.2184367.

Likkason, O.K. (2014) Exploring and Using the Magnetic Methods. In: Marghany, M. ed. Advanced Geoscience Remote Sensing However. 142-174. http://dx.doi.org/10.5772/571631.

Lin, W., Tadai, O., Takahashi, M., Sato, D., Hirose, T., Tanikawa, W., Hamada, Y. and Hatakeda, K. (2015) An Experimental Study on Measurement Methods of Bulk Density and Porosity of Rock Samples. Journal of Geoscience and Environment Protection, 3(5): 72–79.

Lindeque, A., De Wit, M.J., Ryberg, T., Weber, M. and Chevallier, L. (2011) Deep crustal profile across the Southern Karoo basin and beattie magnetic anomaly, South Africa: An integrated interpretation with tectonic implications. South African Journal of Geology, 114(3–4): 265–292.

Lock, B.E. (1980) Flat-plate subduction and the Cape Fold Belt of South Africa. Geology, 8: 35–39.

Luyendyk, A.P.J. (1997) Processing of airborne magnetic data. AGSO Journal of Australian Geology and Geophysics, 17(2): 31–38.

MacLeod, I. N., Jones, K. and Dai, T.F. (1993) 3-D analytic signal in the interpretation of Total magnetic field data at low magnetic latitudes. Exploration Geophysics, 24(4): 679–688.

Maré, L.P. (2015) Geothermal history of the Karoo Basin in South Africa. Inferred from magnetic studies. PHD. University of Johannesburg. South Africa. 1-266.

Mariita, N.O. (2007) The Magnetic Method. In Surface Exploration for Geothermal Resources by UNU-GTP and KenGen. 1–8.

Marsh, J.S. and Mndaweni, M.J. (1998) Geochemical variations in a long karoo dyke,

Eastern Cape. South African Journal of Geology, 101: 119–123.
Marsh, G. (1991) Inaugural field trip to the Northern Cape. The volcanology Group of the Mineralogical Association of South Africa, 11 - 13 October 1991. Guide book. Rhode University, Grahamstown.
Moorcroft, D. and Tonnelier, N. (2016) Contact Metamorphism of Black Shales 8 in the Thermal Aureole of a Dolerite Sill Within the Karoo Basin. In: Linol, B. and de Wit, M. J. eds. Origin and Evolution of the Cape Mountains and Karoo Basin. Springer International Publishing: 75–83.
Moore, A., Blenkinsop, T. and Cotterill, F. (2008) Controls on post-Gondwana alkaline volcanism in Southern Africa. Earth and Planetary Science Letters., 268: 151–164.
Muedi, T.T. (2019) Early Jurassic dolerites of the Karoo Large Igneous Province (KLIP): an analysis of their age and emplacement history from sea level to the Drakensberg Mountains in the Eastern Cape Cape, South Africa. PHD, Nelson Mandela University.
Nengovhela, V., de Wit, M.J., Butcher, I.R. and Honse, E. (2016) High-Resolution Petrographical and Chemical Scanning of Karoo Sedimentary Rocks Near Dolerite Sill Contacts Reveals Metamorphic Effects on Shale Porosity. In: Linol, B. and de Wit, M. J. eds. Origin and Evolution of the Cape Mountains and Karoo Basin. Springer International Publishing: 67–74.
Nengovhela, V. (2018) Petrophysical analysis of thermo-tectonic effects linked to Lower Jurassic dolerite intrusions in sedimentary rocks of the Main Karoo Basin, with implications for shale gas development in South Africa. MSc, Nelson Mandela University.
Newton, A. R., Shone, R. W. and Booth, P.W.K. (2006) The Cape Fold Belt. In: Johnson, M. R., Anhaeusser, A. C. and Thomas, R. J. eds. Geology of South Africa. Johannesburg/Council for Geoscience: Geological Society of South Africa: 521–526.
Nxokwana, N., Cole, D., Mosavel, H., Mahlatji, M., Lenong, S. and Ngobeni, D. (2018) The Karoo Deep Drilling Programme : 2018-19 Q1 and Q2 Quarterly Report. In Council for Geoscience Report 2018-0140. Pretoria.
Paananen, M. (2004) Petrophysical Properties of 24 minidrill Samples from Olkiluoto. Geological Survey of Finland, POSIVA-WR_04_01. Eurajoki, Finland. 1-24.
Pankhurst, R.J., Rapela, C.. W. and Fanning, C.M. (2006) Gondwanide continental collision and the origin of Patagonia. Earth-Science Reviews, 76: 236–257.
Planke, S., Svensen, H., Myklebust, R., Bannister, S., Manton, B. and Lorenz, L. (2014) Geophysics and Remote Sensing. Advances in Volcanology. Springer International Publishing Switzerland. 1-26. DOI: 10.1007/11157_2014_6.
Polteau, S. A., Mazzini, O., Planke, S. and Malthe-Sørenssen, A. (2008) Saucer-shaped intrusions: Occurrences, emplacement and implications. Earth and Planetary Science Letters, 266(1–2): 195–204.
Poudjom-Djomani, Y. H., Ebinger, C. E., Diament, M. and Fairhead, J.D. (1995) Effective elastic thickness variations in West-Central Africa inferred from gravity data. Journal of Geophysical Research, 100: 22047–22070.
Pretorius, P.H. (2006) Electric and magnetic fields from overhead power lines. Empetus Close Corporation Report EMP / D / 06 / 005 / R01. Johannesburg. 1-43.
Ranganai, R.T. (2012) Euler deconvolution and spectral analysis of regional aeromagnetic data from the south-central Zimbabwe craton: tectonic implications. African Journal of Science and Technology, 12(1): 34–50.

Ravat, D. (2007) Reduction to Pole. In: Gubbins, D. and Herrero-Bervera, E. eds. Encyclopedia of Geomagnetism and Paleomagnetism. Springer. Dordrecht. https://doi.org/10.1007/978-1-4020-4423-6_275.

Reeves, C. (2005) Aeromagnetic Surveys. Principles, Practice and Interpretation. Geosoft. Netherlands. 1-170.

Regan, R.D. and Cain, J.C. (1975) The use of geomagnetic field models in magnetic surveys. Geophysics, 40(04): 621–629.

Rochette, P., Jackson, M. and Aubourg, C. (1992) Rock magnetism and the interpretation of magnetic susceptibility. Reviews of Geophysics, 30(3): 209–226. DOI: 10.1029/92RG00733.

Rogers A.W. and Schwarz, E.H.L. (1902) Report on parts of the divisions of Beaufort West, Prince Albert and Sutherland. 7TH Annual Report of Cape Geological Commission of the Cape of Good Hope. 97–128.

Rowsell, D.M. and de Swart, A.M.J. (1976) Diagenesis in Cape and Karoo sediments, South Africa Potential, and its bearing on their hydrocarbon. Transactional. Geological Society South Africa. 81–145.

SACS (South African Committee for Stratigraphy). (1980) Stratigraphy of South Africa. Part 1. L.E. Kent, compiler. Handbook Geological Survey of South Africa, Pretoria, 8: 690.

SACS (South African Committee for Stratigraphy). (2019) Task Group for the Karoo Supergroup minutes held on the 6th February 2019. 5.

Sakala, E.; Havenga, M.; Ledwaba, L.; Dube, M.; Buthelezi, M.; Sekiba, M.; Nxantsiya, Z.; Hobo, M. and Mahlatji, M. (2017) Geophysical interpretation of high resolution airborne geophysical data collected over the alluvial block 1 and 2, South Africa. In Council for Geoscience Report 2017-0009. Pretoria. 6-7.

Scheiber-Enslin, S. E., Ebbing, J. and Webb, S.J. (2015) New Depth Maps Of The Main Karoo Basin, Used To Explore The Cape Isostatic Anomaly. South African Journal of Geology, 118(3): 225–248.

Scheiber-Enslin, S. E., Ebbing, J. and Webb, S.J. (2014a) An integrated geophysical study of the Beattie Magnetic Anomaly, South Africa. Tectonophysics, 636: 228–243. http://dx.doi.org/10.1016/j.tecto.2014.08.021.

Scheiber-Enslin, S.E., Webb, S.J. and Ebbing, J. (2014b) Geophysically Plumbing the Main Karoo Basin, South Africa. South African Journal of Geology, 117(2): 275–300. http://sajg.geoscienceworld.org/cgi/doi/10.2113/gssajg.117.2.275.

Smith, C.B., Clark, T.C., Barton, E.S. and Bristow, J.W. (1994) Emplacement ages of kimberlite occurrences in the Prieska region, southwest border of the Kaapvaal Craton, South Africa. Chemical Geology, 113(1–2): 149–169.

Smith, R.M.H. (1990) A review of stratigraphyand sedimentary environments of the Karoo Basin of South Africa. *Journal Of African Earth Science*, 10: 117–137.

Smith, R.M.H. (1993) Vertebrate taphonomy of Late Permian floodplain deposition in the southwestern Karoo Basin of South Africa. Palaios, 8: 45–67.

Söhnge, A.P.G. (1983) The Cape Fold Belt - perspective. In Söhnge, A.P.G. and Hälbich, I. W. eds. Geodynamics of the Cape Fold Belt. Special Publication Geological Society of South Africa. 184.

Spector, A. and Grant, F.S. (1970) Statistical model for the interpretation of aeromagnetic data. Geophysics, 35: 293–302.

Stettler, E.H; Fourie, C.J.S and Cole, P. (2000) Total magnetic field intensity map of the Republic of South Africa (in 4 panels). Council for Geoscience. Pretoria.

Storey, B. C. and Kyle, P.R. (1997) An active mantle machanism for Gondwana breakup. South African Journal of Geology, 100(4): 283–290.

Struers. (2014) Labotom-5 instruction manual 16047001. Struers. Denmark.
Sunjay, S., S Kumar, S and Jain, N. (2014) Shale Gas: An Unconventional Gas Reservoir. In: Hachay, O. and Gaci, S. eds. Advances in Data, Methods, Models and Their Applications in Oil/Gas Exploration. Science Publishing Group. 3–22.
Svensen, H., Jamtveit, B., Planke, S. and Chevallier, L. (2006) Structure and evolution of hydrothermal vent complexes in the Karoo Basin, South Africa. Journal of the Geological Society, 163: 671–682.
Svensen, H., Planke, S., Chevallier, L., Malthe-sørenssen, A., Corfu, F. and Jamtveit, B. (2007) Hydrothermal venting of greenhouse gases triggering Early Jurassic global warming. Earth and Planetary Science Letters, 256: 554–566.
Talwani, M. and Heirtzler, J.R. (1964) Computation of magnetic anomalies caused by two-dimensional bodies of arbitrary shape. In: Parks, G. A. ed. Computers in the mineral industries. Geological Sciences. 464–480.
Tankard, A., Welsink, H., Aukes, P., Newton, R. and Stettler, E. (2012) Geodynamic interpretation of the Cape and Karoo Basins, South Africa. In: Roberts, D. and Bally, A. eds. Regional Geology and Tectonics: Phanerozoic Passive Margins, Cratonic Basins and Global Tectonic Maps. Amsterdam: Elsevier: 868–945.
Tankard, A., Welsink, H., Aukes, P., Newton, R. and Stettler, E. (2009) Tectonic evolution of the Cape and Karoo basins of South Africa. Marine and Petroleum Geology, 26(8): 1379–1412. http://dx.doi.org/10.1016/j.marpetgeo.2009.01.022.
Telford, W. M., Geldart, L. P. and Sheriff, R. (1990) Applied Geophysics. 2nd ed. New York: Cambridge University Press.
Telford, W.M., Geldart, L.P. and Sheriff, R.E. (1976) Applied Geophysics. 2nd ed. New York: Cambridge University Press.
Thomas, R., Marshal, C., du Plessis, A., Fitch, F., Miller, J., von Brunn, V. and Watkeys, M. (1992) Geological studies in southern Natal and Transkei: Implications for the Cape Orogen. Inversion tectonics of the Cape Fold Belt, Karoo and Cretaceous Basins of Southern Africa. 229–236.
Veevers, J.J., Cole, D.I. and Cowan, E.J. (1994) Southern Africa: Karoo Basin and Cape Fold Belt. Geological Society of America. 1–58.
Viglietti, P.A., Rubidge, B.S. and Smith, R.M.H. (2017) Revised lithostratigraphy of the upper Permian Balfour and Teekloof formations of the main Karoo Basin, South Africa. South African Journal of Geology, 120(1): 45–60.
Viljoen, J.H.A. (1990) K-bentonites in the Ecca Group of the south and central Karoo. South African Journal of Geology, 94: 576–579.
Visser, J.N.J. (1992) Deposition of the Early to Late Permian Whitehill Formation during a sealevel highstand in a juvenile foreland basin. South African Journal of Geology. 181–193.
Visser, J.N.J. (1987) The palaeogeography of part of southwestern Gondwana during the Permo-Carboniferous glaciation. Palaeogeography Palaeoclimatology Palaeoecology, 61: 205–219.
Visser, J.N.J. (1991) The paleoclimatic setting of the late Paleozoic marine ice sheet in the Karoo Basin of southern Africa. In: and Anderson, J. B. and Ashley, G.M. eds. Glacial marine sedimentation: Paleoclimatic significance. Geological Society of America Special Paper 261: 181–189.
Walker, F. and Poldervaart, A. (1949) Karoo dolerites of the Union of South Africa. Geological Society of America Bulletin, 60: 591–706.
Wickens, H.D. V. (1994) Submarines fans of the Ecca Formation. PhD Thesis (unpublished), University of Port Elizabeth, South Africa.
Woodford, A C. and Chevallier, L. (2002a) Hydrogeology of the main Karoo Basin :

Current Knowledge and Future Research Needs. In Water Research Commission Report TT 179/02, Pretoria.

Woodford A.C. and Chevallier, L. (2002b) Regional characterization and mapping of Karoo fractured aquifer systems - An integrated approach using a geographical information system and digital image processing. In Water Research Commission Report 653/1/02. Pretoria.

Zahra, H and Oweis, H.T. (2016) Application of high-pass filtering techniques on gravity and magnetic data of the eastern Qattara Depression area , Western Desert , Egypt. *NRIAG Journal of Astronomy and Geophysics*, 5(1): 106–123. http://dx.doi.org/10.1016/j.nrjag.2016.01.005.

11 APPENDICES

11.1 APPENDIX A: Radially Averaged Power spectrum (RAPS) graphs

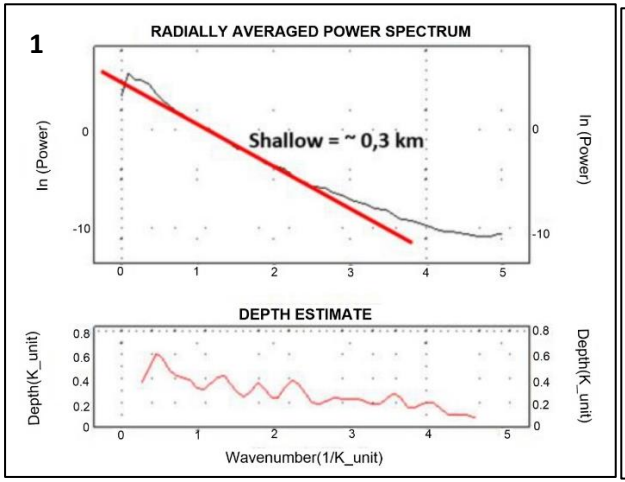

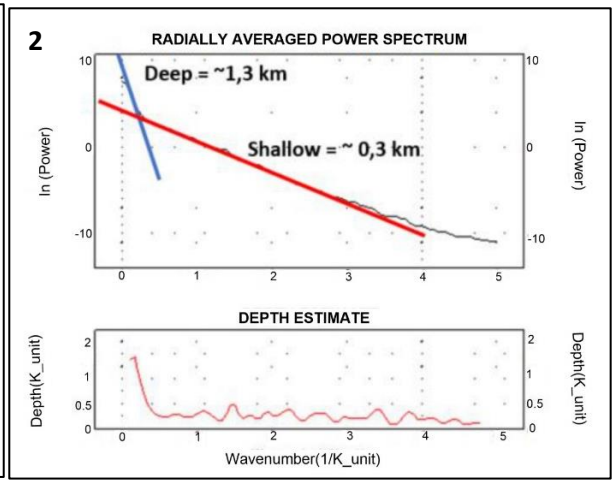

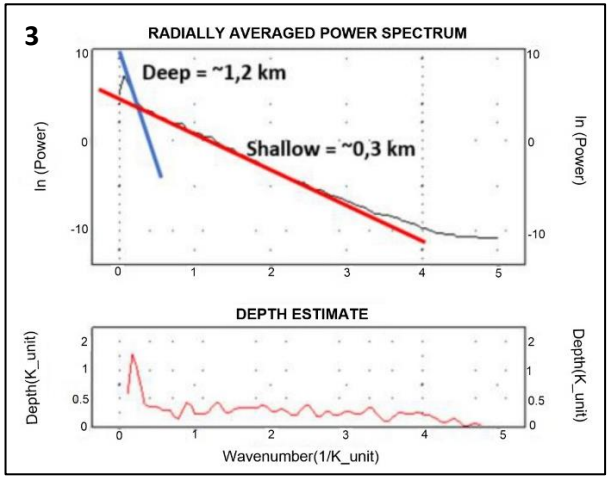

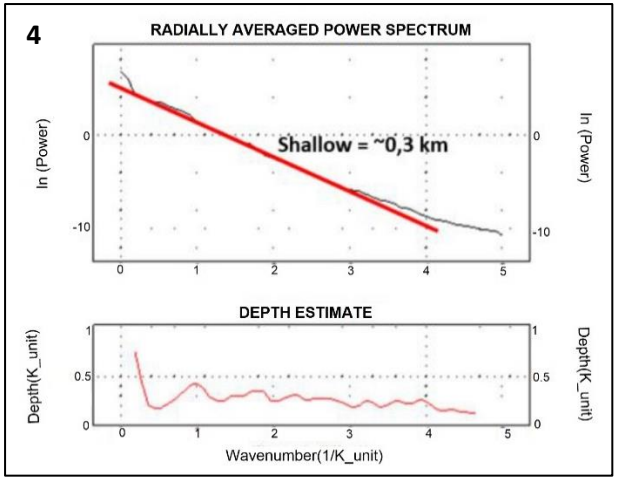
4
RADIALLY AVERAGED POWER SPECTRUM
Shallow = ~0,3 km
ln (Power)
DEPTH ESTIMATE
Depth(K_unit)
Wavenumber(1/K_unit)

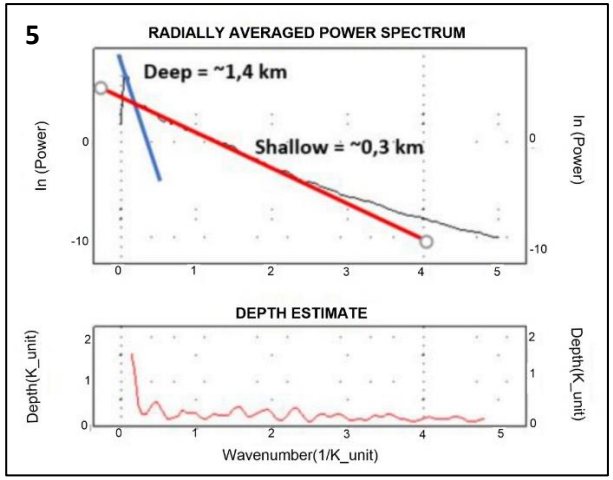
5
RADIALLY AVERAGED POWER SPECTRUM
Deep = ~1,4 km
Shallow = ~0,3 km
ln (Power)
DEPTH ESTIMATE
Depth(K_unit)
Wavenumber(1/K_unit)

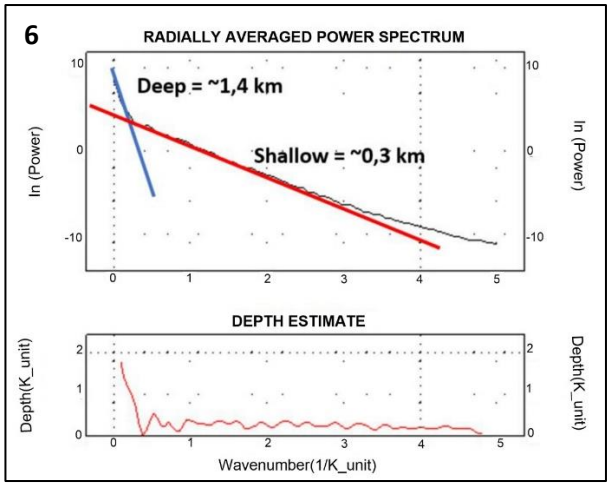
6
RADIALLY AVERAGED POWER SPECTRUM
Deep = ~1,4 km
Shallow = ~0,3 km
ln (Power)
DEPTH ESTIMATE
Depth(K_unit)
Wavenumber(1/K_unit)

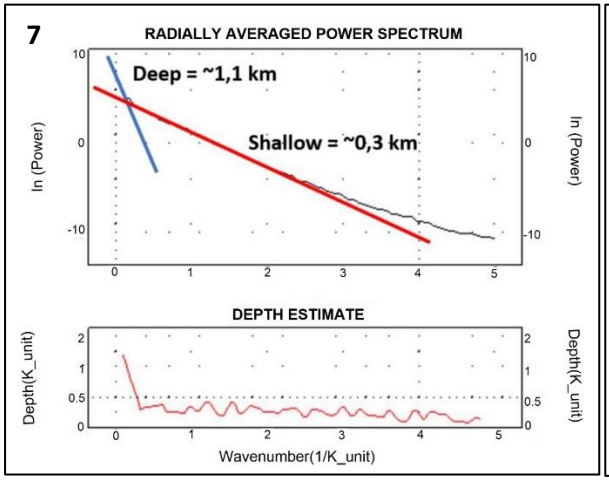
7
RADIALLY AVERAGED POWER SPECTRUM
Deep = ~1,1 km
Shallow = ~0,3 km
ln (Power)
DEPTH ESTIMATE
Depth(K_unit)
Wavenumber(1/K_unit)

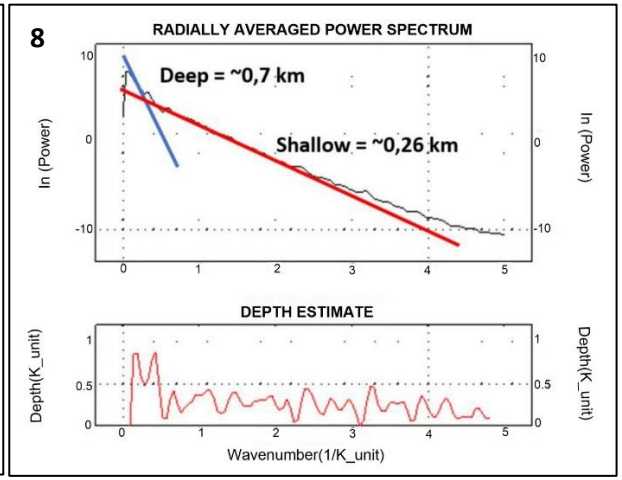
8
RADIALLY AVERAGED POWER SPECTRUM
Deep = ~0,7 km
Shallow = ~0,26 km
ln (Power)
DEPTH ESTIMATE
Depth(K_unit)
Wavenumber(1/K_unit)

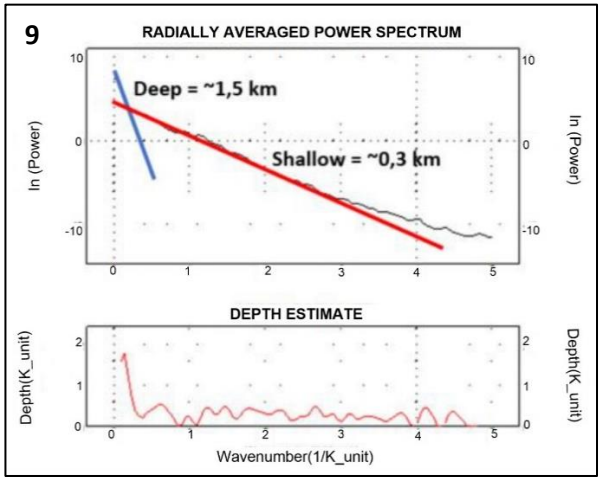
9
RADIALLY AVERAGED POWER SPECTRUM
Deep = ~1,5 km
Shallow = ~0,3 km
ln (Power)
DEPTH ESTIMATE
Depth(K_unit)
Wavenumber(1/K_unit)

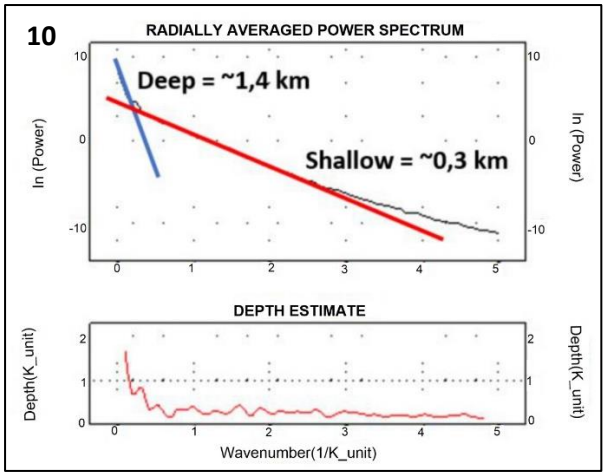
10
RADIALLY AVERAGED POWER SPECTRUM
Deep = ~1,4 km
Shallow = ~0,3 km
ln (Power)
DEPTH ESTIMATE
Depth(K_unit)
Wavenumber(1/K_unit)

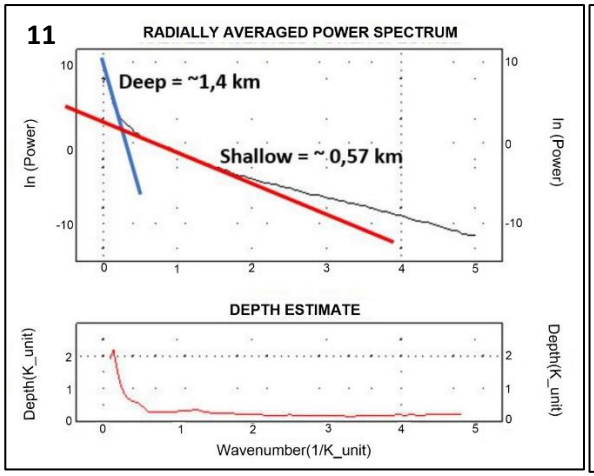
11
RADIALLY AVERAGED POWER SPECTRUM
Deep = ~1,4 km
Shallow = ~ 0,57 km
ln (Power)
DEPTH ESTIMATE
Depth(K_unit)
Wavenumber(1/K_unit)

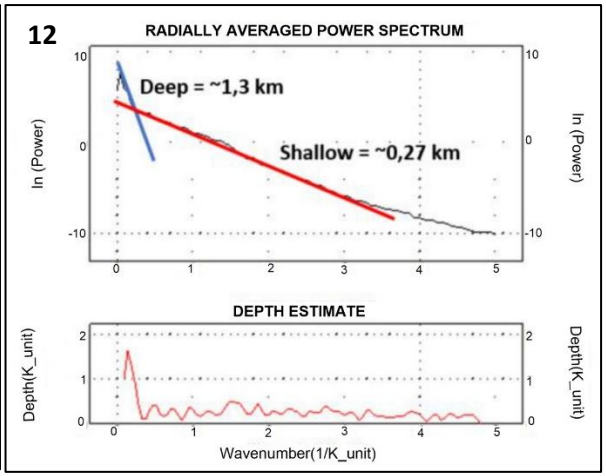
12
RADIALLY AVERAGED POWER SPECTRUM
Deep = ~1,3 km
Shallow = ~0,27 km
ln (Power)
DEPTH ESTIMATE
Depth(K_unit)
Wavenumber(1/K_unit)

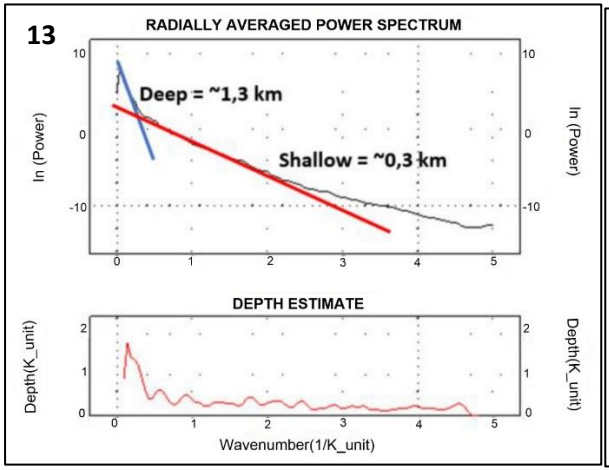
13
RADIALLY AVERAGED POWER SPECTRUM
Deep = ~1,3 km
Shallow = ~0,3 km
ln (Power)
DEPTH ESTIMATE
Depth(K_unit)
Wavenumber(1/K_unit)

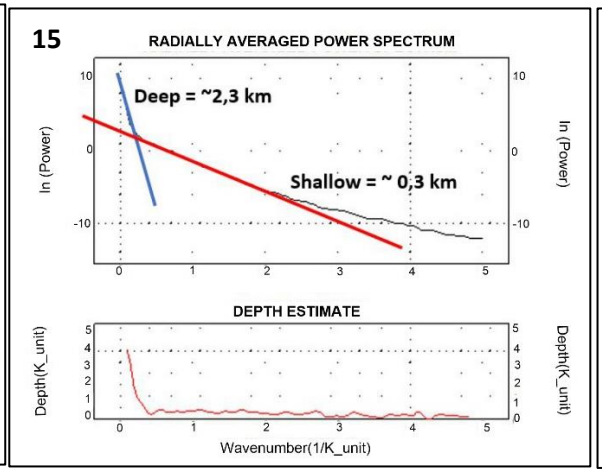
15
RADIALLY AVERAGED POWER SPECTRUM
Deep = ~2,3 km
Shallow = ~ 0,3 km
ln (Power)
DEPTH ESTIMATE
Depth(K_unit)
Wavenumber(1/K_unit)

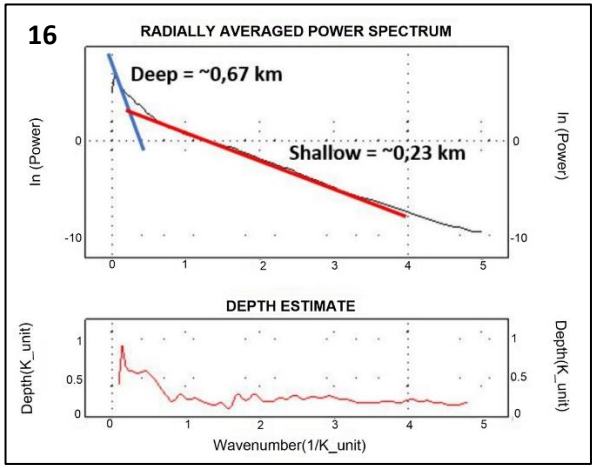
16
RADIALLY AVERAGED POWER SPECTRUM
Deep = ~0,67 km
Shallow = ~0,23 km
ln (Power)
DEPTH ESTIMATE
Depth(K_unit)
Wavenumber(1/K_unit)

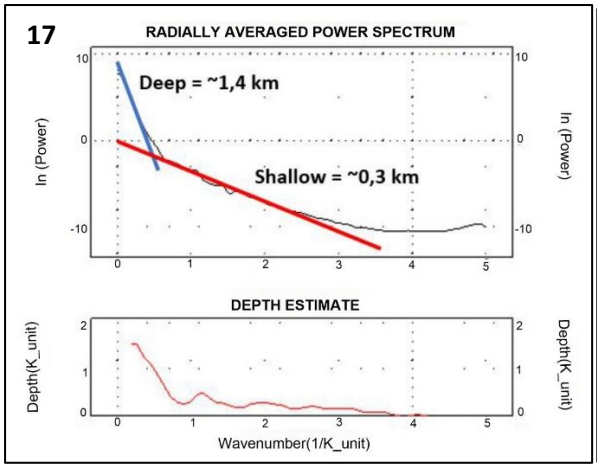
17
RADIALLY AVERAGED POWER SPECTRUM
Deep = ~1,4 km
Shallow = ~0,3 km
ln (Power)
DEPTH ESTIMATE
Depth(K_unit)
Wavenumber(1/K_unit)

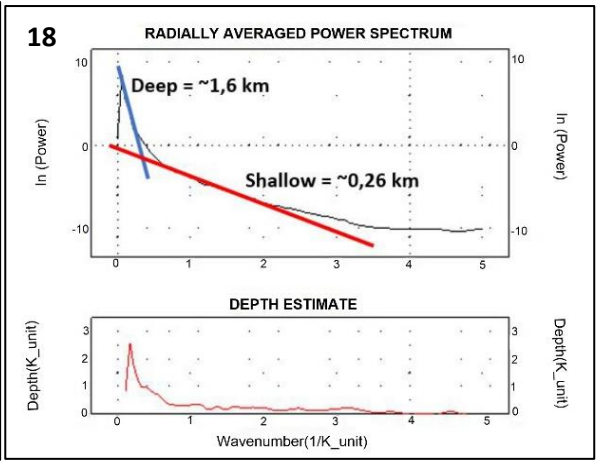
18
RADIALLY AVERAGED POWER SPECTRUM
Deep = ~1,6 km
Shallow = ~0,26 km
ln (Power)
DEPTH ESTIMATE
Depth(K_unit)
Wavenumber(1/K_unit)

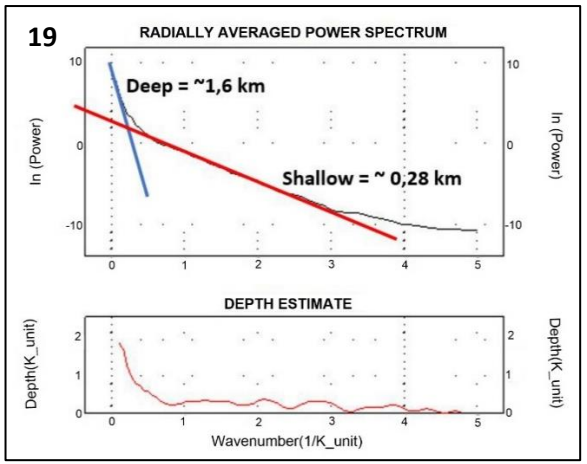
19
RADIALLY AVERAGED POWER SPECTRUM
Deep = ~1,6 km
Shallow = ~ 0,28 km
ln (Power)
DEPTH ESTIMATE
Depth(K_unit)
Wavenumber(1/K_unit)

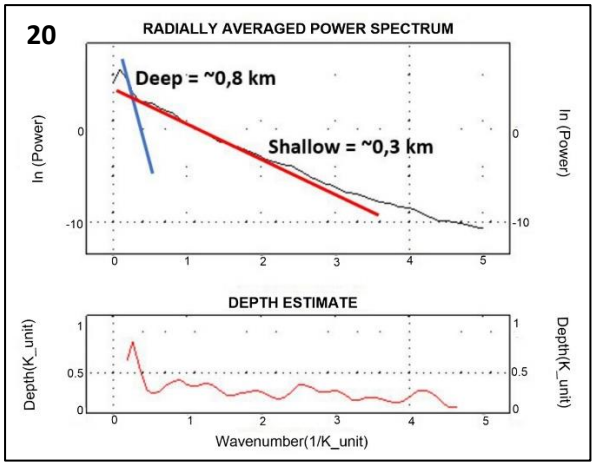
20
RADIALLY AVERAGED POWER SPECTRUM
Deep = ~0,8 km
Shallow = ~0,3 km
ln (Power)
DEPTH ESTIMATE
Depth(K_unit)
Wavenumber(1/K_unit)